Transient and nonlinear dynamics of triadic resonance for internal waves

Kevin Ha

INSTITUT POLYTECHNIQUE DE PARIS

NNT : 2021IPPAX076

Thèse de doctorat

ÉCOLE POLYTECHNIQUE

IP PARIS

Transient and nonlinear dynamics of triadic resonance for internal waves

Thèse de doctorat de l'Institut Polytechnique de Paris
préparée à l'École polytechnique

École doctorale n°626 École doctorale de l'Institut Polytechnique de Paris (EDIPP)
Spécialité de doctorat : Mécanique des fluides et solides, acoustique

Thèse présentée et soutenue à Palaiseau, le 8 novembre 2021, par

KEVIN HA

Composition du Jury :

Michael Le Bars Directeur de recherche, Université Aix-Marseille (IRPHE)	Président
Sylvain Joubaud Maître de conférence, ENS Lyon (Laboratoire de Physique)	Rapporteur
Jean-Christophe Robinet Professeur des Universités, ENSAM (DynFluid)	Rapporteur
Chantal Staquet Professeur de l'Université Grenoble Alpes	Examinatrice
Jean-Marc Chomaz Directeur de recherche, École Polytechnique (LadHyX)	Directeur de thèse
Sabine Ortiz Professeur de l'ENSTA Paris	Codirectrice de thèse

Résumé en français

Depuis plus d'une vingtaine d'années, la modélisation numérique couplée est de plus en plus utilisée en sciences du climat et de l'environnement. Aussi connus sous le nom de modèles de circulation générale ou General Circulation Models (GCM), ces modèles sont idéalisés et permettent de simplifier le système climatique. Pour prévoir l'évolution du climat, les scientifiques utilisent des GCM où interagissent les modèles atmosphériques, océaniques et de la dynamique des surfaces continentales. Un modèle couplé permet d'étudier les différentes modifications futures de l'environnement. Or les études récentes montrent que le climat calculé par ces modèles dépend fortement de la distribution horizontale mais aussi verticale du mélange dans l'atmosphère et l'océan.

Il a été proposé par Garrett & Kunze (2007) que le mélange océanique résulterait du déferlement des ondes internes de gravité engendrées par l'interaction entre la marée océanique et la topographie du fond (du plateau continental, montagne sous-marine). En effet, la présence de corps célestes induit un courant horizontal uniforme sur toute la colonne d'eau dans l'océan, connu comme la marée barotrope très bien mesurée par altimétrie satellitaire. En présence de la topographie, cette marée barotrope interagit avec le fond marin et rayonne des ondes internes, appelées marées internes. Leur dissipation par déferlement induit une turbulence tridimensionnelle qui contribue au mélange vertical de l'océan profond, et donc joue un rôle dans la circulation océanique à grande échelle en induisant un flux vertical de salinité et de chaleur. Il en est de même pour les ondes engendrées par l'action des vents en surface dans la couche mélangée de surface et qui se propagent dans la couche profonde à travers la thermocline (zone de transition thermique rapide entre les eaux superficielles et les eaux profondes). Le déferlement des ondes ainsi engendrées est affecté par des mécanismes analogues à ceux de la marée interne (croissance transitoire, propagation d'instabilités...).

Comprendre la circulation océanique est un ingrédient essentiel pour la prévision du climat. Les marées internes comme les ondes internes engendrées à la surface sont des ondes de moyennes échelles (méso échelle), bien au-dessous des échelles résolues dans les modèles numériques climatiques actuels. La turbulence et le mélange qui en résultent sont eux aussi à très petites échelles et doivent être paramétrés. La variabilité spatiale que ce mécanisme physique induit dans le mélange, à la fois horizontalement et verticalement, pourrait induire une circulation océanique profonde radicalement différente de celle calculée par les modèles actuels reposant sur une hypothèse de mélange uniforme. À l'heure actuelle, il existe peu de théorie pour guider la prise en compte de ces petites échelles dans les méthodes numériques (effets sous-maille). Le passage d'une paramétrisation heuristique

basée sur l'observation à une paramétrisation physique basée sur la compréhension des mécanismes permet d'adapter les modèles à des situations jamais observées induites par le changement climatique.

En utilisant à la fois les codes pour la prévision du climat en géométrie simplifiée mais réaliste ainsi que des modèles théoriques prenant en compte la propagation des perturbations, nous étudierons dans cette thèse différents mécanismes physiques d'instabilité d'ondes internes induisant le mélange turbulent. En particulier, nous analyserons comment de faibles perturbations, infinitésimales ou finies, peuvent déstabiliser une onde dans son plan de propagation, donnant naissance à l'instabilité triadique résonante, issue de l'interaction entre trois ondes internes à la résonance. Un tel mécanisme d'instabilité induit la possibilité de transferts de quantités physiques, comme l'énergie ou l'action d'une onde, à des échelles variables. Deux interactions résonantes (Elastic Scattering et Induced Diffusion) à l'origine de modes verticaux cisaillés horizontalement (Vertically Sheared Horizontal Flow modes) feront l'objet d'une analyse approfondie, étant donné leur capacité à conduire à de fortes croissances non-linéaires, puis transitoires (linéaires) de l'énergie de la perturbation.

Les phénomènes physiques ainsi mis en évidence pourraient modifier radicalement la distribution verticale et horizontale du mélange induit par le déferlement d'ondes, et inversement, permettraient de comprendre comment le rayonnement d'ondes internes par des modes d'instabilité peuvent modifier le mélange induit par un cisaillement et faire qu'il se produise à une altitude différente, ce dernier mécanisme pouvant être à l'oeuvre dans l'océan et transférer le mélange de la thermocline vers l'océan profond.

Acknowledgments

This thesis at LadHyX (Laboratoire d'Hydrodynamique de l'Ecole Polytechnique) developed my interest for research in the field of oceanography and climatology and deepened my knowledge in geophysical fluid dynamics.

I would like to take the opportunity to thank all people who contributed in some ways to this thesis, particularly Professor Jean-Marc Chomaz, director of research at CNRS, who welcomed me in the LadHyX in the best conditions, and Professor Sabine Ortiz, professor at ENSTA Paris. Their availability, knowledge and experience in the field of research truly contributed to the success of this three year project. The rich amount of questions and meaningful information on the various points raised at each step of this project pushed me to conduct a real work of research by exploring all the contours of my subject, going in depth with some key features of my work.

My thanks go to all the researchers of the laboratory, especially to Professor Emmanuel Delangre, Director of the LadHyX, who brought this project to life with the support of the Corps des IPEF (Ingénieurs des Ponts, des Eaux et des Forêts), then to Camille Duprat, Researcher at LadHyX, Francesco Picella, Postdoctoral Researcher, and Todd Currier, visiting PhD student from University of Massachusetts, as my climbing mates every midday for building my way out of my daily routine. They introduced me to a world I was unfamiliar with and brought a new passion in my life, rock climbing, in which I can truly express my full potential and surpass myself. I won't forget what you have done for me along with many other climbers and staff members working at the Ecole Polytechnique who inspired me every day: Sandy, François, Christophe, Vincent, Arnaud, Paul, Jacques, Leo, Alexis, Jean-Eric, Briac, Aldjia, Alice Paulin, and Danijela.

Those three years were also marked with many wonderful people I met during my journey among PhD students, postdocs, researchers and staff members with whom I shared memorable moments: Adèle Moncuquet, Anouk Daguin, Oyvind Ellingsen, Tulio Traverso and Francisco Perez, but also Paul Billant and Ernesto Horne who all brought good vibes at work. A special thanks go to all current and former staff members of the LadHyX, Magali Tutou, Sandrine Laguerre, Caroline Frot, Antoine Garcia, Daniel Guy and Toai Vu for their patience, kindness and attention in helping me out every time I had either a question, a request or simply to discuss about life when swinging by their office, their advice were really useful and appreciated. Thanks to everyone, I discovered a dynamic laboratory that tackles many interesting subjects, had found many answers along this thesis, and experienced a positive working atmosphere.

Lucky me, many people helped me to fulfil this PhD in the best conditions, in partic-

ular my dear friends Robin Despouys and Jean-Sebastien Bloch who truly deepened my computer science knowledge to fully use all the features of the MITgcm in my numerical simulations. I was pleased to be invited at Robin's flat when I had any inquiries or questions with the code. It was also a truly awesome opportunity to listen to your guitar songs and your homemade rap texts while sharing a game of Rocket League with you between two running simulations. To think that we randomly met at a party Matthieu Rambaud invited me to... and finally ended up collaborating in this project was just unexpected, so, again, thank you Robin. I also want to thank Adham El Zaher, whose internship was precious in the success of this thesis. His commitment and initiatives were really appreciated, along with his curiosity, which raised many interesting questions along the project. We also had the chance to share interesting views on existential questions concerning life, along with a couple of prognosis at each game of Euro 2020.

When looking back at those three years, names like Matthieu Rambaud and Christophe Gerbron can't be forgotten, you were literally my brothers in arms. As my true partners, we shared some of the best moments during my PhD. We could literally follow each other everywhere in all kinds of crazy situations, trips and adventures (snowboarding, wakeboarding, kitesurfing, paragliding and so on), giving me the opportunity to fully express my adventurous spirit and reconnect with nature, ultimately reminding me who I am and what I stand for. Along with my former friend from my childhood, Remi Viard, they are the people I can truly count on, anywhere, anytime! Surprisingly enough, I have the chance to be close to my all my childhood friends (in my heart as well as geographically, for 29 years now): Sam Karvanpour, Etienne Fontan, Jonathan Alev, Vivien Aube, Maxime Tayon, Remi Viard, Julien Cantin and Julien Helm. Spending some weekends of my thesis with you guys made me realize that even if we went through a long way together, there is still a long way to go apparently, with, of course, all the positive vibes that characterize our long lasting relationship.

Finally, I would like to warmly thank my family who supported me in my everyday life and especially during my studies from preparatory school at Stanislas to Ecole Polytechnique, including the double diplomas with Columbia University, Ecole des Ponts and AgroParisTech. Thank you for believing in me, even in the hardest moments, you bring me joy, hope and serenity, and forged me into who I have become, bringing me now to the conclusion of eleven years of graduate education.

Contents

Part I

Introduction

Chapter 1

General context

1.1 Description of the climate system

The *climate system* refers to the highly complex system made of five major components that shape the global environment of our planet: the atmosphere, the oceans, the cryosphere (snow, ice and permafrost), the land surface, the biosphere, and the interactions occurring between them as illustrated in figure 1.1. These environments interact continuously through physical, chemical or biological processes. Some have slow evolution, over millions to billions of years, which is the case of solid media such as glaciers, sea ice or the outermost layers of the land surface e.g. the lithosphere and the asthenosphere. The others have a faster evolution: it is the case of the atmosphere and the ocean. These two fluids play a major role by allowing numerous strong and rapid interactions between different regions of the globe, which then exchange mass, heat and momentum fluxes. *Climate* is defined as the set of statistics which describes the climate system in a given location over a period of few decades. The ocean and the atmosphere are at the core of mechanisms that drive climate variations or climate fluctuations and affect our planet on various time scales that go from months to years. Statistics determining the climate and its variations are not only mean values, but also correspond to recurring events like El Niño, or much rarer events (100-year floods and storms).

Despite their importance in the dynamics of the climate system, the atmosphere and ocean are in reality two very thin layers compared to the large-scale view of the Earth's surface: the average radius of our planet is 6400 km, whereas approximately 80% of the mass of the atmosphere are located in the first 15 km near the ground, and the average depth of the ocean is 3,8 km. Even though the atmosphere and ocean are very different due to their density and equations of state, this geometrical particularity makes them similar and a common mechanical description is possible for some phenomena occurring in both of them and that are studied in this manuscript. Indeed, the atmosphere and the ocean share two common characteristics making their movement often not very intuitive: first, they move on a spherical rotating surface and second, they are stratified, meaning that under the effect of gravity, their density decreases with height. The scientific field specialized in the study of stratified rotating fluids is called *geophysical fluid dynamics*.

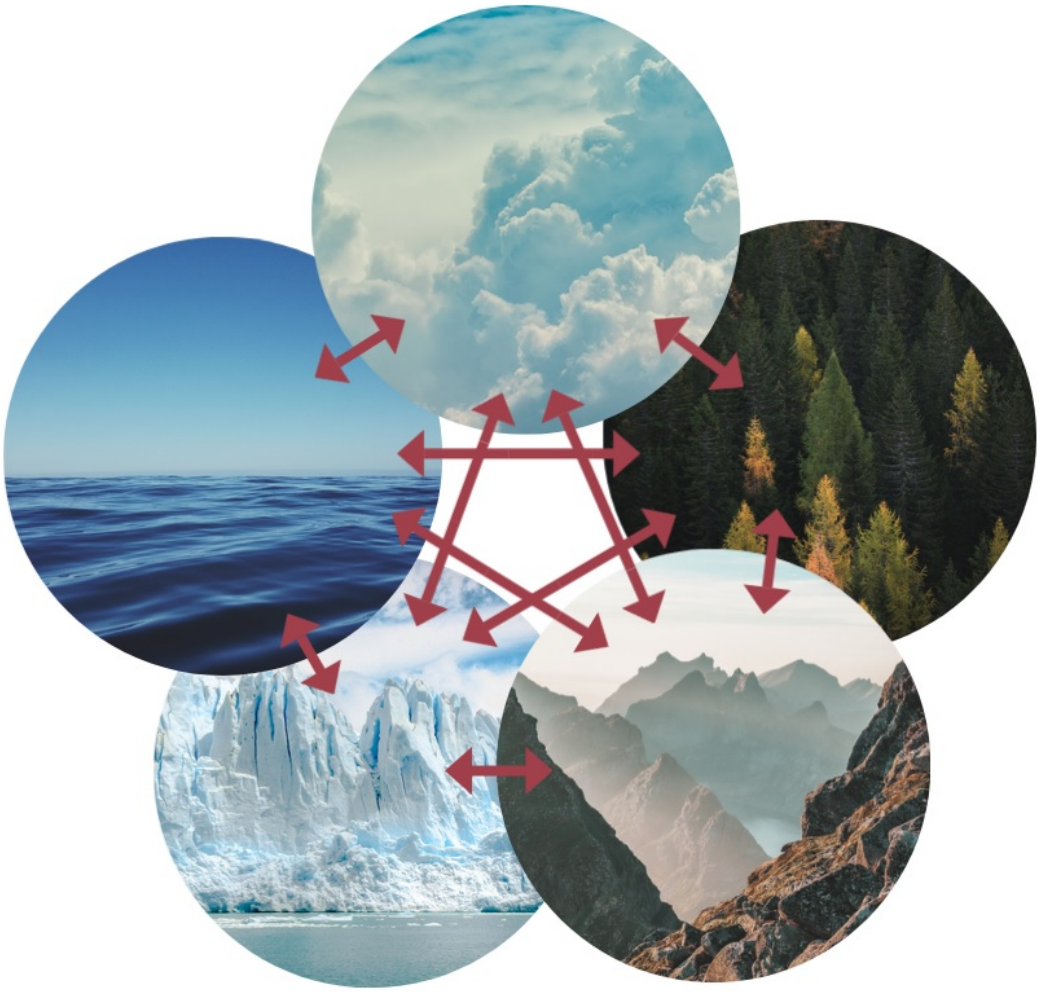

Figure 1.1: The five components of the climate system, the atmosphere, the oceans, the cryosphere, the land surface, the biosphere, and the way they all interact. Source: Wikipedia.

1.2 Numerical climate models

Climate models have made a tremendous step forward over the last decades and major advances are still to come in the next decades. The first IPCC[1] report in 1990 presented simulations based on three models when doubling CO_2 release into the atmosphere. The atmospheric models used at that time were spatially low resolution, e.g. approximately 500 km between two successive horizontal nodes with ten vertical levels, and were coupled with highly idealized oceanic models made of a well-mixed layer of water of tens of meters of thickness. Only one team made preliminary tests with a real coupled ocean-atmosphere model which included a numerical representation of the uppermost layer of the sea and the deep ocean. On the contrary, the models used for the last decade now all are coupled ocean-atmosphere model. The increasing resources in computational time (thousands of calculations per second in the fifties, some ten million in the seventies and some billion recently) generated a consistently supported gain of spatial resolution. The majority of atmospheric models used in the second IPCC report of 1995 presented a 500 km spatial horizontal resolution, and this resolution was improved up to 100 km in the IPCC report of 2007. This step forward might seem modest, but concerns all three dimensions in space, and also affects the time step of models. Furthermore, simulations were extended in time and repeated after perturbation to assess what remains unpredictable. They include a larger variety of physical, chemical and biological processes. However, technological progress cannot explain everything, the combination of computational progress with strong theoretical developments is what highlighted the approximations of Navier-Stokes equations and their significance in many different contexts: from global to regional scales, from tropical to mid latitude systems, short or long term predictions, and so on.

The use of numerical models describing the climate system is essential for a great number of applications such as predicting its short term behavior for meteorologists, or to evaluate the impact of human activity in the long run. The development of those models meets a social need because they are often the unique tools able to guide policy making to preserve the global environment of our planet. For more than twenty years now, coupled numerical models are being used increasingly in environmental and climate sciences. Also known as General Circulation Models (GCM), those computer codes give an idealized representation of the climate system. To predict the evolution of climate, scientists use GCM which couple models describing the dynamics of the atmosphere, the ocean, the continents and glaciers. Observations from direct numerical simulations of these coupled models are key in the study of the future modifications of our environment. The constant growth of computing power will result sooner or later in the reformulation of the climate models in depth, since the frontier between numerically resolved and non-resolved phenomena is constantly moving toward smaller spatial scales.

1. Intergovernmental Panel on Climate Change.

1.3 Vertical mixing in the deep ocean

The climate is strongly controlled by the oceanic circulation, which is still incompletely understood. A key process in the circulation of the ocean is the vertical mixing[2], which makes it possible for dense deep water to reach the surface. As illustrated in figure 1.2a), water masses flow through the entire ocean with a system of oceanic currents whose global circulation forms the Ocean Conveyor Belt (also called Meridional Overturning Circulation[3]). At the poles, ocean water becomes cold and salty as a result of evaporation and ice formation, creating sinking currents that flow and spread in the deepest part of Earth oceans, in the Atlantic, Southern, Indian and Pacific Oceans. When returning to equatorial latitudes where the ocean is heated in surface by air-sea fluxes, the water masses become warmer, rise as a consequence (upwelling), and flow back to the poles to close the global cycle. While the map of the surface horizontal currents and gyres involved in the Ocean Conveyor Belt is shaped by winds and Earth rotation, the vertical currents are sustained by the stratification resulting from density gradients, depending on the amount of heat and salt carried by water masses, responsible for their sinking and upwelling movements[4], as well as their vertical mixing.

Figure 1.2b) strongly emphasizes this verticality and shows that the circulation of heat and salt, namely the thermohaline circulation, is intrinsically 3D[5] as it involves horizontal and vertical currents flowing from Antarctica (surrounded by the Southern Ocean) to three different regions of the globe (Indian, Pacific, and Atlantic Oceans) eventually closing cycles of the Ocean Conveyor Belt. The present 3D representation of the ocean highlights how water masses from different sites merge, corresponding to every color changes in the arrows of the figure, so the Antarctic Bottom Water (AABW) is consumed by North Atlantic (NADW), Pacific (PDW) and Indian (IDW) Deep Waters, before upwelling and flowing back to Antarctica with Antarctic Intermediate Water (AAIW) and Sub Antarctic Mode Water (SAMW), with residual thermocline water. In this global circulation system, the water masses, when merging, constantly change in composition.

Not only does the flow contain heat and salt, but also other compounds coming from nature or human activity. Figure 1.3 indicates the contribution of air-sea fluxes to the transfer of heat, oxygen, anthropogenic and natural carbon to the surface currents at different latitudes of the globe, from the poles to the equator. Mentioned in the present figure, the Gulf Stream plays an important role in the global circulation, as it represents a

2. C. Wunsch and R. Ferrari, "Vertical Mixing, Energy, and the General Circulation of the Oceans", in: *Annu. Rev. Fluid Mech.* 36.*1* (2004), pp. 281–314.

3. E. Kunze, "The Internal-Wave-Driven Meridional Overturning Circulation", in: *J. Phys. Oceanogr.* 47.*11* (Nov. 2017), pp. 2673–2689.

4. R. Ferrari and C. Wunsch, "Ocean Circulation Kinetic Energy: Reservoirs, Sources, and Sinks", in: *Annu. Rev. Fluid Mech.* 41.*1* (2009), pp. 253–282.

5. A. Lefauve, C. Muller, and A. Melet, "A three-dimensional map of tidal dissipation over abyssal hills", in: *J. Geophys. Res.: Oceans* 120.*7* (2015), pp. 4760–4777.

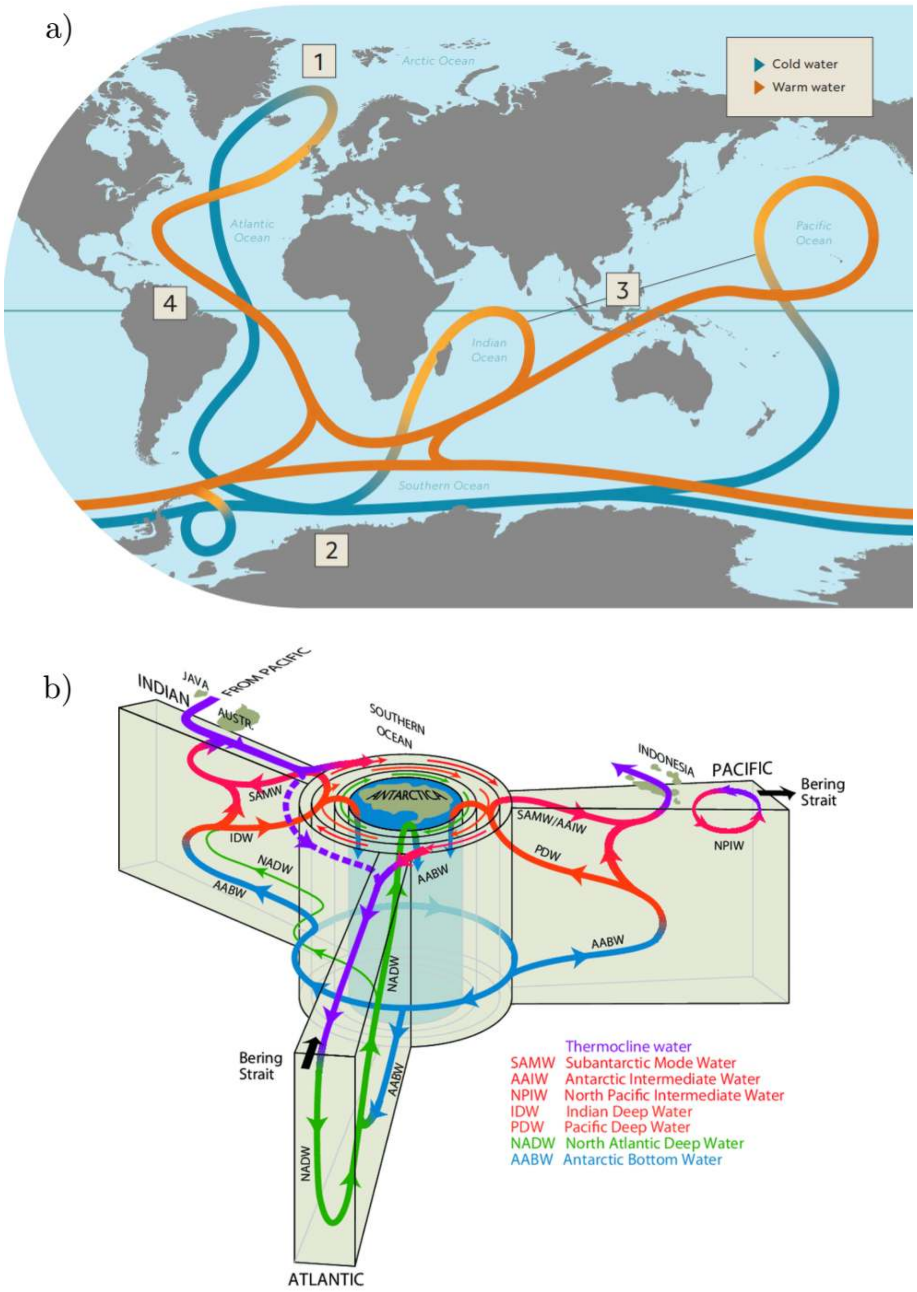

Figure 1.2: a) Illustration of the Ocean Conveyor Belt with a highlight on four main characteristics of the induced thermohaline circulation labeled 1, 2, 3 and 4. Warm currents are represented in orange and cold ones are in blue. In 1, the ocean cooling at the poles resulting from evaporation and ice formation causes cold dense salty water to form, sink and slowly spread at the bottom of the ocean. In 2, this cold salty water freely flows from Arctic to Antarctica, passing through the abyss of the Atlantic Ocean, finally splitting into different currents in the Southern Ocean, one going to the Indian Ocean, the other to the Pacific Ocean. In 3, all the abyssal currents rise to the surface through the upwelling process driven by the surface heating of the ocean when the cold water approaches equatorial latitudes in the Indian, Pacific and Southern Oceans. In 4, the newly formed warm surface currents flows northward, completing the cycle. Source: National Geographic (`https://www.nationalgeographic.org/media/global-conveyor-belt/`). b) 3D representation of the thermohaline circulation due to the currents of the Ocean Conveyor Belt. From Talley (2013).

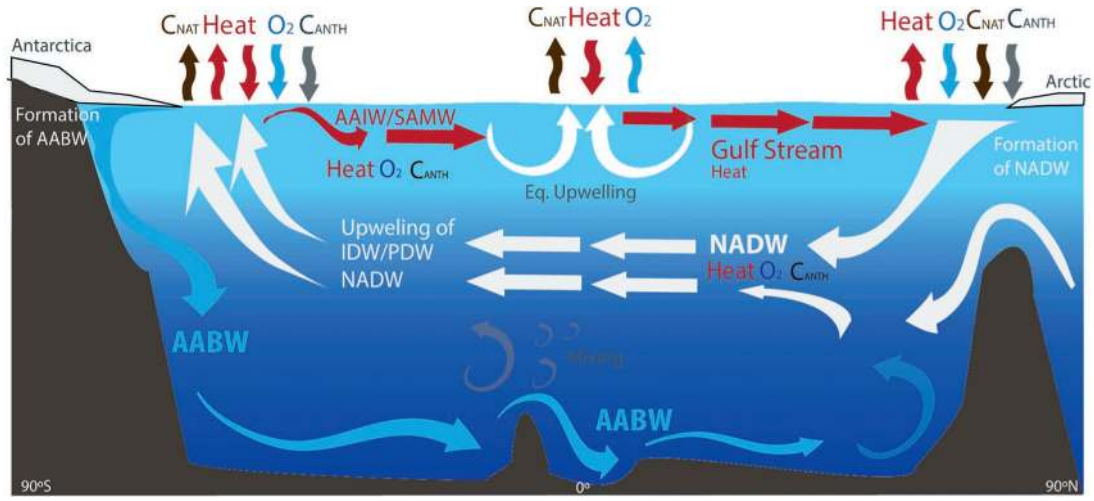

Figure 1.3: 2D schematic detailing the mean air-sea fluxes resulting from the exchanges of heat, oxygen (O_2), anthropogenic (C_{ANTH}) and natural carbon (C_{NAT}), all being then transported throughout the entire ocean by the currents of the Ocean Conveyor Belt. The air-sea fluxes appear in the atmosphere with red, blue, grey and black arrows representing exchanges of heat, O_2, C_{ANTH} and C_{NAT} respectively, and the currents in the ocean are represented in red, white and blue arrows for the surface, intermediate and deep waters respectively. The different water masses correspond to the ones introduced in figure 1.2 where AABW stands for Antarctic Bottom Water, NADW for North Atlantic Deep Water, IDW for Indian Deep Water, PDW for Pacific Deep Water, AAIW for Antarctic Intermediate Waters, and SAMW for Sub Antarctic Mode Water. From Delorme & Eddebar (2016).

strong Atlantic ocean current transporting warm water at a rate of 30 million $m^3\,s^{-1}$ from the Gulf of Mexico, measuring typically 100 km wide and 800 m to 1,2 km deep. In their course, water masses exchange physical (heat), chemical (oxygen, carbon, salt), biological (nutrients, plankton) and geological (sediments) tracers with their local environment over 1000-year cycles[6], essential for the life of marine species, ultimately contributing to the balance of the global ecosystem. How the human activity impacts this equilibrium needs to be understood and modeled accurately to predict future modifications to the environment despite not having been observed up until now.

Global warming regulation by the ocean then depends on mechanisms controlling the vertical mixing of deep water masses. It was recently proposed that the mixing results from the overturning of internal waves generated by interaction between deep oceanic tides and currents with the bottom topography (continental shelf, underwater mounts), along with many other sources of generation, as depicted in figure 1.4. First, tidal flows over abyssal hills, or tall, steep ridges (such as the Hawaiian Ridge) give birth to high and low-mode[7] internal wave. Storm and winds cause inertial oscillations to form in the mixed layer[8], resulting in the radiation of high and low-mode internal waves too. On the other hand, deep currents impinging on topographic features generates lee waves[9] (such as in the Southern Ocean[10]). The present figure shows the topographic scattering of the generated internal waves, which propagates in the open ocean (see ray paths) where they may interact with other propagating waves, geostrophic currents, or mesoscale fronts and eddies until they ultimately dissipate and break. Low-mode propagation may also lead to dissipation near continental slopes and shelves[11]. The scientific community suggested wavewave interactions to be one path leading ultimately to dissipation.

Astronomical data report that approximately 3.5 TW[12] of tidal energy are available for dissipation in the ocean, mainly due to the moon slowing down the Earth rotation and inexorably moving away from us. For a long time, people thought that most of this energy was dissipated in shallow waters where tidal currents are strong. But recent satellite data indicate that approximately 1 TW could be dissipated in the deep ocean as indicated in

6. R. E. Tuerena et al., "Internal Tides Drive Nutrient Fluxes Into the Deep Chlorophyll Maximum Over Mid-ocean Ridges", in: *Glob. Biogeochem. Cycles* 33.*8* (2019), pp. 995–1009.

7. High-mode internal waves dissipate in the near field while low-mode internal waves dissipate in the far field. Waves with vertical scales comparable to the ocean depth have small mode numbers (low-mode internal waves), whereas those with smaller vertical scales have large mode numbers (high-mode internal waves).

8. a.k.a. the thermocline, the transition layer between warmer mixed water at the ocean's surface and cooler deep water below.

9. Lee waves are internal waves that are formed in the lee of a mountain.

10. A. Melet et al., "Sensitivity of the Ocean State to Lee Wave-Driven Mixing", in: *J. Phys. Oceanogr.* 44.*3* (Mar. 2014), pp. 900–921.

11. S. Legg and A. Adcroft, "Internal Wave Breaking at Concave and Convex Continental Slopes*", in: *J. Phys. Oceanogr.* 33 (Jan. 2002); K. Martini et al., "Internal bores and breaking internal tides on the Oregon continental slope", in: (2013).

12. TeraWatts

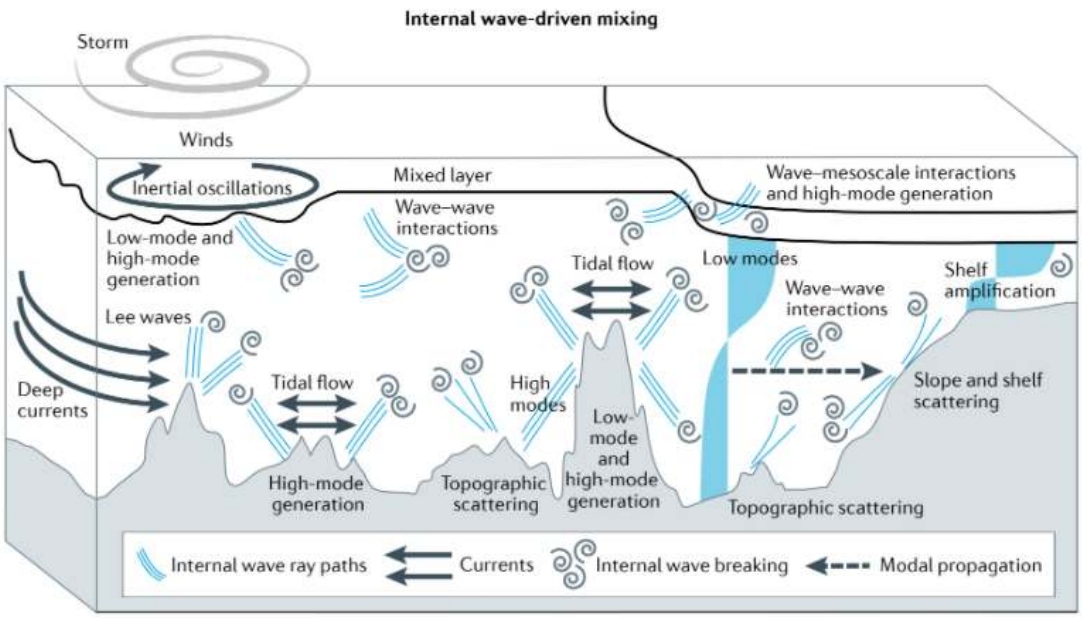

Figure 1.4: Illustration of the different sources of internal wave generation in the open ocean. From MacKinnon et al. (2017).

figure 1.5. The same figure also reveals that the generation of near inertial waves[13] due to the interaction between the wind and the mixed upper layer of the ocean accounts for an energy budget estimated from 0.3 up to 1.4 TW, when being also proposed as a possible source for deep ocean mixing through mechanisms similar to the turbulence[14]. In addition to their contribution to lee wave generation when interacting with topographic features, wind driven currents are also found to feed the previous near-inertial wave field, contributing to 1 TW of the global energy budget of the internal wave field in the ocean. Wave-wave, wave-topography and wave-mean flow interactions are detailed with arrows between the different propagating waves, showing that wave-wave interactions, topographic scattering and reflection, and interaction with the background current field actually play a crucial role in the dissipation of the global energy budget dedicated to internal waves. The underlying physics behind those interactions must be understood and thoroughly investigated to model accurately the ocean state in the context of climate prediction, while bringing answers to the fundamental question: how is tidal energy and surface born internal waves dissipated in the abyssal ocean?

We have seen that one of the mechanisms for tidal dissipation is the breaking of small scale internal waves. The presence of celestial bodies induces a current in the ocean, known as the barotropic tide. In the presence of topography, this barotropic tide interacts with

13. Inertial waves are internal waves with frequency nearly equal to the Coriolis parameter, a measure of Earth rotation frequency at a given latitude. See section 3.2 for more details.

14. Wave turbulence, also called weak turbulence, is a branch of fluid mechanics developed in the 60s studying the evolution of random wave fields on all scales. It typically assumes that weak nonlinear interactions between three waves of the same kind, namely triadic interaction, lead to an energy cascade from large (forcing) scales up to small (dissipative) ones

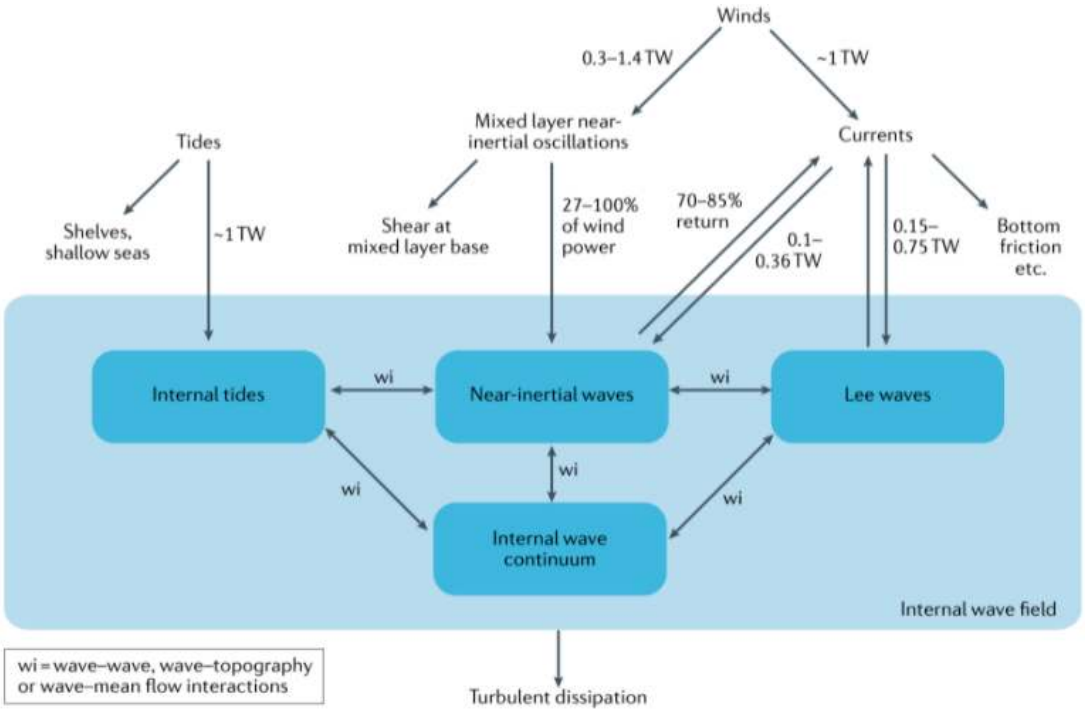

Figure 1.5: A simplified diagram showing the global energy budget of internal waves. From Whalen et al. (2020).

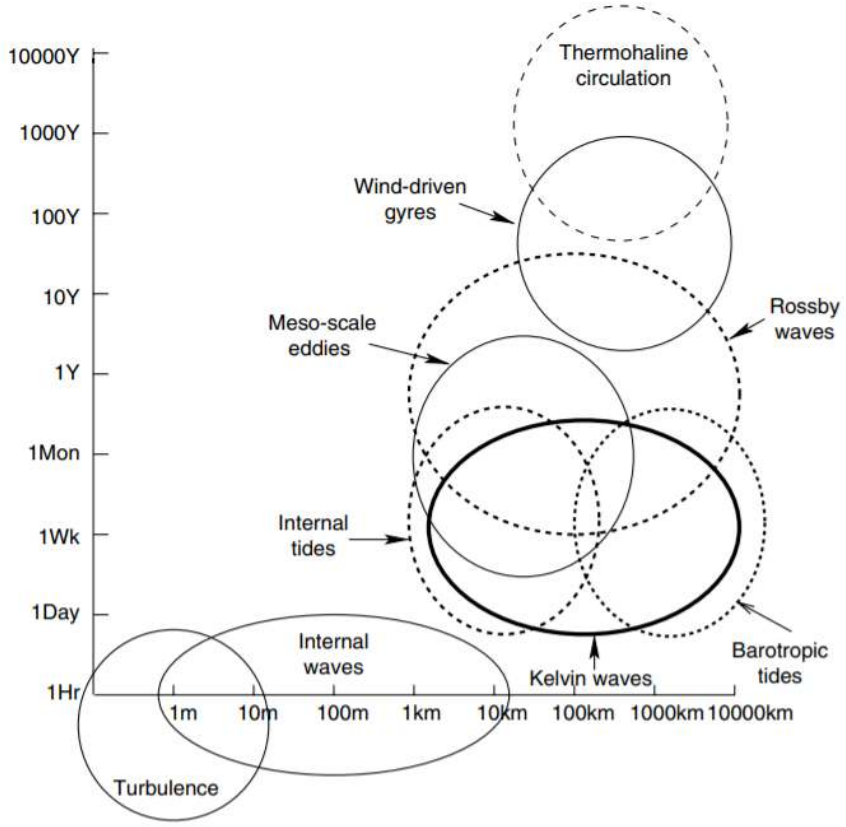

Figure 1.6: Space and time scales of different geophysical phenomenon contributing to the thermohaline circulation and sustaining the global overturning circulation. From Huang (2010).

the seafloor resulting in the radiation of internal waves, known as the internal tides. Their dissipation through wave breaking and concomitant three dimensional turbulence contributes to the vertical mixing in the deep ocean, and plays a role in the large scale ocean circulation. Figure 1.6 displays the typical time and space scales of each process reviewed in this section. The present figure demonstrates that, although the scales inherent to some of the physical processes may intertwine, for instance Kelvin waves[15] and barotropic tides, the scale separation from the turbulence and internal waves up to the thermohaline circulation clearly indicates the role of mesoscale and small scale mechanisms in large scale flows[16]. As a matter of fact, the estimates[17] indicate that typical scales are thousands kilometers and months ($10^2 - 10^6$ km and $10^1 - 10^4$ days) for large scale flows, kilometers and hours ($10^{-1} - 10^3$ km and $10^{-3} - 10^0$ days) for waves, and submeters and seconds ($10^{-6} - 10^{-2}$ km and $10^{-6} - 10^{-3}$ days) for turbulence. The induced small scale mixing (having spatial scales of order centimeter to meter and having spatial scales of seconds) caused by internal waves (0.1100 m and lasting for minutes to hours) is essential for sustaining the global overturning circulation and closing the ocean energy budget, but remains challenging to parametrize numerically in global climate models, which currently rely on idealized empirical mixing schemes. Idealized analytical and numerical studies of tidal conversion have concentrated on the energy conversion rate, which is the rate at which energy is lost by the barotropic tide to the internal waves at the sea floor. Large scale ocean circulation models used for climate prediction require a parametrization of the small scale mixing based on empirical global maps of this energy conversion rate at the sea floor together with ad hoc methods for the distribution of the energy dissipation and diffusivity due to breaking waves throughout the water column, whose estimates are based on the Garrett & Munk spectrum (1979)[18], a stationary state approximation widely used to statistically[19] describe the nonlinear transfer of energy between scales of the deep open ocean. Currently, there is little theory to guide these methods, in particular as far as the vertical distribution of wave breaking is concerned. Previous studies in large scale numerical models typically assumed exponential decay of dissipation away from topography. But is it really exponential?

To summarize, understanding the ocean circulation is not only a fascinating topic in itself, but also a crucial ingredient for climate prediction. Generated at the bottom of the

15. Kelvin waves and Rossby waves are two kinds of planetary waves, i.e. waves having immense scales observed in the atmospheres and oceans of planets.

16. C. Whalen, J. MacKinnon, and L. Talley, "Large-scale impacts of the mesoscale environment on mixing from wind-driven internal waves", in: *Nat. Geosci.* 11 (Nov. 2018).

17. R. X. Huang, *Ocean Circulation: Wind-Driven and Thermohaline Processes*, Cambridge University Press, 2010.

18. C. Garrett and W. Munk, "Internal Waves in the Ocean", in: *Annu. Rev. Fluid Mech.* 11.*1* (1979), pp. 339–369.

19. In natural media, identifying each single process for internal waves from generation and propagation to instability, turbulence and breaking remains difficult, a statistical approach is more appropriate.

ocean where the the currents interact with the bathymetry[20], internal waves propagate upwards and destabilize, causing the mixing of water masses. Internal waves and their induced turbulence are small scale, well below scales resolved by global numerical models. As a consequence, their breaking and dissipation need to be parametrized, ultimately calling for the need to improve the current numerical modeling of all the physical mechanisms related to internal waves, in particular the resulting mixing, from a traditional passive and unchanging parametrization to a fully interactive component of the ocean circulation and the climate system[21]. The induced spatial and temporal variability in the mixing, both horizontally and vertically, could imply a radically different interior circulation in the models than that with uniform mixing schemes.

20. ocean floors, bottom topography.

21. J. A. MacKinnon et al., "Climate Process Team on Internal Wave-Driven Ocean Mixing", in: *Bull. Am. Meteorol. Soc.* 98.*11* (Nov. 2017), pp. 2429–2454.

Chapter 2

Focus on internal waves research

Internal waves develop in the interior of the atmosphere and the ocean due to their intrinsic stratification in heat and salt, and to Earth rotation. More precisely, the term *internal waves* refers to three different types of geophysical waves, the first being *internal gravity waves* formed in a purely stratified medium, the second *inertial waves* driven by Earth rotation, and the third *gravito-inertial waves* due to the combination of stratification and rotation effects. Studies of internal waves in the ocean are motivated by their major role in the vertical mixing of deep water masses, an essential component to understand and model the global circulation of the ocean.

2.1 From internal waves generation to weakly non-linear wave-wave interaction

The linear theory describing the generation and propagation of those waves is well-known and gathered in Gill's textbook (1982)[1] which recalls all the fundamental properties of the corresponding plane waves[2]. One of the most famous experimental evidence of those waves confirming the results given by the linear theory is the experiment from Mowbray & Rarity (1967)[3], whose visual of the St. Andrew's Cross displayed in figure 2.1 usually serves as a pedagogical introduction to internal waves. Their experimental setup consists of a sphere oscillating vertically in a stratified fluid whose density increases linearly with depth, resulting in the generation of four ray paths of internal gravity waves observed by toepler-schlieren method[4]. This fundamental experiment shows the good agreement between predictions from the linear theory and experimental observations in terms of wave frequencies, hence testing the validity of the theoretical dispersion relation of internal gravity waves, which only depends on the direction of the ray paths[5].

1. A. E. Gill, *Atmosphere-ocean dynamics*, International geophysics series, New York: Academic Press, 1982.

2. See part 4.1 for the full linear derivation of internal waves.

3. D. E. Mowbray and B. S. H. Rarity, "A theoretical and experimental investigation of the phase configuration of internal waves of small amplitude in a density stratified liquid", in: *J. Fluid Mech.* 28.*1* (Apr. 1967), pp. 1–16.

4. an optical technique involving an extended light source with a system of mirrors producing contrasting visuals to observe disturbances in an inhomogeneous medium.

5. more precisely, on the angle between one ray and an axis of reference. See part 4.1 for further details.

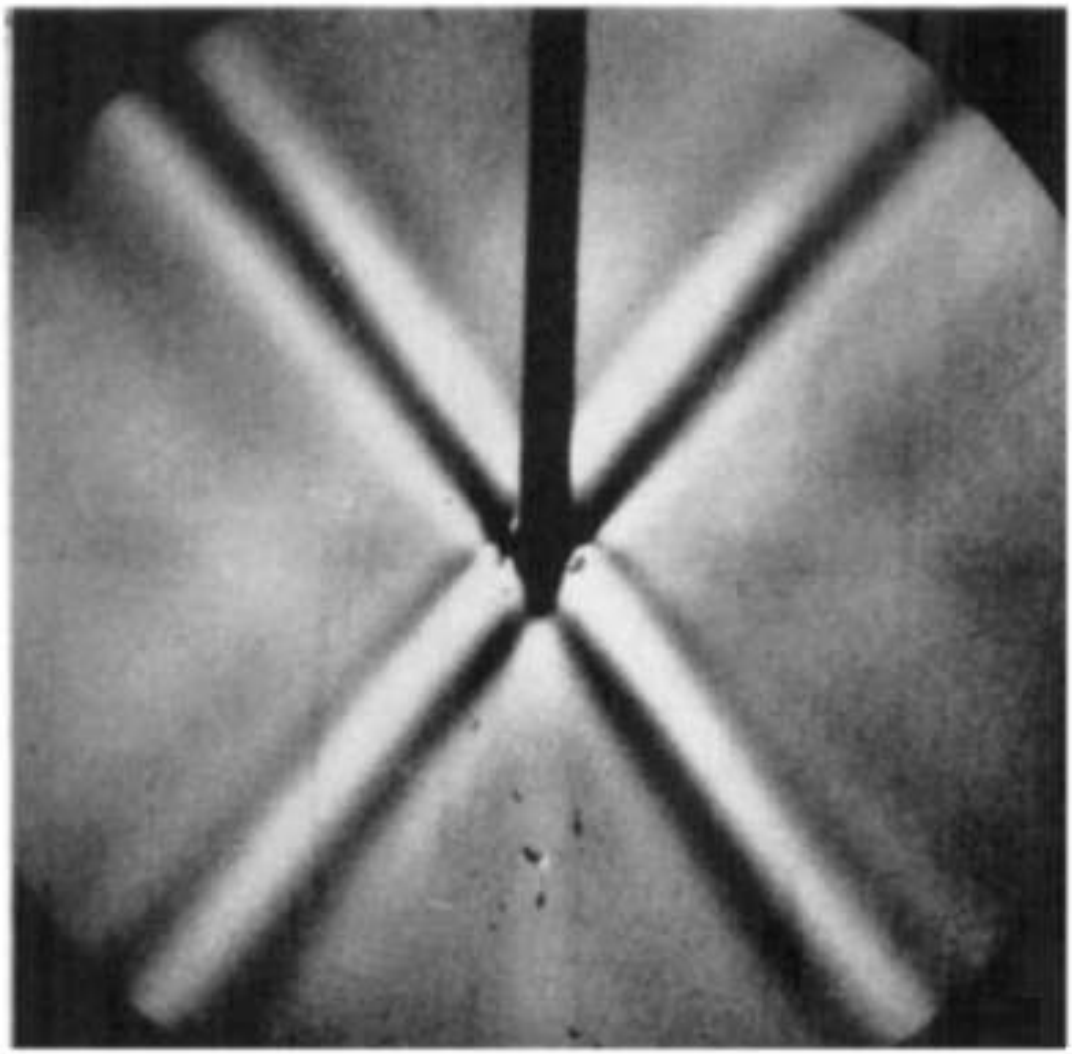

Figure 2.1: Illustration of the St. Andrew's Cross capturing the generation of internal gravity waves in laboratory when a forcing cylinder oscillates in a stratified fluid at a frequency ω equal to a multiple of the BruntVäisälä frequency N, the characteristic frequency of the linearly stratified medium (see part 3.1 for more details). Here $\omega = 0.699N$. From Mowbray & Rarity (1967).

Internal waves generation resulting from the interaction between deep ocean currents and bathymetry is interestingly modeled by the experiment conducted by Sutherland (2002)[6], which demonstrates, in a tank containing a linearly salt-stratified fluid, the radiation of internal waves in the lee of a step-shaped topography towed horizontally at a uniform speed, along with the generation of lee waves, using synthetic schlieren as a technique of visualization as illustrated on figure 2.2 in a) and b). With laboratory measures of the frequencies and amplitudes of both types of waves to see if they match, Sutherland evidenced the ability of the lee waves to radiate internal waves away from the lee of the topography, the former lee waves acting then as radiating "fluidic" hills, and to interact nonlinearly with the generated internal waves, this nonlinearity being enhanced for steeper topographies. Indeed, figure 2.2c) shows diagonal rays, in red/orange and green/blue for positive upward and negative downward vertical displacements respectively, radiating away from the crest and the lee of the "fluidic" hills, characteristics of generated internal waves propagating upward. In addition to reproducing a geophysical configuration in laboratory, this experiment features the combination of linear and nonlinear properties of internal waves, showing how they intertwine, the internal waves not only being passively generated by the topography but also by nonlinearities over the "fluidic" hills[7], and stands as an experimental evidence of wave-wave interaction, theoretically captured by the nonlinear terms of the constitutive equations describing the dynamics of the flow as we will see later on.

One striking feature of wavelike solutions is that not only do they solve the linearized dynamical equations, but also the full nonlinear system of constitutive equations when considering a stratified rotating fluid at rest as the base flow. Developing the fundamental equations of fluid dynamics around this base state when submitted to small perturbations, the resulting weak nonlinearities are characterized by coupling terms between two physical fields that appear to be quadratic in terms of the streamfunction of the wave, allowing three internal waves to be coupled if they satisfy the resonance conditions in terms of their frequencies and wave vectors, ultimately leading to a weakly nonlinear interaction known as the triadic resonant instability. In the steady regime, the stability of internal waves triads is stated by Hasselmann's criterion (1967)[8] as depending on the sign of the secondary waves frequencies product. However, is this criterion still relevant to describe the transient dynamics of such triads[9]? In his work, Hasselmann typically assumes the amplitude of one wave, called primary wave and considered as the base state, to be infinitely larger than the amplitudes of the two other waves, named secondary waves and

6. B. R. Sutherland, "Large-amplitude internal wave generation in the lee of step-shaped topography", in: *Geophys. Res. Lett.* 29.*16* (2002), pp. 16–1–16–4.

7. for a steep topography leading to the radiation of large-amplitude internal waves characterized by a Froude number greater than one, see Sutherland (2002) for more details.

8. K. Hasselmann, "A criterion for nonlinear wave stability", in: *J. Fluid Mech.* 30.*4* (Dec. 1967), pp. 737–739.

9. one key question here that this project will try to answer...

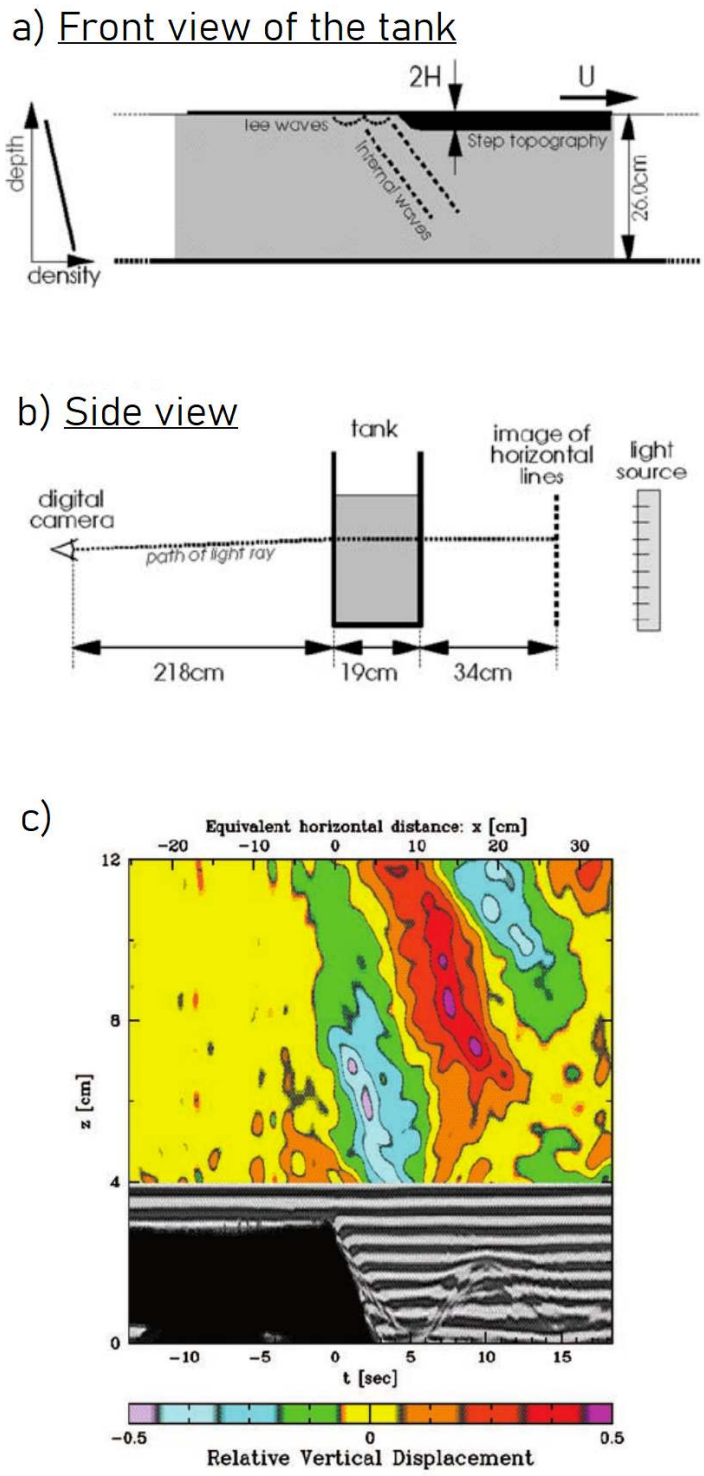

Figure 2.2: a) Schematic of Sutherland's experiment showing the tank in which the step-shaped topography of height $2H$ is towed at a constant speed U in a linearly stratified fluid. b) Synthetic schlieren uses a digital camera to capture the image of horizontal lines after the light source. c) Time series of the relative vertical displacement z as a function of time t. The image of the towed topography is superimposed below $z = 4$ cm keeping the same coordinates z, but as a function of the horizontal coordinates $x = Ut$, the whole picture c) being upside down compared to a). From Sutherland (2002).

representing the perturbation to the base state, so that the primary wave amplitude can be regarded as a constant while the secondary waves amplitudes are depending on a slow-time scale (taken as independent from the real time), such a classical approximation being known as the pump wave approximation.

The set of resonant triads forms a continuum, also called resonance locus, allowing energy to be transferred from the primary wave to the perturbation, in multiple ways, and to different scales. As demonstrated by McComas & Bretherton's work on internal waves (1977)[10], three limiting classes of resonant triads, named Elastic Scattering[11], Induced Diffusion and Parametric Subharmonic Instability, dominate the energy transfer integrated over the whole continuum, the last class being even identified as an efficient energy transfer to smaller scales. Indeed, Parametric Subharmonic Instability involves one high-mode primary wave (large scale) interacting with two low-mode secondary waves (small scales) of equal frequencies, half that of the primary wave, and is even pointed out by recent oceanic studies[12] as the main source of internal waves dissipation. Our work focuses on Elastic Scattering and Induced Diffusion due to their critical role in the early development of the triadic instability, those limiting classes being even affected by a particularly intense transient dynamics while producing shear through the generation of Vertically Sheared Horizontal Flow mode[13].

Pioneering work sometimes assumes the dependency of internal waves amplitudes on both slow-time and slow-space variables, such as McEwan & Plumb (1977)[14] who studied theoretically and experimentally the ability of a triadic instability to develop although being not resonant. Such a process is commonly referred to as off-resonant amplification, or detuning effect, whose distance from a precise triad measured in the wave vector space is assumed small. Their experimental setup consists of a rectangular channel filled with a linearly stratified salt solution and in which a fine-scale wave produced by a wave generator is forced by a large scale wave coming from a wavemaker. The resulting instability is observed in the shadowgraph sequence pictured in figure 2.3. Such an experiment confirms the theoretical prediction according to which *instabilities evolve by the development of the wave packet towards resonance*, meaning that, despite being away from resonance with the background large scale wave, the wavenumber of the forced fine-scale wave tends to be directed *towards the nearest part of the resonant locus*, demonstrating how resonant triads turns out to be a universal path to instability. The theoretical derivation of McEwan &

10. C. H. McComas and F. P. Bretherton, "Resonant interaction of oceanic internal waves", in: *J. Geophys. Res.* 82.*9* (Mar. 1977), pp. 1397–1412.

11. also called interaction trapping by Phillips (1968).

12. J. A. MacKinnon et al., "Parametric Subharmonic Instability of the Internal Tide at 29řN", in: *J. Phys. Oceanogr.* 43.*1* (Jan. 2013), pp. 17–28.

13. F. Waleffe, "The nature of triad interactions in homogeneous turbulence", in: *Phys. Fluids* 4.*2* (Feb. 1992), pp. 350–363.

14. A. D. McEwan and R. A. Plumb, "Off-resonant amplification of finite internal wave packets", in: *Dynam. Atmos. Oceans* 2.*1* (Dec. 1977), pp. 83–105.

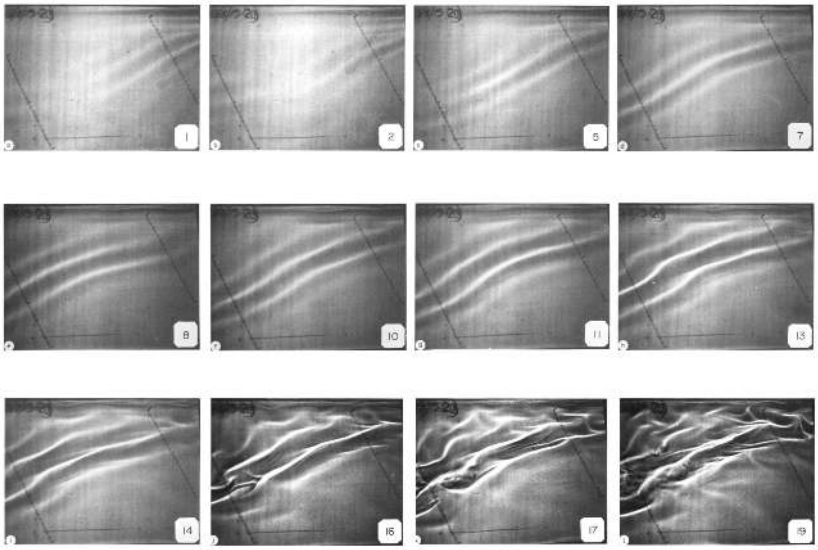

Figure 2.3: Shadowgraph sequence of the growing instability in the experiment of McEwan & Plumb resulting from the interaction between the background large scale wave (traveling left to right) and the off-resonant fine-scale wave (entering from the upper hand corner) at different stages displayed in terms of multiple of the large scale wave period indicated in the bottom right corner of each picture. From McEwan & Plumb (1977).

Plumb will serve as a starting point to our description of internal waves resonant dynamics, even if, in our case, we won't be exploring the detuning effects on the wave field.

Wave-wave interaction in geophysics can be theoretically derived using two different approaches. The first invokes the variational principle as seen in early works from Whitham (1965)[15] when minimizing the Lagrangian corresponding to water wave systems, this method being later reprised by Simmons (1969)[16] in his studies of internal gravity waves. The second theoretical approach involves a spectral analysis to find the eigenmodes of the operators given by the dynamical equations as demonstrated by Andrews & Mcintyre (1978)[17], or Ripa (1981)[18], who used this method to derive triadic resonance between internal gravity waves with a set of coupled equations known as the three wave interaction equations. This generic system of equations follows the classical Manley-Rowe relations (1956)[19], resulting in the conservation of physical quantities such as the total waves energy and pseudomomentum in the inviscid case. All those results

15. G. B. Whitham, "A general approach to linear and non-linear dispersive waves using a Lagrangian", in: *J. Fluid Mech.* 22.*2* (June 1965), pp. 273–283.

16. W. F. Simmons and M. J. Lighthill, "A variational method for weak resonant wave interactions", in: *Proc. Roy. Soc. Lond.* 309.*1499* (Apr. 1969), pp. 551–577.

17. D. G. Andrews and M. E. Mcintyre, "On wave-action and its relatives", in: *J. Fluid Mech.* 89.*4* (Dec. 1978), pp. 647–664.

18. P. Ripa, "On the theory of nonlinear wave-wave interactions among geophysical waves", in: *J. Fluid Mech.* 103 (Feb. 1981), pp. 87–115.

19. J. M. Manley and H. E. Rowe, "Some General Properties of Nonlinear Elements-Part I. General Energy Relations", in: *Proc. IRE* 44.*7* (July 1956), pp. 904–913.

are reviewed in Craik's textbook (1985)[20] for various types of waves that feature triadic resonance, namely capillary gravity waves[21], internal waves[22], and waves in plasma[23]. The universality of those conservation rules, along with the identical dynamics of triadic resonance given by the three wave interaction equations, despite the differences in the coupled coefficients involved in such equations specific to the physics of each system, may extend the scope of our studies to other types of waves found in many other fields of physics ranging from optics to fluid mechanics.

2.2 Objectives of the thesis and roadmap

The present project investigates the early stage dynamics of resonant triads by showing that a small energy perturbation to the base state, a single internal wave propagating in a stratified rotating medium, may experience tremendous transient growth with respect to a well-defined energy norm, this amplification being higher at initial instants for linearly stable triads than unstable ones. The maximum transients are found for triads involving one nearly inertial mode that generates shear: the vertically sheared horizontal flow mode. The sensitivity of these transients to different physical parameters such as Earth rotation, viscosity and nonlinear effects is tested with theoretical simulations, and in geophysical configurations using a numerical code for climate modeling, the MITgcm.

2.3 Roadmap

Part II of the present manuscript is dedicated to the existing classical theories and models that are relevant to our study of internal waves. This synthesis is divided in two chapters. Chapter 3 starts with a pedagogical introduction to understand how internal gravity waves and inertial waves can be easily deduced when only considering the buoyancy and rotation terms respectively in simplified models describing the dynamics of a fluid parcel. This first chapter introduces the notions of buoyancy and Coriolis frequencies, characteristic to the oscillations of the fluid parcel in stratified and rotating media respectively. Then, chapter 4 theoretically derives the linear and nonlinear properties of gravito-inertial waves by taking inspirations from Gill's textbook (1982)[24], and from

20. A. D. D. Craik, *Wave interactions and fluid flows*, Cambridge monographs on mechanics and applied mathematics, Cambridge [Cambridgeshire] ; New York: Cambridge University Press, 1985.

21. L. F. McGoldrick, "Resonant interactions among capillary-gravity waves", in: *J. Fluid Mech.* 21.*2* (Feb. 1965), pp. 305–331.

22. R. E. Davis and A. Acrivos, "The stability of oscillatory internal waves", in: *J. Fluid Mech.* 30.*4* (Dec. 1967), pp. 723–736.

23. J. Weiland and H. Wilhelmsson, "Coherent non-linear interaction of waves in plasmas", in: *Oxford : Pergamon* 88 (1977).

24. Gill, *op. cit.*

the work of McEwan and Plumb (1977)[25], by extending his work when rotation effects are included, but without taking into account the detuning process of internal waves. The chapter starts in 4.1 with the full dynamical equations describing a 3D stratified rotating flow, and key assumptions are made during the derivation to end up with wave-like solutions (nonlinear terms not taken into account, 2D model with 3 components, all fields being invariant along the transverse direction, and Boussinesq approximation). The weakly nonlinear derivation presented in 4.2, consists of three main steps: the first is the non-dimensionalization of all the fields, followed by an asymptotic expansion for weak nonlinearities measured by infinitely small Froude numbers. Wavelike solutions are found at the first order of the expansion and, at the second order, it is shown that three waves may interact, this process being referred to as triadic resonance, and characterized by a resonance spectrum showing all the possible resonant triads. This three-wave interaction is captured by a set of three nonlinear complex equations, called triadic equations, exhibiting quadratic nonlinearities and conserving three integrals of motion, two of them being the total energy and pseudomomentum intrinsic to the three resonating internal waves. The triadic equations may be linearized when assuming two waves of smaller amplitudes compared to the third. This leads to the so-called Hasselmann criterion (1967)[26], dealing with the linear stability of resonant triads, and whose formulation is adapted to the conventions and notations of the present project.

Part III shows the main results of the thesis, and is divided in four different chapters. The first three chapters 5, 6, and 7 are a compilation of research articles (published or in preparation at the moment), so redundancies may be found in this part, especially when recalling the fundamental equations of internal waves nonlinear dynamics.

Chapter 5 is a reprint from our original publication in Physical Review E[27] which takes the comparison between two different systems, rotating rigid body and rotating fluid, as a starting point to describe the transient dynamics of a small perturbation for any three wave systems, when generalizing the properties found on the two former systems to any kind of waves able to form resonant triads, e.g. involving three wave of the same kind at resonance. Indeed, rotating rigid body and rotating fluid obey to identical nonlinear equations, in terms of angular momentum in the first case and wave amplitudes in the second one, and share common conservation properties since two quadratic integrals of motion appear in each system, total energy and total angular momentum in the first case and total energy and helicity in the second one. The trajectories, solutions to those nonlinear systems, can be represented as ellipsoids of constant values of total angular momentum for the solid and of helicity for the fluid, laying on a unit energy sphere, once the energy norm is taken to be the Euclidean norm. Such representation can be

25. McEwan and Plumb, *op. cit.*
26. Hasselmann, *op. cit.*
27. K. Ha, J-M. Chomaz, and S. Ortiz, "Transient growth, edge states, and repeller in rotating solid and fluid", in: *Phys. Rev. E* 103.*3* (Mar. 2021), p. 033102.

generalized to any kind of three-resonating-wave system obeying to certain conditions, and from this representation, a criterion for the transient growth of perturbation energy to occur is found and expressed in terms of the z components of the phase velocities of the three waves involved in triadic resonance. Relaxation oscillations of the amplitudes may occur as nonlinearities become finite.

Chapter 6 presents an article in preparation for Journal of Fluid Mechanics that focuses on the theoretical aspects of the evolution of a base state represented by a single internal gravity wave, called primary wave, when submitted to a small amplitude perturbation represented by two internal gravity waves referred to as secondary waves, as both interact with the primary wave in the process of triadic resonant instability. The former nonlinear derivations introduced in the previous part are reviewed in the purely stratified case, and novel results are introduced when plotting the optimal energy growth and the associated optimal growth rate to measure the transient growth of perturbation energy of the full triadic system. The main focus of this article is the weakly nonlinear regime obtained after simplifying the triadic equations in the domain of validity of the pump wave approximation. Two limiting classes of triads, named Elastic Scattering and Induced Diffusion, stand out as they exhibit higher transient growth than the other resonant triads. The transient growth of linearly stable and unstable triads were also compared, and then studied when varying two parameters, the viscosity and the primary wave angle, to see how they impact the transient dynamics. Finally, the nonlinear growth of the perturbation energy as a response to a finite perturbation of the triadic system is investigated by representing the conserved quantities, total energy, pseudomomentum, and phase invariant, highlighting the possibility of relaxation oscillations during the nonlinear growth of the perturbation. All the appendices of the presented article are also included in this chapter.

Chapter 7 is based on an article in preparation for Physical Review Fluids which aims at giving a thorough analysis of the nonlinear dynamics of three interacting internal waves, when studying its sensitivity to the variations of the Coriolis parameter. Here, the nonlinear dynamics of a small perturbation energy is shown to be a fundamental feature that shapes the local transient dynamics of the triadic system linearized near a base state. Both nonlinear and transient growth of the perturbation obey to scaling laws inversely proportional to the Coriolis parameter, as rotation tends to attenuate those growing processes.

Finally, chapter 8 focuses on the direct numerical simulations conducted through this project on the MITgcm, a GCM widely used by the community, whose main characteristics are reminded in 8. The goal of this chapter is to observe in a 2D simulation box, the nonlinear and transient dynamics of triadic resonance demonstrated theoretically in the three previous chapters, for a chosen triad of the resonant spectrum.

Part II

Synthesis of the classical theories and models

Chapter 3

Stratification and rotation as driving sources in wave generation

Generation of internal gravity waves occurs in a stratified medium where physical properties, such as the temperature and salinity, vary along the vertical direction, thus leading to a vertical gradient of density, like in the atmosphere and ocean. On the other hand, Earth rotation drives the generation of another type of waves called inertial waves whose frequency matches the Coriolis frequency, or Coriolis parameter, which measures the intensity of the inertial force due to Earth rotation at a fixed latitude. The combination of both effects, stratification and rotation, leads to the growth of inertia-gravity waves and all three waves introduced here (internal gravity, inertia and inertia-gravity waves) have the common property to flow through the interior of the fluid so they are called internal waves, by contrast with surface waves which propagates at the interface of two different fluids (e.g. between air and sea). Internal waves are ubiquitous elements of the atmosphere as illustrated in figure 3.1 by the photograph taken in Mawson, Australia, and of the ocean as shown in figure 3.2 with the internal wave trains captured by the satellite image near the north coast of Trinidad. The following simplified analysis serves as an original standpoint in the further theoretical development of internal waves to better understand the separate influence of stratification and Earth rotation on the dynamics of a fluid parcel.

3.1 Buoyancy driven flows

The atmosphere and ocean are the most common examples of stratified fluids where density varies with altitude (or depth). Internal gravity waves, which are commonly observed in those two fluid layers, transfer energy over long distances and across different scales, playing a major role in the energy balance of the ocean and the understanding of the thermohaline global circulation. The study of internal waves is motivated by their role in the rise of abyssal cold water via their induced mixing process between stratified layers in the deep ocean.

Figure 3.1: Regularly spaced clouds observed in Mawson, Australia. This structure is caused by gravity waves in the Antarctic atmosphere. Source: Australian Antarctic Magazine (2015), `https://www.antarctica.gov.au/magazine/issue-28-june-2015/science/refining-gravity-waves-in-climate-models/`

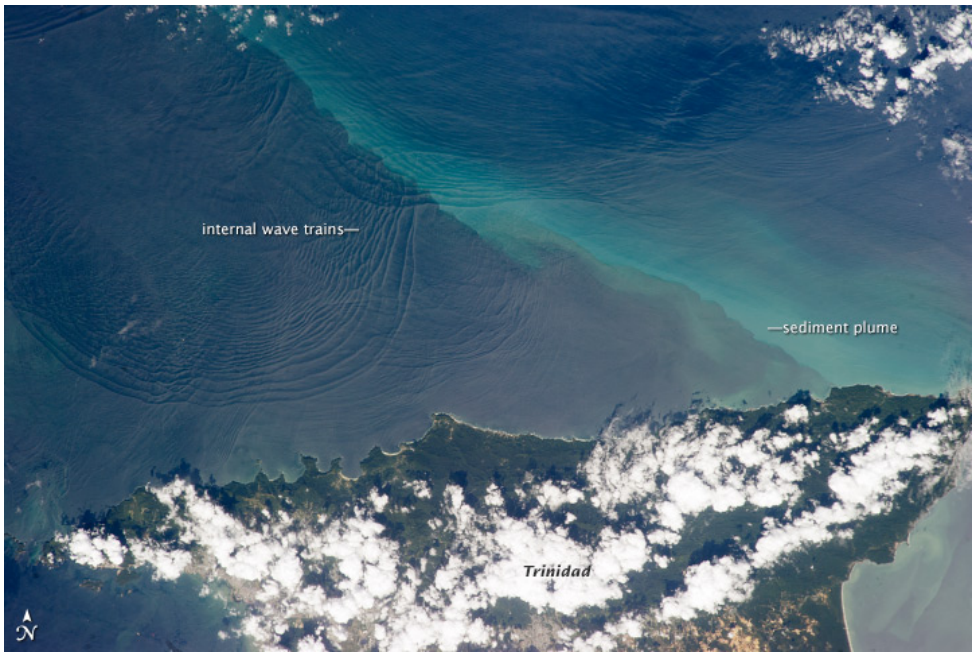

Figure 3.2: North coast of Trinidad with surface manifestation of internal waves which propagates tens of meters beneath the sea surface. The photograph is taken from the International Space Station (ISS) using to reflection of sunlight on the sea surface. Source: NASA (2013), `https://www.nasa.gov/mission_pages/station/multimedia/gallery/iss034e032377.html`

3.1.1 Stratification in density

We consider a fluid parcel of density ρ_r in equilibrium with its surrounding fluid of density at rest $\rho_0(z)$ continuously stratified along the vertical direction (Oz). This dynamical equilibrium leads to $\rho_r = \rho_0(z)$ as a result of the balance between two forces, the weight and Archimedes' buoyancy. Neglecting in the first place the effects of viscosity, diffusivity and convection, a simple perturbation of the fluid parcel out of its equilibrium state by a small increment $\delta z \ll z$ along the vertical direction leads to the momentum equation in time t:

$$\rho_r \frac{d^2\delta z}{dt^2} = \rho_0(z+\delta z)g - \rho_r g \tag{3.1}$$

where g is the standard gravity. The right hand side of the equation can be written as $\rho_0(z+\delta z)g - \rho_r g = \rho_0(z+\delta z)g - \rho_0(z)g = -N^2\delta z$, with the Brunt-Väisälä frequency (or buoyancy frequency):

$$N = \sqrt{-\frac{g}{\rho_r}\frac{d\rho_0}{dz}} \tag{3.2}$$

so that the momentum equation becomes:

$$\ddot{\delta z} + N^2\delta z = 0 \tag{3.3}$$

where the dots are time derivatives. Therefore, stratification induces purely vertical motions characterized by the vertical displacement δz of the fluid. For the rest of our investigation, we consider a layer of linear stratification so that N is independent of z. The different solutions of equation (3.3) are reminded in table 1.1 along with the terminology concerning the stability of a stratification.

Table 3.1: Different types of stratification in density and their analytical solution.

$\frac{d\rho_0}{dz}$	stratification	N^2	solution	$\delta z(t)$
< 0	stable	> 0	oscillating	$\delta z(0)\cos(Nt) + \frac{\dot{\delta z}(0)}{N}\sin(Nt)$
$= 0$	neutral	$= 0$	linear	$\delta z(0) + \dot{\delta z}(0)t$
> 0	unstable	< 0	exponential	$\delta z(0)\cosh(Nt) + \frac{\dot{\delta z}(0)}{N}\sinh(Nt)$

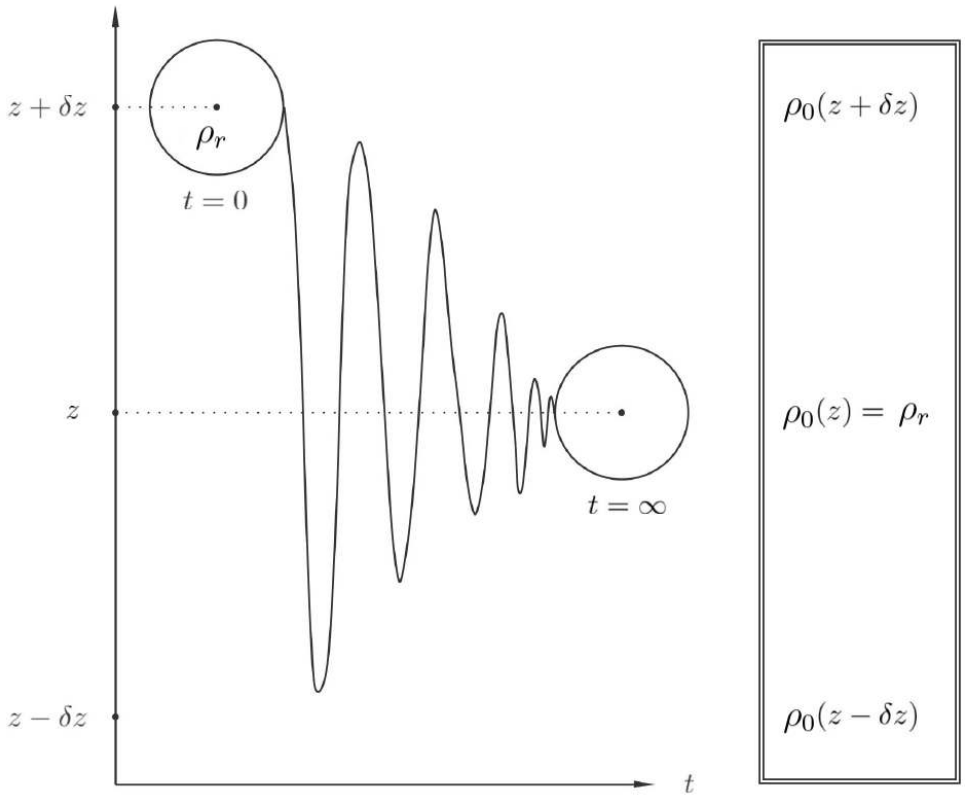

Figure 3.3: Oscillations of a fluid parcel of density ρ_r when perturbed by an increment δz out of its equilibrium state characterized by the altitude z in a medium of linear stable stratification $\rho_0(z)$ (i.e. of buoyancy frequency $N^2 > 0$, meaning that ρ_0 decreases with height) when viscosity is added through an empirical friction force $-K\dot{\delta z}$, K being a constant.

When stable ($N^2 > 0$), stratification acts as a restoring force leading to oscillations of the fluid parcel around its equilibrium state with a frequency matching the buoyancy frequency N of the medium. Internal gravity waves of frequency N thus arises in stably stratified medium. Typical order of magnitudes are $N = 10^{-2}\,\mathrm{s}^{-1}$ (corresponding to a period of 10 min) in the deep ocean versus $N = 10^{-3}\,\mathrm{s}^{-1}$ (about 100 min) in the thermocline and the atmosphere. Viscosity and diffusivity would dampen those oscillations, forcing the fluid parcel to be back at its equilibrium state characterized by the altitude z as illustrated in figure 3.3. An unstable stratification ($N^2 < 0$) typically occurs when a denser fluid happens to be above a lighter one[1]. We will only consider stable stratification in our research. GCM are particularly sensitive to the vertical distribution of internal wave driven mixing which then requires a precise dynamical modeling, i.e. depending on the ocean state[2].

1. This phenomenon is referred as overturning and results in a turbulent convective mixing, which is mentioned here but not detailed in this manuscript.

2. A. Melet et al., "Sensitivity of the Ocean State to the Vertical Distribution of Internal-Tide-Driven Mixing", in: *J. Phys. Oceanogr.* 43.*3* (Dec. 2012), pp. 602–615.

3.1.2 Stratification in temperature

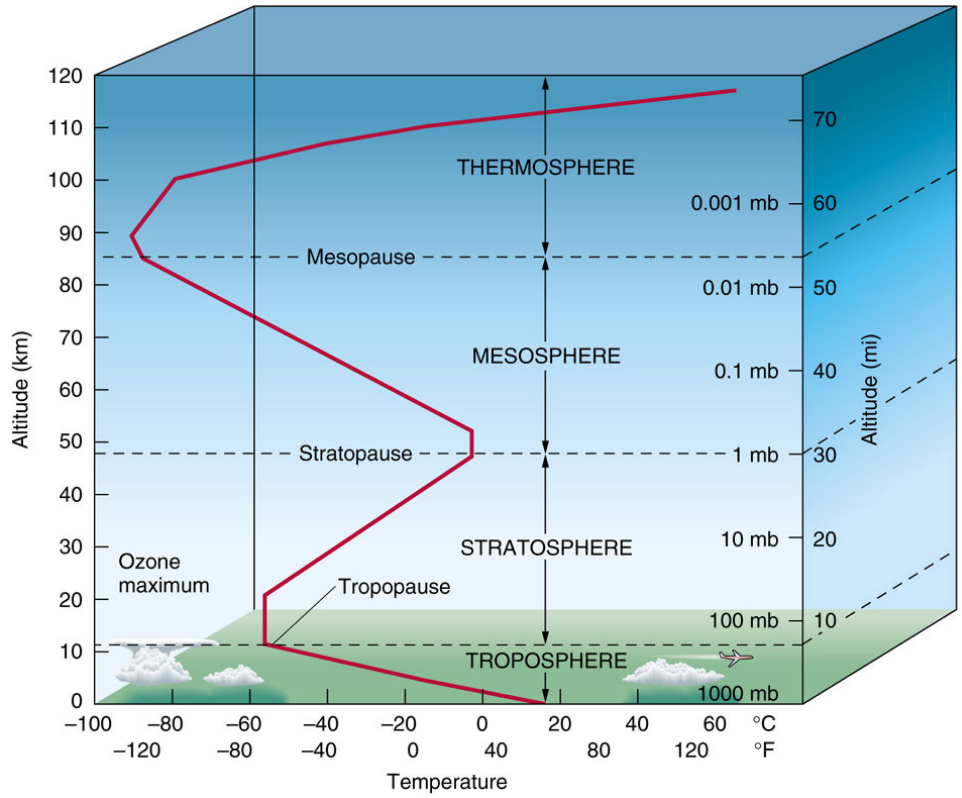

Figure 3.4: Vertical temperature profile of the atmosphere as a function of altitude. Source: University of Lagos (2012), `http://unilaggeography2012.blogspot.com/p/gry-101-introduction-to-physical.html`

In the atmosphere, layers of different densities originate from the vertical variations of temperature T_0 as shown in figure 3.4. In a medium of molar heat capacity C_p, the associated potential temperature is then:

$$\vartheta_0 = T_0 \left(\frac{p_r}{p_0}\right)^{R/C_p} \tag{3.4}$$

where R is the molar gas constant, p_0 the pressure of the medium and p_r a reference pressure. Stratification in temperature is then defined using the vertical profile of potential temperature $\vartheta_0(z)$ (or "classical" temperature $T_0(z)$) of the medium. With the same previous analysis but now using an energy balance on the air parcel and considering air as an ideal gas, the buoyancy frequency becomes:

$$N = \sqrt{\frac{g}{\vartheta_r}\frac{d\vartheta_0}{dz}} = \sqrt{\frac{g}{T_r}\left(\frac{dT_0}{dz} + \frac{g}{C_p}\right)} \tag{3.5}$$

with the same differential equation as (3.3) describing the displacement of a fluid parcel of temperature ϑ_r (or temperature T_r) in equilibrium with its ambient medium at the

altitude z. Table 1.2 summarizes the stability properties of a stratification in temperature. Therefore, the stability of the atmosphere is characterized by the lapse rate $-g/C_p$ (a.k.a dry adiabatic lapse rate). If air is lifted upwards, then its temperature will decrease as a result of cooling when it expands in the lower pressure surroundings at a rate of $-10\,°\mathrm{C}$ for each km upwards. Taking into account the humidity of air, a more realistic order of magnitude for the lapse rate[3] is $-6\,°\mathrm{C}$.

Table 3.2: Different types of stratification in temperature.

$\frac{d\theta_0}{dz}$	$\frac{dT_0}{dz}$	stratification	N^2
> 0	$> -\frac{g}{C_p}$	stable	> 0
$= 0$	$= -\frac{g}{C_p}$	neutral	$= 0$
< 0	$< -\frac{g}{C_p}$	unstable	< 0

The nearly universal stratification of the ocean[4] (apart from very-near surface area) strongly differs from the underlying physics of the atmosphere which often drive statically neutral or unstable regions susceptible to convective instabilities[5]. Moreover, in the ocean, the combination of salinity and temperature effects on density variations adds another complexity when defining the buoyancy frequency N and can be source of ambiguity if not precised. In this investigation, the numerical models of the deep ocean in the GCM assume a vertical density profile based on temperature variations, whereas in our experimental part, density variations are achieved by introducing salted water in the flume.

3.2 Inertial oscillations induced by Earth rotation

Considering a fluid parcel of velocity $\boldsymbol{u}$, Earth rotation is physically modeled through the introduction of an inertial force equal to $-2\boldsymbol{\Omega}\times\boldsymbol{u}$ per mass unit where $\boldsymbol{\Omega}$ is the Earth rotation rate vector (of norm $\Omega = 2\pi\,\mathrm{day}^{-1} = 0.73\times10^{-4}\,\mathrm{s}^{-1}$). For large-scale geophysical flows, it can be shown that this expression simplifies as $(fv, -fu, 0)$ in a (x, y, z) frame attached to the fluid parcel where z is the local vertical direction, $f = 2\Omega\sin\lambda$ being

3. a.k.a wet adiabatic lapse rate.

4. Regions of neutral and unstable stratification developed in the ocean tend to last for hours at most, occupy lateral areas of a few kilometers, and have a wide range of vertical scales (see Wunsch and Ferrari (2004) for more details).

5. A convective situation develops as the heavier fluid moves into the lighter fluid beneath it.

the planetary vorticity, more commonly referred as the Coriolis parameter or Coriolis frequency, and λ the latitude of the fluid parcel. f is positive in the northern hemisphere and negative in the southern and its magnitude $|f|$ varies between 0 at the equator and $1.4 \times 10^{-4}\,\mathrm{s}^{-1}$ at the poles. From the expression of the Coriolis force, Earth rotation induces purely horizontal motions so we restrict the further analysis to the local horizontal plane (x, y). In the inviscid (non-viscous and non-diffusive) medium without convection, stratification and pressure gradients, the momentum equations of the fluid parcel boil down to:

$$\frac{du}{dt} = fv \tag{3.6}$$

$$\frac{dv}{dt} = -fu \tag{3.7}$$

where the two first equations can be rewritten $\dot{\mathcal{V}} + if\mathcal{V} = 0$ using the complex change of variable $\mathcal{V} = u + iv$. Without loss of generality, solving for $\mathcal{V}$ with initial conditions $(u(0), v(0)) = (u_0, 0)$ with $u_0 > 0$ implies $\mathcal{V} = u_0 \exp(-ift)$. We take the imaginary and the real parts to recover:

$$u = u_0 \cos(ft) \tag{3.8}$$

$$v = -u_0 \sin(ft) \tag{3.9}$$

so that the magnitude of the velocity vector $\|\boldsymbol{u}\| = \sqrt{u^2 + v^2}$ is constant and equal to u_0. As $(u, v) = (\dot{\delta x}, \dot{\delta y})$ where $(\delta x, \delta y)$ are the local horizontal displacement from a defined initial location, we get by integration $\delta x = u_0/f \sin(ft)$ and $\delta y = u_0/f \cos(ft)$, so the trajectory of the fluid parcel is a circle of radius[6] u_0/f in the horizontal plane (x, y) described by the equation $\delta x^2 + \delta y^2 = (u_0/f)^2$ in local displacement coordinates. In the horizontal plane, the fluid parcel rotates clockwise in the northern hemisphere where $f > 0$ and counterclockwise in the south with a period $2\pi/f$ equal to 12 h at the poles which increases toward the equator and becomes infinite at the equator because the Coriolis force has no impact on the fluid at the equator. Such a period is called inertial period and the associated motions are inertial oscillations of frequency f. In the ocean, the order of magnitude for the velocity is $u_0 = 0.1\,\mathrm{m/s}$, so at mid-latitude $f = 10^{-4}\,\mathrm{s}^{-1}$, inertial oscillations of period $2\pi/f = 15\,\mathrm{h}$ and radius $u_0/f = 1\,\mathrm{km}$ occur. At mid-latitude in the atmosphere where typically $u_0 = 10\,\mathrm{m/s}$, inertial oscillations over the same period are observed but with radius $u_0/f = 100\,\mathrm{km}$.

6. a.k.a. inertial radius. If $v(0) = v_0 \neq 0$, then the trajectory is a circle of inertial radius $\sqrt{u_0^2 + v_0^2}/f$

Chapter 4

Theoretical aspects for the dynamics of internal waves

Part 4.1 derives internal waves from the equations of geophysical fluid dynamics linearized around a base state, a method directly inspired from Gill's classical textbook (1982)[1]. Then, part 4.2 focuses on those dynamical equations in the weakly nonlinear regime where three internal waves can interact and resonate together through triadic resonant instability (TRI). Hence, the following derivations are inspired from McEwan and Plumb (1977)[2] who investigated the properties of the triadic resonant instability for internal waves in the purely stratified case. We extend their work to the stratified rotating case.

4.1 Linear theory

The dynamical behavior of a fluid parcel of velocity $\boldsymbol{u}$ immersed in an incompressible medium (of the same fluid), characterized by its density ρ, pressure field p, viscosity μ and diffusivity κ, is given by a set of three equations from fluid mechanics theory, namely the incompressibility (4.1), mass-conservation[3] (4.2), and Navier-Stokes (4.3) equations:

$$\boldsymbol{\nabla} \cdot \boldsymbol{u} = 0 \tag{4.1}$$

$$D_t \rho = \kappa \nabla^2 \rho \tag{4.2}$$

$$\rho D_t \boldsymbol{u} = -\boldsymbol{\nabla} p + \rho \boldsymbol{g} - \rho f \left(\boldsymbol{e_z} \times \boldsymbol{u} \right) + \mu \nabla^2 \boldsymbol{u} \tag{4.3}$$

where $\boldsymbol{g}$ is the gravity, f the Coriolis parameter introduced in part 1.2, $(\boldsymbol{\nabla}, \nabla^2)$ denote respectively the gradient and laplacian operators, and D_t the particle derivative, which is the sum of the temporal and the convective derivatives $D_t = \partial_t + \boldsymbol{u} \cdot \boldsymbol{\nabla}$. We use the Reynolds decomposition to model the disturbance of the density, pressure and velocity

1. Gill, *op. cit.*
2. McEwan and Plumb, *op. cit.*
3. a.k.a. continuity equation.

fields:

$$\rho = \overline{\rho} + \rho', \quad p = \overline{p} + p', \quad \boldsymbol{u} = \boldsymbol{u}' \tag{4.4}$$

where the prime over each physical quantity corresponds to the disturbance, or perturbed fields at the first order with $\rho' \ll \overline{\rho}$ and $p' \ll \overline{p}$, and the bar to each field at rest, which only depends on z. The velocity field at rest is assumed to be $\mathbf{0}$ (motionless basic state). The pressure and density fields at rest follow the hydrostatic balance:

$$\overline{p}_{,z} = -\overline{\rho} g \tag{4.5}$$

For sake of clarity, we denote the partial derivative of a field $\boldsymbol{A}$ with respect to a variable q, $\partial_q \boldsymbol{A} = \boldsymbol{A}_{,q}$. At the leading order of perturbations, the dynamical equations (4.1), (4.2) and (4.3), combined with (4.5), result in the following linearized equations:

$$\begin{aligned}
\boldsymbol{\nabla} \cdot \boldsymbol{u} &= 0 && (4.6)\\
\rho'_{,t} + (\boldsymbol{u}' \cdot \boldsymbol{\nabla})\,\overline{\rho} &= \kappa \nabla^2 \rho' && (4.7)\\
\overline{\rho} \boldsymbol{u}'_{,t} &= -\boldsymbol{\nabla} p' + \rho' \boldsymbol{g} - \overline{\rho} f\,(\boldsymbol{e_z} \times \boldsymbol{u}) + \mu \nabla^2 \boldsymbol{u}' && (4.8)
\end{aligned}$$

We consider a 2D-3C[4] model so that all the physical quantities considered in a (x, y, z) Cartesian space[5] are invariant by translation along the y axis i.e. $\partial_y = 0$. From now on, vector fields written with only two components refer to the two main directions of our model (x, z), e.g. in the Cartesian basis $(\boldsymbol{e_x}, \boldsymbol{e_y}, \boldsymbol{e_z})$ corresponding to coordinates $\boldsymbol{r} = (x, y, z)$, $\boldsymbol{A} = (A_x, A_y, A_z) = A_x \boldsymbol{e_x} + A_y \boldsymbol{e_y} + A_z \boldsymbol{e_z}$ v.s. $\boldsymbol{A} = (A_x, A_z) = A_x \boldsymbol{e_x} + A_z \boldsymbol{e_z}$. As $\boldsymbol{\nabla} = (\partial_x, \partial_z)$ and $\nabla^2 = \partial_x^2 + \partial_z^2$, the projections of the linearized equations (4.6),(4.7) and (4.8) in Cartesian coordinates are, under Boussinesq approximation[6]:

$$\begin{aligned}
u_{,x} + w_{,z} &= 0 && (4.9)\\
b_{,t} + N^2 w &= \kappa \nabla^2 b && (4.10)\\
u_{,t} &= -P_{,x} + f v + \nu \nabla^2 u && (4.11)\\
v_{,t} &= -f u + \nu \nabla^2 v && (4.12)\\
w_{,t} &= -P_{,z} + b + \nu \nabla^2 w && (4.13)
\end{aligned}$$

4. A model which allows variations along two main dimensions/axis (2D), and composed of three components (3C).

5. where x is the zonal direction (west-to-east), y is the meridional direction (south-to-north), and z the vertical axis (low-to-high).

6. Boussinesq approximation assumes weak density fluctuations ρ' compared to the mean value ρ_r, the direct consequence being the possibility to replace ρ by ρ_r except when multiplied by $\boldsymbol{g}$.

where N is the buoyancy frequency defined in (3.2), the density field at rest being the sum of a reference density ρ_r with the background density profile $\rho_0(z)$, $\overline{\rho} = \rho_r + \rho_0$ with $\rho_r \gg \rho'$, and $b = -g\rho'/\rho_r$ is the buoyancy field, $\nu = \mu/\rho_r$ the kinematic viscosity, $P = p'/\rho_r$ the normalized pressure field associated to the disturbance, $\boldsymbol{u'} = \boldsymbol{u} = (u, v, w)$ the perturbed velocity field, so the disturbance is characterized by the perturbed fields $(\boldsymbol{u}, P, b)$. From (4.9), we can introduce the streamfunction ψ so that:

$$u = \psi_{,z}, \quad w = -\psi_{,x} \tag{4.14}$$

and rewrite (4.10)-(4.13) as:

$$\begin{aligned} b_{,t} - N^2\psi_{,x} &= \kappa\nabla^2 b && (4.15)\\ \psi_{,zt} &= -P_{,x} + fv + \nu\nabla^2\psi_{,z} && (4.16)\\ v_{,t} &= -f\psi_{,z} + \nu\nabla^2 v && (4.17)\\ \psi_{,xt} &= P_{,z} - b + \nu\nabla^2\psi_{,x} && (4.18) \end{aligned}$$

so the derivative of (4.16) with respect to z added to the derivative of (4.18) with respect to x leads to the following set of equations in variables (ψ, b, v):

$$\begin{aligned} b_{,t} - N^2\psi_{,x} &= \kappa\nabla^2 b && (4.19)\\ \nabla^2\psi_{,t} &= fv_{,z} - b_{,x} + \nu\nabla^4\psi && (4.20)\\ v_{,t} &= -f\psi_{,z} + \nu\nabla^2 v && (4.21) \end{aligned}$$

and combining (4.19), (4.20) and (4.21) leads to the wave equation of internal waves:

$$\nabla^2\psi_{,tt} + N^2\psi_{,xx} + f^2\psi_{,zz} = \nu\nabla^4\psi_{,t} + f\nu\nabla^2 v_{,z} - \kappa\nabla^2 b_{,x} \tag{4.22}$$

Some key properties of internal waves

We investigate an inviscid[7] medium to capture the internal wave dynamics. In this case, the right hand side of the equation (4.22) is zero since $\nu = \kappa = 0$:

$$\nabla^2\psi_{,tt} + N^2\psi_{,xx} + f^2\psi_{,zz} = 0 \tag{4.23}$$

7. non-viscous and non-diffusive medium.

For 2D wavelike solutions in complex notations of the form:

$$\begin{pmatrix} \psi \\ v \\ b \end{pmatrix} = \begin{pmatrix} \Psi_0 \\ V_0 \\ B_0 \end{pmatrix} \exp i(k_{x0}x + k_{z0}z - \omega_0 t) + c.c \tag{4.24}$$

with complex amplitudes (Ψ_0, V_0, B_0), real frequency ω_0 and wave vector $\boldsymbol{k_0} = (k_{x0}, k_{z0})$ of norm $k_0 = \sqrt{k_{x0}^2 + k_{z0}^2}$, and where $c.c$ denotes the complex conjugate, the polarization relations resulting from (4.19) and (4.21) are:

$$V_0 = \frac{f k_{z0}}{\omega_0}\Psi_0 \tag{4.25}$$

$$B_0 = -\frac{N^2 k_{x0}}{\omega_0}\Psi_0 \tag{4.26}$$

implying that the model is described by only two components (ψ, b) in the purely stratified case, and (ψ, v) purely rotating case, whereas in the stratified rotating case, the three components remain (ψ, v, b). Equation (4.22) reduces to the dispersion relation of internal waves:

$$\omega_0^2 = \left(N\frac{k_{x0}}{k_0}\right)^2 + \left(f\frac{k_{z0}}{k_0}\right)^2 = (N\sin\theta_0)^2 + (f\cos\theta_0)^2 \tag{4.27}$$

where θ_0 is the angle defined by $\boldsymbol{k_0} = k_0(\sin\theta_0, \cos\theta_0)$ so $L_0 = 1/k_0$ appears to be the typical length scale of the internal wave. Since $f < N$ in geophysical applications (see part 1.1 and 1.2), internal waves propagate if $f \leq |\omega_0| \leq N$. The sign of ω_0 is denoted $s_0 = \text{sign}(\omega_0)$ so the associated phase and group velocities defined by:

$$\boldsymbol{c_0} = \frac{\omega_0}{k_0}\frac{\boldsymbol{k_0}}{k_0}, \quad \boldsymbol{c_g} = \frac{\partial\omega_0}{\partial k_{x0}}\boldsymbol{e_x} + \frac{\partial\omega_0}{\partial k_{z0}}\boldsymbol{e_z} \tag{4.28}$$

are explicitly evaluated:

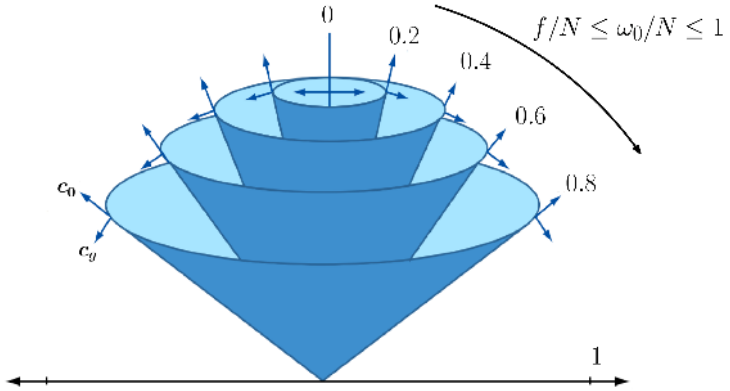

Figure 4.1: Surfaces of equal frequencies ω_0 given by (4.27) for angles θ_0 ranging from 0 to $\pi/2$ corresponding to different values of ω_0/N indicated on the figure. Internal waves propagate if $f/N \leq \omega_0/N \leq 1$, resulting in perpendicular group and phase velocity vectors $(\boldsymbol{c_g}, \boldsymbol{c_0})$ indicated on the figure. Inspired from Gill's textbook (1982) p.134

Phase and group velocities

When $f \leq |\omega_0| \leq N$, internal waves propagate with phase and group velocity vectors equal to:

$$\boldsymbol{c_0} = s_0 \frac{|\omega_0|}{k_0}(\sin\theta_0 \boldsymbol{e_x} + \cos\theta_0 \boldsymbol{e_z}) \tag{4.29}$$

$$\boldsymbol{c_g} = s_0 \frac{N^2 - f^2}{|\omega_0| k_0} \cos\theta_0 \sin\theta_0 (\cos\theta_0 \boldsymbol{e_x} - \sin\theta_0 \boldsymbol{e_z}) \tag{4.30}$$

therefore:

$$\boldsymbol{c_0} \cdot \boldsymbol{c_g} = 0 \tag{4.31}$$

and $\boldsymbol{c_0} \times \boldsymbol{c_g} = -(N^2 - f^2)/k_0^2 \cos\theta_0 \sin\theta_0 \boldsymbol{e_y}$, meaning that the phase and group velocities of internal waves are orthogonal[a], the phase velocity being along the direction $s_0 \boldsymbol{k_0}$.

a. $(\boldsymbol{c_0}, \boldsymbol{c_g}, -\boldsymbol{e_y})$ form a direct orthogonal system when $0 \leq \theta_0 \leq \pi/2$.

Surfaces of equal frequencies ω_0 are cones of angle θ_0 with respect to the vertical axis and are represented in figure 4.1. Indeed, the dispersion relation (4.27) verifies $\omega_0(\theta_0) = \omega_0(-\theta_0) = \omega_0(\pi - \theta_0) = \omega_0(\pi + \theta_0)$, so one frequency leads to four possible waves in a (x, z) plane forming a St. Andrew's Cross as illustrated in figure 4.2 from Mowbray and Rarity (1967)[8]. The first wave has wave vector and frequency $(\boldsymbol{k_0}, \omega_0)$, the second $(-\boldsymbol{k_0}, \omega_0)$, the third $(\boldsymbol{k_s}, \omega_0)$, and the fourth $(-\boldsymbol{k_s}, \omega_0)$ with $\boldsymbol{k_s} = (-k_{x0}, k_{z0})$.

The convective term being zero in the linearized equation, we can infer the trajectory

8. Mowbray and Rarity, *op. cit.*

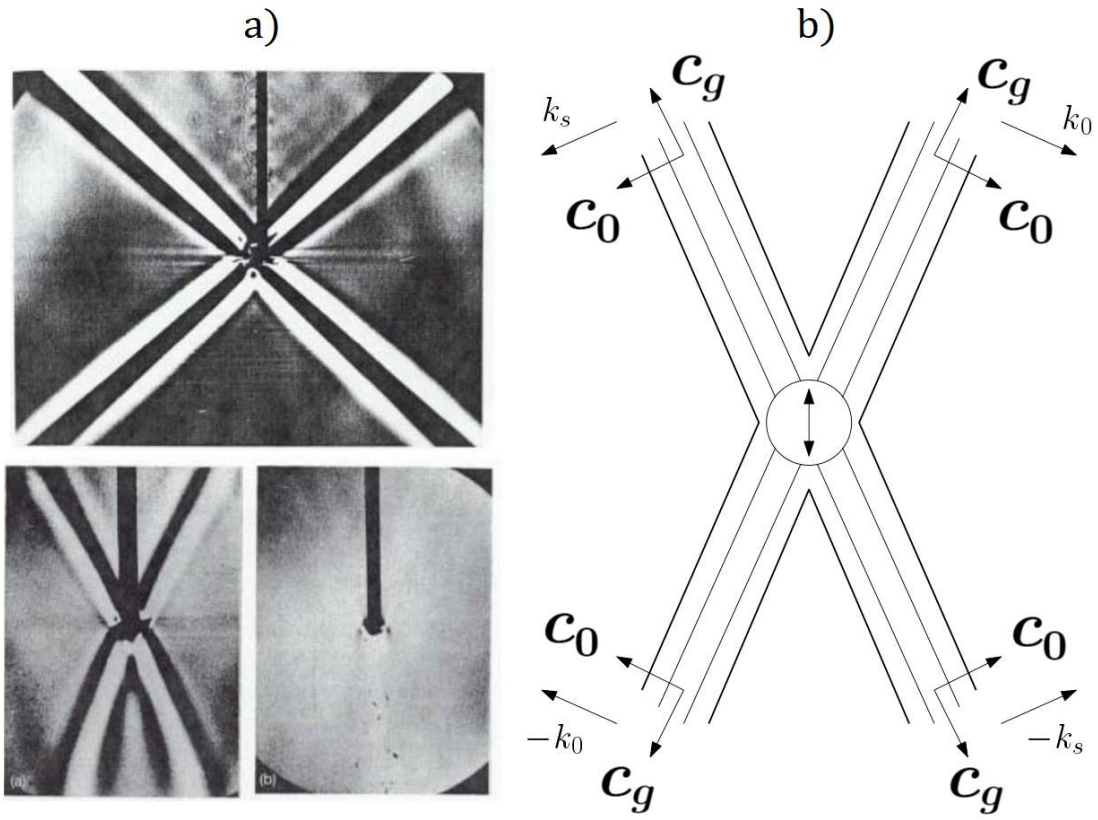

Figure 4.2: a) Pattern of internal waves, referred to as St Andrew's Cross, generated experimentally by an oscillating cylinder in a stratified fluid and observed by toepler-schlieren technique from Mowbray and Rarity (1967). In the top figure $\omega/N = 0.9$, in the left bottom figure $\omega/N = 0.7$ and the bottom right figure shows the fluid at rest when the cylinder is not moving. b) Group and phase velocity vectors along the four rays of the St Andrew's Cross for a fixed frequency $\omega_0(\theta_0)$ given by the dispersion relation (4.27).

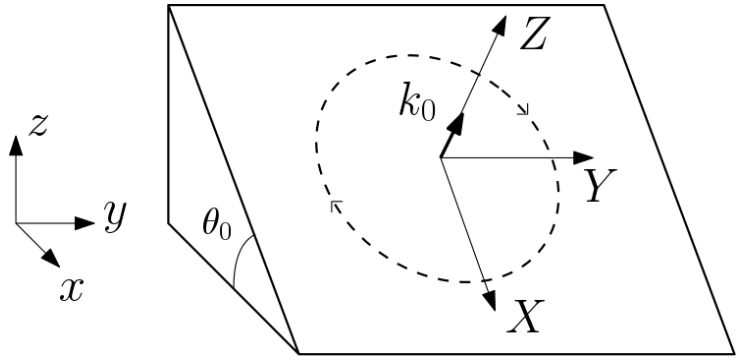

Figure 4.3: Elliptic trajectory of a fluid parcel, the motion being confined to the plane perpendicular to the wave vector (X, Y). The Z axis is oriented toward $\boldsymbol{k_0}$ which forms an angle θ_0 with the vertical z.

of the fluid parcel as the particle derivative is exactly equal to the time derivative. Identically to part 1.1, we define the local displacement $(\delta x, \delta y, \delta z)$ in the Cartesian coordinate system (x, y, z) so that $(u, v, w) = (\dot{\delta x}, \dot{\delta y}, \dot{\delta z})$. For wavelike solutions, the incompressible condition (4.1) implies that the movement of the fluid parcel is in a plane normal to the wave vector $\boldsymbol{k_0}$. Therefore, the trajectories have a simple form in the new tilted coordinate system (X, Y, Z) where the vertical Z is aligned with $\boldsymbol{k_0}$ as represented in figure 4.3. Let $(\delta X, \delta Y, \delta Z)$ be the displacement in the tilted coordinate system so that $\delta X = (\cos\theta_0)\delta x - (\sin\theta_0)\delta z$, $\delta Y = \delta y$ and $\delta Z = (\sin\theta_0)\delta x + (\cos\theta_0)\delta z$. With this change of coordinate, (4.11)-(4.13) in the inviscid case ($\nu = \kappa = 0$) lead to the following equations in displacement at a fixed Z, $\ddot{\delta X} = -\left(N \sin\theta_0\right)^2 \delta X + \left(f \cos\theta_0\right) \dot{\delta Y}$ and $\ddot{\delta Y} = -\left(f \cos\theta_0\right) \dot{\delta X}$. We use the dispersion relation (4.27) to obtain $\ddot{\delta X} + \omega_0^2 \delta X = 0$. Solving for initial conditions $(\delta X(0), \delta Y(0)) = (\delta X_0, 0)$ and $(\dot{\delta X}(0), \dot{\delta Y}(0)) = (0, 0)$, we get $\delta X = \delta X_0 \cos\omega_0 t$ and $\delta Y = \delta Y_0 \sin\omega_0 t$ with $\delta Y_0 = -\left(f \cos\theta_0/\omega_0\right) \delta X_0$. Combining those parametric equations, the trajectory of the fluid parcel is described in Cartesian coordinate by the equation:

$$\left(\frac{\delta X}{\delta X_0}\right)^2 + \left(\frac{\delta Y}{\delta Y_0}\right)^2 = 1 \tag{4.32}$$

with $|\delta Y_0| = |f \cos\theta_0/\omega_0||\delta X_0| \leq |\delta X_0|$ so the fluid parcel has an elliptic trajectory in a plane normal to $\boldsymbol{k_0}$ with radii $|\delta X_0|$ and $|\delta Y_0|$. In the purely rotating case, $|\delta Y_0| = |\delta X_0|$ so we recover the inertial oscillations described in part 1.2 with circular trajectories of frequency f. In the purely stratified case, the particle has an oscillating trajectory following the X axis, same as in part 1.1 but tilted by an angle θ_0 with respect to the vertical due to gradients of the perturbed pressure field.

4.1.1 Energy transport

The total energy of internal waves is derived by writing (4.7) and (4.8) as followed:

$$b_{,t} + N^2 w = 0 \tag{4.33}$$

$$\boldsymbol{u}_{,t} = -\boldsymbol{\nabla} P + b\boldsymbol{e_z} - f\left(\boldsymbol{e_z} \times \boldsymbol{u}\right) \tag{4.34}$$

Keeping in mind (4.1), we combine (4.33) and (4.34) to get the energy balance equation:

$$e_{tot,t} = -\boldsymbol{\nabla} \cdot \boldsymbol{S} \tag{4.35}$$

the total energy e_{tot} being the sum of the kinetic and potential energies per mass unit, e_k and e_p:

$$e_{tot} = e_k + e_p, \quad e_k = \frac{1}{2}\boldsymbol{u}^2, \quad e_p = \frac{1}{2}\left(\frac{b}{N}\right)^2 \tag{4.36}$$

and the wave energy flux[9] $\boldsymbol{S}$ defined by $\boldsymbol{S} = P\boldsymbol{u}$. The ratio of kinetic to potential energies is then:

$$\frac{e_k}{e_p} = 1 + \left(\frac{f}{N}\cot\theta_0\right)^2 \tag{4.37}$$

hence, the equipartition of kinetic and potential energy is only ensured for internal gravity waves, but not for inertial waves as f increases. For wavelike solutions (4.24), the equations (4.14), (4.15), (4.17) and (4.17) become in complex notations:

$$u = ik_{z0}\psi \tag{4.38}$$

$$v = \frac{fk_{z0}}{\omega_0}\psi \tag{4.39}$$

$$w = -ik_{x0}\psi \tag{4.40}$$

$$P = i\frac{k_{x0}}{k_{z0}}\left(\frac{N^2}{\omega} - \omega\right)\psi \tag{4.41}$$

$$b = -\frac{N^2 k_{x0}}{\omega_0}\psi \tag{4.42}$$

so the mean[10] total energy and the mean energy flux of a single internal wave (4.24) is:

$$\langle e_{tot}\rangle_{\boldsymbol{r},t} = \left\langle \frac{1}{2}(u^2+v^2+w^2) + \frac{1}{2}\left(\frac{b}{N}\right)^2 \right\rangle_{\boldsymbol{r},t} = \frac{|k_0\Psi_0|^2}{4} = \Phi_0^2 \tag{4.43}$$

$$\langle \boldsymbol{S}\rangle_{\boldsymbol{r},t} = \langle P\boldsymbol{u}\rangle_{\boldsymbol{r},t} = \boldsymbol{c_g}\langle e_{tot}\rangle_{\boldsymbol{r},t} \tag{4.44}$$

9. a.k.a the Poynting vector by analogy to electromagnetic waves energy balance.
10. averaged in space $\boldsymbol{r} = (x, y, z)$ and time t.

where the brackets denote the space-time average and $\Phi_0 = k_0\Psi_0/2$. The previous expression remains true in the purely stratified or purely rotating cases. From (4.44), the energy flux is directed toward $\boldsymbol{c_g}$, hence internal waves transport energy in the direction given by the group velocity. Let $\mathcal{E} = \langle e_{tot} \rangle_{\boldsymbol{r}}$ be the spatial mean of the total energy, then (4.35) implies the conservation of $\mathcal{E}$.

4.1.2 Geometrical aspects and hydrostatic approximation

The aspect ratio of an internal wave r is defined as the ratio of vertical to horizontal scales:

$$r = \frac{k_{x0}}{k_{z0}} = \pm\sqrt{\frac{\omega_0^2 - f^2}{N^2 - \omega_0^2}} = \pm\tan\theta_0 \tag{4.45}$$

so that the dispersion relation (4.27) becomes[11]:

$$\left(\frac{\omega}{N}\right)^2 = \frac{1}{1+r^2}\left(r^2 + \left(\frac{f}{N}\right)^2\right) \tag{4.46}$$

First case: the non-hydrostatic regime

$$r \geq 1 \quad \Rightarrow \quad \left(\frac{\omega_0}{N}\right)^2 \sim \frac{r^2}{1+r^2} \tag{4.47}$$

Vertical scales are dominating horizontal scales so that the Coriolis effects can be neglected. The perturbed pressure and density fields then obey to:

$$\rho_r w_{,t} = -i\omega_0\rho_r w = -p'_{,z} - \rho' g \tag{4.48}$$

In this regime, $r \geq 1$ so ω_0/N can not be neglected. Hence the non-hydrostatic balance (4.5) can not be extended to the perturbed pressure and density fields.

Second case: hydrostatic non-rotating regime

$$\frac{f}{N} \ll r \ll 1 \quad \Rightarrow \quad \left(\frac{\omega_0}{N}\right)^2 \sim r^2 \tag{4.49}$$

Horizontal scales dominate vertical scales, the Coriolis effects are second order effects. Due to the small value of aspect ratio corresponding to small angles $\theta_0 \ll 1$ and small frequency ω_0/N, the perturbed pressure and density fields follows a relation identical to the hydrostatic balance (4.5), meaning that (4.48) becomes:

$$p'_{,z} = -\rho' g \tag{4.50}$$

11. f/N is commonly called the Prandtl ratio.

Third case: hydrostatic rotating regime

$$r \leq \frac{f}{N} \quad \Rightarrow \quad \left(\frac{\omega_0}{N}\right)^2 \sim r^2 + \left(\frac{f}{N}\right)^2 \tag{4.51}$$

Horizontal scales dominate vertical scales, the Coriolis effects, but the Coriolis effects can not be neglected. Here again, small values of aspect ratio implies the extended hydrostatic balance to the perturbed pressure and density fields, so (4.50) is also valid in this regime.

Hydrostatic approximation

$$r \ll 1 \quad \Rightarrow \quad p'_{,z} = -\rho' g \tag{4.52}$$

4.2 Weakly nonlinear interaction between internal waves

Dimensionless quantities

We define all the following dimensionless variables:

$$\tilde{\boldsymbol{r}} \rightarrow \frac{\boldsymbol{r}}{L_0} \tag{4.53}$$
$$\tilde{t} \rightarrow Nt \tag{4.54}$$
$$\tilde{\psi} \rightarrow \frac{\psi}{NL_0^2} \tag{4.55}$$
$$\tilde{b} \rightarrow \frac{\psi}{N^2 L_0} \tag{4.56}$$
$$\tilde{v} \rightarrow \frac{v}{L_0/N} \tag{4.57}$$

Dimensionless quantities such as the Prandtl ratio, the dimensionless viscosity and diffusivity are then defined by:

$$\tilde{f} \rightarrow \frac{f}{N} \tag{4.58}$$
$$\tilde{\nu} \rightarrow \frac{\nu}{NL_0^2} \tag{4.59}$$
$$\tilde{\kappa} \rightarrow \frac{\kappa}{NL_0^2} \tag{4.60}$$

From now on, all the equations are dimensionless and for the sake of simplicity, we drop the tilde for all dimensionless variables and ratios defined above. In the former equations (4.2) and (4.3), the convective term can be written using the streamfunction ψ

as $(\boldsymbol{u}\cdot\boldsymbol{\nabla})\boldsymbol{u} = -J(\psi,\boldsymbol{u})$ and $(\boldsymbol{u}\cdot\boldsymbol{\nabla})b = -J(\psi,b)$, with the Jacobian $J(f,g) = f_{,x}g_{,z} - g_{,x}f_{,z}$. The non-dimensional dynamical equations are:

$$b_{,t} - \psi_{,x} = J(\psi,b) + \tilde{\kappa}\nabla^2 b \tag{4.61}$$

$$v_{,t} + \tilde{f}\psi_{,z} = J(\psi,v) + \tilde{\nu}\nabla^2 v \tag{4.62}$$

$$\begin{aligned}\nabla^2\psi_{,tt} + \psi_{,xx} + \tilde{f}^2\psi_{,zz} = {} & J(\psi,\nabla^2\psi)_{,t} - J(\psi,b)_{,x} - \tilde{f}J(\psi,v)_{,z} \\ & + \tilde{\nu}\nabla^4\psi_{,t} + \tilde{f}\tilde{\nu}\nabla^2 v_{,z} - \tilde{\kappa}\nabla^2 b_{,x}\end{aligned} \tag{4.63}$$

We now take into account the slow variations of amplitude in time so that the perturbed fields (4.4) have space-time dependencies of the form:

$$\psi = Fr\Psi(T)f(\boldsymbol{r},t) + \mathcal{O}(Fr^2) \tag{4.64}$$

$$v = FrV(T)g(\boldsymbol{r},t) + \mathcal{O}(Fr^2) \tag{4.65}$$

$$b = FrB(T)h(\boldsymbol{r},t) + \mathcal{O}(Fr^2) \tag{4.66}$$

with the introduction of the expanded scale $T = Frt$, Fr being the Froude number, a dimensionless measure of amplitudes. Time derivatives become $\partial_t = \partial_t + Fr\partial_T$, then to leading order, providing $(\tilde{\nu},\tilde{\kappa}) \ll Fr$:

$$b_{,t} = \psi_{,x} \tag{4.67}$$

$$v_{,t} = -\tilde{f}\psi_{,z} \tag{4.68}$$

$$\nabla^2\psi_{,tt} = -\psi_{,xx} - \tilde{f}^2\psi_{,zz} \tag{4.69}$$

which admit wavelike solutions of the form:

$$\psi = \sum_n \Psi_n(T)\exp i(k_{xn}x + k_{zn}z - \omega_n t) + c.c \tag{4.70}$$

$$v = \sum_n V_n(T)\exp i(k_{xn}x + k_{zn}z - \omega_n t) + c.c \tag{4.71}$$

$$b = \sum_n B_n(T)\exp i(k_{xn}x + k_{zn}z - \omega_n t) + c.c \tag{4.72}$$

whose wave frequency ω_n and wave vector $\boldsymbol{k_n} = (k_{xn},k_{zn}) = k_n(\sin\theta_n,\cos\theta_n)$ are connected through the dispersion relation (4.25) and the amplitudes (Ψ_0,V_0,B_0) through the polarization relations (4.26):

Dispersion and polarization relations

The dispersion relation resulting from (4.69) is:

$$\omega_n^2 = \left(\frac{k_{xn}}{k_n}\right)^2 + \left(\tilde{f}\frac{k_{zn}}{k_n}\right)^2 = \sin\theta_n{}^2 + (\tilde{f}\cos\theta_n)^2 \tag{4.73}$$

and the polarization relations from (4.67) and (4.68):

$$V_n = \frac{\tilde{f}k_{zn}}{\omega_n}\Psi_n, \quad B_n = -\frac{k_{xn}}{\omega_n}\Psi_n \tag{4.74}$$

with n arbitrary but with anticipation to the resonance condition $n = 0, 1, 2$ for triadic resonance, $n = 0$ being the basic state.

and the non-dimensionalized amplitude of the primary wave $n = 0$ is chosen such that $\Psi_0(0)$ is unity giving the definition of the Froude[12] number $Fr = \Psi_0(0)/(NL_0^2)$.

To next order in Fr,

$$\begin{aligned} 2\nabla^2\psi_{,tT} = \; & J(\psi, \nabla^2\psi)_{,t} - J(\psi, b)_{,x} - \tilde{f}J(\psi, v)_{,z} \\ & + \frac{\tilde{\nu}\nabla^4\psi_{,t}^{(res)} + \tilde{f}\tilde{\nu}\nabla^2 v_{,z}^{(res)} - \tilde{\kappa}\nabla^2 b_{,x}}{Fr} \end{aligned} \tag{4.75}$$

with superscript $^{(res)}$ gathering all resonant forcing terms such that the triadic resonance condition is fulfilled:

Triadic resonance conditions

The wave frequencies ω_n and wave vectors $\boldsymbol{k_n} = (k_{xn}, k_{zn})$ obey:

$$\omega_0 + \omega_1 + \omega_2 = 0 \tag{4.76}$$

$$\boldsymbol{k_0} + \boldsymbol{k_1} + \boldsymbol{k_2} = \boldsymbol{0} \tag{4.77}$$

Replacing (4.73), and (4.74) in (4.75), we get $(\partial_T + Fr^{-1}(\nu+\kappa)k_n^2/2)\Psi_n = iS_n\Psi_p^*\Psi_q^*$ where (n, p, q) are any circular permutations of $(0, 1, 2)$, and S_n are the interaction coefficients:

$$S_n = \frac{k_{xp}k_{zq} - k_{xq}k_{zp}}{2k_n^2}\left(k_q^2 - k_p^2 + \frac{k_{xn}}{\omega_n}\left(\frac{k_{xq}}{\omega_q} - \frac{k_{xp}}{\omega_p}\right) + \frac{\tilde{f}^2 k_{xn}}{\omega_n}\left(\frac{k_{xq}}{\omega_q} - \frac{k_{xp}}{\omega_p}\right)\right) \tag{4.78}$$

12. where $(\Psi_0(0), N, L_0)$ are dimensional.

Setting $\lambda_n = k_n^2/2$ and $R = Re/(1+1/Pr)$ with the Reynolds and Prandtl numbers, $Re = \Psi_0(0)/\nu$ and $Pr = \nu/\kappa$, the change of variable $\psi \to \mathrm{e}^{-i\pi/3}\psi$ gives the triadic resonance equations:

$$\frac{d\Psi_n}{dT} + \frac{\lambda_n}{R}\Psi_n = S_n \Psi_p^* \Psi_q^* \tag{4.79}$$

From now on, the Prandtl ratio will be denoted f/N instead of $\tilde{f}$. The dispersion relation (4.73) can also be written $k_n^2 = (k_{xn}/\omega_n)^2 + (f/N)^2(k_{zn}/\omega_n)^2$, so we can write the interaction coefficient S_n in a compact form:

$$S_n = \frac{1}{2k_n^2}\left(\Lambda_x\left(\frac{1}{c_{xq}} - \frac{1}{c_{xp}}\right) + \left(\frac{f}{N}\right)^2 \Lambda_z\left(\frac{1}{c_{zq}} - \frac{1}{c_{zp}}\right)\right) \tag{4.80}$$

where (Λ_x, Λ_z) are defined by:

$$\Lambda_x = \frac{\Delta}{k_0 k_1 k_2}\left(\frac{1}{c_{x0}} + \frac{1}{c_{x1}} + \frac{1}{c_{x2}}\right) \tag{4.81}$$

$$\Lambda_z = \frac{\Delta}{k_0 k_1 k_2}\left(\frac{1}{c_{z0}} + \frac{1}{c_{z1}} + \frac{1}{c_{z2}}\right) \tag{4.82}$$

Δ being twice the area of the triangle $(\boldsymbol{k_0}, \boldsymbol{k_1}, \boldsymbol{k_2})$:

$$\begin{aligned}\Delta &= k_{x1}k_{z2} - k_{x2}k_{z1} \\ &= k_{x2}k_{z0} - k_{x0}k_{z2} \\ &= k_{x0}k_{z1} - k_{x1}k_{z0}\end{aligned} \tag{4.83}$$

so that:

$$\begin{aligned}&\Lambda_x = 0 \text{ if } N = 0 \\ &\Lambda_z = 0 \text{ if } f = 0\end{aligned} \tag{4.84}$$

4.2.1 Triadic equations in the inviscid case

In the inviscid case, $\lambda_n = 0$ and (4.79) implies the conservation of three invariants. Let $\Phi_n = k_n\Psi_n/2$ be the normalized amplitude and φ the phase of $\Phi_0\Phi_1\Phi_2$ so that the total energy (sum of the kinetic and potential energies) and wave action of the n-th wave are $\mathcal{E}_n = |\Phi_n|^2$ and $\mathcal{A}_n = \mathcal{E}_n/\omega_n = |\Phi_n|^2/\omega_n$. Then[13]:

13. Weiland and Wilhelmsson, *op. cit.*

Conservation laws

The total energy, pseudomomentum vector, and Hamiltonian, respectively defined by:

$$\mathcal{E} = \sum_n \mathcal{A}_n \omega_n, \quad \boldsymbol{\mathcal{P}} = \sum_n \mathcal{A}_n \boldsymbol{k_n}, \quad \mathcal{K} = |\Phi_0 \Phi_1 \Phi_2| \sin\varphi \tag{4.85}$$

are conserved by the triadic equations (4.79) in the inviscid case ($\lambda_n = 0$).

The pseudomomentum vector $\boldsymbol{\mathcal{P}}$ is a characteristic intrinsic to the wave which needs to be distinguished from the momentum vector $\boldsymbol{\mathcal{M}}$, a characteristic of the matter (fluid parcels here). In general, $\boldsymbol{\mathcal{P}} \neq \boldsymbol{\mathcal{M}}$ as reminded by Pippard (1992)[14] when investigating the properties of wave reflection on an obstacle in quantum mechanics, the most obvious example being the photon in quantum mechanics which has no mass so $\boldsymbol{\mathcal{M}} = \mathbf{0}$, yet $\boldsymbol{\mathcal{P}} = \hbar \boldsymbol{k}$, $\hbar$ being the quanta of energy and $\boldsymbol{k}$ the wave vector. More precisely, when an electromagnetic wave reflects on an obstacle, the radiation pressure and associated force exerted on the surface of the obstacle results from the rate of change of pseudomomentum of the wave. $\boldsymbol{\mathcal{P}}$ is also called quasi-momentum or crystal momentum vector in the case of electrons moving through a crystal lattice in which $\boldsymbol{\mathcal{P}} \neq \boldsymbol{\mathcal{M}}$. The only case where $\boldsymbol{\mathcal{P}} = \boldsymbol{\mathcal{M}}$ is for free particle (no constraints on their mass or on their movement i.e. no force exerted).

The triadic equations (4.79) when $\lambda_n = 0$ are written in different forms in the literature, depending on the chosen definition of the wave amplitudes. To demonstrate those conservation laws, we will use these different formulations[15]. Here is a quick overview:

Formulation 1

The amplitude Ψ_n of the streamfunction ψ_n follows:

$$\frac{d\Psi_n}{dT} = S_n \Psi_p^* \Psi_q^* \tag{4.86}$$

(n, p, q) being any circular permutation of $(0, 1, 2)$ and S_n being defined in (4.80).

14. A. B. Pippard, "Momentum and pseudo-momentum: I. classical pseudo-momentum and wave pressure", in: *Eur. J. Phys.* 13.*2* (Mar. 1992), pp. 82–87.

15. The three formulations listed here are inspired from the works of McEwan and Plumb (1977) for formulation 1, of Waleffe (1992) for formulation 2, and of Hasselmann (1967) for formulation 3.

Formulation 2

With the change of variable $\Phi_n = k_n \Psi_n / 2$:

$$\frac{d\Phi_n}{dT} = L_n \Phi_p^* \Phi_q^* \tag{4.87}$$

(n, p, q) being any circular permutation of $(0, 1, 2)$ and:

$$L_n = \Lambda_x \left(\frac{1}{c_{xq}} - \frac{1}{c_{xp}} \right) + \left(\frac{f}{N} \right)^2 \Lambda_z \left(\frac{1}{c_{zq}} - \frac{1}{c_{zp}} \right) \tag{4.88}$$

and (Λ_x, Λ_z) being defined in (4.81) and (4.82).

Formulation 3

With the change of variable $a_n = \Phi_n / \omega_n = k_n \Psi_n / (2\omega_n)$:

$$\omega_n \frac{da_n}{dT} = \Lambda a_p^* a_q^* \tag{4.89}$$

Note that, in this form, the interaction coefficient is the same for all three equations:

$$\Lambda = \Lambda_x (k_{xq}\omega_p - k_{xp}\omega_q) + \left(\frac{f}{N} \right)^2 \Lambda_z (k_{zq}\omega_p - k_{zp}\omega_q) \tag{4.90}$$

(p, q) being either $(0, 1)$, $(1, 2)$, or $(2, 0)$.

Note that in those expressions, $(\Lambda_x, \Lambda_z, \Lambda)$ are constant since they involve terms that remains identical by any circular permutation (n, p, q) of $(0, 1, 2)$.

Using the last form (4.89), we get the Manley-Rowe relations (1956)[16] which state that:

Manley-Rowe relations (1956)

The wave action of each wave n, $\mathcal{A}_n = \mathcal{E}_n / \omega_n = |\Phi_n|^2 / \omega_n = (\omega_n a_n) a_n^*$, satisfies $\mathcal{A}_{n,T} = 2\Lambda \Re(a_0 a_1 a_2)$, implying:

$$\frac{d\mathcal{A}_0}{dT} = \frac{d\mathcal{A}_1}{dT} = \frac{d\mathcal{A}_2}{dT} \tag{4.91}$$

16. Manley and Rowe, *op. cit.*

introducing three quadratic invariants $\mathcal{A}_0-\mathcal{A}_1 = |\Phi_0|^2/\omega_0-|\Phi_1|^2/\omega_1$, $\mathcal{A}_1-\mathcal{A}_2 = |\Phi_1|^2/\omega_1-|\Phi_2|^2/\omega_2$, and $\mathcal{A}_2-\mathcal{A}_0 = |\Phi_2|^2/\omega_2-|\Phi_0|^2/\omega_0$. Hence, as $\sum_n \omega_n = 0$ and $\sum_n \boldsymbol{k_n} = \boldsymbol{0}$ at resonance:

$$\frac{d\mathcal{E}}{dT} = \frac{d}{dT}\sum_n \mathcal{A}_n\omega_n = 2\Lambda\Re(a_0a_1a_2)\sum_n \omega_n = 0 \tag{4.92}$$

$$\frac{d\boldsymbol{\mathcal{P}}}{dT} = \frac{d}{dT}\sum_n \mathcal{A}_n\boldsymbol{k_n} = 2\Lambda\Re(a_0a_1a_2)\sum_n \boldsymbol{k_n} = \boldsymbol{0} \tag{4.93}$$

resulting in the conservation of the total energy and pseudomomentum vector. It can be shown that this conservation is strictly equivalent to the Manley-Rowe relations at resonance. Indeed, if $\sum_n \omega_n = 0$ and $\sum_n \boldsymbol{k_n} = \boldsymbol{0}$, then the vector $\boldsymbol{1} = (1,1,1)$ is orthogonal to $\boldsymbol{\Omega} = (\omega_0,\omega_1,\omega_2)$, $\boldsymbol{K_x} = (k_{x0},k_{x1},k_{x2})$ and $\boldsymbol{K_z} = (k_{z0},k_{z1},k_{z2})$[17]. Assuming the conservation of energy and pseudomomentum, we get $\sum_n \mathcal{A}_{n,T}\omega_n = 0$ and $\sum_n \mathcal{A}_{n,T}\boldsymbol{k_n} = \boldsymbol{0}$, so that vector $\boldsymbol{A}_{,T} = (\mathcal{A}_{0,T},\mathcal{A}_{1,T},\mathcal{A}_{2,T})$ is also orthogonal to $\boldsymbol{\Omega}$, $\boldsymbol{K_x}$ and $\boldsymbol{K_z}$. As $\boldsymbol{\Omega}$ and $\boldsymbol{K_x}$ are different from the dispersion relation, they generate a plane (Π) of normal vector $\boldsymbol{1}$ as shown in figure 4.4. So $\boldsymbol{A}_{,T}$ is orthogonal to this plan, hence colinear to $\boldsymbol{1}$ which results in the Manley-Rowe relations. This proof also shows that one component of the pseudomomentum along with the conservation of energy, leading to two quadratic invariants in $|\Phi_n|$, is sufficient to describe the dynamics of triadic interaction for real amplitudes. In fact, as $\boldsymbol{\Omega}$, $\boldsymbol{K_x}$ and $\boldsymbol{K_z}$ are all different but belong to the same plane, we can find constants such that $\boldsymbol{K_z}$ is expressed as a linear combination of $\boldsymbol{\Omega}$ and $\boldsymbol{K_x}$. Thus, at resonance, either Manley-Rowe relations, or equivalently the conservation of energy and pseudomomentum, give rise to two independent quadratic invariants. With (4.87) (or equivalently (4.86) or (4.89)) having effectively 6 equations (for the three amplitudes modulus $|\Phi_n|$, n being 0, 1 or 2, and their three associated phases, or equivalently real and imaginary parts of ϕ_n), we demonstrate that the triadic equations actually constraint the time evolution of the total phase φ of $\Phi_0\Phi_1\Phi_2$.

We use (4.87) again to prove the existence of a third invariant, the Hamiltonian. For $\chi = \Phi_0\Phi_1\Phi_2 = |\chi|e^{i\varphi}$, φ being the phase of $\Phi_0\Phi_1\Phi_2$:

$$\arg\left(\frac{d\chi}{dT}\right) = \arctan\left(\frac{|\chi|\varphi_{,T}}{|\chi|_{,T}}\right) + \varphi \mod 2\pi \tag{4.94}$$

and using (4.87), we find that $\chi_{,T}$ is real so $\arg(\chi_{,T}) = 0 \mod \pi$, and taking the tangent of the previous equality, we find after multiplying by $|\chi|_{,T}\cos\varphi$:

$$|\chi|\frac{d\varphi}{dT}\cos\varphi + \frac{d|\chi|}{dT}\sin\varphi = \frac{d|\chi|\sin\varphi}{dT} = 0 \tag{4.95}$$

17. with respect to the canonical scalar product $\boldsymbol{a}\cdot\boldsymbol{b} = \sum_n a_nb_n$, with $\boldsymbol{a} = (a_1,a_2,a_3)$ and $\boldsymbol{b} = (b_1,b_2,b_3)$.

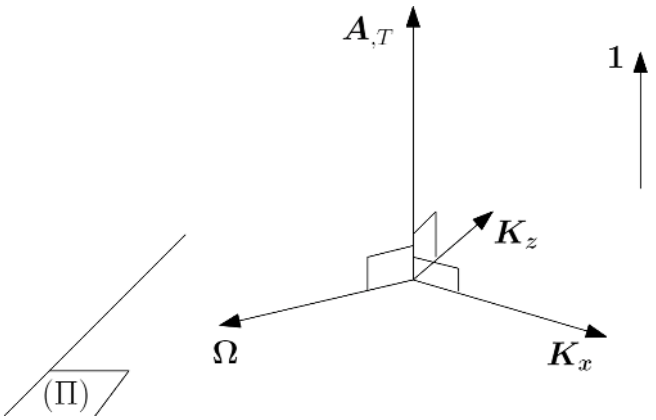

Figure 4.4: Orthogonality of $\mathbf{1}$ and $\boldsymbol{A}_{,T}$ to the plane (Π) containing $(\boldsymbol{\Omega}, \boldsymbol{K_x}, \boldsymbol{K_z})$.

which implies that $\mathcal{K} = |\Phi_0\Phi_1\Phi_2| \sin\varphi$ is constant. $\mathcal{K}$ is referred to as the Hamiltonian in the literature when investigating properties of three-wave interaction equations in classical problems such as the swinging spring[18], or capillary-gravity waves[19]. The universality of three wave resonance in various fields of physics including optics, electronics, plasma physics and fluid originates from common dynamics, fully described by a set of general conservative equations for resonance, the so-called three wave interaction equations:

General form of the three waves interaction equations

At resonance $\sum_n \omega_n = 0$ and $\sum_n \boldsymbol{k_n} = \mathbf{0}$, the renormalized amplitudes $A_n = C\sqrt{|\omega_n|}a_n$ obey to:

$$\frac{dA_n}{dT} = s_n A_p^* A_q^* \tag{4.96}$$

s_n being the sign of ω_n and $C = \Lambda/\sqrt{|\omega_n\omega_p\omega_q|}$ a normalization factor.

4.2.2 Linearized triadic system

From now on, we set the energy norm to be the Euclidean norm so that, in equations (4.85), the energy, pseudomomentum and phase invariant are now given by:

$$\mathcal{E} = \sum_n |\Phi_n|^2, \quad \boldsymbol{\mathcal{P}} = \sum_n \frac{\boldsymbol{k_n}}{\omega_n}|\Phi_n|^2, \quad \mathcal{K} = |\Phi_0\Phi_1\Phi_2| \sin\varphi \tag{4.97}$$

with this specific choice, the triadic equations (4.87) read:

18. D. D. Holm and P. Lynch, "Stepwise Precession of the Resonant Swinging Spring", in: *SIAM J. Appl. Dyn. Syst.* 1.*1* (Jan. 2002), pp. 44–64.
19. McGoldrick, *op. cit.*

$$\frac{d\Phi_0}{dt} = L_0\Phi_2^*\Phi_1^* \tag{4.98}$$
$$\frac{d\Phi_1}{dt} = L_1\Phi_0^*\Phi_2^* \tag{4.99}$$
$$\frac{d\Phi_2}{dt} = L_2\Phi_1^*\Phi_0^* \tag{4.100}$$

where Φ_n^* is the complex conjugate of Φ_n and the interaction coefficients L_n are expressed using the phase velocities $\boldsymbol{c}_n = (c_{xn}, c_{zn}) = (\omega_n/k_{xn}, \omega_n/k_{zn})$:

$$L_0 = \Lambda_x\left(\frac{1}{c_{x2}} - \frac{1}{c_{x1}}\right) + \left(\frac{f}{N}\right)^2\Lambda_z\left(\frac{1}{c_{z2}} - \frac{1}{c_{z1}}\right) \tag{4.101}$$
$$L_1 = \Lambda_x\left(\frac{1}{c_{x0}} - \frac{1}{c_{x2}}\right) + \left(\frac{f}{N}\right)^2\Lambda_z\left(\frac{1}{c_{z0}} - \frac{1}{c_{z2}}\right) \tag{4.102}$$
$$L_2 = \Lambda_x\left(\frac{1}{c_{x1}} - \frac{1}{c_{x0}}\right) + \left(\frac{f}{N}\right)^2\Lambda_z\left(\frac{1}{c_{z1}} - \frac{1}{c_{z0}}\right) \tag{4.103}$$

The nonlinear triadic equations (4.98)-(4.100) is linearized assuming that one wave, let's say Φ_0, referred to as the primary wave, has an amplitude much greater than the two other waves, Φ_1 and Φ_2 called secondary waves:

Pump wave approximation

The primary wave amplitudes Φ_0 and the secondary waves amplitudes Φ_1 and Φ_2 are such that:

$$|\Phi_1| \ll |\Phi_0|, \text{ and } |\Phi_2| \ll |\Phi_0| \tag{4.104}$$

This means that Φ_1 and Φ_2 act as an infinitesimal perturbation of the base state Φ_0, the corresponding perturbation energy being equal to $e = |\Phi_1|^2 + |\Phi_2|^2$ and verifying $e \ll \mathcal{E}$. The secondary waves varies much more than the primary, so the pump wave approximation implies:

$$\frac{d\Phi_0}{dT} = 0 \tag{4.105}$$

and the triadic equations (4.98)-(4.100) can be linearized around the base state Φ_0:

Linearized triadic equations

Under the pump wave approximation, the triadic equations read:

$$\frac{d\mathbf{\Phi'}}{dT} = \mathscr{L}\mathbf{\Phi'}^*, \text{ with } \mathscr{L} = \begin{pmatrix} 0 & L_1 \\ L_2 & 0 \end{pmatrix} \tag{4.106}$$

where $\mathbf{\Phi'} = (\Phi_1, \Phi_2)$, when setting, without loss of generality, $\mathcal{E} = 1$ and Φ_0 real, close to unity, so that $e = \|\mathbf{\Phi'}\|^2 \ll 1$, $\|\mathbf{\Phi'}\|^2 = |\Phi_1|^2 + |\Phi_2|^2$ being the 2D Euclidean norm.

Knowing that the interaction coefficients are such that $\omega_0 L_1 \omega_2 = \omega_1 L_2 \omega_0$, if (s_0, s_1, s_2) are the signs of $(\omega_0, \omega_1, \omega_2)$, we get the following stability criterion[20] for the linearized system (4.106):

Hasselmann criterion (1967)

With the chosen convention for resonance given by (4.76) and (4.77), the linear stability of the solutions of (4.106) is given by the sign of $L_1 L_2$, which verifies:

$$\text{sign}(L_1 L_2) = s_1 s_2 \tag{4.107}$$

so that, if $s_1 s_2 > 0$, the system is linearly unstable, whereas, if $s_1 s_2 < 0$, the system is linearly stable.

If we fix $s_0 = +1$, then, as $|\omega_0| + s_1|\omega_1| + s_2|\omega_2| = 0$, all the possible sign combinations (s_0, s_1, s_2) are $(+,+,+)$, which is linearly unstable, $(+,+,-)$ and $(+,-,+)$, which are both linearly stable. The $(+,+,+)$ case leads to exponential growth of the amplitudes (Φ_1, Φ_2), whereas the $(+,+,-)$ and $(+,-,+)$ cases result in bounded periodic oscillations. The $(+,+,-)$ and $(+,-,+)$ are equivalent cases obtained by exchanging the roles played by Φ_1 and Φ_2. Indeed, solving (4.106), we get, for n equals 1 or 2, and complex integration constants (A_n, B_n, C_n, D_n):

$$\Phi_n = \begin{cases} A_n \exp(\sigma_{\text{th}}) + B_n \exp(-\sigma_{\text{th}}) & \text{in the } (+,+,+) \text{ case} \\ C_n \exp(i\sigma_{\text{th}}) + D_n \exp(-i\sigma_{\text{th}}) & \text{in the } (+,\pm,\mp) \text{ cases} \end{cases} \tag{4.108}$$

and the associated theoretical[21] growth rate σ_{th} of the perturbation field (Φ_1, Φ_2) in the

20. Hasselmann, *op. cit.*
21. given by Hasselmann theory.

steady state reached at longer times T then equals:

$$\sigma_{\text{th}} = \begin{cases} \sqrt{L_1 L_2} & \text{in the } (+,+,+) \text{ case} \\ 0 & \text{in the } (+,\pm,\mp) \text{ cases} \end{cases} \tag{4.109}$$

The resonance conditions (4.76) and (4.77)[22], combined with the dispersion relation (4.73) gives:

$$\begin{aligned} s_0\sqrt{\frac{k_{x0}^2+\left(\frac{f}{N}\right)^2 k_{z0}^2}{k_{x0}^2+k_{z0}^2}} + s_1\sqrt{\frac{k_{x1}^2+\left(\frac{f}{N}\right)^2 k_{z1}^2}{k_{x1}^2+k_{z1}^2}} \\ + s_2\sqrt{\frac{(k_{x0}+k_{x1})^2+\left(\frac{f}{N}\right)^2 (k_{z0}+k_{z1})^2}{(k_{x0}+k_{x1})^2+(k_{z0}+k_{z1})^2}} = 0 \end{aligned} \tag{4.110}$$

where (s_0, s_1, s_2) are the signs of $(\omega_0, \omega_1, \omega_2)$ respectively. Without loss of generality, we can fix wave 0 such that $s_0 = +1$, $k_0 = 1$ and $\theta_0 = 0.13$ to plot the resonance locus defined by the implicit equation (4.110) in a $\boldsymbol{k_1}$ plane on figure 4.5. For all geophysical values of f/N from 0 to 0.15, the $(+,+,+)$, $(+,+,-)$ and $(+,-,+)$, plotted in red, blue and green lines respectively, follow Hasselmann criterion of linear stability, so that the red curve $(+,+,+)$ is linearly unstable, whereas, the blue and green curves, $(+,+,-)$ and $(+,-,+)$ respectively, are linearly stable. Moreover, the plots on figure 4.5 exhibit the same symmetries $\boldsymbol{k} \to -\boldsymbol{k_0} - \boldsymbol{k}$, as the curves are invariant by exchanging the roles played by $\boldsymbol{k_1}$ and $\boldsymbol{k_2}$. So the properties captures by the green and blue curves are the same and the roles played by the two portions of red curves (positive k_z versus negative k_z on figure 4.5) are strictly identical by exchanging $\boldsymbol{k_1}$ and $\boldsymbol{k_2}$. From this remark, we can focus on the study of the linearly stable blue curve $(+,+,-)$, and the linearly unstable red curve $(+,+,+)$ in the negative k_z space, without loss of information.

22. Another possible convention would be $\omega_0 = \omega_1 + \omega_2$ and $\boldsymbol{k_0} = \boldsymbol{k_1} + \boldsymbol{k_2}$, e.g. Hasselmann (1967). The chosen convention in this manuscript tends to "symmetrize" the roles played by waves 0, 1, and 2.

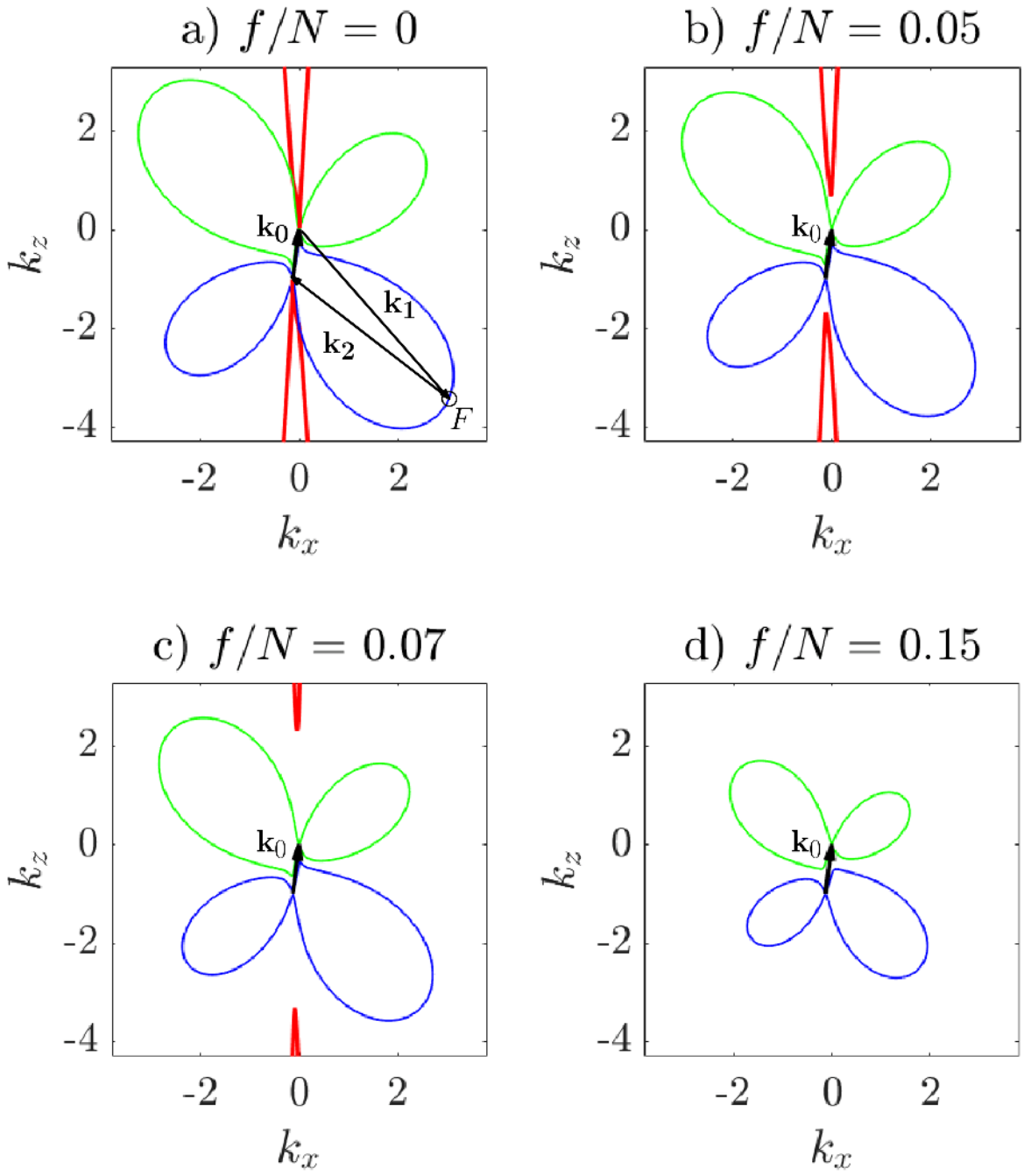

Figure 4.5: Plots of the resonance locus in a (k_x, k_z) plane corresponding to the components of the wave vector $\boldsymbol{k_1}$ for different values of f/N, 0 in a), 0.05 in b), 0.07 in c), 0.15 in d). In all figures, the $(+,+,+)$, $(+,+,-)$ and $(+,-,+)$ are plotted in red, blue and green lines respectively, the wave vector $\boldsymbol{k_0}$ is plotted in dark arrow. On figure a), a resonant triad located by point F is taken as an example by plotting $\boldsymbol{k_1}$ from the tip of $\boldsymbol{k_0}$ to point F and $\boldsymbol{k_2} = -\boldsymbol{k_0} - \boldsymbol{k_1}$.

Part III

Main results of the thesis

Chapter 5

Transient growth, edge states and repeller in rotating solid and fluid (reprint *Physical Review E*)

5.1 Abstract

For the classical problem of the rotation of a solid, we show a somehow surprising behavior involving large transient growth of perturbation energy that occurs when the moment of inertia associated to the unstable axis approaches the moment of inertia of one of the two stable axes. In that case, small but finite perturbations around this stable axis may induce a total transfer of energy to the unstable axis leading to relaxation oscillations where the stable and unstable manifolds of the unstable axis play the role of a separatrix, an edge state. For a fluid in solid body rotation, a similar linear and nonlinear dynamics apply to the transfer of energy between three inertial waves respecting the triadic resonance condition. We show that the existence of large transient energy growth and of relaxation oscillations may be physically interpreted as in the case of a solid by the existence of two quadratic invariants, the energy and the helicity in the case of a rotating fluid. They occur when two waves of the triad have helicities that tend towards each other, when their amplitudes are set such that they have the same energy. We show that this happens when the third wave has a vanishing frequency which corresponds to a nearly horizontal wave vector. An inertial wave, perturbed by a small amplitude wave with a nearly horizontal wave vector, will then be periodically destroyed, its energy being transferred entirely to the unstable wave, although this perturbation is linearly stable, resulting in relaxation oscillations of wave amplitudes. In the general case, we show that the dynamics described for particular triads of inertial waves is valid for a class of triadic interactions of waves in other physical problems, where the physical energy is conserved and is linked to the classical conservation of the so-called pseudomomentum, which singles out the role of waves with vanishing frequency.

5.2 Rotating rigid body

The motion of a solid is a well-studied problem. For a non-symmetric rigid body, the rotation around the two axes with the highest and the smallest moments of inertia are stable whereas the intermediate axis is unstable resulting in the so-called tennis racket effect[1] (see video at `https://www.youtube.com/watch?v=1VPfZ_XzisU`). We reconsider this classic example and show that surprising phenomena occur also for a rotation around a stable axis when the smallest or the highest moment of inertia of the solid J_1 or J_0 gets close to the intermediate one J_2 and discuss the extension to conservative waves systems.

The rotation of a rigid body in the reference frame with its axes fixed to the body obey to[2]:

$$\begin{aligned}\frac{dM_0}{dt} &= \left(\frac{1}{J_2}-\frac{1}{J_1}\right)M_2M_1\\ \frac{dM_1}{dt} &= \left(\frac{1}{J_0}-\frac{1}{J_2}\right)M_0M_2\\ \frac{dM_2}{dt} &= \left(\frac{1}{J_1}-\frac{1}{J_0}\right)M_1M_0\end{aligned} \tag{5.1}$$

where $\mathbf{M}=(M_0,M_1,M_2)^{\mathrm{T}}$ is the angular momentum vector and $0<J_1<J_2<J_0$ are the moments of inertia. Equations (5.1) conserve the total energy $\mathcal{E}$ and the total momentum $\mathcal{M}$ (with the change of variables $M'_n=M_n/\sqrt{2J_n}$):

$$\mathcal{E}=\sum_n M_n'^2, \quad \mathcal{M}^2=\sum_n 2J_nM_n'^2 \tag{5.2}$$

In a (M'_0,M'_1,M'_2) space, the energy is the Euclidean norm and trajectories are given by the intersection of the sphere of energy $\mathcal{E}$ and constant momentum ellipsoids with $\mathcal{M}^2$ between $2J_1\mathcal{E}$ and $2J_0\mathcal{E}$. By rescaling the angular momentum, we may set $\mathcal{E}=1$. Figure 5.1 represents those intersections for different values of $\mathcal{M}^2$ when $J_2=(1-\varepsilon)J_0$ with $\varepsilon=2.10^{-2}$ and $J_1=(1-\Sigma)J_0$ with $\Sigma=0.9$. On the sphere, the point $\mathbf{M'_2}=(0,0,1)^{\mathrm{T}}$ is unstable and surrounded locally by hyperbolic trajectories, the points $\mathbf{M'_1}=(0,1,0)^{\mathrm{T}}$ and $\mathbf{M'_0}=(1,0,0)^{\mathrm{T}}$ are stable and surrounded by ellipses (in blue and red). The two basins of solutions nutating around $\mathbf{M'_1}$ in blue or $\mathbf{M'_0}$ in red are separated by the separatrix given by $\mathcal{M}^2=2J_2$.

Linear perturbations $(m'_0,m'_1,m'_2)^{\mathrm{T}}$ around the stable point $\mathbf{M'_0}$ belong to the tangent

1. L. Van Damme, P. Mardesic, and D. Sugny, "The tennis racket effect in a three-dimensional rigid body", in: *Physica D* 338 (Jan. 2017), pp. 17–25.
2. L. Euler, "Du mouvement de rotation des corps solides autour d'un axe variable", in: *Memoires de l'academie des sciences de Berlin* 8.*14* (1758), pp. 154–193.

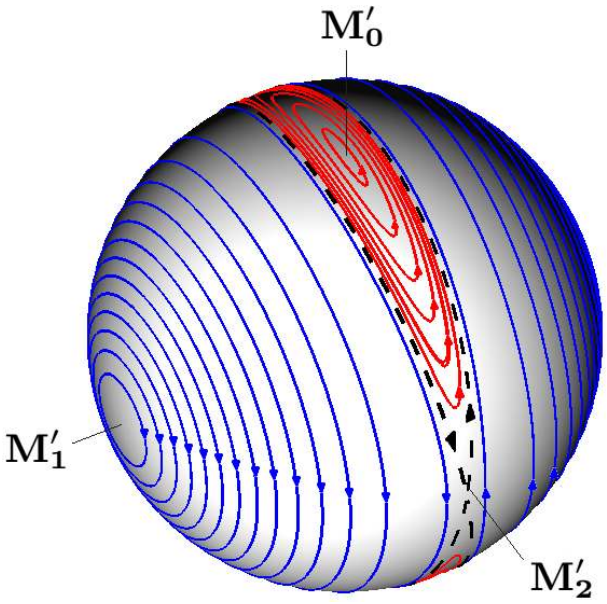

Figure 5.1: Trajectories on the sphere unity $\mathcal{E} = 1$ in the (M'_0, M'_1, M'_2) space with $J_2 = (1-\varepsilon)J_0$, $\varepsilon = 2.10^{-2}$, $J_1 = (1-\Sigma)J_0$ and $\Sigma = 0.9$. The point $\mathbf{M'_1} = (0,1,0)^{\mathrm{T}}$ is stable and close trajectories around $\mathbf{M'_1}$ are plotted in blue, $\mathbf{M'_0} = (0,0,1)^{\mathrm{T}}$ is stable too and close trajectories around $\mathbf{M'_0}$ are in red.

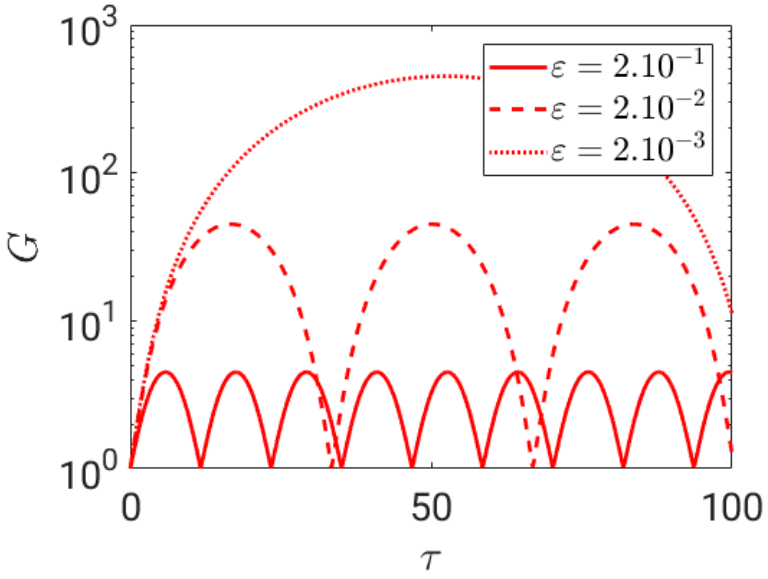

Figure 5.2: Energy gain G defined in (5.4) as a function of time τ for the linearized problem around the stable point $\mathbf{M'_0} = (0,0,1)^{\mathrm{T}}$ for $\Sigma = 0.9$ and $\varepsilon = 2.10^{-1}$ (continuous line), $\varepsilon = 2.10^{-2}$ (dashed line) and $\varepsilon = 2.10^{-3}$ (dotted line).

plane $\mathbf{m}' = (m_1', m_2')^{\mathrm{T}}$ since $dm_0'/dt = 0$ at leading order:

$$\frac{d\mathbf{m}'}{d\tau} = \mathscr{L}\mathbf{m}' \quad \text{with} \quad \mathscr{L} = \begin{pmatrix} 0 & -\varepsilon \\ \Sigma & 0 \end{pmatrix} \tag{5.3}$$

with $\tau = t\sqrt{2/(1-\varepsilon)(1-\Sigma)J_0}$. We define the optimal perturbation energy gain G as:

$$G(\tau) = \max_{e(0)=1} e(\tau) \tag{5.4}$$

where $e = m_1'^2 + m_2'^2$ is the energy of the perturbation. When $\varepsilon \neq \Sigma$, the evolution operator $\mathscr{L}$ is nonnormal with respect to the classical Euclidean inner product, its associated norm being the energy e, and $\mathscr{L}\mathscr{L}^{\mathrm{T}} \neq \mathscr{L}^{\mathrm{T}}\mathscr{L}$. The energy gain G is plotted as a function of time on figure 5.2. The gain is periodic and when ε decreases, the maximum value of G, $G_{\max} = \Sigma/\varepsilon$, and the period of oscillations $T = 2\pi/\sqrt{\varepsilon\Sigma}$ increase. This transient growth corresponds to the elongated elliptic trajectories around the stable point $\mathbf{M_0'}$ on figure 5.2.

For finite initial amplitude, the trajectories are no more on the tangent plane but on the sphere meaning that to conserve energy, $\mathbf{M_0'}$ has to depart from unity. They keep being closed around the point $\mathbf{M_0'}$ until they pass the separatrix that links the saddle $\mathbf{M_2'}$ and $-\mathbf{M_2'}$ and crosses the $M_2' = 0$ plane on the point $\mathbf{M}_\varepsilon' = (\sqrt{1-\varepsilon/\Sigma}, \sqrt{\varepsilon/\Sigma}, 0)^{\mathrm{T}}$. Therefore, a perturbation of the point $\mathbf{M_0'}$ along the $\mathbf{M_1'}$ axis of perturbation energy ε/Σ will trigger a motion no more nutating around $\mathbf{M_0'}$ but around $\mathbf{M_1'}$ with periodic extinction of the rotation around the point $\mathbf{M_0'}$. The trajectories show relaxation with extremely large time spent around the unstable point $\mathbf{M_2'}$ that acts as a repeller and transient short passage close to the stable point $\mathbf{M_0'}$.

5.3 Rotating fluid

Similar transient growth mechanism and nonlinear separatrix concern other conservative systems and we consider here the case of resonant triad of inertial waves in rotating fluids[3]. When an incompressible, inviscid fluid is in solid body rotation at angular velocity Ω along the z axis, the Coriolis force acts as a conservative restoring force and is associated with the propagation of waves given by the dispersion relation:

$$\left(\frac{\omega}{f}\right)^2 = \left(\frac{k_z}{k}\right)^2 \tag{5.5}$$

where $f = 2\Omega$ is the Coriolis parameter, $\boldsymbol{k}$ the wave vector, k its modulus and k_z its

3. H. K. Moffatt, "Note on the triad interactions of homogeneous turbulence", in: *J. Fluid Mech.* 741 (Feb. 2014), R3.

vertical component. This dispersion relation is derived linearizing the incompressible rotating Euler equation. When the wave amplitude is not infinitesimal, the Rossby number $Ro = U/(Lf)$, where U and L are the typical velocity and length scale in the wave field, becomes finite. The nonlinearity in the rotating Euler equation being quadratic, three waves $(\omega_0, \boldsymbol{k_0})$, $(\omega_1, \boldsymbol{k_1})$, $(\omega_2, \boldsymbol{k_2})$ independent at leading order in Rossby number will be coupled at the second order if they form a triad:

$$\begin{aligned} \omega_0 + \omega_1 + \omega_2 &= 0 \\ \boldsymbol{k_0} + \boldsymbol{k_1} + \boldsymbol{k_2} &= \boldsymbol{0} \end{aligned} \tag{5.6}$$

If we note s_n the sign of the frequency ω_n of the n-th wave, the triadic resonance conditions (5.6) give by eliminating $\boldsymbol{k_2}$:

$$s_0 \frac{|k_{z0}|}{k_0} + s_1 \frac{|k_{z1}|}{k_1} + s_2 \frac{|k_{z0} + k_{z1}|}{k_{01}} = 0 \tag{5.7}$$

where k_0, k_1 and k_{01} are respectively the modulus of $\boldsymbol{k_0}$, $\boldsymbol{k_1}$ and $\boldsymbol{k_0} + \boldsymbol{k_1}$. For simplicity, we will assume the plane formed by the three resonant wave vectors to be vertical ($k_{yn} = 0$). In this so-called 2D-3C (two-dimensional, three components) model[4], waves may be defined by their streamfunction with a complex amplitude Ψ_n, the associated velocity along x, y and z being $u_n = -ik_{zn}\Psi_n \exp i(k_{xn}x + k_{zn}z - \omega_n t) + c.c.$, $v_n = -fk_{zn}/\omega_n \Psi_n \exp i(k_{xn}x + k_{zn}z - \omega_n t) + c.c.$ and $w_n = -k_{xn}/k_{zn} u_n$ where $c.c.$ indicates the complex conjugate. Formally, the derivation involves a multiscale expansion with the introduction of a slow time scale $T = Rot$, the wave amplitude $\Psi_n(T)$ then being a function of T as in the derivation of the WKB approximation[5]. A second order expansion in Rossby number leads to the amplitude equations for the resonant waves (see[6] for more details). When transforming back the slow time scale T in the primitive time t, those equations read:

$$\begin{aligned} \frac{d\Phi_0}{dt} &= \Lambda_z(\sigma_2 k_2 - \sigma_1 k_1)\Phi_2^* \Phi_1^* \\ \frac{d\Phi_1}{dt} &= \Lambda_z(\sigma_0 k_0 - \sigma_2 k_2)\Phi_0^* \Phi_2^* \\ \frac{d\Phi_2}{dt} &= \Lambda_z(\sigma_1 k_1 - \sigma_0 k_0)\Phi_1^* \Phi_0^* \end{aligned} \tag{5.8}$$

4. G. Bordes et al., "Experimental evidence of a triadic resonance of plane inertial waves in a rotating fluid", in: *Phys. Fluids* 24.*1* (Jan. 2012), p. 014105.

5. C. M. Bender and S. A. Orszag, "Advanced Mathematical Methods for Scientists and Engineers I: Asymptotic Methods and Perturbation Theory", in: *Advanced Mathematical Methods for Scientists and Engineers I: Asymptotic Methods and Perturbation Theory*, New York, NY: Springer, 1999, pp. 484–543.

6. L. M. Smith and F. Waleffe, "Transfer of energy to two-dimensional large scales in forced, rotating three-dimensional turbulence", in: *Phys. Fluids* 11.*6* (June 1999), pp. 1608–1622.

with the change of variable $\Phi_n = k_n\Psi_n/2$, $\sigma_n = s_n\text{sign}(k_{zn})$ the vertical orientation of the phase velocity, and $\Lambda_z = \Delta(\sigma_0 k_0 + \sigma_1 k_1 + \sigma_2 k_2)/(k_0 k_1 k_2)$, Δ being twice the oriented area of the triangle ($\boldsymbol{k_0}$, $\boldsymbol{k_1}$, $\boldsymbol{k_2}$), $\Delta = k_{x1}k_{z2} - k_{x2}k_{z1}$[7]. Equations (5.8) admit three invariants:

$$\begin{gathered}\mathcal{E} = \sum_n |\Phi_n|^2, \quad \mathcal{H} = \sum_n 2\sigma_n k_n |\Phi_n|^2, \\ \mathcal{K} = |\Phi_0|\,|\Phi_1|\,|\Phi_2| \sin\varphi\end{gathered} \tag{5.9}$$

where φ is the phase of $\Phi_0\Phi_1\Phi_2$. $\mathcal{E}$ is the energy, the sum of each wave total energy $|\Phi_n|^2$, and $\mathcal{H}$ the helicity[8] conserved within the triad as discussed in[9]. Only the invariant $\mathcal{K}$, also called Hamiltonian by[10], involves the phases of Φ_n, as discussed in[11]. The analogy with the solid body rotation is direct comparing the quadratic invariants of the two systems with $|\Phi_n|$ playing the role of $|M'_n|$ and k_n the role of the moments of inertia J_n, the differences being that the wave amplitudes Φ_n are complex and that when one σ_n is negative, the helicity $\mathcal{H}$ is not a definite positive form. For simplicity, we study the triad T plotted in black on figure 5.3 whose helicity signs are all positive i.e. $(\sigma_0, \sigma_1, \sigma_2) = (+,+,+)$ with $k_0 = 1$ by rescaling the space. By rescaling the time, the energy $\mathcal{E}$ is set to unity. Figure 5.4a) plots in the amplitude space $|\Phi_n|$ the lines where both $\mathcal{E}$ and $\mathcal{H}$ are constant for the triad T. The trajectories lie on the lines of intersection between the unit energy sphere and constant helicity ellipsoid following the same reasoning as for the solid with a separatrix issuing from the unstable wave $(\omega_2, \boldsymbol{k_2})$ splitting the modulus space between trajectories oscillating around $(\omega_0, \boldsymbol{k_0})$ and around $(\omega_1, \boldsymbol{k_1})$. The separatrix is then given by the helicity of wave $(\omega_2, \boldsymbol{k_2})$, $\mathcal{H} = 2k_2$ and starts from the point $\mathbf{M'_2} = (0,0,1)^{\mathrm{T}}$ with $\mathbf{M'} = (|\Phi_0|, |\Phi_1|, |\Phi_2|)^{\mathrm{T}}$ and crosses the plane $|\Phi_2| = 0$ at $\mathbf{M'_\varepsilon} = (\sqrt{1-\varepsilon/\Sigma}, \sqrt{\varepsilon/\Sigma}, 0)^{\mathrm{T}}$ with $\varepsilon = 1 - \sigma_2 k_2/(\sigma_0 k_0)$ and $\Sigma = 1 - \sigma_1 k_1/(\sigma_0 k_0)$. The separatrix passes at a distance in perturbation energy of ε/Σ from the point $\mathbf{M'_0} = (1,0,0)^{\mathrm{T}}$ corresponding to the stable wave $(\omega_0, \boldsymbol{k_0})$. If for the solid, the lines on the sphere unity are trajectories traveled in a unique direction, the lines on figure 5.4a) are only projections of the trajectories in the modulus space. A point on a particular trajectory on figure 5.4a) is defined by a unique value of the modulus $|\Phi_2|$ ($|\Phi_0|$ and $|\Phi_1|$ being given by the invariants $\mathcal{E}$ and $\mathcal{H}$) but may be realized by different initial values of φ (the phase of the three waves) giving different initial values of the invariant $\mathcal{K}$ between 0 and the initial value of $|\Phi_0||\Phi_1||\Phi_2|$. The conservation of $\mathcal{K}$ imposes that the time evolutions of $|\Phi_2|$ and φ are linked, the vector

7. The coefficient Γ from the original article is replaced by the notation Λ_z to fit the rest of the manuscript.

8. Appendix A demonstrates the equality between helicity, an invariant of the rotating flow derived from the dynamical equations as seen in Appendix B, and pseudomomentum, a characteristic of inertial waves.

9. Moffatt, *op. cit.*

10. P. Lynch, "Resonant Rossby Wave Triads and the Swinging Spring", in: *Bull. Amer. Meteor. Soc.* 84.5 (May 2003), pp. 605–616.

11. Weiland and Wilhelmsson, *op. cit.*

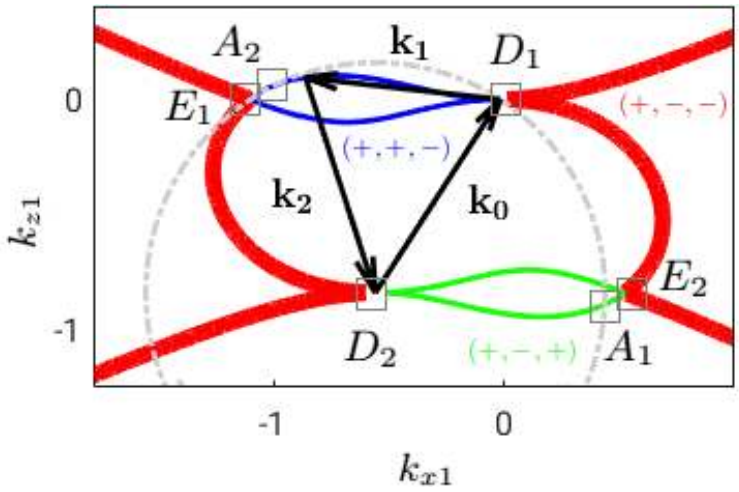

Figure 5.3: Resonant triads in the wave vector space (k_{x1}, k_{z1}) when the wave $(\omega_0, \boldsymbol{k_0})$ is fixed with $s_0 = +1$, $k_0 = 1$ and $\omega_0/f = 0.84$ (value taken from Bordes & al. 2012), $\boldsymbol{k_0}$ being plotted on the figure in black arrow. The unstable branches $(+,-,-)$ are represented in red whereas the stable branches to $(+,-,+)$ and $(+,+,-)$ are represented in blue and green. The unit circle centered on $-\boldsymbol{k_0}$ is plotted in dashed grey lines. The points (E_1, D_1, A_1) marked with squares indicate triads where $\sigma_2 k_2 \to \sigma_0 k_0 = 1$. (E_2, D_2, A_2) are the symmetric of (E_1, D_1, A_1) by exchanging $\boldsymbol{k_1}$ and $\boldsymbol{k_2}$ such that $\sigma_1 k_1 \to \sigma_0 k_0 = 1$. The exemplified triad T ($\boldsymbol{k_0} \sim (0.54, 0.84)$, $\boldsymbol{k_1} \sim (-0.83, 0.1)$ and $\boldsymbol{k_2} \sim (0.29, -0.94)$) is plotted in black.

$(|\Phi_0|, |\Phi_1|, |\Phi_2|)$ being on a particular line on the energy sphere 5.4a) and the phase φ and the modulus $|\Phi_2|$ being on the trajectory corresponding to different values of $\mathcal{K}$. Figure 5.4b) shows such a set of trajectories for modulus on the separatrix i.e. for the helicity $\mathcal{H} = 2k_2$, this phase portrait is symmetric with respect to $\varphi = 0$ and only $\varphi \geq 0$ has been plotted. Trajectories where $\mathcal{K} \neq 0$ are closed and never reaches the axis $|\Phi_2| = 0$ or $|\Phi_2| = 1$, nor the axis $\varphi = 0$ or $\varphi = \pi$. The axis $\varphi = 0$ or $\varphi = \pi$ corresponds to the cases where $\mathcal{K} = 0$ with trajectories going from $|\Phi_2| = 1$ to $|\Phi_2| = 0$ and inversely. These cases where $\mathcal{K} = 0$ correspond to the real solutions of the system (5.8) since it is straightforward to prove that, when the initial conditions Φ_n are real, they stay real at all times and that any initial conditions with $\mathcal{K} = 0$ and non of the modulus $|\Phi_n|$ zero initially is equivalent to a real initial condition. Using the two phases invariances associated to the time and space translation, two of the Φ_n may be initially taken as real, the initial phase of the third Φ_n being then 0 modulo π to respect $\mathcal{K} = 0$. The cases where $\mathcal{K} = 0$ are then strictly equivalent to the solid case and the discussion on the nonlinear effects holds.

To capture the linear and nonlinear dynamics close to the wave $(\omega_0, \boldsymbol{k_0})$ in the triad T, we consider an initial condition such that $|\Phi_0|$ is close to unity and $|\Phi_1|$ and $|\Phi_2|$ small meaning that the invariant $\mathcal{K}$ is small and will be assumed zero to simplify the discussion. For the triad T, the waves $(\omega_0, \boldsymbol{k_0})$ and $(\omega_1, \boldsymbol{k_1})$ are stable, the wave $(\omega_2, \boldsymbol{k_2})$ unstable and $\varepsilon = 1 - \sigma_2 k_2/(\sigma_0 k_0) = 0.02$ and $\Sigma = 1 - \sigma_1 k_1/(\sigma_0 k_0) = 0.17$. Since ε is small compared to Σ, k_2 being close to k_0, large transient growth of the perturbation is possible around the wave

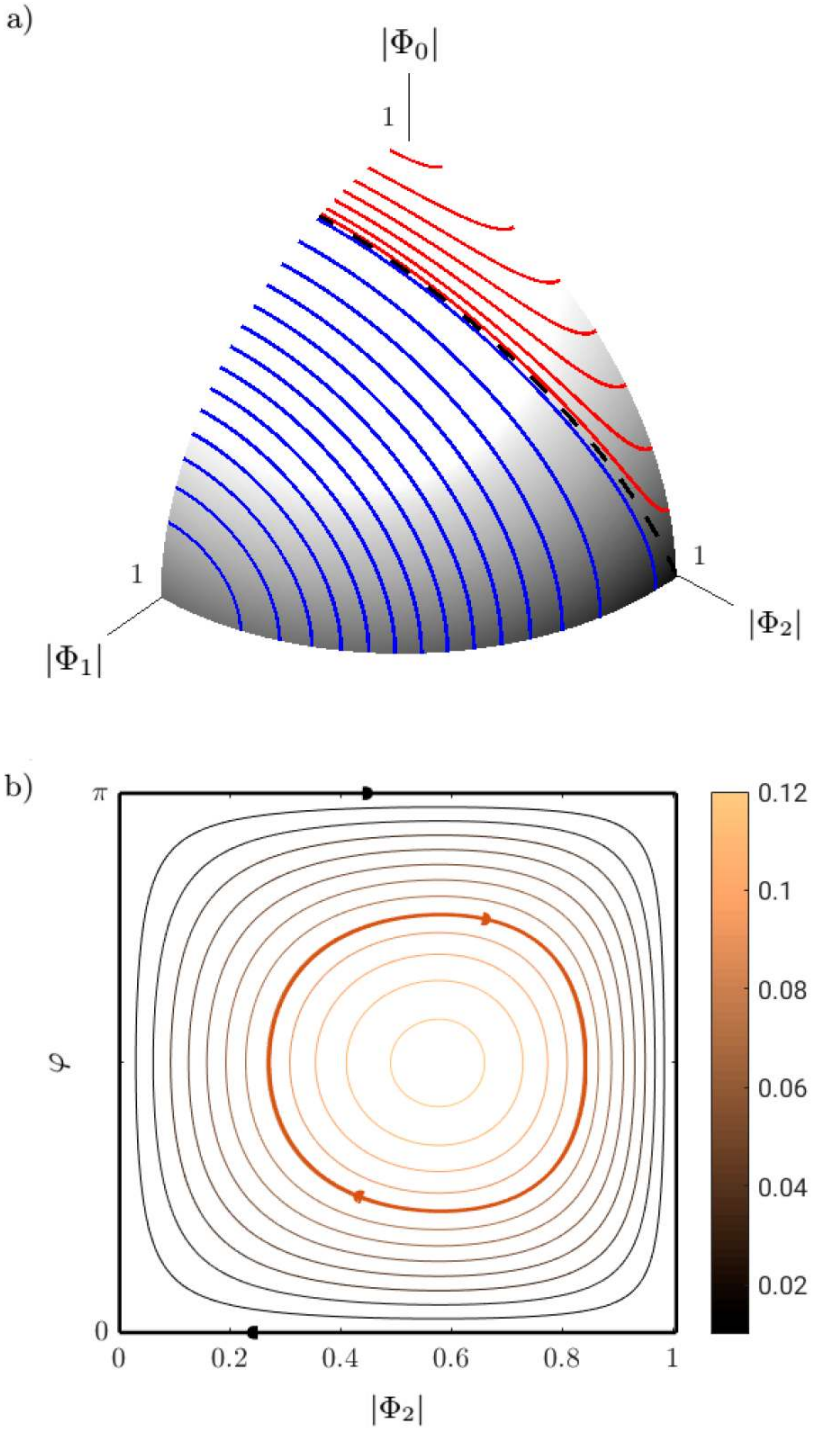

Figure 5.4: Trajectories corresponding to the dynamics given by equation (5.8) for the triad T plotted on figure 5.3, with $\varepsilon = 1 - \sigma_2 k_2/(\sigma_0 k_0) = 0.02$ and $\Sigma = 1 - \sigma_1 k_1/(\sigma_0 k_0) = 0.16$. a) Projection in the modulus space $(|\Phi_0|, |\Phi_1|, |\Phi_2|)$, trajectories are on the sphere of constant energy $\mathcal{E} = 1$ and corresponds to lines of constant helicity $\mathcal{H}$. b) Trajectories along the separatrix in black dashed lines on a) in the plane $(\varphi, |\Phi_2|)$. Since $\mathcal{K}$ is an invariant, contour plots of $\mathcal{K}$ for values given by the colorbar defines the trajectories. Three trajectories obtained by numerical integration of (5.8) for different initial conditions are also reported in heavy lines: $(\varphi, |\Phi_2|) = (\pi/4, 0.44)$ in copper, $(0, 0.99)$ in black, and $(\pi, 0.01)$ also in black.

$(\omega_0, \boldsymbol{k_0})$ corresponding to the elliptic trajectory in red on figure 5.4a) for which the aspect ratio is scaling like $\sqrt{\varepsilon/\Sigma}$ for a small perturbation amplitude. For larger amplitudes, the ellipses deform when approaching the point $\mathbf{M'_2} = (0,0,1)^{\mathrm{T}}$ where $|\Phi_2| = 1$. The separatrix is reached when the helicity approaches the one of the point $\mathbf{M'_2}$, $\mathcal{H} = 2k_2$. As for the solid, trajectories close to the separatrix correspond to relaxation oscillations with a frequency that vanishes on the separatrix. On these relaxation trajectories, the energy in the triad is transferred fast on a time duration proportional to $1/\Sigma$ from the stable wave $(\omega_0, \boldsymbol{k_0})$ to the unstable wave $(\omega_2, \boldsymbol{k_2})$ and stays close to this unstable wave for a long time. Such a behavior is close to the concept of edge states[12] corresponding to an unstable point, a repeller which still dominates the dynamics, the trajectories being attracted close to that point and leaving it slowly leading to intermittency. For extended flow like boundary layer, the intermittency is in time space and the edge state defines the coherent structuration of the turbulent flow[13]. Here, the edge state is the unstable wave $(\omega_2, \boldsymbol{k_2})$ with many initial conditions leading to trajectories that will spend long time close to $(\omega_2, \boldsymbol{k_2})$.

Since waves are continuous, it is standard not to study a single triad but families of triads as in[14],[15]. The resonant curves for the vector $\boldsymbol{k_0}$ fixed and the vector $\boldsymbol{k_1}$ varying ($\boldsymbol{k_2}$ being $-\boldsymbol{k_0} - \boldsymbol{k_1}$) solutions of (5.7) are plotted on figure 5.3 for $\omega_0/f = 0.84$. The wave $(\omega_0, \boldsymbol{k_0})$ is such that $k_0 = 1$ and $s_0 = +1$ (i.e. upward and rightward propagating wave), the other cases being easily deduced by symmetry. The signs (s_0, s_1, s_2) are reported on figure 5.3 and Hasselmann's criterion[16] states that the wave $(\omega_0, \boldsymbol{k_0})$ is unstable on the $(+,-,-)$ branch (in red lines), and stable on the $(+,-,+)$ and $(+,+,-)$ branches (in blue and green lines respectively). On figure 5.3, the points (E_1, D_1, A_1) are such that $\sigma_2 k_2 = \sigma_0 k_0 = 1$, and their symmetric points when changing $k_2 \leftrightarrow k_1$, (E_2, D_2, A_2), are such that $\sigma_1 k_1 = \sigma_0 k_0 = 1$. Close to (E_1, D_1), $\boldsymbol{k_1}$ tends to be horizontal and k_1 approaches $2k_{x0}$ and 0 respectively with ω_1 vanishing in the two cases.

The study made for a single triad T extends directly for all the triads on the resonant branches for the wave $(\omega_0, \boldsymbol{k_0})$ and close to the points (E_1, D_1, A_1) where $\sigma_2 k_2 \to \sigma_0 k_0 = 1$, the maximum gain is proportional to Σ/ε with $\varepsilon = 1 - \sigma_2 k_2/(\sigma_0 k_0)$, $\Sigma = 1 - \sigma_1 k_1/(\sigma_0 k_0)$ and the separatrix defining the edge of the different dynamics by a perturbation energy of order ε/Σ, the two being only function of k_1. Large transient growth and small threshold for the nonlinear stability (smallest perturbation to have the transition to a different state) then occur, the wave $(\omega_2, \boldsymbol{k_2})$ playing the role of a repeller attracting for long time the dynamics of the system. In the rotating fluid, the secondary wave with wave vector nearly

12. T. M. Schneider and B. Eckhardt, "Edge states intermediate between laminar and turbulent dynamics in pipe flow", in: *Philos. Trans. R. Soc. A* 367.*1888* (Feb. 2009), pp. 577–587.
13. *Ibid.*
14. Hasselmann, *op. cit.*
15. McComas and Bretherton, *op. cit.*
16. Hasselmann, *op. cit.*

horizontal and vanishing frequency is associated to the geostrophic and quasi-geostrophic balance originating in the well-known Taylor column phenomenon where the motion in all three directions is uniform along the axis of rotation i.e. in an entire column of fluid. The transient growth of perturbation for linearly stable triads, and more importantly for nonlinear instability characterized by a small threshold amplitude to cross the separatrix, corresponds to the energy transfer between coupled inertial waves of finite amplitudes and arbitrary wave vectors, and small Taylor column motions of horizontal wavelength half that of the wave $(\omega_0, \boldsymbol{k_0})$ in case E, and of long horizontal period in case D. In the case D, the secondary wave $(\omega_2, \boldsymbol{k_2})$ is close to wave $(\omega_0, \boldsymbol{k_0})$ since $(-\omega_0, -\boldsymbol{k_0})$ and $(\omega_0, \boldsymbol{k_0})$ represent the same wave and this transfer corresponds to a sideband instability whereas in the case E, the exchange of energy occurs with the secondary wave $(\omega_2, \boldsymbol{k_2})$ identical to $(\omega_0, \boldsymbol{k_0})$ but propagating in the opposite horizontal direction reproducing the periodic flip described for the tennis racket but here for wave in continuous liquid in rotation. As for the racket, the dynamics is given by the separatrix leading to the relaxation from one unstable state to its opposite. In this intermittent solution, the dynamics is led the majority of the time by the unstable state playing the role of a repeller, its stable and unstable manifold defining the edge state, here the separatrix.

5.4 Generalization to triadic wave resonance

Triadic resonance is a generic feature of *any* systems where small amplitude solutions may be represented by a superposition of waves described by a dispersion relation $\mathcal{D}(\omega, \boldsymbol{k}) = 0$ and when the resonant condition (5.6) is fulfilled by three particular wave vectors $(\boldsymbol{k_0}, \boldsymbol{k_1}, \boldsymbol{k_2})$.

As we already did for inertial waves, we follow Craik's derivation[17] in the two-dimensional case (2D) for a scalar state field q. The field q follows an equation involving nonlinear quadratic terms $\hat{\mathcal{D}}(q) = \hat{\mathcal{N}}(q, q)$ where $\hat{\mathcal{D}}$ is a linear operator and $\hat{\mathcal{N}}$ a bilinear form[18]. This nonlinear equation is analyzed assuming the magnitude of q small enough of order ε by an asymptotic procedure introducing a multiscale expansion in time with a slow time $T = \varepsilon t$. Expanding q in ε with $q = \varepsilon q_1 + o(\varepsilon)$, we obtain at leading order in ε that $\hat{\mathcal{D}}(q_1) = 0$ whose solution is a superposition of waves $\exp i(k_{xn}x + k_{zn}z - \omega_n t)$ with an arbitrary amplitude $Q_n(T)$, function of the slow time scale only, and where $(\omega_n, \boldsymbol{k}_n)$ obey the dispersion relation $\mathcal{D}(\omega_n, \boldsymbol{k}_n) = 0$ deduced from the operator $\hat{\mathcal{D}}$. At second order in ε, waves respecting the triadic resonance condition (5.6) are coupled and when going back to the primitive time variable t (see[19] for more details), the compatibility condition for a particular triad reads $i\partial\mathcal{D}/\partial\omega_{|n} \times dQ_n/dt = \lambda_n Q_m^* Q_l^*$, (n, m, l) being any

17. Craik, *op. cit.*
18. W. Eckhaus, *Studies in Non-Linear Stability Theory*, Springer Tracts in Natural Philosophy, Berlin Heidelberg: Springer-Verlag, 1965.
19. Craik, *op. cit.*

circular permutation of $(0,1,2)$, λ_n the nonlinear interaction coefficients, and $\partial\mathcal{D}/\partial\omega_{|n}$ is $\partial\mathcal{D}/\partial\omega$ evaluated at $(\omega_n, \boldsymbol{k}_n)$. λ_n and $\partial\mathcal{D}/\partial\omega_{|n}$ being both real. Rescaling the amplitudes Q_n by introducing $A_n = \kappa \left|\partial\mathcal{D}/\partial\omega_{|n}/\lambda_n\right|^{1/2} Q_n$, with the normalization factor $\kappa = -i \left|\lambda_0\lambda_1\lambda_2/\left(\partial\mathcal{D}/\partial\omega_{|0}\partial\mathcal{D}/\partial\omega_{|1}\partial\mathcal{D}/\partial\omega_{|2}\right)\right|^{1/2}$, leads to the generic three wave interaction equations:

$$\begin{aligned} \frac{dA_0}{dt} &= s_0 A_2^* A_1^* \\ \frac{dA_1}{dt} &= s_1 A_0^* A_2^* \\ \frac{dA_2}{dt} &= s_2 A_1^* A_0^* \end{aligned} \tag{5.10}$$

with the notations $s_n = \operatorname{sign}\left(\partial\mathcal{D}/\partial\omega_{|n}\lambda_n\right)$. Two cases should be distinguished. In the first case, all signs s_n are identical, solutions of (5.10) may diverge at finite time, and this singularity, if it occurs, implies an explosive breakdown of the solution[20]. This case is frequent in plasma physics[21] and also possible in three-layer Kelvin-Helmholtz flow[22]. In the other case, s_n are different, solutions of (5.10) are bounded, which is the case of most waves in fluid at rest, like surface, interfacial and internal waves as discussed by[23] and[24]. Multiplying each line of (5.10) by A_n^* and adding the complex conjugate of the equation, we get $d\left|A_n\right|^2/dt = 2s_n\Re(A_0A_1A_2)$ leading to relations equivalent to the Manley-Rowe relations[25]:

$$\frac{d}{dt}(s_0\left|A_0\right|^2) = \frac{d}{dt}(s_1\left|A_1\right|^2) = \frac{d}{dt}(s_2\left|A_2\right|^2) \tag{5.11}$$

which imply the existence of two quadratic invariants $C_0 = s_1\left|A_1\right|^2 - s_2\left|A_2\right|^2$ and $C_1 = s_2\left|A_2\right|^2 - s_0\left|A_0\right|^2$, the third permutation being a combination of these two invariants $C_2 \equiv -C_0 - C_1 = s_0\left|A_0\right|^2 - s_1\left|A_1\right|^2$. These two invariants may be combined in infinitely many linear combinations, as for example for any three real coefficients $\alpha = (\alpha_0, \alpha_1, \alpha_2)$ such that $\alpha_0 + \alpha_1 + \alpha_2 = 0$, $\mathcal{B} = \sum_n s_n\alpha_n\left|A_n\right|^2$ is an integral of motion, but only in particular cases, some invariants $\mathcal{B}$, linked to a particular trinomial $\alpha = (\alpha_0, \alpha_1, \alpha_2)$, have a physical interpretation.

For many classical cases of waves in a medium initially at rest, triadic resonance between waves conserves the total energy, sum of the kinetic and potential energy of the three waves. This physically conserved quantity correspond to a particular choice of

20. B Coppi, M. N. Rosenbluth, and R. N. Sudan, "Nonlinear interactions of positive and negative energy modes in rarefied plasmas (I)", in: *Annals of Physics* 55.*2* (Nov. 1969), pp. 207–247.

21. Weiland and Wilhelmsson, *op. cit.*

22. A. D. D. Craik and J. A. Adam, "Explosive resonant wave interactions in a three-layer fluid flow", in: *J. Fluid Mech.* 92.*1* (May 1979), pp. 15–33.

23. F. K. Ball, "Energy transfer between external and internal gravity waves", in: *J. Fluid Mech.* 19.*3* (July 1964), pp. 465–478.

24. T. M. Joyce, "Nonlinear interactions among standing surface and internal gravity waves", in: *J. Fluid Mech.* 63.*4* (May 1974), pp. 801–825.

25. Manley and Rowe, *op. cit.*

trinomial $\alpha = (\alpha_0, \alpha_1, \alpha_2)$, but this choice is a priori complex since the normalization from the wave amplitudes Q_n to the rescaled amplitudes A_n depends on the form of the dispersion relation and on the nonlinear operator $\hat{\mathcal{N}}(q, q)$, and may be an intricate function of ω_n and $\boldsymbol{k}_n$. Still, in some particular cases as the one treated here (inertial waves[26]) and for capillary gravity waves[27], internal waves[28], waves in plasma[29], and the swinging spring[30], the normalization is such that choosing then $\alpha = (\omega_0, \omega_1, \omega_2)$, the three wave frequencies, leads to the energy invariant up to a normalization constant K_{triad} that depends on the considered triad[31], $\mathcal{E} = \sum_n s_n \omega_n |A_n|^2 / K_{triad} = \sum_n \mathcal{E}_n$, the energy of the n-th wave being $\mathcal{E}_n = s_n \omega_n |A_n|^2 / K_{triad}$. In the studied cases, choosing $\alpha = (k_{x0}, k_{x1}, k_{x2})$ gives the conservation of the x component of the pseudomomentum $\mathcal{P}_x = \sum_n s_n k_{xn} |A_n|^2 / K_{triad} = \sum_n \mathcal{A}_n k_{xn}$ with the classical wave action $\mathcal{A}_n = s_n |A_n|^2 / K_{triad} = \mathcal{E}_n / \omega_n$ up to the same normalization constant as for the energy[32] K_{triad}. Similarly, $\alpha = (k_{z0}, k_{z1}, k_{z2})$ gives the conservation of the z component of the pseudomomentum $\mathcal{P}_z = \sum_n s_n k_{zn} |A_n|^2 / K_{triad} = \sum_n \mathcal{A}_n k_{zn}$. However, we should insist on the fact that this direct matching between energy and wave action definitions with the invariants of (5.10) is not imposed by the present derivation given by choosing respectively the frequencies and the components of the wave vectors as the prefactor α_n, and should be specifically verified. In particular, we may remark that choosing $\alpha = (\omega_0 + ck_{x0}, \omega_1 + ck_{x1}, \omega_2 + ck_{x2})$, equivalent to a Doppler shift along the x direction, where c would be a uniform velocity, also leads to an invariant of equation (5.10), which would be the physical energy for an inertial wave, only if the fluid were not at rest but in a uniform motion at velocity $-c$ along the x direction. As for inertial waves, equations (5.10) admit a third invariant linking the phase of the waves to their amplitudes, which imposes $\mathcal{K} = \Im(A_0 A_1 A_2)$ is constant in time, leading to the same equation for $\mathcal{K}$ as (5.9).

In the cases where the physical energy is such that $\mathcal{E} = \sum_n s_n \omega_n |A_n|^2 / K_{triad}$, all the results discussed for inertial waves apply, and the dynamics of resonating triads is characterized by the intersection of energy and pseudomomentum ellipsoids. The distance measured in the energy norm between the separatrix, the unstable manifold of the unstable wave, and the stable wave with the closest pseudomomentum, depends only on the frequencies and wave vectors of the three waves in the triad. Relaxation oscillations may dominate in systems where this distance can become infinitely small for some particular triads. If subscript 2 indicates the unstable wave, 0 and 1 the stable ones as we did for inertial waves, relaxation oscillations dominate in triadic resonant systems achieving the condition that, on the unit energy ellipsoid, the x and z components of $\boldsymbol{\mathcal{P}}_0 - \boldsymbol{\mathcal{P}}_2$ are small

26. Bordes et al., *op. cit.*
27. McGoldrick, *op. cit.*
28. Davis and Acrivos, *op. cit.*
29. Weiland and Wilhelmsson, *op. cit.*
30. Lynch, *op. cit.*
31. Joyce, *op. cit.*
32. Whitham, *op. cit.*

compared to those of $\boldsymbol{\mathcal{P}}_0 - \boldsymbol{\mathcal{P}}_1$, with $\boldsymbol{\mathcal{P}}_n = \boldsymbol{k}_n/\omega_n$ the pseudomomentum of the n-th wave at unit energy $\mathcal{E}_n = 1$. It is easy to show that the two vectors $\boldsymbol{\mathcal{P}}_0 - \boldsymbol{\mathcal{P}}_2$ and $\boldsymbol{\mathcal{P}}_0 - \boldsymbol{\mathcal{P}}_1$ are co-linear and co-directed as a result of the definitions of energy and pseudomomentum on the separatrix, $\boldsymbol{\mathcal{P}}_0 - \boldsymbol{\mathcal{P}}_2 = \gamma \times (\boldsymbol{\mathcal{P}}_0 - \boldsymbol{\mathcal{P}}_1)$ with $\gamma > 0$, and that relaxation oscillations dominate if $\gamma \ll 1$. In terms of phase velocity of the n-th wave $\boldsymbol{c}_n = (c_{xn}, c_{zn}) = (\omega_n/k_{xn}, \omega_n/k_{zn})$, we have, when the denominator is not nil:

$$\gamma = \frac{c_{x0}^{-1} - c_{x2}^{-1}}{c_{x0}^{-1} - c_{x1}^{-1}} = \frac{c_{z0}^{-1} - c_{z2}^{-1}}{c_{z0}^{-1} - c_{z1}^{-1}} \tag{5.12}$$

that should be small for large transient growth of perturbation energy and relaxation oscillations to be present. Achieving this criterion depends solely on the form of the dispersion relation $\mathcal{D}(\omega, \boldsymbol{k}) = 0$ specific to the studied waves. In the case of inertial waves, those criteria can be simplified using the dispersion relation (5.5), and we show that the previous condition, $\gamma \ll 1$, is equivalent to $\sigma_2 k_2 \to \sigma_0 k_0$ for triads indicated by points (E_1, D_1, A_1) on figure 5.3, and $\sigma_1 k_1 \to \sigma_0 k_0$ for (E_2, D_2, A_2), hence recovering the main results of the previous part.

5.5 Conclusion and discussion

The analogy between rotating solid and fluid is based on the conservation of two quadratic invariants: energy and momentum for the rotating solid, and energy and helicity for the triadic resonance of inertial waves in a rotating fluid. Both systems, when initially rotating around a stable mode and submitted to a perturbation of small but finite amplitude, exhibit high transient growth of perturbation energy and relaxation oscillations towards the unstable mode. Those dynamics are captured by the intersection of constant energy sphere and varying momentum ellipsoids in the solid case, and constant energy sphere and varying helicity ellipsoids for triadic resonant inertial waves.

The general case of resonant wave triads may be reduced to two cases depending on the three signs of the coupling coefficients. In the first case, these three coefficients have the same sign, the amplitude of the waves may grow unbounded. In the other case, a quadratic invariant of the motion corresponds to a definite positive form, preventing the solution to diverge to infinity. The stability of the three waves is then well-defined and studied, one wave being unstable and the other stable, for any finite amplitude initial condition. In many specific problems where the energy may be defined as a physically conserved quantity in the triads, the dynamics described for inertial waves applies with the possibility to define the energy of the perturbation around a single wave in the triads, the main result being that this departure from a single wave may exhibit large transient growth.

In particular, for a a large class of systems such as capillary gravity waves[33], internal waves[34], waves in plasma[35], and the swinging spring[36], the conservation of energy and the properties of triadic interaction allow to define the pseudomomentum, by introducing the wave action, as we did for inertial waves, and to show that the pseudomomentum is also conserved. Then, for triads such that, at equal energy, the pseudomomentum of the unstable wave 2 gets closer to that of the stable wave 0 than that of wave 1, the linear dynamics around the perturbed wave 0 exhibits strong transient growth of perturbation energy, and the distance in energy norm between the stable mode 0 and the separatrix (i.e. the stable manifold of wave 2) becomes small leading to relaxation oscillations towards the unstable wave 2.

Such dynamics may be evidenced experimentally in the solid case by taking inspiration from the experiment shown in the YouTube video mentioned in the introduction, which demonstrates the tennis racket effect by unscrewing a T-handle in zero gravity at the International Space Station, resulting in a spinning motion around its unstable axis with a periodic 180° twist. The T-handle is such that the screwed bar has the intermediate moment of inertia along the symmetry axis of the T. This moment is smaller, but close to the highest moment of inertia along the normal axis to the plane of the T, since the two differ by the moment of inertia of the vertical branch of the T, which is thin for the T-handle used. The third moment around the upper branch of the T is much smaller, since it involves mainly the rotation of the thin vertical branch. The present study predicts the dynamics of a solid object having its intermediate moment of inertia close to the greatest one when spinning such object around its stable axis of greatest moment of inertia. Such object could be shaped as an ellipsoid of semi-axes $a < b < c$ with $b \to a$ and scratched on its axis of greatest moment of inertia a to distinguish it from the intermediate axis b indicated by a dot. In zero gravity, we may spin this ellipsoid around the stable axis a, scratched, and, for a small perturbation, we expect to observe a growth of the perturbation and a rapid reorientation of the rotation from this stable axis, toward the unstable one b indicated by the dot. The solid should then keep spinning around the unstable axis b (dotted) for a large time with relaxation oscillations, where the rotation axis turns and passes close to the stable axis a (scratched) before finishing the 180° flip rotating along the unstable axis, but in the opposite direction and so on and so forth.

This YouTube video also shows a second experiment under zero gravity condition. A liquid-filled cylinder, initially spinning around its stable axis of smallest moment of inertia, becomes unstable, and the cylinder ends up rotating around its stable axis of greatest moment of inertia. The physical interpretation proposed is that the inner fluid adds the possibility of dissipation of energy, effective as soon as a small nutation is imposed

33. McGoldrick, *op. cit.*
34. Davis and Acrivos, *op. cit.*
35. Weiland and Wilhelmsson, *op. cit.*
36. Lynch, *op. cit.*

in the initial condition, and as this viscous fluid motion dissipates energy leading to the destabilization of the stable axis with transfer of momentum towards the direction with the largest inertia. This phenomenon was already described by Lord Kelvin in his 1880 paper in Nature on the difference of stability in the dynamics of a liquid-filled gyroscope with a slight prolate ovoidal shape[37]. He attributed this difference to the property of the support:

> *The rotation of a liquid in a rigid shell of oval figure, being a configuration of maximum energy for given vorticity, would be unstable if the containing vessel is left to itself supported on imperfectly elastic supports, although it would be stable if the vessel were held absolutely fixed, or borne by perfectly elastic supports, or left to itself in space unacted on by external force.*

This physical interpretation may be partial, since the destabilization of the stable axis of the solid may not only be due to dissipation or to the holding support properties, but also to the coupling with internal degrees of freedom in the fluid. Indeed, the nutation and precession of the solid filled with a liquid have been shown to excite inertial waves[38] via resonance mechanisms, similar to triadic interaction, involving the destabilization of the secondary flow induced by the solid motion. Instead of the viscous damping of this secondary flow, its coupling with resonnant internal wave would add to equations (5.1) other degrees of freedom, corresponding to secondary wave amplitudes, able to change the stability properties of the initial condition of a pure solid body rotation along the axis of smallest moment of inertia. Such system remains to be derived and explored.

Though the dynamics described in this second experiment is quite different from the one described in the present article (as the liquid introduces extra degrees of freedom and adds internal dissipation), the same experiment could be adapted with a spinning liquid-filled ellipsoid of semi-axes $a < b < c$ with $b \to a$, same as before (scratched on the a axis and dotted on the b axis). We may conjecture that adding an inner fluid should suppress the relaxation oscillations around a. Experimental evidences of the dynamics predicted here is not straightforward, but we may suggest that, for a rotating fluid in an infinite domain, the present model predicts that, in the presence of a weak mode with nearly zero frequency, characterized by columns of fluid moving in a vertically nearly uniform way (Taylor columns), any wave moving vertically up will progressively transfer its energy to a similar wave moving down and back again.

37. W. Thomson, "On An Experimental Illustration of Minimum Energy", in: *Nature* 23.*577* (Nov. 1880), pp. 69–70.

38. M. Le Bars, D. Cebron, and P. Le Gal, "Flows Driven by Libration, Precession, and Tides", in: *Annu. Rev. of Fluid Mech.* 47.*1* (2015), pp. 163–193.

Chapter 6

Transient growth of triadic instability for internal gravity waves (in preparation for *Journal of Fluid Mechanics*)

6.1 Abstract

Triadic resonant instability is a key component in the understanding of the breaking process of inertia gravity waves in geophysical applications when the fluid is stably stratified. We reconsider this classical triadic instability for a single wave of finite but small amplitude[1] and demonstrate that, due to the nonnormality of the evolution operator linearized around this base wave, stable as well as unstable triadic resonant interactions result in large transient amplification of perturbation energy. Stable triads can sustain longer and more intense transient growth than unstable triads. The augmented initial energy growth is related to the differential growth of the two leading eigenmodes that are making a shallow angle in the energy norm between each other for unstable triads in a manner similar to the mathematical structure of the classical lift-up mechanism. Instead, the transient growth of stable triads originates from the differential rotation (i.e. phase shift) of two stable eigenmodes making a small angle between each other. We show that for a small but finite amplitude perturbation around a stable base wave, the nonlinear dynamics of the system features high transient growth of perturbation energy and relaxation oscillations towards an unstable mode.

6.2 Introduction

Global warming regulation by the ocean depends on mechanisms controlling the vertical mixing of deepwater masses. It was recently proposed by Garrett & Kunze (2007)[2]

1. O. M. Phillips, *The dynamics of the upper ocean*, 2d ed, Cambridge monographs on mechanics and applied mathematics, Cambridge ; New York: Cambridge University Press, 1966.

2. C. Garrett and E. Kunze, "Internal Tide Generation in the Deep Ocean", in: *Annu. Rev. Fluid Mech.* 39.*1* (2007), pp. 57–87.

that this mixing results in an important proportion from the breaking of internal tides, the gravity waves generated by the barotropic tide interacting with the bottom topography,

Understanding the ocean circulation is a key ingredient for climate modeling[3]. Internal tide is believed to have a crucial role in the ocean dynamics. Its wave vector spectrum is broad with energy injected in small scale waves, well below scales resolved in global numerical models. The mechanisms by which internal tide breaks and transfers energy to small scale turbulence are also not resolved in numerical models. As a consequence, all the dynamics of internal tide (generation, breaking and dissipation) needs to be parametrized. Wunsch & Ferrari[4] and Melet et al.[5] found that changing the horizontal or vertical distribution of the parametrized turbulent mixing in the ocean model from uniform to horizontally and vertically localized radically modifies the deep ocean circulation in the models. Idealized analytical and numerical studies of gravity wave generation have evaluated the energy conversion rate of the barotropic tide to the internal tides at the seafloor[6]. Large scale numerical ocean circulation models used for climate prediction require a parametrization of small scale mixing based on the horizontal global maps of this barotropic tide conversion rate to the internal tide, together with the vertical estimates, throughout the water column, of the transfer of internal tide energy towards turbulence and mixing[7]. Classically, the transfer of energy from internal wave to turbulence is analyzed in terms of instability mechanisms and the present work proposes to reconsider the instability route by analyzing and computing the transient growth of perturbation energy, and nonlinear transfer.

Wave-wave interaction is part of a significant research effort on the dynamics of internal waves in a stratified medium whose density varies with the vertical[8]. The Garrett & Munk[9] spectrum models empirically the spectral energy distribution as a function of the vertical and horizontal wave vector components, resulting from nonlinear interactions of waves with different wavenumbers. In the regime of weak nonlinearities, the stability of gravity waves was first investigated by Davis & Acrivos[10] and Hasselmann (1967)[11] who both derived specific conditions to form an instability when a finite amplitude internal wave (referred as primary wave) is submitted to perturbations. The resulting instability which involves three resonant gravity waves (the primary and two secondary waves) inter-

3. W. Munk and C. Wunsch, "Abyssal recipes II: energetics of tidal and wind mixing", in: *Deep Sea Res. I* 45.*12* (Dec. 1998), pp. 1977–2010; G. Siedler, J. Church, and J. Gould, *Ocean circulation and climate: observing and modelling the global ocean*, San Diego: Academic Press, 2001; Melet et al., *op. cit.*
4. Wunsch and Ferrari, *op. cit.*
5. A. Melet, S. Legg, and R. Hallberg, "Climatic Impacts of Parameterized Local and Remote Tidal Mixing", in: *J. Climate* 29.*10* (Dec. 2015), pp. 3473–3500.
6. Garrett and Kunze, *op. cit.*
7. J. M. Klymak, S. Legg, and R. Pinkel, "A Simple Parameterization of Turbulent Tidal Mixing near Supercritical Topography", in: *J. Phys. Oceanogr.* 40.*9* (May 2010), pp. 2059–2074.
8. Phillips, *op. cit.*
9. Garrett and Munk, *op. cit.*
10. Davis and Acrivos, *op. cit.*
11. Hasselmann, *op. cit.*

acting together, is called triadic resonant instability (TRI). Studies conducted by McEwan (1971)[12] and Mied (1976)[13] predicted the resulting growth rate of instability and underlined that this growth originates from resonant triads where two secondary internal waves extract energy from the primary internal wave. Koudella & Staquet[14] investigated the properties of the parametric subharmonic instability (PSI), as a mechanism leading a plane, monochromatic, small amplitude internal gravity wave, the primary wave, to instability, and adressed the breaking mechanisms of internal gravity waves. They found that the parametric subharmonic instability, a particular case of triadic resonant instability for secondary waves of large wavenumbers compared to the primary wave, transfers energy from this wave to the perturbation. The transferred energy is in kinetic form when locally the primary wave shear is negative, and potential form for a locally positive shear, limiting the reverse transfer to the primary wave.

The present work considers the problem of triadic resonant instability with a primary finite amplitude uniform internal gravity wave interacting with two secondary infinitesimal internal gravity waves but instead of considering only the classical stability problem that characterize the exponential growth of decay at large time, it takes a different approach by analyzing the possibility of transient growth of perturbation energy at finite time. We reconsider the classical 2D problem of triadic resonant instability when linearized around a wave of small amplitude as the base state, but instead of searching for instability and exponential or algebraic growth, we compute, for each time horizon T, the initial perturbation that leads to the maximum gain of perturbation energy at time T. The derivation of the linearized problem results in an evolution operator, referred to as the triadic instability operator, that describes the dynamics of the linearized triadic system.

This approach is motivated by the nonnormality of the triadic instability operator according to the well-defined energy norm resulting in nonorthogonal eigenvectors and then in transient growth of the disturbances. Transient growth is a phenomenon in which linearized perturbations to a stable state of a system may initially show large growth of perturbation energy before relaxing to zero. For unstable states, transient growth may also be defined as the initial gain in energy of the perturbation larger than the exponential growth given by the leading eigenvalue. Reddy & Henningson (1993)[15], Trefethen et al.(1993)[16] and Schmid & Henningson (1994)[17] investigated this phenomenon when look-

12. A. D. McEwan, "Degeneration of resonantly-excited standing internal gravity waves", in: *J. Fluid Mech.* 50.*3* (Dec. 1971), pp. 431–448.

13. R. P. Mied, "The occurrence of parametric instabilities in finite-amplitude internal gravity waves", in: *J. Fluid Mech.* 78.*4* (Dec. 1976), pp. 763–784.

14. C. R. Koudella and C. Staquet, "Instability mechanisms of a two-dimensional progressive internal gravity wave", in: *J. Fluid Mech.* 548 (Feb. 2006), pp. 165–196.

15. S. C. Reddy and D. S. Henningson, "Energy growth in viscous channel flows", in: *J. Fluid Mech.* 252 (July 1993), pp. 209–238.

16. L. N. Trefethen et al., "Hydrodynamic Stability Without Eigenvalues", in: *Science* 261.*5121* (July 1993), pp. 578–584.

17. P. J. Schmid and D. S. Henningson, "Optimal energy density growth in Hagen-Poiseuille flow", in:

ing at the transition from laminar to turbulent regimes in Couette and Poiseuille 2D flows of a viscous incompressible fluid. The present work follows the same path to revisit the classical problem of triadic resonant interactions by bringing concepts of nonnormal operator theory into the field of wave-wave interactions and to consider the transient growth of the energy of resonant triads that may represent a different route to turbulence and mixing.

6.3 Derivation of the triadic resonant instability

6.3.1 Derivation in a two-dimensional space

We are looking at the linear evolution of the perturbation of a basic state characterized by a single internal gravity wave of finite amplitude, by following the derivation of McEwan & Plumb (1977)[18]. We assume the space to be two-dimensional (x', z'), the prime symbol being used to indicate a dimensional quantity, and the fluid to be linearly stratified, the dynamics being then given by the Boussinesq approximation. The motion of the fluid is defined by the velocity vector $\boldsymbol{u}' = (u', w')$, the pressure p' and the total density of a fluid parcel $\rho'_t = \rho'_r + \rho'_0 + \rho'$, ρ'_r being the constant reference density, ρ'_0 the mean density profile, a linear function of z' only, and ρ' the perturbation density, a function of x' and z'. The flow being two dimensional, we introduce the stream function ψ' such that $(u', w') = (\partial\psi'/\partial z', -\partial\psi'/\partial x')$. The typical frequency of this system, the Brunt-Väisälä frequency, defined by $N' = \sqrt{-g'/\rho'_r d\rho'_0/dz'}$ with g' the gravity, is constant. We define L'_0 as the typical length scale characteristic of the spatial variations of the velocity and density fields.

We nondimensionalize the space variables (x', z') by L'_0, and time t' by the Brunt-Väisälä frequency N'. The streamfunction ψ' is nondimensionalized by $N'L'^2_0$, and the density perturbation ρ' by $\rho'_r N'^2 L'_0/g'$. The buoyancy field is defined by $b' = -\rho' g'/\rho'_r$. All dimensionless quantities are indicated by dropping the prime of the corresponding dimensional quantity. To ease the notations, derivatives are marked by $\partial f/\partial x = f_{,x}$, $\partial f/\partial z = f_{,z}$ and $\partial f/\partial t = f_{,t}$. Under Boussinesq approximation, dimensionless streamfunction ψ and buoyancy b obey to Navier-Stokes and mass conservation equations:

$$\begin{aligned} \nabla^2\psi_{,tt} + \psi_{,xx} &= J(\psi, \nabla^2\psi)_{,t} - J(\psi, b)_{,x} \\ b_{,t} - \psi_{,x} &= J(\psi, b) \end{aligned} \tag{6.1}$$

where $J(f, g) \equiv f_{,x}g_{,z} - g_{,x}f_{,z}$ is the Jacobian of f and g, and $\nabla^2 = \partial^2/\partial_x^2 + \partial^2/\partial_z^2$ the Laplacian. We follow the derivation of McEwan & Plumb (1977)[19] and assume Ψ and b

J. Fluid Mech. 277 (Oct. 1994), pp. 197–225.

18. McEwan and Plumb, *op. cit.*
19. *Ibid.*

small. Their order of magnitude is denoted Fr and we introduce a multiscale expansion with variations both on the fast and slow timescales, respectively t and $T = Frt$, but contrary to them, we do not introduce a multiscale expansion in space. Thus, we assume $\psi = Frf(x,z,t,T) + O(Fr^2)$, $b = Frg(x,z,t,T) + O(Fr^2)$, and using the multiscale expansion in time, $\partial/\partial t \to \partial/\partial t + Fr\partial/\partial T$.

At the first order of the asymptotic expansion $O(Fr)$, equations (6.1) leads to:

$$\begin{aligned} \nabla^2 f_{,tt} + f_{,xx} &= 0 \\ g_{,t} - f_{,x} &= 0 \end{aligned} \tag{6.2}$$

whose solutions are an arbitrary superposition of linear internal gravity waves with amplitudes function of the slow time T, wave vectors $\boldsymbol{k_n} = (k_{xn}, k_{zn})$ and frequencies ω_n:

$$\begin{aligned} f &= \sum_n \Psi_n(T) \exp i(\boldsymbol{k_n} \cdot \boldsymbol{r} - \omega_n t) + \text{c.c} \\ g &= \sum_n B_n(T) \exp i(\boldsymbol{k_n} \cdot \boldsymbol{r} - \omega_n t) + \text{c.c} \end{aligned} \tag{6.3}$$

with n arbitrary (but with anticipation to the resonance condition $n = 0, 1, 2$ for triadic interactions), and c.c being the complex conjugate. The polarization relation deduced from (6.3) injected in (6.2), reads:

$$B_n(T) = -\frac{k_{xn}\Psi_n(T)}{\omega_n} \tag{6.4}$$

and the dispersion relation:

$$\omega_n = s_n \frac{|k_{xn}|}{k_n} \tag{6.5}$$

with $s_n = \text{sign}(\omega_n)$ and $k_n = \sqrt{k_{xn}^2 + k_{zn}^2}$.

At the second order $O(Fr^2)$, equation (6.1) leads to:

$$2\nabla^2 f_{,tT} = J(f, \nabla^2 f)^{(\text{res})}_{,t} - J(f,g)^{(\text{res})}_{,x} \tag{6.6}$$

with superscript (res) gathering all resonant forcing terms such that the triadic resonance condition is fulfilled:

$$\begin{aligned} \omega_0 + \omega_1 + \omega_2 &= 0 \\ \boldsymbol{k_0} + \boldsymbol{k_1} + \boldsymbol{k_2} &= \boldsymbol{0} \end{aligned} \tag{6.7}$$

The non-dimensionalized wave vector of the primary wave $\boldsymbol{k_0}$ is chosen of norm unity and then L_0' is such that $k_0' = 1/L_0'$ so the wavelength is $2\pi L_0'$. Similarly, the non-

dimensionalized amplitude of the primary wave $n = 0$ is chosen such that $\Psi_0(0) \equiv 1$, which gives the definition of the Froude number $Fr = \Psi_0'(0)/(N'L_0'^2)$.

With the change of variable $\Phi_n \to (k_n\Psi_n/2)\mathrm{e}^{-i\pi/4}$ compared to the derivation of McEwan & Plumb (1977)[20], the total energy of the n-th wave can be written as $\mathcal{E}_n = \langle u_n^2 + w_n^2 + b_n^2 \rangle /2 = |\Phi_n|^2$, where the brackets are the spatial average over the domain and (u_n, w_n, b_n) the velocity components and buoyancy field of the studied wave. Equations (6.3) injected in (6.6) when (6.7) is fulfilled, result in the triadic interaction equations:

$$\begin{aligned}
\frac{d\Phi_0}{dT} &= \Lambda_x \left(\frac{1}{c_{x2}} - \frac{1}{c_{x1}} \right) \Phi_2^* \Phi_1^* \\
\frac{d\Phi_1}{dT} &= \Lambda_x \left(\frac{1}{c_{x0}} - \frac{1}{c_{x2}} \right) \Phi_0^* \Phi_2^* \\
\frac{d\Phi_2}{dT} &= \Lambda_x \left(\frac{1}{c_{x1}} - \frac{1}{c_{x0}} \right) \Phi_1^* \Phi_0^*
\end{aligned} \tag{6.8}$$

with $\Lambda_x = \Delta(k_{x0}/\omega_0 + k_{x1}/\omega_1 + k_{x2}/\omega_2)/(k_0 k_1 k_2)$, $\Delta = k_{x1}k_{z2} - k_{x2}k_{z1}$ twice the oriented area of the triangle $(\boldsymbol{k_0}, \boldsymbol{k_1}, \boldsymbol{k_2})$, and $c_{xn} = \omega_n/k_{xn}$ the x component of the phase velocity $\boldsymbol{c_n} = (c_{xn}, c_{zn})$ of the n-th wave.

Equations (6.8) conserve three invariants: the total energy $\mathcal{E} = \sum_n \mathcal{E}_n$, the x component of the pseudo-momentum $\mathcal{P} = \sum_n \mathcal{E}_n/c_{xn}$, and a phase invariant $\mathcal{K} = \Im(\Phi_0\Phi_1\Phi_2)$, as demonstrated by Whitham (1965)[21], Andrews & Mcintyre (1978)[22] and Ripa (1981)[23]. Those invariants can be expressed as a function of the amplitudes Φ_n:

$$\mathcal{E} = \sum_n |\Phi_n|^2, \quad \mathcal{P} = \sum_n \frac{|\Phi_n|^2}{c_{xn}}, \quad \mathcal{K} = |\Phi_0\Phi_1\Phi_2| \, |\sin\varphi| \, . \tag{6.9}$$

where φ is the phase of $\Phi_0\Phi_1\Phi_2$. The analogy between the triadic resonant instability and the rotation of a rigid body around its principal axis is pointed out by Moffatt (2014)[24] in the case of inertial waves. The two first invariants in (6.9) are quadratic, and $\mathcal{E}$ is here a positive definite form, which is not the case for $\mathcal{P}$. In the case of internal gravity waves, McComas & Bretherton (1977)[25] discussed those invariants by expressing them in terms of wave action $\mathcal{A}_n = |\Phi_n|^2/\omega_n$, such that $\mathcal{E} = \sum_n \mathcal{A}_n\omega_n$ and $\mathcal{P} = \sum_n \mathcal{A}_n k_{xn}$.

6.3.2 Linearization of the triadic equations around a base state

We linearize the triadic resonant equations (6.8) by assuming the secondary waves small compared to the primary wave, $|\Phi_1| \ll |\Phi_0|$ and $|\Phi_2| \ll |\Phi_0|$, so that the amplitude

20. *Ibid.*
21. Whitham, *op. cit.*
22. Andrews and Mcintyre, *op. cit.*
23. Ripa, *op. cit.*
24. Moffatt, *op. cit.*
25. McComas and Bretherton, *op. cit.*

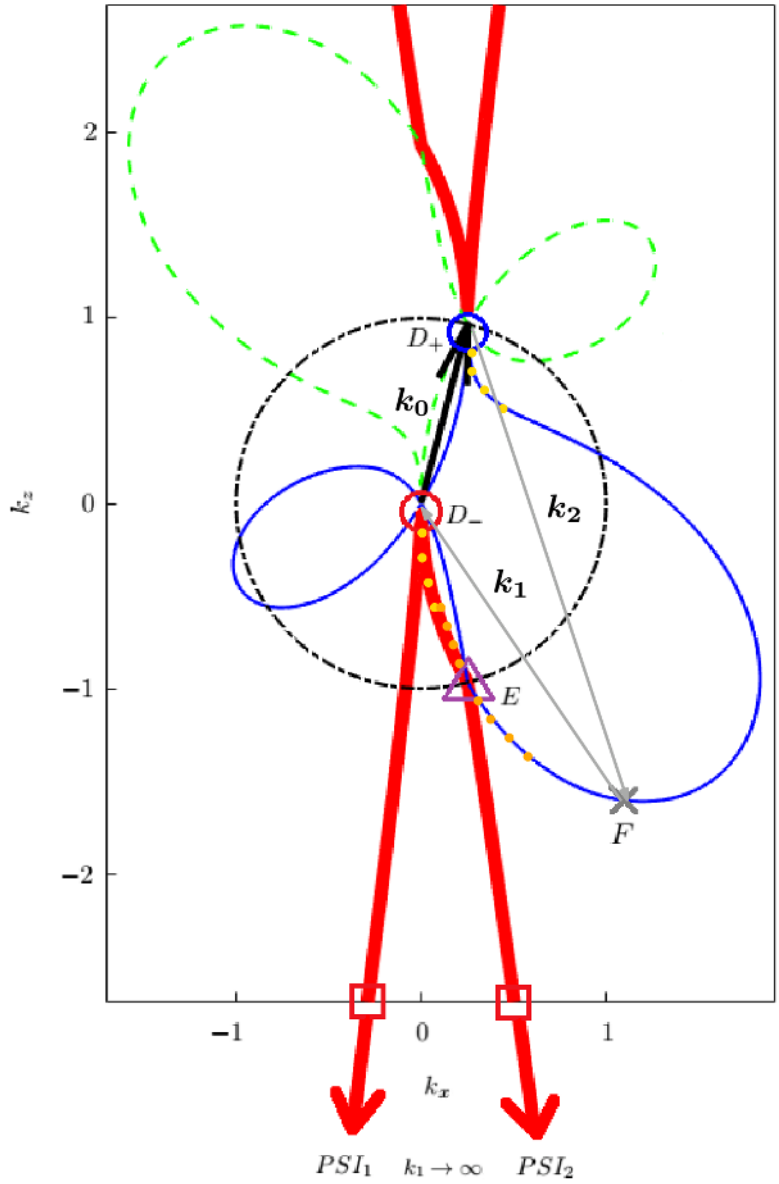

Figure 6.1: Resonance locus for the stable and unstable triads represented in the wave vector space $-\boldsymbol{k_1} = (k_x, k_z)$ ($\boldsymbol{k_2}$ being $-\boldsymbol{k_1} - \boldsymbol{k_0}$) for $\boldsymbol{k_0} = (k_{x0}, k_{z0}) = (\sin\theta_0, \cos\theta_0)$ represented by the heavy black arrow with $\theta_0 = 0.25$. The heavy red, thin blue and dashed green curves correspond respectively to the combinations of frequency signs (s_0, s_1, s_2) equal to $(+,-,-)$, $(+,-,+)$ and $(+,+,-)$. The black dotted curve is the unit circle $k_1 = k_0 = 1$. Three limiting classes of triads are represented on the red and blue curves we have chosen to study: Elastic Scattering located by point E with the $\triangle$ symbol, Induced Diffusion by points (D_+, D_-) with the $\bigcirc$ symbols, and parametric subharmonic instability by (PSI_1, PSI_2) at the end of heavy red arrows prolongating the branches indicated by $\square$ symbols as $k_1 \to \infty$. Point F will be introduced in part 3.2 and the corresponding triad is plotted as an example, with $(\boldsymbol{k_1}, \boldsymbol{k_2})$ in thin black arrows joining both ends of $\boldsymbol{k_0}$ to F. Yellow and orange dots near points D_-, D_+ and E indicate the equally spaced points at distances $\delta k = \{0.1, 0.2, 0.3, 0.4\}$ from D_-, D_+, E_-, and E_+ introduced in figure 6.3.

of the primary wave Φ_0 is considered constant. Without loss of generality, the phase of Φ_0 is chosen to be nil. Denoting the transpose by superscript $^{\mathrm{T}}$, the complex rescaled amplitudes $\mathbf{\Phi} = (\Phi_1, \Phi_2)^{\mathrm{T}}$ of the secondary waves then obey to the linearized system:

$$\partial_T \mathbf{\Phi} = \mathscr{L} \mathbf{\Phi}^* \text{ with } \mathscr{L} = \begin{pmatrix} 0 & L_1 \\ L_2 & 0 \end{pmatrix} \tag{6.10}$$

where $\mathbf{\Phi}^*$ is the conjugate of $\mathbf{\Phi}$, and the real coupling coefficients (L_1, L_2) are:

$$L_1 = \Lambda_x \left(\frac{1}{c_{x0}} - \frac{1}{c_{x2}} \right) \Phi_0, \quad L_2 = \Lambda_x \left(\frac{1}{c_{x1}} - \frac{1}{c_{x0}} \right) \Phi_0 \tag{6.11}$$

with the notations introduced in (6.8). Using (6.5) and (6.7), it can be shown that each coefficient only depends on k_1, $L_1(k_1)$ and $L_2(k_1)$, for a fixed primary wave $(\boldsymbol{k_0}, \omega_0)$. The evolution operator $\mathscr{L}$ is real and $\mathbf{\Phi}$ is complex. The sum of the energies of the secondary waves 1 and 2 is the energy of the perturbation $\|\mathbf{\Phi}\|^2 = |\Phi_1|^2 + |\Phi_2|^2$, where $\|.\|$ is the Euclidean norm. As a result of (6.11), the coupling coefficients verify the identity $\omega_0 L_1 \omega_2 = \omega_1 L_2 \omega_0$ for a resonant triad, or, equivalently:

$$\frac{L_1}{L_2} = \frac{\omega_1}{\omega_2} \tag{6.12}$$

6.3.3 Stability of the resonant triads

Combining the frequency and wave vector resonance conditions (6.7) leads to:

$$s_0 \frac{|k_{x0}|}{\sqrt{k_{x0}^2 + k_{z0}^2}} + s_1 \frac{|k_{x1}|}{\sqrt{k_{x1}^2 + k_{z1}^2}} + s_2 \frac{|k_{x0} + k_{x1}|}{\sqrt{(k_{x0} + k_{x1})^2 + (k_{z0} + k_{z1})^2}} = 0 \tag{6.13}$$

whose solutions in the $\boldsymbol{k_1}$ plane are resonant lines presented in figure 6.1. In figure 6.1, we have set $\sigma_0 = +1$ and $s_0 = +1$ without loss of generality and represented the wave vector of the primary wave $\boldsymbol{k_0} = (k_{x0}, k_{z0}) = (\sin\theta_0, \cos\theta_0)$ by a black arrow for a fixed value of $\theta_0 = 0.25$. The unit circle is indicated in black dotted lines. As $s_0 = +1$, all the possible frequency sign combinations (s_0, s_1, s_2) in (6.13) are $(+,-,-)$, $(+,-,+)$ and $(+,+,-)$, represented respectively in heavy red, thin blue and dashed green lines in figure 6.1.

Hasselmann's criterion for stability (1967) states that the sign combination $(+,-,-)$ corresponds to an unstable interaction, whereas $(+,-,+)$ and $(+,+,-)$ correspond to stable interactions. Hasselmann's derivation is valid for all systems of waves and only implies conservation of energy and symmetries.

From equation (6.12), Hasselmann's criterion is recovered since $\text{sign}(L_1 L_2) = s_1 s_2$, so equation (6.10) corresponds to a saddle node in the Φ plane when $L_1 L_2 > 0$ with a stable and an unstable manifold respectively with a positive and negative growth rate $\sigma_{\text{th}} = \sqrt{L_1 L_2}$ and $-\sigma_{\text{th}}$, and to a neutral node associated to two complex eigenvalues corresponding to perturbations rotating at frequencies $\pm\sqrt{-L_1 L_2}$ when $L_1 L_2 < 0$.

6.3.4 Remarkable limit triads

The symmetry $\boldsymbol{k} \to -\boldsymbol{k_0} - \boldsymbol{k}$ of the resonance locus transforms $\boldsymbol{k_1}$ in $\boldsymbol{k_2}$, thus we only need to study the unstable and stable combinations $(+,-,-)$ and $(+,-,+)$ which correspond respectively to the heavy red and thin blue curves in figure 6.1 and all the figures presented thereafter.

Along those curves in figure 6.1, points E, D, and PSI indicate three limiting classes of triads identified by McComas & Bretherton (1977), respectively called Elastic Scattering, Induced Diffusion, and parametric subharmonic instability, denoted E_- for Elastic Scattering, D_- for Induced Diffusion, PSI_1 and PSI_2 for parametric subharmonic instability along the $(+,-,-)$ unstable curve, and E_+ for Elastic Scattering and D_+ for Induced Diffusion along the $(+,-,+)$ stable curve.

All the three types of triads, Elastic Scattering, Induced Diffusion, and parametric subharmonic instability, are limiting cases meaning they can be approached infinitely close by the set of resonant triads but these limits are singular. We investigate properties of triads in the vicinity of these limiting cases.

Table 1 is used as a chart to locate these three limiting triads in later plots and analyze the associated effect on energy gain at finite time. Elastic Scattering and Induced Diffusion triads exist along stable and unstable curves when ω_1 or ω_2 tend to 0 whereas parametric subharmonic instability is only defined along the unstable branch for secondary wavenumbers going to infinity. These triads have dominant contributions to energy transfers as stated by McComas & Bretherton (1977).

We revisit this problem and give a different interpretation by focusing on the stability of a single primary wave considering the possibility of transient growth for each identified triad. Our approach is motivated by the nonnormality of the operator involved in the linearized problem describing the triadic resonant interaction at a finite amplitude primary wave.

6.4 Transient growth

6.4.1 Nonnormality of the triadic resonant instability operator

Since we choose the variables such that the energy norm is the Euclidean norm $\|\boldsymbol{\Phi}\|^2 = |\Phi_1|^2 + |\Phi_2|^2$, the evolution operator $\mathscr{L}$ introduced in (6.10) is normal with respect to

Table 6.1: Notations and properties of the three limiting classes of triads, Elastic Scattering, Induced Diffusion and parametric subharmonic instability, along the unstable $(+,-,-)$ and stable $(+,-,+)$ resonant curves. The generic notation E (resp. D) refers to both points E_- and E_+ (resp. D_- and D_+).

limit triad	symbol	notation	declinations	properties	comments
Elastic scattering	$\triangle$	E	(E_-, E_+)	$\boldsymbol{k_1} \to (-k_{x0}, k_{z0})$ $\boldsymbol{k_2} \to (0, -2k_{z0})$ $\omega_1 \to -\omega_0$ $\omega_2 \to 0$	$E_- \in (+,-,-)$ $E_+ \in (+,-,+)$ $\omega_2 \to 0^-$ for E_- $\omega_2 \to 0^+$ for E_+
Induced diffusion	$\bigcirc$	D	(D_-, D_+)	$\boldsymbol{k_i} \to -\boldsymbol{k_0}$ $\boldsymbol{k_j} \to \boldsymbol{0}$ $\omega_i \to -\omega_0$ $\omega_j \to 0$	$D_- \in (+,-,-)$ $D_+ \in (+,-,+)$ $(i,j) = (2,1)$ for D_- $(i,j) = (1,2)$ for D_+
Parametric subharmonic instability	$\square$	PSI	(PSI_1, PSI_2)	$\boldsymbol{k_1} \to -\boldsymbol{k_2}$ $k_1 \sim k_2 \to \infty$ $\omega_1 \sim \omega_2 \to -\frac{\omega_0}{2}$	$PSI_1 \in (+,-,-)$ $PSI_2 \in (+,-,-)$ $k_{x1}+ \to \infty$ for PSI_1 $k_{x1} \to -\infty$ for PSI_2

this energy norm only when $\mathscr{L}\mathscr{L}^{\mathrm{H}} = \mathscr{L}^{\mathrm{H}}\mathscr{L}$, superscript $^{\mathrm{H}}$ being the transconjugate of a matrix, which imposes $|L_1| = |L_2|$. For all the resonant triads plotted in figure 6.1, $|L_1| \neq |L_2|$ so:

$$\mathscr{L} \text{ is always nonnormal with respect to the energy norm } \|\boldsymbol{\Phi}\|^2 \tag{6.14}$$

This nonnormality is exacerbated when $\mathscr{L}$ becomes singular as one of the coefficient tends to be infinitely small compared to the other, which is the case when one of the two ratios, $L_1/L_2 = \omega_1/\omega_2$ or $L_2/L_1 = \omega_2/\omega_1$, tends to 0. From table 1, this is only the case for the Elastic Scattering and Induced Diffusion limiting classes of triads. High nonnormality of $\mathscr{L}$ results in strong transient growth of perturbation energy $\|\boldsymbol{\Phi}\|^2$.

6.4.2 Optimal growth rate of stable and unstable triads

Short-time growth of perturbation energy is studied by optimizing the energy norm $\|\boldsymbol{\Phi}\|^2$ over initial conditions, and the associated optimal energy gain is defined by:

$$G(T, k_1) = \max_{\|\boldsymbol{\Phi}(0)\|=1} \|\boldsymbol{\Phi}(T)\|^2 = |||\exp(T\mathscr{L})|||^2 \tag{6.15}$$

where $|||.|||$ is the operator norm induced by the Euclidean norm $\|.\|$.

Figure 6.2 features the optimal growth rate σ between times 0 and T, computed numerically with Matlab as a function of k_1 for all the resonant triads, using the computation of the optimal energy gain G based on the singular value decomposition of the operator

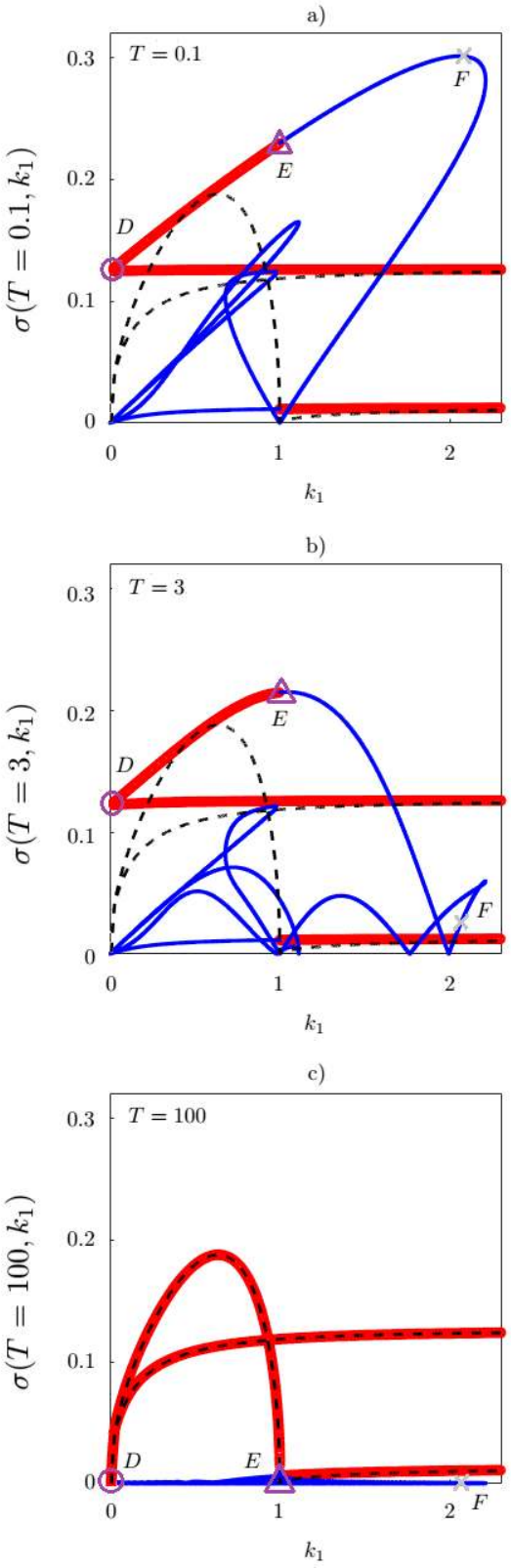

Figure 6.2: Plots of the optimal growth rate σ as a function of k_1 for $T = 0.1$ in a), $T = 3$ in b), and $T = 100$ in c), for stable and unstable resonant triads represented in thin blue and in bold red lines respectively. In c), σ has converged toward the growth rate σ_{th} of the classical triadic instability theory plotted as a dark dashed line on all the graphics. The points (E, D_-, D_+, F) from figure 6.1 are reported on all three figures, point D being in reality D_-, as D_- and D_+ lead to the same growth rate.

$\exp(T\mathscr{L})$, whose anlytical expression is given in appendix 6.9.2. The optimal growth rate σ is defined by:

$$\sigma\left(T,k_1\right)=\frac{\ln G\left(T,k_1\right)}{2T} \tag{6.16}$$

so, when T goes to infinity, $\sigma(T\to\infty,k_1)=\sigma_{\text{th}}$, the growth rate given by the classical stability theory equal to $\sigma_{\text{th}}=\sqrt{L_1L_2}$ for the $(+,-,-)$ unstable branches and $\sigma_{\text{th}}=0$ for the $(+,-,+)$ and $(+,-,+)$ stable branches[26]. When T goes to zero, $\sigma(T\to 0,k_1)=|L_1+L_2|/2$, which is the slope of G at $T=0$ divided by 2 as demonstrated by Schmid & Henningson (1994)[27] (see appendix 6.9.1).

σ is plotted in figure 6.2 as a function of k_1 for different instants $T=0.1$ in 6.2a), $T=3$ in 6.2b), $T=100$ in 6.2c). At longer times $T=100$, $\sigma(T=100,k_1)$ has converged toward the growth rate of the linear stability theory σ_{th} plotted as a dashed line that overlays exactly the optimal growth rate of the wave. The limiting case corresponding to the initial optimal growth rate at short time $T=0.1$ plotted in figure 6.2 shows that for all the triads in the vicinity of E, the initial growth is higher for stable triads than unstable triads. The perturbation energy grows more rapidly at early times for stable triads, the maximum $\max_{k_1}\sigma(T=0.1,k_1)$ being reached by a stable resonant triad corresponding to point F in figure 6.1. This emphasizes the major role of stable triads during the initial growth of perturbation. The plots of $\sigma(T=0.1,k_1)$ and $\sigma(T=3,k_1)$ in figure 6.2a-b) show that the optimal growth rate σ is larger at early times than later times. These curves feature a shift of the maximum of optimal growth rate curves σ from stable triads (thin blue curve) to unstable triads (bold red curve) when T increases. The time at which the maximum of σ shifts from a stable $(+,-,+)$ curve to an unstable curve $(+,-,-)$ estimates the typical time at which the unstable triads take over the stable triads. With the settings of parameters of figure 6.1 ($\theta_0=0.25$), this time is close to $T=3$. The plot of $\sigma(T=3,k_1)$ for stable triads exhibits a large number of oscillations associated to the form of stable solutions in equation (6.19) which oscillate with a period $2\pi/\sqrt{|L_1L_2|}$. This period depends on the norm of the wave vector k_1 and for a particular time presently $T=3$ this leads to constructive or destructive interferences.

At points E, D_- and D_+, the evolution operator $\mathscr{L}$ becomes nonnormal and singular as shown in part 6.4, resulting in high transient growth of perturbation energy quantified by the optimal energy gain G. Figure 6.3 represents G as a function of time T for the four equally spaced points plotted in yellow and orange dots in figure 6.1, and located at an arbitrary distance $\delta k=\{0.1,0.2,0.3,0.4\}$ of E_-, E_+, D_- and D_+, those limit points corresponding to $\delta k\to 0$. The curves of G taken at four equally spaced points δk from E_-, E_+, D_- and D_+ have the same initial slope as their limit points and the same short

26. Davis and Acrivos, *op. cit.*
27. Schmid and Henningson, *op. cit.*

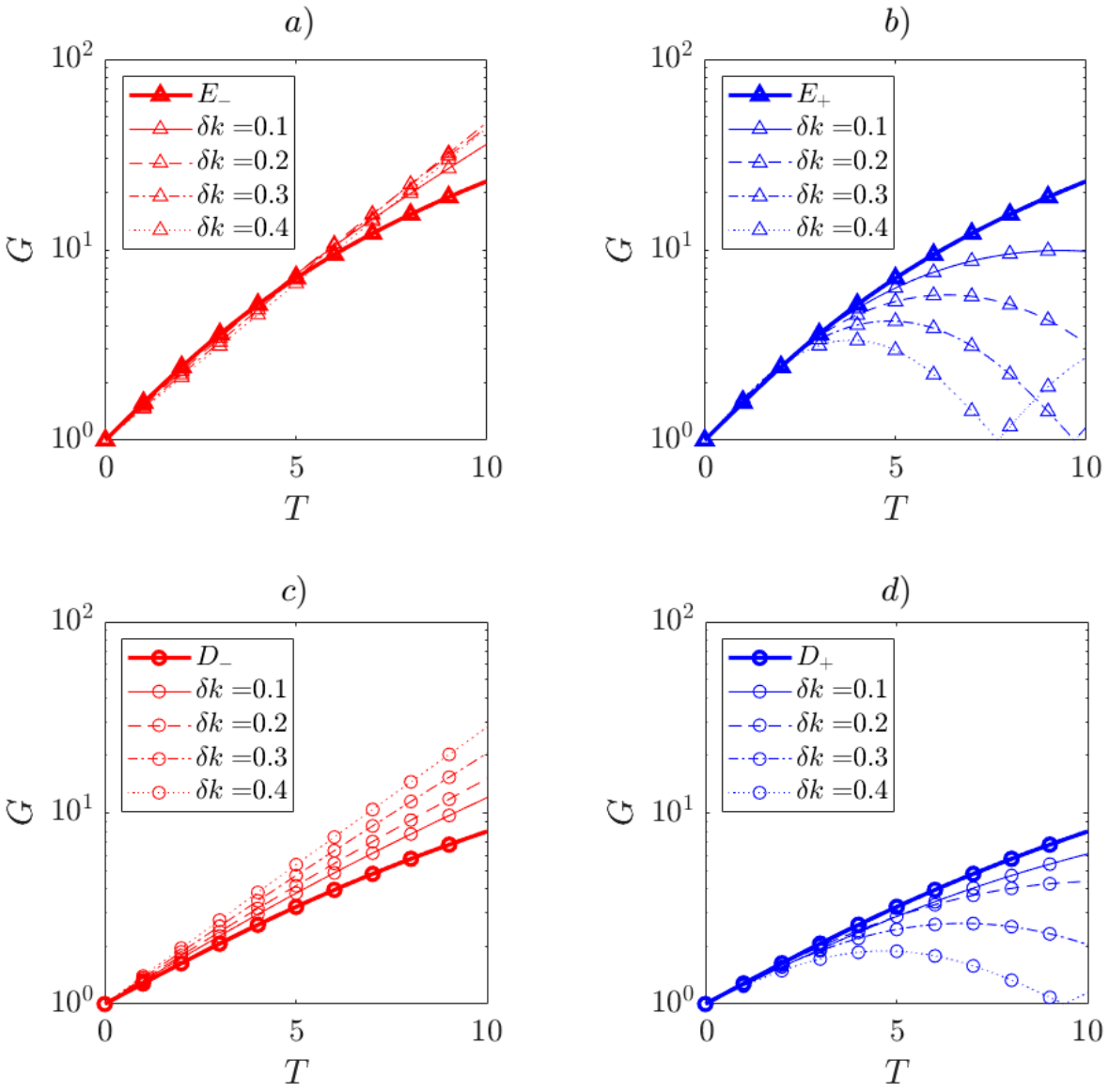

Figure 6.3: Semilog plots of the optimal energy gain G as a function of time T for four equally-spaced points at a distance $\delta k = \{0.1, 0.2, 0.3, 0.4\}$ (respectively in thin solid, dashed, dash-dotted and dotted lines on each plot) of E_-, E_+, D_- and D_+ along the resonant curves, and indicated by yellow and orange dots in figure 6.1. On all figures, the curves in heavy lines represent G at the limiting points E_- in a) and E_+ b) (with $\triangle$ markers), D_- in c) and D_+ in d) (with $\circ$ markers). Denoting $(k_{x1E-}, k_{x1E+}, k_{x1D-}, k_{x1D+})$ the values of k_{x1} taken at points E, D_- and D_+, the x component of the four equally-spaced points are chosen such that $k_{x1} < k_{x1E-}$ near E_-, $k_{x1} < k_{x1E+}$ near E_+, $k_{x1} < k_{x1D-}$ near D_-, and $k_{x1} < k_{x1D+}$ near D_+, the same graphs being obtained when considering four equally-spaced points reversing the order of these inequalities.

term evolution. When δk increases (thin continuous, dashed, dash-dotted and dotted lines for $\delta k = \{0.1, 0.2, 0.3, 0.4\}$ respectively), the long term evolution of G of the four points at a distance δk from E_-, E_+, D_- and D_+ differs from that of the corresponding singular points (represented in heavy lines). In 6.3b-d), the points at a distance δk from a singular point E_+ or D_+ belongs to the stable branch, so the corresponding solutions are oscillating with an initial growth given by the optimal energy gain G of the singular points and when δk increases, the amplitude and the period of those oscillations decrease. In 6.3a-c), the unstable solution at the equally spaced points described by δk grows rapidly and when δk increases, the curves of G in thin lines increases from their initial asymptotes given by the singular points E_- or D_-. Up until $T = 5$, the optimal growth rate G of resonant points at a distance $\delta k \leq 0.4$ of the singular points follow the transient growth given by the singular operator $\mathscr{L}$ taken at points E, D_-, D_+ and given by equation (6.17).

We locate the points E, D_- and D_+ along the resonant branches in figure 6.1 by the values of k_1 at those points, denoted $(k_{1E}, k_{1D-}, k_{1D+})$ respectively. One point along the resonant curves and corresponding to a value k_1 is in the vicinity of E if $\delta k = k_1 - k_{1E} \ll 1$, and the same remark applies to D_- and D_+ if $\delta k = k_1 - k_{1D-} \ll 1$ and $\delta k = k_1 - k_{1D+} \ll 1$ respectively. In a vicinity δk of E, D_- and D_+ along the resonant branches, the evolution operator can be developed asymptotically in $\mathscr{L}_E$, $\mathscr{L}_{D_-}$ and $\mathscr{L}_{D_+}$ respectively:

$$\mathscr{L}_E \sim \begin{pmatrix} 0 & L_1^E \\ L_2'^E \delta k & 0 \end{pmatrix}, \quad \mathscr{L}_{D_-} \sim \begin{pmatrix} 0 & L_1'^D \delta k \\ L_2^D & 0 \end{pmatrix}, \quad \mathscr{L}_{D_+} \sim \begin{pmatrix} 0 & L_2^D \\ L_1'^D \delta k & 0 \end{pmatrix} \tag{6.17}$$

where L_1' and L_2' are the derivatives of L_1 and L_2 with respect to k_1, and $L_1^E = L_1(k_{1E})$, $L_2'^E = L_2'(k_{1E})$, $L_1'^D = L_1'(k_{1D-}) = L_2'(k_{1D+})$, and $L_2^D = L_2(k_{1D-}) = L_1(k_{1D+})$.

The nonnormality of the evolution operator $\mathscr{L}$ gives rise to transient amplification of perturbation energy as described by Trefethen et al. (1993)[28] for a two dimensional system following similar equations than (6.10), and those transients are significant as $\mathscr{L}$ becomes singular. The Elastic Scattering and Induced Diffusion limiting classes of triads may experience high transient growth of perturbation energy. More specifically, at those limits symbolized by points E, D_- and D_+ and their corresponding evolution operators, $\mathscr{L}_E$, $\mathscr{L}_{D_-}$ and $\mathscr{L}_{D_+}$ respectively, the solutions of system (6.10), denoted $\mathbf{\Phi}_E$, $\mathbf{\Phi}_{D_-}$ and $\mathbf{\Phi}_{D_+}$, exhibit algebraic growth with complex initial conditions $\mathbf{\Phi}(0) = (\Phi_1^0, \Phi_2^0)^{\mathrm{T}}$:

$$\mathbf{\Phi}_E = \begin{pmatrix} L_1^E \Phi_2^0 T + \Phi_1^0 \\ \Phi_2^0 \end{pmatrix} \quad \mathbf{\Phi}_{D_-} = \begin{pmatrix} \Phi_1^0 \\ L_2^D \Phi_1^0 T + \Phi_2^0 \end{pmatrix} \quad \mathbf{\Phi}_{D_+} = \begin{pmatrix} L_2^D \Phi_2^0 T + \Phi_1^0 \\ \Phi_2^0 \end{pmatrix} \tag{6.18}$$

28. Trefethen et al., *op. cit.*

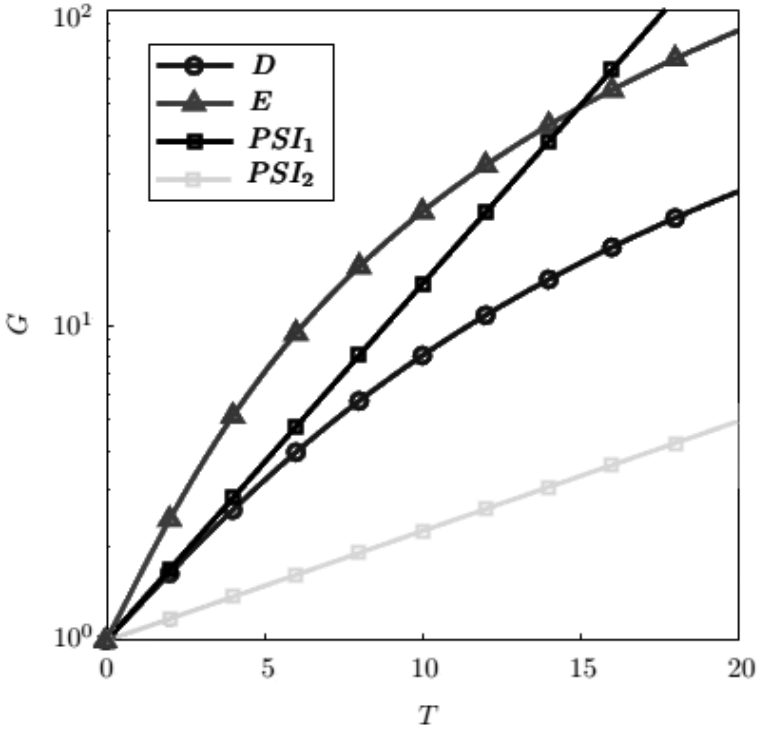

Figure 6.4: Semilog plots of the optimal energy gain G as a function of time T for early times $T \in [0, 20]$, at the singular limits E in orange line with $\triangle$ markers, D in purple line with $\circ$ and (PSI_1, PSI_2) in black and grey lines with $\square$ markers respectively. The limiting points D_+ and D_- leads to the same gain G and are then gathered in a single curve G at point D.

Figure 6.4 uses Matlab to compute numerically the optimal energy gain G for a time horizon $0 < T < 20$ by calculating the limit of $|||\exp(T\mathscr{L})|||^2$ for the limiting classes of triads along the resonant branches indicated by D_-, D_+, PSI_1 and PSI_2 marked on figure 6.1. The limiting points D_- and D_+ lead to the same optimal energy gain G, so both points are referenced as D in figure 6.4. The curves of G at the limits D, E, PSI_1 and PSI_2 are denoted $G(D)$, $G(E)$, $G(PSI_1)$ and $G(PSI_2)$ respectively. All curves of G slowly depart from their associated algebraic growth, the intensity of it being different from one curve to the next. In the limit case of parametric subharmonic instability indicated by (PSI_1, PSI_2), the evolution operator $\mathscr{L}$ is normal, G follows an exponential growth with a larger slope for PSI_1 than for PSI_2 as shown by the dark and grey curves with $\square$ markers. In the case of Induced Diffusion and Elastic Scattering indicated respectively by D and E, $\mathscr{L}$ is nonnormal and singular, resulting in remarkable transient growth, as displayed when comparing the curves of D with PSI_2, and of E with PSI_1. The two comparisons show that the nonnormality of $\mathscr{L}$ results in an extra gain at short times, as the curves of optimal energy gain of D and E are above that of PSI_2 and PSI_1 respectively. $G(E)$ and $G(PSI_1)$ intersect at time $T = 15$ from figure 6.4. The plots of the optimal energy gain G for longer durations (not displayed here) show that $G(D)$ and $G(PSI_2)$ intersect near $T = 60$, and that $G(E)$ and $G(PSI_2)$ intersect near $T = 100$, whereas $G(E)$ remains above $G(D)$, and $G(PSI_1)$ also remains above $G(PSI_2)$. The duration of the extra gain due to the nonnormality of $\mathscr{L}$ is given by the previous intersections when comparing one nonnormal case (points D and E) to one normal case (points PSI_1 and PSI_2). We conclude that the longest extra gain due to nonnormality can last up to $T = 100$ in slow timescales and is obtained when comparing the optimal gains $G(E)$ and $G(PSI_2)$, as $G(E) > G(PSI_2)$ for $T < 100$.

6.4.3 Finite time solution

The solutions of equation (6.10) for a particular triad along the stable $(+,-,+)$ or unstable $(+,-,-)$ resonant branches can be written in the general form:

$$\mathbf{\Phi}(T) = \frac{\left\langle \mathbf{\Phi}(0) | \mathbf{\Phi}_\alpha^{\mathrm{A}} \right\rangle}{\left\langle \mathbf{\Phi}_\alpha | \mathbf{\Phi}_\alpha^{\mathrm{A}} \right\rangle} \mathbf{\Phi}_\alpha \mathrm{e}^{\alpha T} + \frac{\langle \mathbf{\Phi}(0) | \mathbf{\Phi}_\beta^{\mathrm{A}} \rangle}{\langle \mathbf{\Phi}_\beta | \mathbf{\Phi}_\beta^{\mathrm{A}} \rangle} \mathbf{\Phi}_\beta \mathrm{e}^{\beta T} \tag{6.19}$$

where $(\mathbf{\Phi}_\alpha, \mathbf{\Phi}_\beta)$ are the eigenvectors associated to the eigenvalues (α, β) respectively, $\langle \mathbf{\Phi}_p | \mathbf{\Phi}_q \rangle = \mathbf{\Phi}_p \mathbf{\Phi}_q^{\mathrm{H}}$, and superscript A corresponds to the eigenvectors of the adjoint problem.

In the stable case, $L_1 L_2 < 0$, the eigenvalues are $(\alpha, \beta) = (i\sqrt{|L_1 L_2|}, -i\sqrt{|L_1 L_2|})$, and

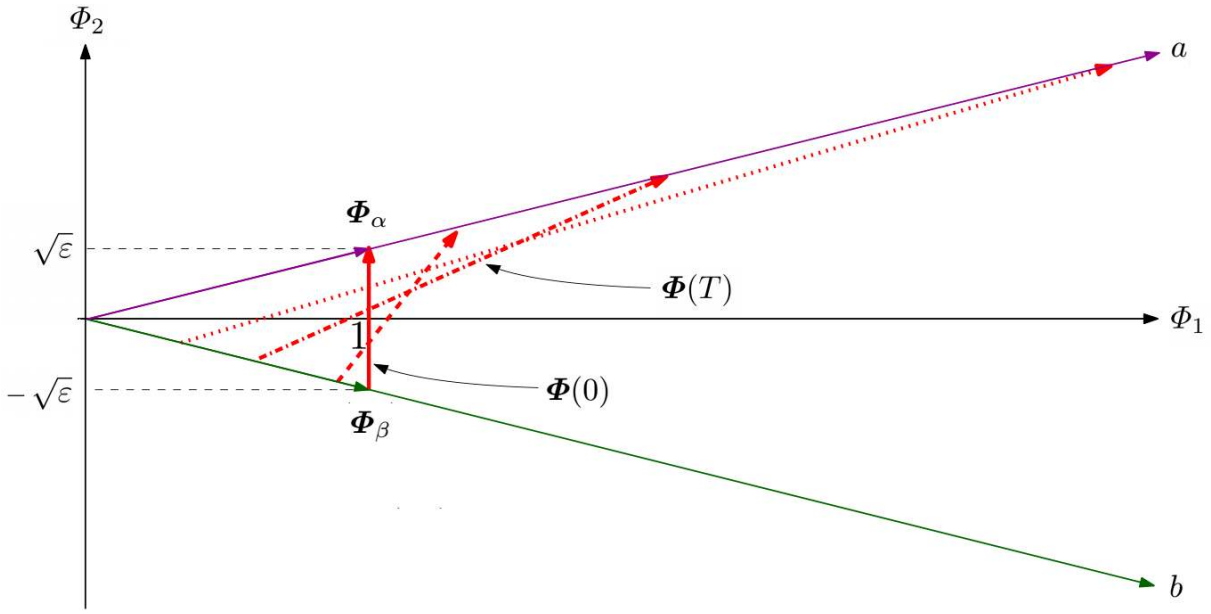

Figure 6.5: Representation, when $\varepsilon = |L_2/L_1| \ll 1$, of the solution $\boldsymbol{\Phi}(T)$, defined in (6.19), for the initial condition $\boldsymbol{\Phi}(0) = \boldsymbol{\Phi}_\alpha - \boldsymbol{\Phi}_\beta$, in red vectors in the (Φ_1, Φ_2) plane at different instants $T > 0$. As T increases, the linestyle of the represented vectors $\boldsymbol{\Phi}(T)$ are going from solid to dashed, then dashed dotted to dotted lines. The scales indicated are $1/\sqrt{1+\varepsilon} \sim 1$ and $\sqrt{\varepsilon/(1+\varepsilon)} \sim \sqrt{\varepsilon}$ and the vectors $(\boldsymbol{\Phi}_\alpha, \boldsymbol{\Phi}_\beta)$, represented in purple and green respectively, generate two axes a and b that are not orthogonal, forming an angle that is narrowed as ε becomes nil. High transients occur as ε tends to 0.

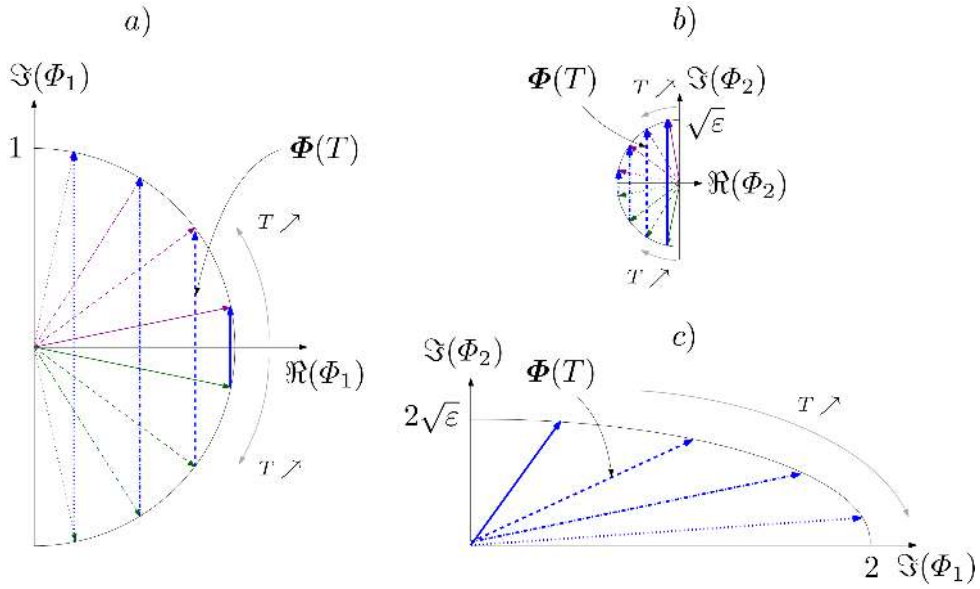

Figure 6.6: Representation, when $\varepsilon = |L_2/L_1| \ll 1$, of the solution $\boldsymbol{\Phi}(T)$, defined in (6.19), for the initial condition $\boldsymbol{\Phi}(0) = \boldsymbol{\Phi}_\alpha - \boldsymbol{\Phi}_\beta$, in blue vectors in the Φ_1 plane in a) and in the Φ_2 plane in b), and in a $(\Im(\Phi_1), \Im(\Phi_2))$ plane in c) at different instants $0 < T < \sqrt{|L_1 L_2|}\pi/2$ with. As T increases, the linestyle of the represented vectors are going from solid to dashed then dashed dotted to dotted lines. The radius of the circles in a) and b) are respectively $1/\sqrt{1+\varepsilon} \sim 1$ and $\sqrt{\varepsilon/(1+\varepsilon)} \sim \sqrt{\varepsilon}$ and the vectors $(\boldsymbol{\Phi}_\alpha \exp(\alpha T), \boldsymbol{\Phi}_\beta \exp(\beta T))$ are represented in purple and green respectively,. In the $(\Im(\Phi_1), \Im(\Phi_2))$ plane of figure c), $\boldsymbol{\Phi}(T)$ experiences transient growth when T increases, leading to a quarter ellipse shape of semi-minor axis $2\sqrt{\varepsilon}$ and semi-major axis 2. High transients occur as ε tends to 0.

the associated eigenvectors read:

$$\begin{aligned}\boldsymbol{\Phi}_\alpha &= (1, i\sqrt{|L_2/L_1|})^{\mathrm{T}}/\sqrt{1+|L_2/L_1|}\\ \boldsymbol{\Phi}_\beta &= (1, -i\sqrt{|L_2/L_1|})^{\mathrm{T}}/\sqrt{1+|L_2/L_1|}\end{aligned} \tag{6.20}$$

In the unstable case, $L_1L_2 > 0$, the eigenvalues are $(\alpha, \beta) = (\sqrt{|L_1L_2|}, -\sqrt{|L_1L_2|})$, and the associated eigenvectors read:

$$\begin{aligned}\boldsymbol{\Phi}_\alpha &= (1, \sqrt{|L_2/L_1|})^{\mathrm{T}}/\sqrt{1+|L_2/L_1|}\\ \boldsymbol{\Phi}_\beta &= (1, -\sqrt{|L_2/L_1|})^{\mathrm{T}}/\sqrt{1+|L_2/L_1|}\end{aligned} \tag{6.21}$$

Figures 6.5 and 6.6 illustrate the time evolution of the solution $\boldsymbol{\Phi}(T)$, defined in (6.19), for the initial condition $\boldsymbol{\Phi}(0) = \boldsymbol{\Phi}_\alpha - \boldsymbol{\Phi}_\beta$, along the unstable and stable branches respectively, when ε is equal to $|L_2/L_1| = |\omega_2/\omega_1| \ll 1$, which is the case at point E and D_+. At point D_-, the figures 6.5 and 6.6 are still valid if the roles of Φ_1 and Φ_2 are exchanged. Instead of being related to the differential growth of two eigenmodes for unstable triads as illustrated in figure 6.5a), the transient growth of stable triads originates from the differential rotation (i.e. phase shift) of two eigenmodes as shown in figures 6.6a) and 6.6b). When comparing figures 6.5b) and 6.6c), $\boldsymbol{\Phi}(T)$ grows similarly for unstable and stable triads from $2\sqrt{\varepsilon}$ to 2 in a time horizon $0 < T < |L_1L_2|^{-1/2}$, meaning the transient growth of stable and unstable triads are comparable and both have a characteristic time equal to $|L_1L_2|^{-1/2}$.

6.5 Effect of viscosity and diffusivity

Following calculations of McEwan & Plumb (1977)[29], the triadic wave interaction can also be extended to take into account all viscous effects when the Reynolds and Prandtl numbers are finite. The 2×2 linearized equation describing the stability of a constant finite amplitude wave remains valid when viscous effects are included $\partial_T \boldsymbol{\Phi} = \mathscr{L}\boldsymbol{\Phi}^*$, the $\mathscr{L}$ matrix being modified as:

$$\mathscr{L} = \begin{pmatrix} -\dfrac{\lambda_1}{\mathrm{R}} & L_1 \\ L_2 & -\dfrac{\lambda_2}{\mathrm{R}} \end{pmatrix} \tag{6.22}$$

with the diagonal terms $\lambda_n = k_n^2/2$, and $\mathrm{R} = Re/(1 + 1/Pr)$ a nondimensional number associated to the dissipative effects described by $Re = \Psi_0'(0)/\nu'$ and $Pr = \nu'/\kappa'$, the Reynolds and Prandtl numbers of the flow of viscosity and diffusivity (ν', κ').

29. McEwan and Plumb, *op. cit.*

In the unstable case $L_1 L_2 > 0$, $\mathscr{L}$ has eigenvalues (α, β) with:

$$\begin{aligned} \alpha &= -\frac{\lambda_1+\lambda_2}{2\mathrm{R}} + \sqrt{\left(\frac{\lambda_1-\lambda_2}{2\mathrm{R}}\right)^2 + L_1 L_2} \\ \beta &= -\frac{\lambda_1+\lambda_2}{2\mathrm{R}} - \sqrt{\left(\frac{\lambda_1-\lambda_2}{2\mathrm{R}}\right)^2 + L_1 L_2} \end{aligned} \tag{6.23}$$

and associated eigenvectors $\boldsymbol{\Phi}_\alpha = \boldsymbol{\eta}_\alpha / \|\boldsymbol{\eta}_\alpha\|$ and $\boldsymbol{\Phi}_\beta = \boldsymbol{\eta}_\beta / \|\boldsymbol{\eta}_\beta\|$ with:

$$\begin{aligned} \boldsymbol{\eta}_\alpha &= \begin{pmatrix} 1 \\ \dfrac{1}{2L_1}\left(\dfrac{\lambda_1-\lambda_2}{\mathrm{R}} + \sqrt{\left(\dfrac{\lambda_1-\lambda_2}{\mathrm{R}}\right)^2 + 4L_1 L_2}\right) \end{pmatrix} \\ \boldsymbol{\eta}_\beta &= \begin{pmatrix} 1 \\ \dfrac{1}{2L_1}\left(\dfrac{\lambda_1-\lambda_2}{\mathrm{R}} - \sqrt{\left(\dfrac{\lambda_1-\lambda_2}{\mathrm{R}}\right)^2 + 4L_1 L_2}\right) \end{pmatrix} \end{aligned} \tag{6.24}$$

Following the notations of (6.19), the considered unstable solution can be written as:

$$\boldsymbol{\Phi}(T) = \frac{\left\langle \boldsymbol{\Phi}(0) | \boldsymbol{\Phi}_\alpha^{\mathrm{A}} \right\rangle}{\left\langle \boldsymbol{\Phi}_\alpha | \boldsymbol{\Phi}_\alpha^{\mathrm{A}} \right\rangle} \boldsymbol{\Phi}_\alpha \mathrm{e}^{\alpha T} + \frac{\langle \boldsymbol{\Phi}(0) | \boldsymbol{\Phi}_\beta^{\mathrm{A}} \rangle}{\langle \boldsymbol{\Phi}_\beta | \boldsymbol{\Phi}_\beta^{\mathrm{A}} \rangle} \boldsymbol{\Phi}_\beta \mathrm{e}^{\beta T} \tag{6.25}$$

so the growth rate in the classical theory of triadic resonant instability is $\sigma_{\mathrm{th}} = \alpha$:

$$\sigma_{\mathrm{th}} = -\frac{\lambda_1+\lambda_2}{2\mathrm{R}} + \sqrt{\left(\frac{\lambda_1-\lambda_2}{2\mathrm{R}}\right)^2 + L_1 L_2} \tag{6.26}$$

and, if σ_{th} becomes negative, the solution becomes stable due to dissipation effects.

Figure 6.7 represents σ_{th} as a function of k_1 for unstable resonant triads when $\theta_0 = 0.25$ in the inviscid case and in the viscous case with $Re = 1000$ and $Pr = 7$. σ_{th} remains identical in the inviscid and viscous case for triads with $k_1 \leq 1.5$ and then viscosity attenuates the growth rate σ_{th} for higher wavenumbers $k_1 \geq 1.5$. The triads near (PSI_1, PSI_2) with large k_1 have a negative growth rate $\sigma_{\mathrm{th}} < 0$ as a result of viscosity so the optimal energy gain G of PSI triads decreases from 1 to 0 when T increases. On the unstable resonant branches containing the limiting branches (PSI_1, PSI_2), σ_{th} reaches a maximum indicated by the point M' at $k_1 \sim 1.5$. The corresponding triad has the most amplified exponential growth compared to the other triads near (PSI_1, PSI_2) along the resonant branches. When $k_1 \leq 1.5$, the most amplified triad due to exponential growth at later time horizons correspond to another maximum of σ_{th} indicated by point M. Both triads indicated by points M and M' experience exponential growth of energy at later time horizons without attenuation due to viscosity. At a high fixed Re, when getting close to E in

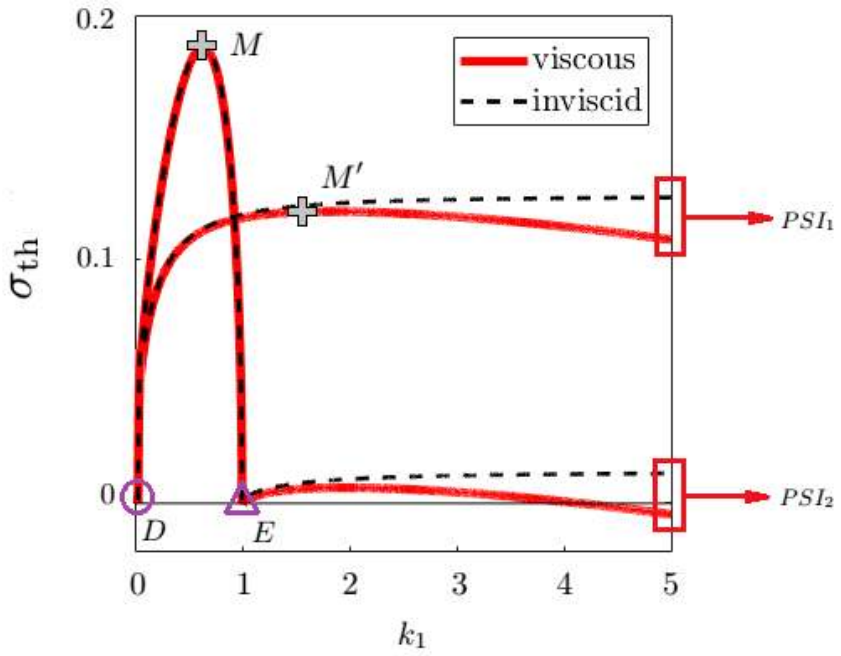

Figure 6.7: Growth rate from Hasselmann's theory $\sigma_{\rm th}$ as a function of k_1 in the inviscid case (dark dashed line) and the viscous case (heavy red line) with $Re = 1000$ and $Pr = 7$ corresponding to the ocean. M and M' are two points on the unstable branch where the two first maximum values of $\sigma_{\rm th}$ are reached and are marked by pink and green cross symbols. In the inviscid case, at longer time horizons (after the transient growth) for which the exponential growth dominates, M' is the most amplified point on the unstable resonant branches outside the unit circle $k_1 > 1$, whereas M is the most amplified point on the unstable resonant branch inside the unit circle $k_1 < 1$. The points (D, E, PSI_1, PSI_2) from figure 6.2 are reported in the present figure.

a radius $\delta k \ll 1$ along the resonant branches, there exist δk^{R} such that, when $\delta k < \delta k^{\mathrm{R}}$, the unstable solution becomes linearly stable as σ_{th} becomes negative. The scaling of δk^{R} as a function of Re is $\delta k^{\mathrm{R}} \propto Re^{-2}$ as demonstrated in appendix 6.9.3. This stabilization due to the introduction of viscosity does not occur in the vicinity of D_- or D_+, since σ_{th} remains positive close to those singular points. The stability properties are different near D_- or D_+, since one of the resonant wave vectors vanishes leading to vanishing dissipation effects. This is evident from the expression of $\sigma_{\mathrm{th}} > 0$ as, for any number R, δk may be taken sufficiently small to give $\sigma_{\mathrm{th}} > 0$.

Figure 6.8 is the same as figure 6.2 but for the viscous case $Re = 1000$ and $Pr = 7$ with $T = 0.1$ in 6.8a), $T = 3$ in 6.8b) and $T = 100$ in 6.8c), for stable and unstable resonant triads. The comparison of figure 6.8 with figure 6.2 shows that the introduction of viscosity and diffusivity does not change the main features of the dynamics, but globally decreases σ along the resonant branches. Higher wavenumbers are more affected by this decrease than lower ones. The convergence of σ when $T \to \infty$ toward the theoretical growth rate σ_{th} is shown in figure 6.8c) which displays $\sigma(T = 100, k_1)$, σ_{th} being represented as a black dashed curve in 6.8a), 6.8b) and 6.8c). In the viscous case, the shifting time T_c defined as the time at which the maximum of σ shifts from a stable $(+,-,+)$ curve to an unstable curve $(+,-,-)$ remains the same as in the inviscid case $T_c \sim 3$. The energy of stable triads being more amplified than unstable ones during the transient growth is a key feature of the triadic resonant instability that does not depend on viscosity and diffusivity.

Figure 6.9 shows the plots of the optimal energy gain G as a function of time T at the different singular points on the resonant branches E and D (D_+ and D_- lead to the same gain so D refer to both points), same as in figure 6.2, and at the points of largest modal growth defined as M and M' for two time horizons, $0 < T < 20$ in a) and $0 < T < 4000$ in b), in the viscous case with $Re = 1000$ and $Pr = 7$. For the singular points D and E, the gain G is identical at early times in the inviscid case and in the viscous case when comparing figures 6.9a) and 6.4. The optimal energy gain G is superior at E than at M (resp. M') for $T < 5$ (resp. $T < 15$). Triads in the vicinity of E have the highest transient growth compared to the other triads so they dominate the early increase of G. The influence of viscosity is illustrated by the plots of G for a longer duration $0 < T < 4000$ in figure 6.9b), which show that the curve of G at point E decreases at later times $T \geq 1000$, leading to a maximum $G_{\max}$ reached at time $T_{\max}$ verifying:

$$\begin{aligned} G_{\max} &\propto Re^2 \\ T_{\max} &\propto Re \end{aligned} \tag{6.27}$$

as demonstrated analytically in appendix 6.9.3. This exponential decrease due to viscosity

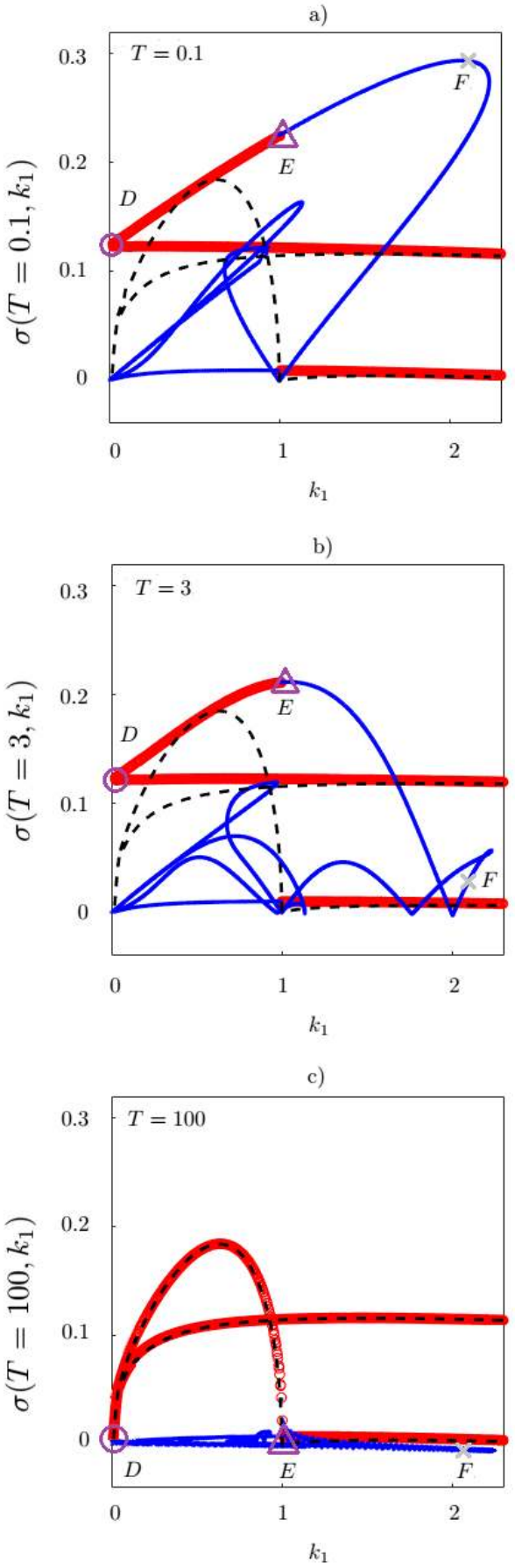

Figure 6.8: Same as in figure 6.2 in the viscous case with $Re = 1000$ and $Pr = 7$.

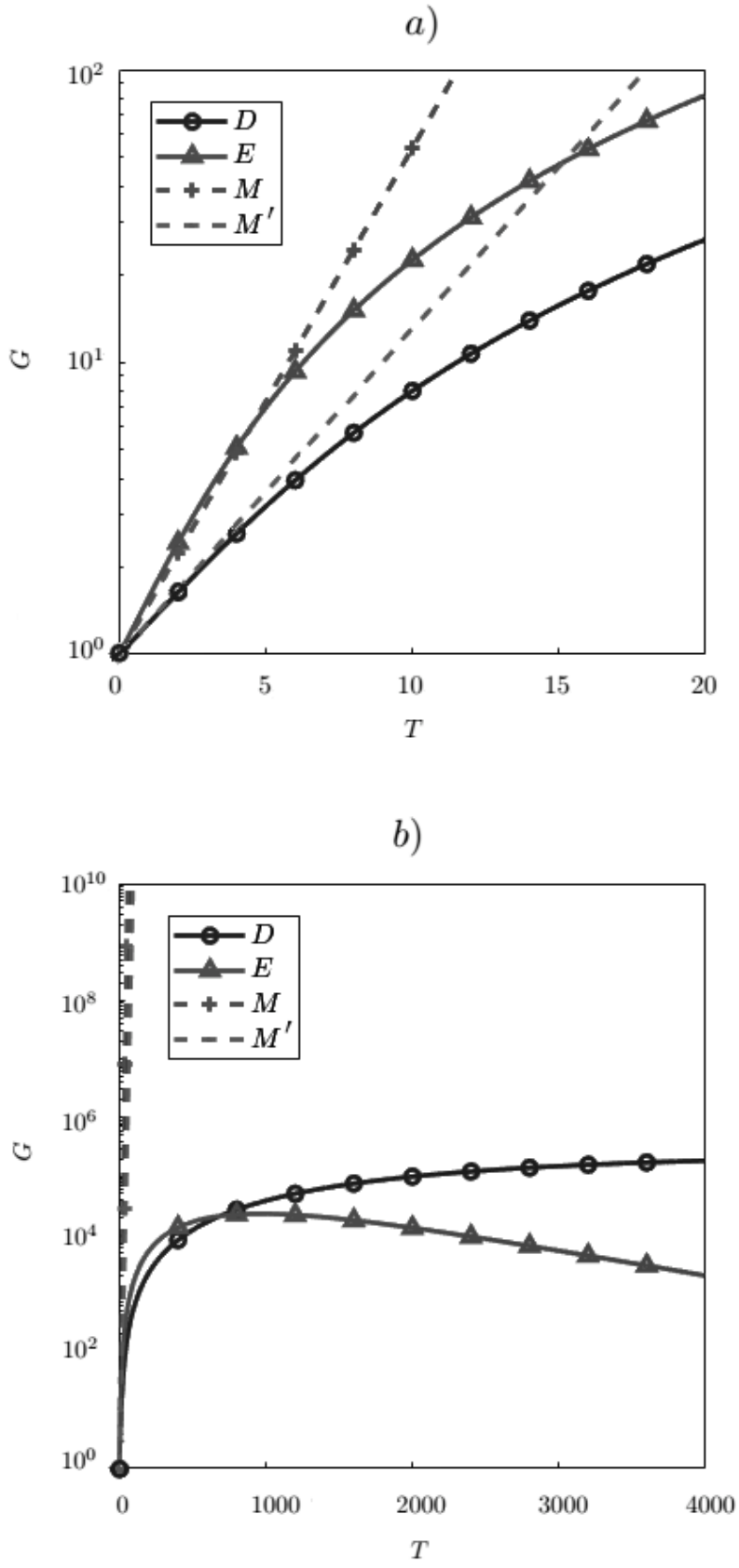

Figure 6.9: Same as figure 6.4 but in the viscous case with $Re = 1000$ and $Pr = 7$ and for two time horizons, $0 < T < 20$ in a), and $0 < T < 4000$ in b). M and M' are defined in figure 6.7.

concerns triads in the vicinity of E, whereas triads near D are not affected by the viscous effects. Triads in the vicinity of D have a less intense energy growth than for triads near E up until $T \sim 600$. After this time horizon, the optimal energy gain of triads near D dominates the energy growth of triads near E. In all cases, the energy gain of triads in the vicinity of those singular points is significant during the transient growth. For longer time horizons, the exponential growth of energy at M and M' takes over.

6.6 Variations of the transient growth with the primary wave angle

Figure 6.10 shows the evolution of the resonant locus shape for different angles θ_0 of the primary wave of wave vector $\boldsymbol{k_0} = (k_{x0}, k_{z0}) = (\sin\theta_0, \cos\theta_0)$. For nearly horizontal primary wave vectors $\theta_0 = 1.6$ close to $\pi/2$ as in figure 6.10b), ω_0 is close to unity, the unstable branches $(+,-,-)$ remain, and the stable branches $(+,-,+)$ and $(+,-,+)$ tend to be reduced to the point D corresponding to $\boldsymbol{k_i} = \boldsymbol{k_0}$ and $\boldsymbol{k_j} = \boldsymbol{0}$. Conversely, for nearly vertical primary wave vectors as in figure 6.10a) with $\theta_0 = 0.05$, the two stable solutions $(+,-,+)$ and $(+,-,+)$ exist and the two unstable branch are nearly vertical with PSI_1 and PSI_2 getting infinitely close as θ_0 goes to zero. Intermediate angles $\theta_0 = 0.4$ and $\theta_0 = 0.8$ are shown in figure 6.10b) and 6.10c) respectively. For intermediate angles, the resonant triads conserve their features on the resonant branches.

We introduce two variants of the limit point E, denoted E^- and E^+, depending on the sign of the x component of the phase velocity of the secondary wave 2 equal to $\text{sign}(c_{x2}) = -1$ for E^- and $\text{sign}(c_{x2}) = +1$ for E^+. Points D_- and D_+ leads to the same energy growth G so both points will be referred to as D when comparing the transient growth of D with E^- and E^+. Figures 6.11 represents the optimal growth rate σ as a function of k_1 at different instants T in the inviscid case for stable and unstable resonant triads in thin blue and bold red lines respectively for different angles θ_0 : $\theta_0 = 0.05$ in a-b-c), $\theta_0 = 0.4$ in d-e-f), $\theta_0 = 0.8$ in g-h-i), and $\theta_0 = 1.6$ in j-k-l). For small angles $\theta_0 = 0.05$ corresponding to geophysical flows, the optimal growth rate of stable triads dominates the growth rate unstable triads at early times as seen in 6.11a-b) since $\max_{k_1}\sigma$ is obtained along the thin blue curve corresponding to stable triads, same result as in figure 6.2a-b) for $\theta_0 = 0.25$. The time at which the maximum of σ shifts from a stable $(+,-,+)$ branch to an unstable branch $(+,-,-)$ is found numerically : $T_c = 20$ for $\theta_0 = 0.05$ whereas $T_c = 3$ for $\theta_0 = 0.25$ as seen previously in figure 6.2b). The characteristic time T_c at which the energy growth of unstable triads takes over the stable triads increases when the primary wave angle θ_0 decreases. The magnitude of the growth rate σ differs significantly when T increases for $\theta_0 = 0.05$: when comparing 6.11a), b) and c), the early maximum of $\sigma(T = 0.1, k_1)$ reached for stable triads with $k_1 = 10$ is 0.25 whereas the maximum at

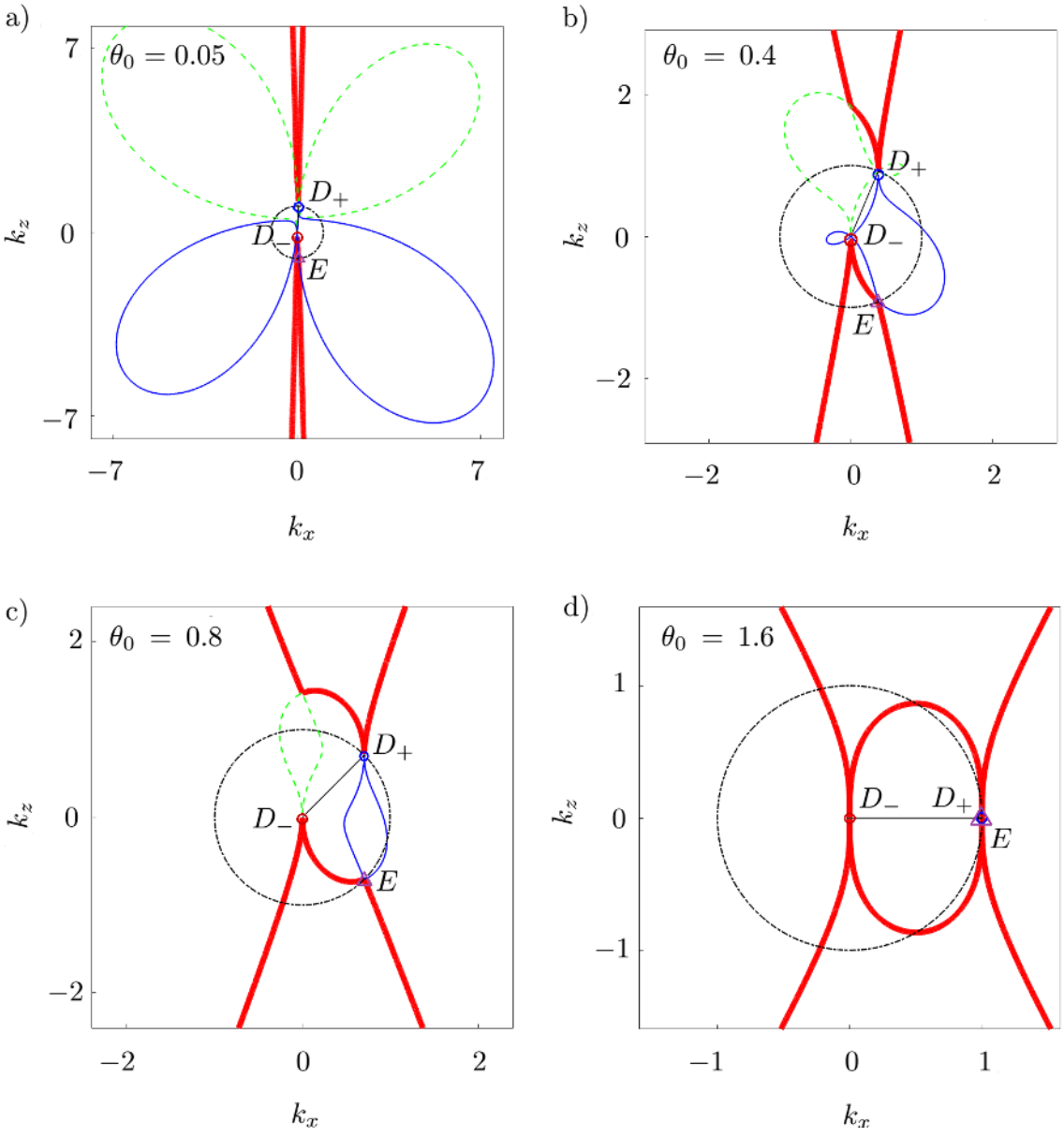

Figure 6.10: Plots of the resonant curves in the $-\boldsymbol{k_1}$ domain for extreme angles $\theta_0 = 0.05$ in a) and $\theta_0 = 1.6$ in d), and for intermediate angles $\theta_0 = 0.4$ in b) $\theta_0 = 0.8$ in c). Same conventions as in figure 6.1.

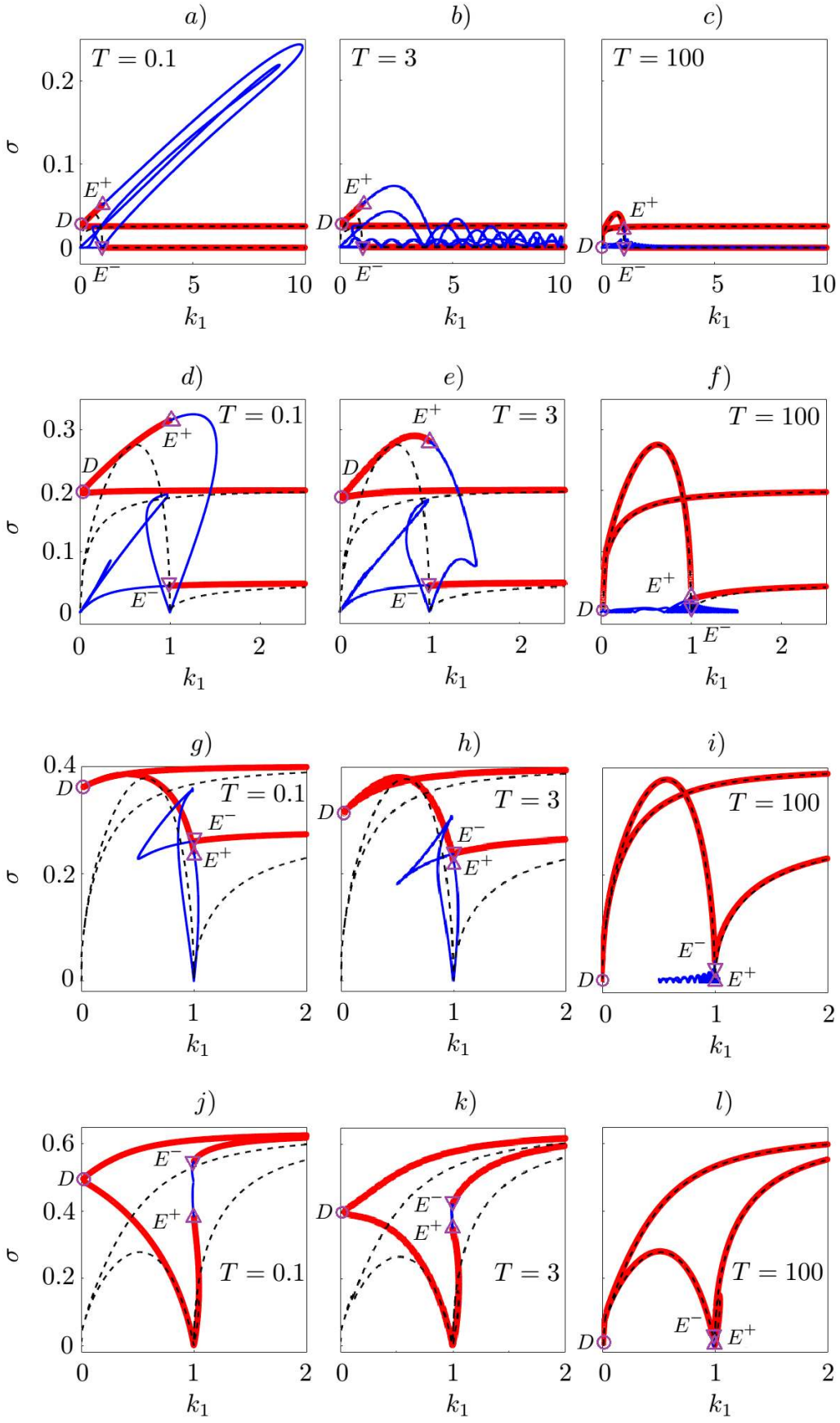

Figure 6.11: Same as in figure 6.2 but for $\theta_0 = 0.05$ in a-b-c), for $\theta_0 = 0.4$ in d-e-f), for $\theta_0 = 0.8$ in g-h-i), and for $\theta_0 = 1.6$ in j-k-l). In each figure, the points D, E^+ and E^- are indicated with circles and triangles pointing upward and downward respectively. Vertical scales are the same for graphs in the same row.

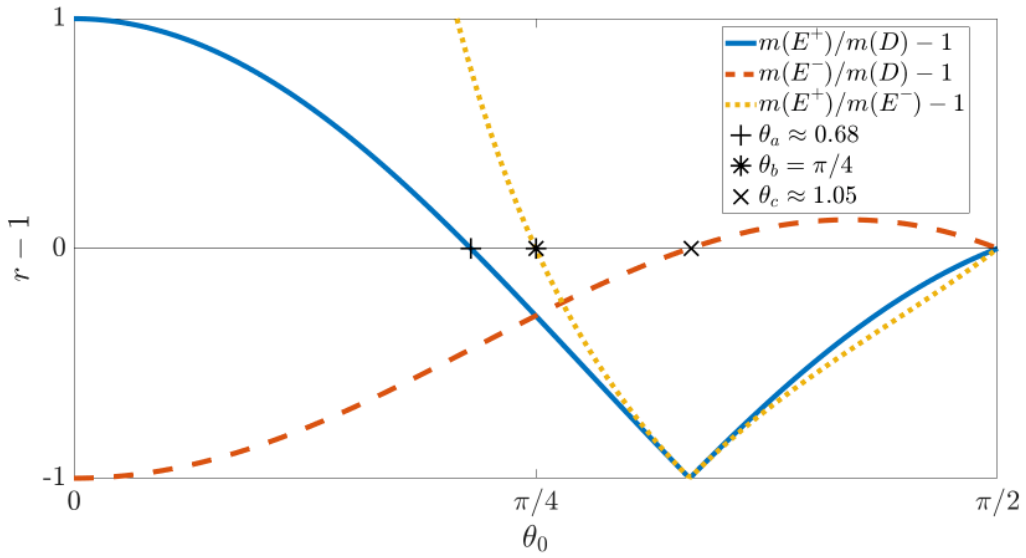

Figure 6.12: Plots of the slope ratios minus one $r-1$ as a function of the primary wave angle $0 < \theta_0 < \pi/2$ for the ratios $m(E^+)$ over $m(D)$ in solid blue line, $m(E^-)$ over $m(D)$ in dashed line, and $m(E^+)$ over $m(E^-)$ in dotted line. Each curve respectively crosses the horizontal zero axis at $\theta_a \approx 0.68$, $\theta_b = \pi/4$, and $\theta_c \approx 1.05$.

later times $\sigma(T = 100, k_1)$ reached for unstable triads with $k_1 = 1$ is 0.05. This difference of 0.20 between $\max_{k_1} \sigma(T = 0.1, k_1)$ and $\max_{k_1} \sigma(T = 100, k_1)$ shows that stable triads are more amplified at early times than unstable triads are at later times for small angles $\theta_0 = 0.05$. When the wave angle increases, the gap between $\max_{k_1} \sigma(T = 0.1, k_1)$ and $\max_{k_1} \sigma(T = 100, k_1)$ is reduced and the shifting time decreases as $T_c = 1.5$ for $\theta_0 = 0.4$ and $T_c = 0.01$ for $\theta_0 = 0.8$. The convergence of the optimal growth rate σ toward the theoretical growth rate $\sigma_{\text{th}} = \sqrt{L_1 L_2}$ (represented in dark dash-dotted lines) at a longer time horizon is shown in 6.11c-f-i-l). The maximum value of the optimal growth rate at later times $\max_{k_1} \sigma(T = 100, k_1)$ is then reached by an unstable triad near E^- for smaller angles $\theta_0 = 0.05$ and $\theta_0 = 0.4$ from 6.11c-f) whereas $\max_{k_1} \sigma(T = 100, k_1)$ is reached by unstable triads near PSI_1 for higher angles $\theta_0 = 0.8$ and $\theta_0 = 1.6$ from 6.11i-l). To summarize, a decreasing primary wave angle increases the duration and the intensity of the early growth rate of stable resonant triads compared to the late growth rate of unstable resonant triads given by Hasselmann's theory of instability (1967).

Comparing all the curves of $\sigma(T = 0.1, k_1)$ 6.11a), d), g), and j) to rank the intensity of the transient growth of the limiting points D, E^+ and E^-, as $\sigma(T \to 0, k_1) = m/2$, m being the slope of G at $T = 0$, we observe that the relative position between those points varies depending on the primary wave angle θ_0. The expressions of m at those three points are $m(D) = 2\,|\Phi_0 k_0 \sin(\theta_0)|$ and $m(E^\pm) = m(D)|1 \mp \text{sign}(c_{x2}) \cos(\theta_0) - 2\cos^2(\theta_0)|$. Figure 6.12 plots the three ratios r of the slopes of G at $T = 0$, $m(E^+)/m(D)$, $m(E^-)/m(D)$ and $m(E^+)/m(E^-)$, as a function of θ_0. For a primary wave angle $0 < \theta_0 < \pi/2$, the three represented curves of $r-1$ crosses the horizontal zero axis at three points $\theta_a \approx 0.68$,

$\theta_b = \pi/4$, and $\theta_c \approx 1.05$ delimiting four distinct regimes in which the relative intensity of the transient growth of E^+, E^-, and D changes. In the first regime, $0 < \theta_0 \leq \theta_a$ and $m(E^+) \geq m(D) > m(E^-)$, so the transient growth of triads near D dominates that of triads near E^-, but is less intense than that of triads near E^+. When $\theta_a < \theta_0 \leq \theta_b$, the intensities of the transient growth near the three points of interest, measured by their initial slopes of G, are such that $m(D) > m(E^+) \geq m(E^-)$. For $\theta_b < \theta_0 \leq \theta_c$, $m(D) > m(E^-) \geq m(E^+)$, and for $\theta_c < \theta_0 < \pi/2$, $m(E^-) > m(D) > m(E^+)$. In geophysical applications, as the primary wave angle becomes small, $0 < \theta_0 \ll \theta_a$ and $m(E^+) \gg m(D) > m(E^-)$, so, from figures 6.11a) and 6.12, the fastest transient growth of perturbation energy among all the resonant triads is obtained for stable triads near E^+, in the Elastic Scattering limit with two secondary waves propagating in the same x direction as the primary wave, $(\text{sign}(c_{x0}), \text{sign}(c_{x1}), \text{sign}(c_{x2}))$ being all equal to $+1$.

6.7 Effect of nonlinearities

When nonlinear effects are important, the complex amplitudes of the secondary waves become finite. (Φ_0, Φ_1, Φ_2) obey to equations (6.8) whose solutions are described by Coppi et al. (1969)[30] and Cairns (1979)[31]. They identified two types of solutions depending on if the frequency signs s_n are different or if they are all identical. From equation (6.13), s_n are different in our case, resulting in bounded periodic modulations of amplitudes Φ_n. This case applies for most waves in fluid at rest, such as surface, interfacial, inertial and internal waves as investigated by Ball (1964)[32] and Joyce (1974)[33]. The other case corresponds to identical frequency signs s_n. Such condition is achieved by waves in plasma physics as studied by Weiland & Wilhelmsson (1977)[34], or in a three-layer Kelvin Helmholtz as seen by Craik & Adam (1979)[35], and in those cases, solutions of (6.8) may diverge at finite time.

The nonlinear triadic equations (6.8) admit three invariants, the total energy $\mathcal{E}$, the x component of the pseudomomentum $\mathcal{P}$, and the phase invariant $\mathcal{K}$ whose expressions are given by (6.9). Without loss of generality, we can set $\mathcal{E} = 1$ and first consider the case of the triad F plotted in figure 6.1 for $\theta_0 = 0.25$, characterized by the phase velocities $(\boldsymbol{c_0}, \boldsymbol{c_1}, \boldsymbol{c_2})$ such that $c_{x0}^{-1} < c_{x1}^{-1} < c_{x2}^{-1}$, and $(\text{sign}(c_{x0}), \text{sign}(c_{x1}), \text{sign}(c_{x2}))$ are all equal to $+1$, so that $\mathcal{P}$ is positive definite.

In the quarter space $(|\Phi_0|, |\Phi_1|, |\Phi_2|)$, the possible trajectories are given by the intersection of the unit energy sphere of radius $\mathcal{E} = 1$ and the $\mathcal{P}$-ellipsoid of semi-axes

30. Coppi, Rosenbluth, and Sudan, *op. cit.*
31. R. A. Cairns, "The role of negative energy waves in some instabilities of parallel flows", in: *J. Fluid Mech.* 92.*1* (May 1979), pp. 1–14.
32. Ball, *op. cit.*
33. Joyce, *op. cit.*
34. Weiland and Wilhelmsson, *op. cit.*
35. Craik and Adam, *op. cit.*

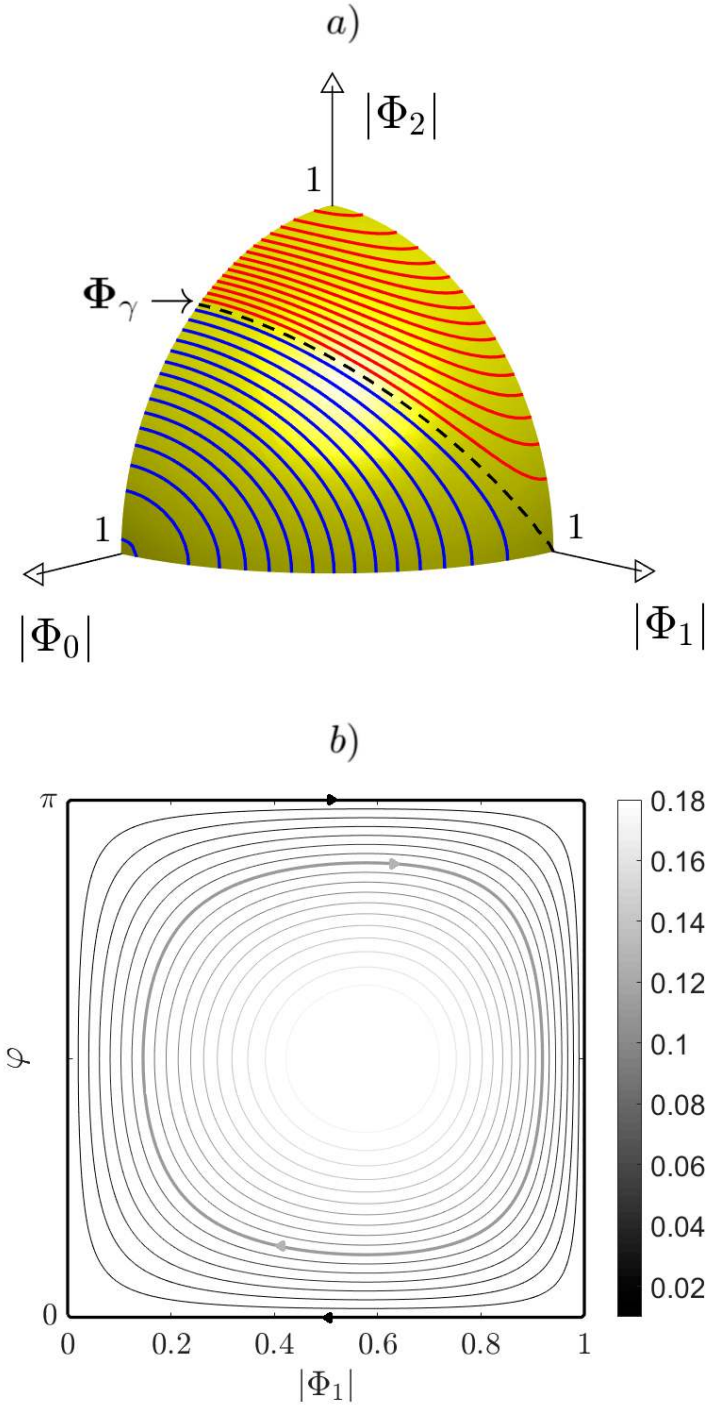

Figure 6.13: a) Plots of the trajectories given by (6.8) for the exemplified triad F plotted in figure 6.1 in a $(|\Phi_0|, |\Phi_1|, |\Phi_2|)$ space. At point F, $\gamma = 0.4$. The trajectories are represented by lines of constant momentum $c_{x0}^{-1} < \mathcal{P} < c_{x2}^{-1}$ on the unit energy sphere $\mathcal{E} = 1$ in the quarter space $(|\Phi_0|, |\Phi_1|, |\Phi_2|)$. The blue lines correspond to the trajectories $c_{x0}^{-1} < \mathcal{P} < c_{x1}^{-1}$, the red to $c_{x1}^{-1} < \mathcal{P} < c_{x2}^{-1}$, and the black dashed lines to the separatrix of equation $\mathcal{P} = c_{x1}^{-1}$. b) Plots of the trajectories along the separatrix in a $(\varphi, |\Phi_1|)$ plane. In b), trajectories are contour lines corresponding to different values of the phase invariant $\mathcal{K}$ given by the colorbar. Some trajectories obtained by numerical integration of (6.8) for different initial conditions are represented in heavy lines in b) : $(\varphi, |\Phi_1|) = (0, 0.99)$ in dark, $(\pi, 0.01)$ also in dark, and $(\pi/2, 0.8)$ in grey.

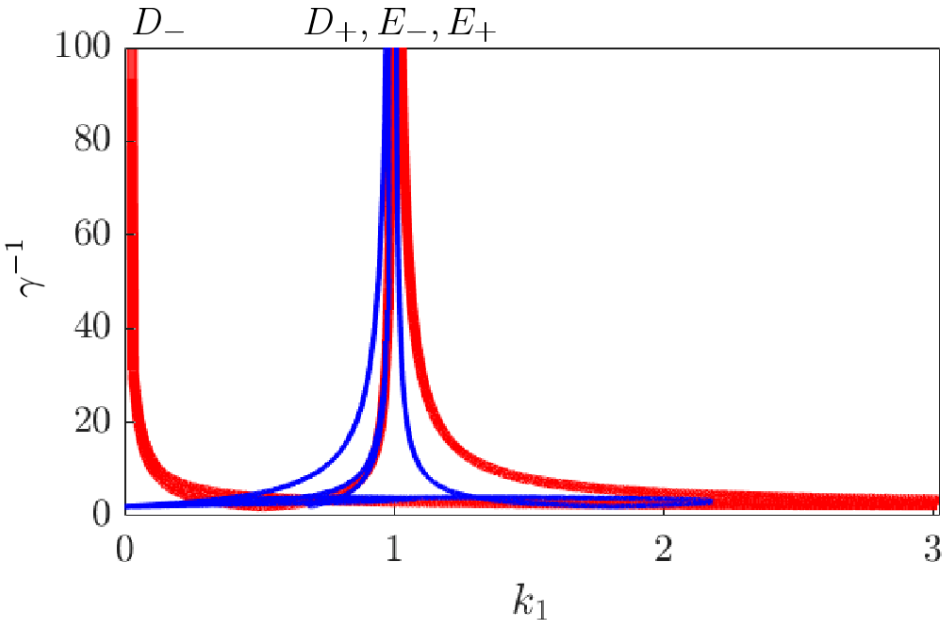

Figure 6.14: Plots of γ^{-1} as a function of k_1 along the resonant branches $(+,-,-)$ and $(+,-,+)$ represented in bold red and thin blue lines respectively. Four peaks to infinity located at points D_-, D_+, E_-, E_+ are indicated on the figure.

$\sqrt{\mathcal{P}c_{x0}}$, $\sqrt{\mathcal{P}c_{x1}}$ and $\sqrt{\mathcal{P}c_{x2}}$ as represented in figure 6.13a) for different values of $\mathcal{P}$ between c_{x0}^{-1} and c_{x2}^{-1}. The saddle point $\mathbf{\Phi_1} = (0,1,0)^{\mathrm{T}}$ is unstable and surrounded locally by parabolas of axis $|\Phi_2|$, whereas the stable points, $\mathbf{\Phi_0} = (1,0,0)^{\mathrm{T}}$ and $\mathbf{\Phi_2} = (0,0,1)^{\mathrm{T}}$, are circled by elliptic trajectories as represented in figure 6.13a) by blue and red ellipses respectively. Those different regimes are delimited by a separatrix of equation $\mathcal{P} = c_{x1}^{-1}$ represented in dark dashed lines. The separatrix crosses the plane $|\Phi_1| = 0$ on the point $\mathbf{\Phi_\gamma} = (\sqrt{\gamma}, 0, \sqrt{1-\gamma})^{\mathrm{T}}$ with $\gamma = (c_{x2}^{-1} - c_{x1}^{-1})/(c_{x2}^{-1} - c_{x0}^{-1})$, such that $0 < \gamma < 1$. For the examplified triad F, $\gamma = 0.41$. In the general case, for a resonant triad such that $c_{x0}^{-1} < c_{x1}^{-1} < c_{x2}^{-1}$, different cases appear when linearizing the problem (6.8) as demonstrated in appendix 6.9.5. If the considered triad is unstable, the 2D linearized problem (6.10) consists in linearizing the triadic equations (6.8) around the saddle point $\mathbf{\Phi_1}$ ($d\Phi_1/dT = 0$). If the considered triad is stable, the triadic equations (6.8) is linearized around one of the base states $\mathbf{\Phi_0}$ or $\mathbf{\Phi_2}$ ($d\Phi_0/dT = 0$ or $d\Phi_2/dT = 0$ respectively), leading to (6.10). In this last case, if $c_{x2}^{-1} - c_{x1}^{-1} < c_{x2}^{-1} - c_{x0}^{-1}$ (resp. $c_{x2}^{-1} - c_{x1}^{-1} > c_{x2}^{-1} - c_{x0}^{-1}$), higher transient growth of perturbation energy $|\Phi_0|^2 + |\Phi_1|^2$ (resp. $|\Phi_1|^2 + |\Phi_2|^2$) are observed when considering $(\Phi_2, \boldsymbol{k_2}, \omega_2)$ (resp. $(\Phi_0, \boldsymbol{k_0}, \omega_0)$) as a base state. For the exemplified triad F, $c_{x2}^{-1} - c_{x1}^{-1} < c_{x2}^{-1} - c_{x0}^{-1}$ so $(\Phi_2, \boldsymbol{k_2}, \omega_2)$ is taken as the base state, then perturbed by a small energy perturbation to observe higher transients, instead of considering $(\Phi_0, \boldsymbol{k_0}, \omega_0)$ like in part 6.3.2.

Figure 6.13b) shows the contour plots of the phase invariant $\mathcal{K}$ defined in (6.9) in a $(|\Phi_1|, \varphi)$ space. When the total phase φ equals to 0 or π, Φ_1 remains real and its modulus varies between 0 and 1 as illustrated by the trajectories in dark bold lines in the phase

portrait. This case is equivalent to the rotation of a rigid body around its axis of inertia in which the components of the momentum in all three directions are real. The case of φ non-equal to 0 or π shows the behavior of a system when complex initial conditions are imposed. $|\Phi_1|$ is then only bounded by 0 and 1, without reaching those bounds. On the unit energy sphere in figure 6.13a), the trajectory along the separatrix never reaches the saddle point $\mathbf{\Phi_1}$ or the point $\mathbf{\Phi_\gamma}$. In figure 6.13a), all the represented trajectories are oscillatory, and the trajectory described by the separatrix in black dashed lines is characterized by relaxation oscillations towards the unstable mode $\mathbf{\Phi_1}$, with a large time spent around the unstable point and a short time spent around $\mathbf{\Phi_\gamma}$, leading to the periodic destruction of the base state $(\Phi_2, \boldsymbol{k_2}, \omega_2)$ when initially perturbed along $(\Phi_0, \boldsymbol{k_0}, \omega_0)$.

For finite amplitudes, as $\gamma \ll 1$, figure 6.13a) shows that, around the focal point $\mathbf{\Phi_2}$, a small amplitude perturbation of magnitude greater than $\sqrt{\gamma}$ along the $|\Phi_0|$ axis is sufficient to cross the separatrix leading to the nonlinear growth of the perturbation, up until it destroys the primary wave $(\Phi_2, \boldsymbol{k_2}, \omega_2)$. Below this threshold, the perturbation is bounded and oscillates with high excursion characterized by an increase in amplitude of order $\sqrt{\gamma}$, or γ in terms of energy gain G. In the linearized problem, the exemplified triad F maximizes the optimal growth rate σ as $T \to 0$, so F is the triad having the fastest initial growth. As γ is not small compared to one in the case of F, the intensity of the linear transients and of the nonlinear growth of perturbation energy measured in terms of energy gain G is approximately $\gamma^{-1} = 2.44$ at F, and is overwhelmed by far by other resonant triads.

Resonant triads for which the separatrix gets infinitely close to one stable axis exhibit higher linear transients and nonlinear growth than other resonant triads. In terms of the x components of the phase velocity, this condition reads :

$$\gamma = \frac{\min(c_{x2}^{-1} - c_{x1}^{-1}, c_{x1}^{-1} - c_{x0}^{-1})}{c_{x2}^{-1} - c_{x0}^{-1}} \tag{6.28}$$

which must be small to develop high transients of perturbation energy as demonstrated in appendix 6.9.4. This generic criterion captures the greatest transient reached by any resonant triad of the spectrum in figure 6.1, and gives a wider view than the linearization method around $(\Phi_0, \boldsymbol{k_0}, \omega_0)$ introduced in part 6.3.2, some linear transients and nonlinear growth of stable triads being actually higher when considering $(\Phi_2, \boldsymbol{k_2}, \omega_2)$ as a base state instead of $(\Phi_0, \boldsymbol{k_0}, \omega_0)$. Figure 6.14 plots γ^{-1} as a function of k_1 along the resonant branches of figure 6.1. We observe two peaks which correspond to γ^{-1} going to infinity for the two limit triads, Elastic Scattering and Induced Diffusion, as $k_1 \to 0$ or $k_1 \to 1$. For finite amplitude waves, the highest transients and nonlinear growth of perturbation energy is reached for triads in the vicinity of the two limit cases, Elastic Scattering and Induced Diffusion.

6.8 Discussion and conclusion

In the linearized problem (6.10) of a primary wave perturbed by two secondary waves leading to triadic resonance, the nonnormality of the evolution operator $\mathscr{L}$ results in transient growth of perturbation energy whose intensity is measured by the energy growth G and the associated growth rate σ. When $\mathscr{L}$ becomes singular, this nonnormality is exacerbated and generates higher transients. Along the resonant branches represented in figure 6.1, $\mathscr{L}$ is always nonnormal and becomes singular at the limit points E and D, as one of the interaction coefficients goes to zero. The corresponding triads refer to as Elastic Scattering and Induced Diffusion respectively by McComas & Bretherton (1977)[36].

Figure 6.15 represents the two limit triads, Induced Diffusion and Elastic Scattering. The primary wave vector $\boldsymbol{k_0}$ is represented in black arrow and the secondary wave vectors $(\boldsymbol{k_1}, \boldsymbol{k_2})$ are represented either in blue for points (D_+, E_+), or in red for (D_-, E_-). One key feature for both Elastic Scattering and Induced Diffusion triads is the generation of a zero frequency mode since one of the secondary wave has a nearly vertical wave vector as represented on the right column in figure 6.15. This nearly vertical mode refers to as the Vertically Sheared Horizontal Flow (VSHF) modes investigated by Smith & Waleffe (2002)[37] in the context of forced three-dimensional turbulence. They found an anisotropic transfer of energy to the VSHF modes in a 3D purely stratified flow at small Froude number ($Fr = 0.2$) randomly forced at small scales. The VSHF modes are characterized by zero vertical vorticity, they have vanishing vertical velocity and only have kinetic energy, the associated buoyancy field being zero. Those modes create vertically sheared horizontal layers in which energy piles up selectively at specific wavenumbers. In rotating stratified turbulence, this accumulation of energy is the result of a strong growth of kinetic energy. For slow motion flows, Smith & Waleffe (2002)[38] highlighted the major implications of the VSHF mode on the dynamics as the vertical shearing leads to strong shear-Induced Diffusion of the potential vorticity component and the flow tends to a layered or pancake structure. Smith & Waleffe (2002)[39] considered rotating stratified turbulence with small f/N where f is the Coriolis parameter. In that case, the VSHF modes are inertial and correspond to the frequency f, small compared to N.

The plots of the optimal growth rate σ as a function of k_1 in figure 6.2 for short durations $T = 0.1$ reveal that stable resonant triads initially grow faster than unstable ones, in particular for triads near E^+, in the Elastic Scattering limit with two secondary waves propagating in the same x direction as the primary wave, $(\mathrm{sign}(c_{x0}), \mathrm{sign}(c_{x1}), \mathrm{sign}(c_{x2}))$ being all equal to $+1$. $\sigma(k_1, T = 0.1)$ reaches its maximum for a stable triad indicated by

36. McComas and Bretherton, *op. cit.*
37. L. M. Smith and F. Waleffe, "Generation of slow large scales in forced rotating stratified turbulence", in: *J. Fluid Mech.* 451 (Jan. 2002), pp. 145–168.
38. *Ibid.*
39. *Ibid.*

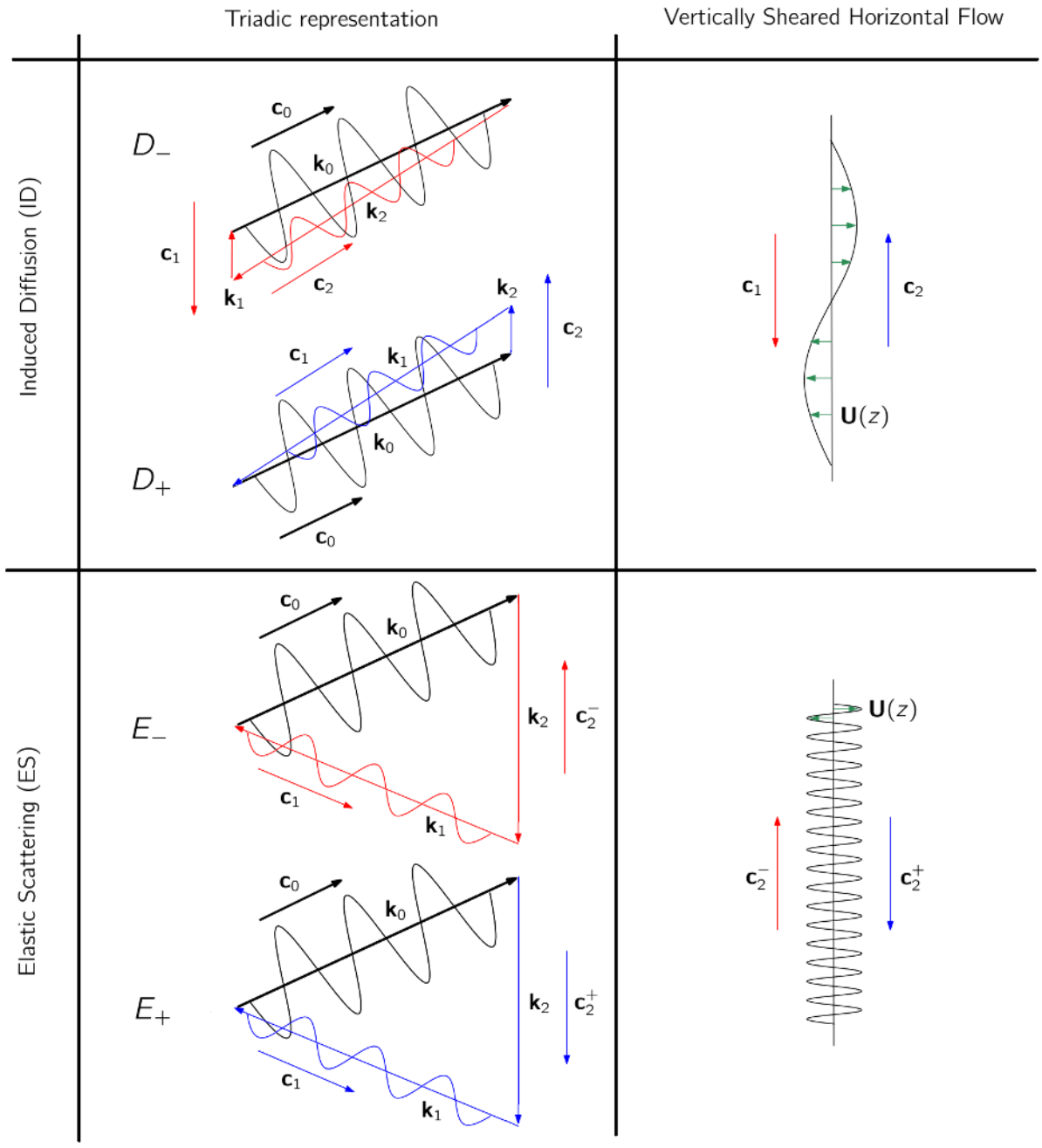

Figure 6.15: Illustration of Elastic Scattering and Induced Diffusion triads with the resulting Vertically Sheared Horizontal Flow (VSHF) mode of velocity field $\boldsymbol{U}(z)$ (green vectors). The phase velocity of the each mode $\boldsymbol{c_n}$ is indicated in red vectors for unstable triads D_-, E_- and in blue vectors for stable triads D_+, E_+. The wave amplitudes are represented by oscillations located on the vectors $(\boldsymbol{k_0}, \boldsymbol{k_1})$ on the left column and on the vertical axis on the right column for $\boldsymbol{k_2}$.

point F, corresponding to the fastest growth. Those key results remain when considering realistic values of viscous effects (Re, Pr) and smaller primary wave angles with respect to the vertical θ_0 for geophysical applications. Viscosity primarly affects higher wavenumbers by decreasing the growth rate and making it negative, which may stabilize unstable triads in a vicinity $\delta k^{\mathrm{R}} \propto Re^{-2}$ of E_- as predicted by the scalings (6.27), as G reaches a maximum $G_{\max} \propto Re^2$ at time $T_{\max} \propto Re$, confirmed by figure 6.9b).

When amplitudes are finite, nonlinear effects appear as discussed in part 6.7. High transients and nonlinear growth of perturbation energy occur if the x components of one resonant wave gets close to that of another resonant wave as stated in (6.28). An energy perturbation of order γ along the Vertically Sheared Horizontal Flow mode (VSHF) is amplified by a factor γ^{-1} up until it destroys the energy of the primary wave $(\Phi_2, \boldsymbol{k_2}, \omega_2)$. The nonlinear solution is limited to those three modes corresponding to an exchange of energy between the primary wave $(\Phi_2, \boldsymbol{k_2}, \omega_2)$ and one secondary wave $(\Phi_1, \boldsymbol{k_1}, \omega_1)$ with $c_{x1} \sim c_{x2}$ catalyzed by the VSHF mode i.e. the secondary wave $(\Phi_0, \boldsymbol{k_0}, \omega_0)$ of weakly varying amplitude.

6.9 Appendices

6.9.1 Appendix A: Initial slope of the optimal energy gain

At short times, the optimal energy gain G introduced in (6.15) can be developed following Schmid & Henningson (1994)[40]:

$$G\left(T, k_1\right) \underset{T \to 0}{\sim} \max_{\|\boldsymbol{\Phi}(0)\|=1} \left\langle \Big(\mathscr{I} + T(\mathscr{L} + \mathscr{L}^{\mathrm{H}}) \Big) \boldsymbol{\Phi}\left(0\right) | \boldsymbol{\Phi}\left(0\right) \right\rangle \tag{6.29}$$

with $\mathscr{I}$ the identity matrix. In the present 2D case, with the evolution operator $\mathscr{L}$ given in equation (6.10) :

$$G\left(T, k_1\right) \underset{T \to 0}{\sim} 1 + T|L_1 + L_2| \tag{6.30}$$

so the optimal energy gain G experiences initial linear growth characterized by the positive slope at $T = 0$ equal to $|L_1 + L_2|$.

40. Schmid and Henningson, *op. cit.*

Using the definition of the optimal growth rate (6.16), we get :

$$\begin{aligned}\sigma\left(T,k_1\right) &\underset{T\to 0}{\sim} \frac{1}{2T}\ln\left(1+T\frac{\partial G}{\partial T}(T=0,k_1)\right)\\ &\underset{T\to 0}{\sim} \frac{1}{2}\frac{\partial G}{\partial T}(T=0,k_1)\\ &\underset{T\to 0}{\sim} \frac{|L_1+L_2|}{2}\end{aligned} \tag{6.31}$$

6.9.2 Appendix B: Computation of the optimal energy gain

The general expression of the optimal energy gain G in (6.15) involves the computation of the exponential operator $\exp(T\mathscr{L})$ which has the explicit analytical form :

$$\exp(T\mathscr{L}) = \begin{cases} \begin{pmatrix} \cos(T/\tau) & \sqrt{|L_1/L_2|}\sin(T/\tau) \\ -\sqrt{|L_2/L_1|}\sin(T/\tau) & \cos(T/\tau) \end{pmatrix} & \text{if } L_1L_2<0 \\ \begin{pmatrix} \cosh(T/\tau) & \sqrt{|L_1/L_2|}\sinh(T/\tau) \\ \sqrt{|L_2/L_1|}\sinh(T/\tau) & \cosh(T/\tau) \end{pmatrix} & \text{if } L_1L_2>0 \end{cases} \tag{6.32}$$

where sinh and cosh are the hyperbolic sines and cosines functions, and when one of the interaction coefficients is nil, $L_1L_2=0$:

$$\exp(T\mathscr{L}) = \begin{cases} \begin{pmatrix} 1 & L_1T \\ 0 & 1 \end{pmatrix} & \text{if } L_2=0 \\ \begin{pmatrix} 1 & 0 \\ L_2T & 1 \end{pmatrix} & \text{if } L_1=0 \end{cases} \tag{6.33}$$

6.9.3 Appendix C: Scaling of the optimal energy gain in the viscous case

When getting infinitely close to E, D_- or D_+ in a radius $\delta k \ll 1$ along the resonant branches, the operator $\mathscr{L}$ asymptotes :

$$\mathscr{L}_E \sim \begin{pmatrix} -\dfrac{1}{2\mathrm{R}} & L_1^E \\ L_2'^E\delta k & -\dfrac{2k_{z0}^2}{\mathrm{R}} \end{pmatrix} \quad \mathscr{L}_{D_-} \sim \begin{pmatrix} -\dfrac{\delta k^2}{2\mathrm{R}} & L_1'^D\delta k \\ L_2^D & -\dfrac{1}{2\mathrm{R}} \end{pmatrix} \quad \mathscr{L}_{D_+} \sim \begin{pmatrix} -\dfrac{1}{2\mathrm{R}} & L_1^D \\ L_2'^D\delta k & -\dfrac{\delta k^2}{2\mathrm{R}} \end{pmatrix} \tag{6.34}$$

with the same notations introduced in equation (6.17). Geophysical flows involve high

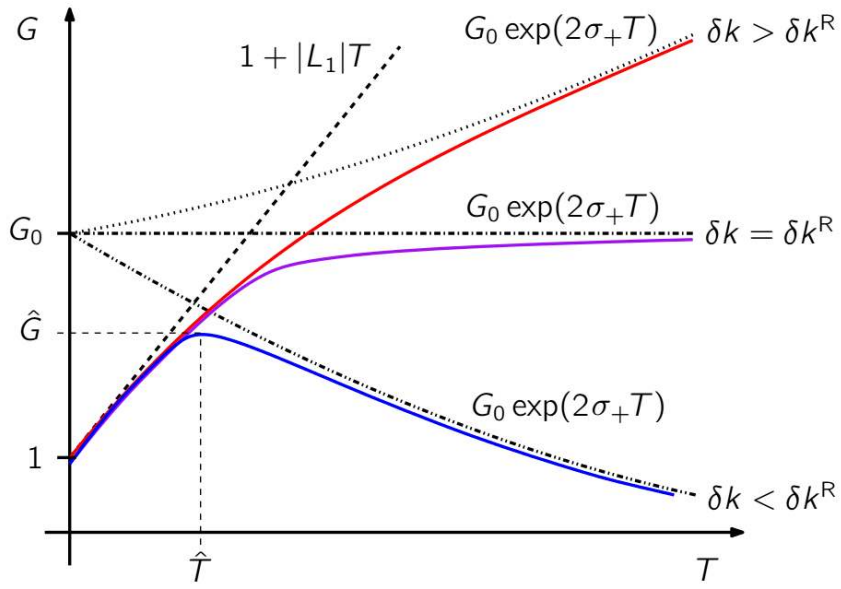

Figure 6.16: Illustration of the optimal energy gain G as a function of T at one of the singular points E_- in the viscous case. Different types of solution are represented depending on the value of δk near δk^{R}. The blue and red curves represent stable (exponentially decaying) and unstable (exponentially growing) solutions respectively obtained when $\delta k > \delta k^{\mathrm{R}}$ and $\delta k < \delta k^{\mathrm{R}}$ whereas the purple curve corresponds to the case $\delta k = \delta k^{\mathrm{R}}$. The asymptotes of all curves are also displayed : $1 + |L_1|T$ in dashed line and $G_0 \exp(2\sigma_{\mathrm{th}} T)$ (with $G_0 = 1/|\left\langle \mathbf{\Phi}_\alpha | \mathbf{\Phi}^{\mathrm{A}}_\alpha \right\rangle|^2$ and σ_{th} the greatest eigenvalue of the evolution operator) in dotted, dash dotted and dash dot dotted lines when $\delta k > \delta k^{\mathrm{R}}$, $\delta k = \delta k^{\mathrm{R}}$ and $\delta k < \delta k^{\mathrm{R}}$ respectively. In the last case, $G_{\max}$ and $T_{\max}$ are also indicated.

Reynolds number $Re \geq 10^3$ and for different environments, Pr can vary over three decades, from 0.7 for heat in the atmosphere up to 700 for salt in the ocean. At a high fixed Re when getting close to E in a radius $\delta k \ll 1$ along the resonant branches, the condition for viscous stabilization is $\sigma_{\rm th} < 0$, which, from (6.26) and (6.34), reads :

$$L_1^E L_2'^E \delta k + \left(\frac{1-2k_{z0}^2}{2\mathrm{R}}\right)^2 < \left(\frac{1+2k_{z0}^2}{2\mathrm{R}}\right)^2 \tag{6.35}$$

so there exist $\delta k^{\rm R} = 2k_{z0}^2/(L_1^E L_2'^E \mathrm{R}^2)$ such that, when $\delta k < \delta k^{\rm R}$, the unstable solution becomes linearly stable as $\sigma_{\rm th}$ becomes negative. The scaling of $\delta k^{\rm R}$ as a function of Re is $\delta k^{\rm R} \propto Re^{-2}$. Close to the singular points D_- or D_+, the stability properties are different since one of the resonant wave vectors vanishes leading to vanishing dissipation effects. This is evident from the expression of $\sigma_{\rm th}$ in (6.26) as, for any number R, δk may be taken sufficiently small to give $\sigma_{\rm th} > 0$.

From equations (6.30) and (6.25), the asymptotic behavior of the optimal energy gain G in the vicinity of point E is $G \sim 1 + |L_1|T$ as $T \to 0$ and $G \sim G_0 \mathrm{e}^{2\sigma_{\rm th}T}$ as $T \to \infty$ with $G_0 = 1/|\left\langle \boldsymbol{\Phi}_\alpha | \boldsymbol{\Phi}_\alpha^{\rm A} \right\rangle|^2$. Figure 6.16 illustrates the different regimes for triads in the vicinity of E due to viscous effects : exponential decay versus exponential growth depending on the sign of the maximum eigenvalue $\sigma_{\rm th}$. The transition from one regime to the other is delimited by $\delta k^{\rm R}$. At a high fixed Reynolds number Re, the scalings of $G_{\max}$ and $T_{\max}$ as a function of Re are approximated by those of $G_0 = 1/|\langle \boldsymbol{\Phi}_\alpha | \boldsymbol{\Phi}_\alpha^{\rm A} \rangle|^2$ and T^* defined by $1 + |L_1|T^* = G_0 \mathrm{e}^{2\sigma_{\rm th}T^*}$. The asymptotic developments of G_0 and T^* are obtained analytically for $\delta k \ll \delta k^{\rm R} \propto Re^{-2}$ at a high fixed Reynolds number. The adjoint mode corresponding to the highest eigenvalue is $\boldsymbol{\Phi}_\alpha^{\rm A} = \boldsymbol{\eta}_\alpha^{\rm A}/\|\boldsymbol{\eta}_\alpha^{\rm A}\|$ with :

$$\boldsymbol{\eta}_\alpha^{\rm A} = \begin{pmatrix} \\ \dfrac{1}{2L_2}\left(\dfrac{\lambda_1-\lambda_2}{\mathrm{R}} + \sqrt{\left(\dfrac{\lambda_1-\lambda_2}{\mathrm{R}}\right)^2 + 4L_1L_2}\right) \end{pmatrix} \tag{6.36}$$

Calculating $G_0 = 1/|\left\langle \boldsymbol{\Phi}_\alpha | \boldsymbol{\Phi}_\alpha^{\rm A} \right\rangle|^2$ and $1 + |L_1|T^* = G_0 \mathrm{e}^{2\sigma_{\rm th}T^*} \sim G_0(1 + 2\sigma_{\rm th}T^*)$ for $\delta k \ll \delta k^{\rm R}$, the different scalings obtained analytically for fixed high Reynolds number are :

$$\begin{aligned} G_{\max} &\propto Re^2 \\ T_{\max} &\propto Re \end{aligned} \tag{6.37}$$

6.9.4 Appendix D: Criterion for transient growth for finite amplitudes

Considering the unit energy sphere, the two conserved quantities, the total energy and the x component of the pseudomomentum given by (6.9), can be written :

$$\begin{aligned} \mathcal{E} &= |\Phi_0|^2 + |\Phi_1|^2 + |\Phi_2|^2 = 1 \\ \mathcal{P} &= \frac{|\Phi_0|^2}{c_{x0}} + \frac{|\Phi_1|^2}{c_{x1}} + \frac{|\Phi_2|^2}{c_{x2}} \end{aligned} \tag{6.38}$$

Without loss of generality, we order the x components of the phase velocity c_{xn} of each wave of the triad assuming :

$$\frac{1}{c_{x0}} < \frac{1}{c_{x1}} < \frac{1}{c_{x2}} \tag{6.39}$$

Using (6.38), we get :

$$\begin{aligned} \frac{1}{c_{x0}} - \mathcal{P} &= \left(\frac{1}{c_{x0}} - \frac{1}{c_{x1}}\right)|\Phi_1|^2 + \left(\frac{1}{c_{x0}} - \frac{1}{c_{x2}}\right)|\Phi_2|^2 < 0 \\ \frac{1}{c_{x1}} - \mathcal{P} &= \left(\frac{1}{c_{x1}} - \frac{1}{c_{x0}}\right)|\Phi_0|^2 + \left(\frac{1}{c_{x1}} - \frac{1}{c_{x2}}\right)|\Phi_2|^2 \\ \frac{1}{c_{x2}} - \mathcal{P} &= \left(\frac{1}{c_{x2}} - \frac{1}{c_{x0}}\right)|\Phi_0|^2 + \left(\frac{1}{c_{x2}} - \frac{1}{c_{x1}}\right)|\Phi_1|^2 > 0 \end{aligned} \tag{6.40}$$

which shows that $\mathcal{P}$ is bounded and :

$$\frac{1}{c_{x0}} < \mathcal{P} < \frac{1}{c_{x2}}, \text{ and } \mathcal{P} = \frac{1}{c_{x1}} \text{ at the separatrix.} \tag{6.41}$$

At the crossing between the plane $|\Phi_1| = 0$ and the separatrix, we get :

$$\begin{aligned} \frac{1}{c_{x0}} - \frac{1}{c_{x1}} &= \left(\frac{1}{c_{x0}} - \frac{1}{c_{x2}}\right)|\Phi_2|^2 \\ \frac{1}{c_{x2}} - \frac{1}{c_{x1}} &= \left(\frac{1}{c_{x2}} - \frac{1}{c_{x0}}\right)|\Phi_0|^2 \end{aligned} \tag{6.42}$$

or equivalently :

$$\begin{aligned} |\Phi_0|^2 &= \frac{c_{x2}^{-1} - c_{x1}^{-1}}{c_{x2}^{-1} - c_{x0}^{-1}} \\ |\Phi_2|^2 &= \frac{c_{x1}^{-1} - c_{x0}^{-1}}{c_{x2}^{-1} - c_{x0}^{-1}} \end{aligned} \tag{6.43}$$

The separatrix gets infinitely close to one of the axes $|\Phi_0|$ or $|\Phi_2|$ if $|\Phi_0|^2 \ll 1$ or

$|\Phi_2|^2 \ll 1$. This condition reads :

$$\gamma = \frac{\min(c_{x2}^{-1} - c_{x1}^{-1}, c_{x1}^{-1} - c_{x0}^{-1})}{c_{x2}^{-1} - c_{x0}^{-1}} \tag{6.44}$$

which should be small compared to 1, so that strong transient growth of perturbation energy and relaxation oscillations occur.

6.9.5 Appendix E: Linearized problem from the nonlinear triadic equations

We consider the triadic equations (6.8), with the assumption introduced previously (6.39). Three linearized problems can be derived from (6.8).

Assuming Φ_0 real, the linearized problem around Φ_0 reads $d\Phi_0/dT = 0$ and :

$$\frac{d}{dT}\begin{pmatrix}\Phi_1\\ \Phi_2\end{pmatrix} = \mathscr{L}_0\begin{pmatrix}\Phi_1^*\\ \Phi_2^*\end{pmatrix}, \text{ with } \mathscr{L}_0 = \frac{\Lambda_x\Phi_0}{c_{x0}}\begin{pmatrix}0 & 1 - c_{x0}/c_{x2}\\ c_{x0}/c_{x1} - 1 & 0\end{pmatrix} \tag{6.45}$$

Assuming Φ_1 real, the linearized problem around Φ_1 reads $d\Phi_1/dT = 0$ and :

$$\frac{d}{dT}\begin{pmatrix}\Phi_0\\ \Phi_2\end{pmatrix} = \mathscr{L}_1\begin{pmatrix}\Phi_0^*\\ \Phi_2^*\end{pmatrix}, \text{ with } \mathscr{L}_1 = \frac{\Lambda_x\Phi_1}{c_{x1}}\begin{pmatrix}0 & c_{x1}/c_{x2} - 1\\ 1 - c_{x1}/c_{x0} & 0\end{pmatrix} \tag{6.46}$$

Assuming Φ_2 real, the linearized problem around Φ_2 reads $d\Phi_2/dT = 0$ and :

$$\frac{d}{dT}\begin{pmatrix}\Phi_0\\ \Phi_1\end{pmatrix} = \mathscr{L}_2\begin{pmatrix}\Phi_0^*\\ \Phi_1^*\end{pmatrix}, \text{ with } \mathscr{L}_2 = \frac{\Lambda_x\Phi_2}{c_{x2}}\begin{pmatrix}0 & 1 - c_{x2}/c_{x1}\\ c_{x2}/c_{x0} - 1 & 0\end{pmatrix} \tag{6.47}$$

The determinants of $\mathscr{L}_0$ and $\mathscr{L}_2$ are positive, whereas that of $\mathscr{L}_1$ is negative, so (6.45) and (6.47) lead to bounded solutions in amplitudes corresponding to stable resonant triads represented in thin blue and green lines in figure 6.1, whereas (6.46) results in exponential growth of amplitudes corresponding to the dynamics of unstable resonant triads in bold red lines in figure 6.1.

For stable resonant triads described by equations (6.45) or (6.47), we show that the linearized problem (6.45) (resp. or (6.47)) leads to the highest transient growth of perturbation energy if $c_{x1} \to c_{x0}$ (resp. $c_{x1} \to c_{x2}$). Without loss of generality, we assume $c_{x1} \to c_{x0}$ such that $\gamma = (c_{x1}^{-1} - c_{x0}^{-1})/(c_{x2}^{-1} - c_{x0}^{-1})$. Then, the evolution operator $\mathscr{L}_0$ in (6.45)

reads :

$$\mathscr{L}_0 = \Lambda_x \Phi_0 (c_{x2}^{-1} - c_{x0}^{-1}) \begin{pmatrix} 0 & -1 \\ \gamma & 0 \end{pmatrix} \tag{6.48}$$

so nonnormality is ensured if $\gamma \neq 1$, and when $\gamma \ll 1$, $\mathscr{L}_0$ becomes singular (i.e. highly nonnormal). In this case, high transients are observed in the linearized problem (6.45), which is not the case of (6.47), as :

$$\mathscr{L}_2 = \Lambda_x \Phi_2 (c_{x2}^{-1} - c_{x0}^{-1}) \begin{pmatrix} 0 & 1-\gamma \\ -1 & 0 \end{pmatrix} \tag{6.49}$$

hence, in the limit $\gamma \ll 1$, $\mathscr{L}_2$ becomes normal, whereas $\mathscr{L}_0$ becomes nonnormal and singular.

Chapter 7

Internal waves: nonlinear growth and linear transients of perturbation energy (in preparation for *Physical Review Fluids*)

Some information available in the previous sections, such as a review of the fundamental equations describing our systems and their properties, may be found in the following article as an introduction to the theoretical basis needed for the novel results. Despite some extra terms in the coupling coefficients when including rotation effects in the description of a stratified medium, we find the previous transients to form in weakly rotating medium for gravito-inertial waves submitted to small perturbations. The transient growth of perturbation energy, as well as the nonlinear growth for a finite perturbation, are sensitive to the variations of the Coriolis parameter captured by some novel scalings.

7.1 Abstract

Internal waves play an important role in the evolution of the global climate system, the atmosphere and the ocean being the host of intense local mixing resulting from internal waves activity. Internal wave-driven mixing is regulated by the energy transfers resulting from wave-wave interaction, a key element whose understanding needs to be advanced to accurately represent the energy transfers within the internal wave field, which ultimately leads to dissipation, turbulence, breaking and mixing. Our investigation focuses on the triadic resonant instability, a nonlinear interaction involving three internal waves whose frequencies and wave vectors follow a specific resonance condition. We show that, in a stratified rotating medium, the triadic system is analytically constrained by three invariants, the total energy, pseudo momentum and a phase invariant, such that, when this system is submitted to a finite perturbation, nonlinear growth of the perturbation energy characterized by relaxation oscillations take place, and may represent another path to instability. This nonlinear process is enhanced by triads involving one zero wave frequency, but, as rotation increases, the disappearance of waves of zero frequency in the triadic

resonant spectrum leaves room for triadic interactions involving inertial waves, and the magnitude of the associated nonlinear growth of perturbation energy decreases compared to the non-rotating case, with a growth rate being inversely proportional to the Coriolis parameter.

7.2 Introduction

The evolution of the global climate system is sensitive to the distribution and the magnitude of the vertical mixing of deep water masses in the ocean[1], and of layers of different densities in the atmosphere[2]. This turbulent mixing is driven by waves generated inside the high atmosphere and the deep ocean, called internal waves[3], as a result of the natural stratification occurring in both media. Internal waves transport nutrients, greenhouse gases and carbon around the planet[4], and contribute to the Meridional Overturning Circulation (MOC), one major large-scale ocean circulation system on Earth, which redistributes heat and salt all over the entire ocean during a one thousand year cycle[5], mixing deep, cold, salty, dense water with warmer, less dense surface currents.

Oceanic internal waves are generated by tides, surface winds and geostrophic currents, and each of these sources accounts for a fraction of the total energy budget dedicated to internal waves of order 1 TW[6]. Once generated, internal waves propagate throughout the ocean, and interact with other waves, currents and topography, causing energy to transfer across different spatio-temporal scales. One major process contributing to this energy transfer is triadic resonant instability (TRI), a nonlinear interaction involving three resonating internal waves of different wave vectors and frequencies[7], that continuously exchange energy[8]. The parametrization of vertical mixing in numerical climate model is part of an international effort to accurately model and predict the evolution of climate[9], which necessarily includes a thorough understanding of wave interaction.

7.3 Triadic equations and invariants

Internal waves propagate in the atmosphere and the ocean, two geophysical fluids that are stratified and rotating media, as both fluids undergo Earth's rotation and gravity,

1. Melet, Legg, and Hallberg, *op. cit.*
2. J. Holton et al., "Stratosphere-Troposphere Exchange", in: *Rev. Geophys.* 33 (Nov. 1995), pp. 403–439.
3. Klymak, Legg, and Pinkel, *op. cit.*
4. Tuerena et al., *op. cit.*
5. Kunze, *op. cit.*
6. Wunsch and Ferrari, *op. cit.*
7. Ripa, *op. cit.*
8. McComas and Bretherton, *op. cit.*
9. MacKinnon et al., "Climate Process Team on Internal Wave-Driven Ocean Mixing".

which makes heavier fluid stay at the bottom while fluid of smaller density is generally found at higher elevations. Stratification in density originates from layers arranged in order of increasing temperature in the atmosphere, and layers of different temperature and salinity in the ocean, from cold and salty deep water masses to light and warm seawater at the surface.

We consider an incompressible, inviscid flow characterized by a constant BruntVäisälä frequency $N = \sqrt{-g/\rho_r d\rho_0/dz}$ measuring the strength of the stratification, ρ_r being the constant reference density, ρ_0 the mean density profile, a linear function of the vertical coordinate z, and by a Coriolis parameter $f = 2\Omega \sin\lambda$, where Ω is the norm of the Earth's rotation vector, and λ the latitude. We assume the flow, described by the Cartesian coordinates (x, y, z), to be invariant along the y direction, so the so-called 2D-3C (two-dimensional, three components) model is used to model the flow. In this 2D flow in the (x, z) plane, the dispersion relation of an internal wave of nondimensional frequency ω and wave vector $\boldsymbol{k} = (k_x, k_z)$, propagating in the considered fluid is[10]:

$$\omega^2 = \left(\frac{k_x}{k}\right)^2 + \left(\frac{f}{N}\right)^2 \left(\frac{k_z}{k}\right)^2 \tag{7.1}$$

where $k = \sqrt{k_x^2 + k_z^2}$ is the norm of the wave vector $\boldsymbol{k}$. This dispersion relation is derived by linearizing the incompressible, stratified, rotating Euler equations in which time t and space variables (x, z) are nondimensionalized respectively by N and L, the typical length scale of the wave field. As a result of (7.1), $(f/N)^2 \leq \omega^2 \leq 1$, and the two limiting cases correspond to inertial waves as[11] $\omega = \pm f/N$, and to internal gravity waves as[12] $\omega = \pm 1$. In geophysical applications, $|f|$ ranges from 0 at the equator to approximately $1.5 \times 10^{-4} \mathrm{rad\,s^{-1}}$ at the poles, and the order of magnitude of N varies between $10^{-3} \mathrm{rad\,s^{-1}}$ and $10^{-2} \mathrm{rad\,s^{-1}}$, so we are interested in flows characterized by values of f/N, also known as Prandtl ratio, ranging from 0 to 0.15.

When the wave amplitude is not infinitesimal, the Froude and Rossby numbers, $Fr = U/(NL)$ and $Ro = U/(fL)$, where U is the typical velocity in the wave field, become finite. The nonlinearities in the Euler equations being quadratic, three waves $(\omega_0, \boldsymbol{k_0})$, $(\omega_1, \boldsymbol{k_1})$, $(\omega_2, \boldsymbol{k_2})$ independent at leading order in Froude and Rossby numbers will be coupled at the second order if they form a triad[13]:

$$\begin{aligned} \omega_0 + \omega_1 + \omega_2 &= 0 \\ \boldsymbol{k_0} + \boldsymbol{k_1} + \boldsymbol{k_2} &= \boldsymbol{0} \end{aligned} \tag{7.2}$$

10. Gill, *op. cit.*
11. O. M. Phillips, "Energy Transfer in Rotating Fluids by Reflection of Inertial Waves", in: *Phys. Fluids* 6.4 (Apr. 1963), pp. 513–520.
12. McEwan and Plumb, *op. cit.*
13. Hasselmann, *op. cit.*

so, denoting s_n the sign of the frequency ω_n of the n-th wave, the triadic resonance conditions (7.2) combined with the dispersion relation of each wave (7.1) to eliminate $\boldsymbol{k_1}$ or $\boldsymbol{k_2}$ give:

$$s_0\mathcal{D}(\boldsymbol{k_0}) + s_1\mathcal{D}(\boldsymbol{k}) + s_2\mathcal{D}(\boldsymbol{k_0}+\boldsymbol{k}) = 0 \tag{7.3}$$

with $\mathcal{D}(\boldsymbol{k}) = \sqrt{k_x^2 + (f/N)^2 k_z^2}/k$, $\boldsymbol{k}$ being indifferently $\boldsymbol{k_1}$ or $\boldsymbol{k_2}$.

Without loss of generality, we can fix one of the wave vector, for instance $\boldsymbol{k_0}$ and the associated frequency sign s_0, to study the set of resonant triads by plotting the implicit equation (7.3) in the $\boldsymbol{k}$ plane, the wave vector $\boldsymbol{k}$ corresponding indifferently to $\boldsymbol{k_1}$ or $\boldsymbol{k_2}$ in (7.2). Setting $\boldsymbol{k_0} = (k_{x0}, k_{z0}) = k_0(\sin\theta_0, \cos\theta_0)$ with $k_0 = 1$ and $\theta_0 = 0.13$, and $s_0 = +1$, the resonance loci defined by equation (7.3) are plotted on figure 7.1 for different values of f/N. Each possible sign combination (s_0, s_1, s_2) in (7.3) leads to a distinct resonant branch represented in a specific color: the red curves correspond to the sign combination $(+,+,+)$, the blue ones to $(+,+,-)$, and the green ones to $(+,-,+)$. The red curves cease to exist when $f/N > \omega_0/2$, or equivalently when $f/N > \sin\theta_0/(3+\sin^2\theta_0)^{1/2}$. Each resonant triad is obtained by joining the tip of $\boldsymbol{k_0}$ to one resonant curve, forming the vector $\boldsymbol{k}$, and closing the triangle by plotting $-\boldsymbol{k_0} - \boldsymbol{k}$, as presented by the exemplified triad indicated by point F at the tip of $\boldsymbol{k}$.

We introduce the normalized streamfunction Φ_n of the n-th wave so that the associated velocities along the (x, y, z) directions, respectively denoted (u_n, v_n, w_n), and the buoyancy field b_n can be expressed as $u_n = -2ik_{zn}/k_n\Phi_n \exp i(k_{xn}x + k_{zn}z - \omega_n t) + c.c.$, $v_n = if/\omega_n u_n$, $w_n = -k_{xn}/k_{zn}u_n$, and $b_n = -iN^2/\omega_n w_n$, where $c.c.$ indicates the complex conjugate[16]. Formally, the derivation involves a multiscale expansion with the introduction of a slow time scale $T = Frt$, the wave amplitude $\Phi_n(T)$ then being a function of T as in the derivation of the WKB approximation[17]. A second order expansion in Froude number leads to the amplitude equations for the resonant waves (see[18] for more details). When transforming back the slow time scale T in the primitive time t, those equations read[19]:

$$\begin{aligned}
\frac{d\Phi_0}{dt} &= L_0\Phi_2^*\Phi_1^* \\
\frac{d\Phi_1}{dt} &= L_1\Phi_0^*\Phi_2^* \\
\frac{d\Phi_2}{dt} &= L_2\Phi_1^*\Phi_0^*
\end{aligned} \tag{7.4}$$

16. Gill, *op. cit.*
17. Bender and Orszag, *op. cit.*
18. McEwan and Plumb, *op. cit.*
19. F. P. Bretherton, "Resonant interactions between waves. The case of discrete oscillations", in: *J. Fluid Mech.* 20.*3* (1964), pp. 457–479.

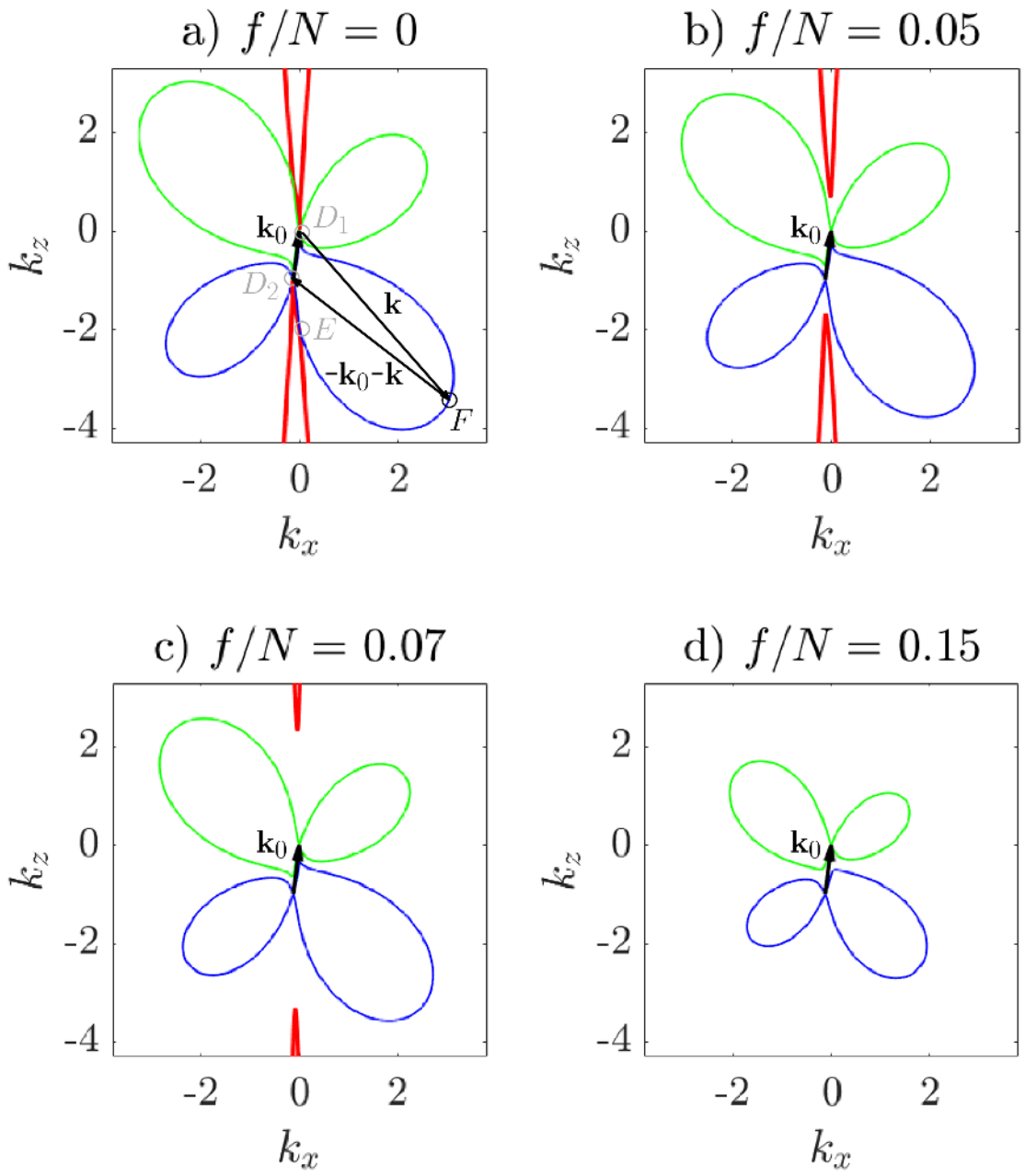

Figure 7.1: Plots of the resonant branches defined by the implicit equation (7.3) in the $\boldsymbol{k} = (k_x, k_z)$ plane for different values of Prandtl ratios f/N for a fixed wave vector $\boldsymbol{k_0} = k_0(\sin\theta_0, \cos\theta_0)$ with $k_0 = 1$ and $\theta_0 = 0.13$, the primary wave angle being taken from simulations in[15], and a fixed frequency sign $s_0 = +1$: $f/N = 0$ in a), $f/N = 0.05$ in b), $f/N = 0.1$ in c), and $f/N = 0.15$ in d). In each figure, the black arrow represents the wave vector $\boldsymbol{k_0}$, the red curves correspond to the wave frequency signs $(s_0, s_1, s_2) = (+,+,+)$ in equation (7.3), the blue curve to $(+,+,-)$, and the green curve to $(+,-,+)$. In figure a), the exemplified triad F is represented with wave vectors $\boldsymbol{k}$ and $-\boldsymbol{k_0} - \boldsymbol{k}$ in black arrows and the tip of vector $\boldsymbol{k}$ is indicated by the circles point F. The tip of vector $\boldsymbol{k}$ for Induced Diffusion triads is indicated by points (D_1, D_2), and, for Elastic Scattering triads, by point E.

where Φ_n^* is the complex conjugate of Φ_n and the interaction coefficients L_n are expressed using the phase velocities $\boldsymbol{c_n} = (c_{xn}, c_{zn}) = (\omega_n/k_{xn}, \omega_n/k_{zn})$:

$$\begin{aligned} L_0 &= \Lambda_x \left(\frac{1}{c_{x2}} - \frac{1}{c_{x1}}\right) + \left(\frac{f}{N}\right)^2 \Lambda_z \left(\frac{1}{c_{z2}} - \frac{1}{c_{z1}}\right) \\ L_1 &= \Lambda_x \left(\frac{1}{c_{x0}} - \frac{1}{c_{x2}}\right) + \left(\frac{f}{N}\right)^2 \Lambda_z \left(\frac{1}{c_{z0}} - \frac{1}{c_{z2}}\right) \\ L_2 &= \Lambda_x \left(\frac{1}{c_{x1}} - \frac{1}{c_{x0}}\right) + \left(\frac{f}{N}\right)^2 \Lambda_z \left(\frac{1}{c_{z1}} - \frac{1}{c_{z0}}\right) \end{aligned} \tag{7.5}$$

with $\Lambda_x = \Delta(k_0 k_1 k_2)^{-1}(c_{x0}^{-1} + c_{x1}^{-1} + c_{x2}^{-1})$ and $\Lambda_z = \Delta(k_0 k_1 k_2)^{-1}(c_{z0}^{-1} + c_{z1}^{-1} + c_{z2}^{-1})$, Δ being twice the oriented area of the triangle ($\boldsymbol{k_0}$, $\boldsymbol{k_1}$, $\boldsymbol{k_2}$), $\Delta = k_{x1}k_{z2} - k_{x2}k_{z1}$. The three interaction coefficients defined here are linked by the relations $\omega_2 L_0 \omega_1 = \omega_0 L_1 \omega_2 = \omega_1 L_2 \omega_0$. Hence, the triadic equations (7.4) are identical to other formulations found in the literature[20] that feature different expressions for the interaction coefficients than those given in (7.5), those expressions depending in fact on the definition of the wave amplitudes chosen by the authors. Our choice of wave amplitudes Φ_n is motivated by the definition of the energy norm, so that the total energy of the n-th wave, sum of the kinetic and potential energy averaged in space, is now equal to $|\Phi_n|^2$.

The plots of the resonant curves on figure 7.1 reveal the existence of triads with one wave of nearly vertical wave vector, whose corresponding frequency approaches f/N, suggesting that triadic resonant instability may involve one nearly inertial wave if f differs from zero, and one nearly zero frequency wave otherwise. In a non-rotating flow, such limiting classes of triads were given names, Elastic Scattering and Induced Diffusion[21], and are located on the resonant branches by points E and (D_1, D_2) respectively on figure 7.1. Those triads contributes to the numerically computed transfer of energy in the Garrett and Munk models of the oceanic internal wave spectrum[22]. From equations (7.5), one of the interaction coefficients, L_1 or L_2, becomes nil when considering those limiting triads, and the corresponding wave, Φ_1 or Φ_2, is time independent. Induced Diffusion triads physically refer to the diffusion of wave action $|\Phi_0|^2/\omega_0$ mainly along the k_z direction in the wave spectrum, towards waves of nearly same wave vector and frequency $(\boldsymbol{k_2}, \omega_2)$, with $\boldsymbol{k_2} \to \boldsymbol{k_0}$ and $\omega_2 \to \omega_0$, mediated by a nearly zero frequency wave $(\boldsymbol{k_1}, \omega_1)$, with $\omega_1 \to 0$[23]. Elastic Scattering triads correspond to an energy transfer between an upward and a downward propagating higher-frequency waves with little change in energy of a third low-frequency wave. The last limiting case tends to equalize the intensities of the upward

20. *Ibid.*
21. McComas and Bretherton, *op. cit.*
22. C. Garrett and W. Munk, "Space-time scales of internal waves: A progress report", in: *J. Geophys. Res.* 80.*3* (1975), pp. 291–297.
23. McComas and Bretherton, *op. cit.*

and downward propagating waves leading to the vertical symmetry of the spectrum[24]. From figure 7.1, as f/N increases, the resonant curves do not cross the singular points (E, D_1, D_2) anymore, so the corresponding singularity vanishes. Increasing rotation then attenuates the two effects associated to Induced Diffusion and Elastic Scattering triads, respectively the diffusion of wave action between waves of nearly same wave vector and frequencies, and the energy transfer between waves of horizontally symmetric wave vector. However, for small values $f/N \ll 1$, the singular points (E, D_1, D_2) are nearly resonant and the two effects described as Induced Diffusion and Elastic Scattering remain relevant.

Those two limiting classes of triads induce the emergence of Vertically Sheared Horizontal Flow modes (VSHF)[25], an ubiquitous feature in non-rotating and weakly rotating stratified turbulence[26], and identified as resonant waves characterized by purely vertical wave vectors. Triadic resonant instability is one of the mechanisms proposed for the generation of such modes[27], which oscillate at the inertial frequency, thus considered as being roughly time independent if $f/N \ll 1$, have kinetic energy only and transfer energy to large scales, as shown in simulations conducted by[28] of homogeneous, forced turbulence in 3D rotating, stably stratified flow in the Boussinesq approximation, in which energy is injected through an isotropic, white-noise forcing localized at small scales. In those simulations, as $f/N \ll 1$, energy piles up in VSHF modes, organized as vertically sheared, horizontal layers, and referred to as pancake structure, suggesting that wave interactions are responsible for the energy transfer to scales larger than the forcing scales.

The triadic equations (7.4) conserve the total energy $\mathcal{E}$, the pseudo-momentum vector $\boldsymbol{\mathcal{P}} = (\mathcal{P}_x, \mathcal{P}_z)$, and the phase invariant $\mathcal{K}$, also known as Hamiltonian[29], respectively defined by:

$$\begin{gathered} \mathcal{E} = \sum_n |\Phi_n|^2, \quad \boldsymbol{\mathcal{P}} = \sum_n |\Phi_n|^2 \left(\frac{1}{c_{xn}}, \frac{1}{c_{zn}} \right), \\ \mathcal{K} = |\Phi_0 \Phi_1 \Phi_2| \sin \varphi \end{gathered} \tag{7.6}$$

where φ is the phase of $\Phi_0\Phi_1\Phi_2$. The conservation of the two first invariants, energy $\mathcal{E}$ and pseudo-momentum $\boldsymbol{\mathcal{P}}$, is identical to the Manley-Rowe relations[30], derived from the triadic equations (7.4), which state that $\omega_0^{-1} d|\Phi_0|^2/dt = \omega_1^{-1} d|\Phi_1|^2/dt = \omega_2^{-1} d|\Phi_2|^2/dt$, leading to the existence of two independent quadratic invariants $C_0 = |\Phi_1|^2/\omega_1 - |\Phi_2|^2/\omega_2$ and $C_1 = |\Phi_2|^2/\omega_2 - |\Phi_0|^2/\omega_0$, the third being the sum of these two invariants $C_2 = -C_0 - C_1$. Two integrals of motion that have a physical interpretation emerge as a linear combination

24. O. M. Phillips, "The interaction trapping of internal gravity waves", in: *J. Fluid Mech.* 34.*2* (1968), pp. 407–416.
25. Waleffe, *op. cit.*
26. Smith and Waleffe, "Transfer of energy to two-dimensional large scales in forced, rotating three-dimensional turbulence".
27. *Idem*, "Generation of slow large scales in forced rotating stratified turbulence".
28. *Ibid.*
29. Whitham, *op. cit.*
30. Manley and Rowe, *op. cit.*

of the C_n, e.g. for any trinome $(\alpha_0, \alpha_1, \alpha_2)$ such that $\alpha_0 + \alpha_1 + \alpha_2 = 0$, $\mathcal{B} = \sum \alpha_n |\Phi_n|^2/\omega_n$ is an integral of motion (demonstration in[31]). In the purely rotating case, $\mathcal{E}$ and $\mathcal{P}_z$, which correspond to the trinomes $(\alpha_0, \alpha_1, \alpha_2)$ equal to $(\omega_0, \omega_1, \omega_2)$ and to (k_{z0}, k_{z1}, k_{z2}) respectively, were chosen as they physically represent the energy and helicity of resonant triads respectively[32], up to a constant factor that does not depend on the selected triad[33]. The current investigation focuses on geophysical fluids, the atmosphere and the ocean, two stratified weakly rotating media such that f/N is small compared to unity. Therefore, we choose $\mathcal{E}$ and $\mathcal{P}_x$, associated to the trinomes $(\omega_0, \omega_1, \omega_2)$ and (k_{x0}, k_{x1}, k_{x2}) respectively, to be the two physically meaningful quadratic invariants, this choice being motivated by the purely stratified case.

7.4 Nonlinear growth of perturbation energy

Without loss of generality, we change the indices $(0, 1, 2)$ of each resonant triad represented on figure 7.1, so that each involves three resonating waves $(\omega_0, \boldsymbol{k_0})$, $(\omega_1, \boldsymbol{k_1})$, $(\omega_2, \boldsymbol{k_2})$ such that:

$$\frac{1}{c_{x0}} < \frac{1}{c_{x1}} < \frac{1}{c_{x2}} \tag{7.7}$$

along with the condition:

$$\frac{1}{c_{x1}} - \frac{1}{c_{x0}} < \frac{1}{c_{x2}} - \frac{1}{c_{x1}} \tag{7.8}$$

so that the quantity defined by:

$$\gamma = \frac{c_{x1}^{-1} - c_{x0}^{-1}}{c_{x2}^{-1} - c_{x0}^{-1}} \tag{7.9}$$

varies between 0 and 1. γ is the colinearity factor such that $\boldsymbol{p_1} - \boldsymbol{p_0} = \gamma \times (\boldsymbol{p_2} - \boldsymbol{p_0})$ with $\boldsymbol{p_n} = (1/c_{xn}, 1/c_{zn})$, implying that $\gamma = (c_{z1}^{-1} - c_{z0}^{-1})/(c_{z2}^{-1} - c_{z0}^{-1})$, or, in terms of wave frequencies $\gamma = -\omega_2/\omega_1$. Along the resonant branches, γ is minimum for the limiting classes of triad, Elastic Scattering and Induced Diffusion, even reaching 0 as f/N becomes nil, Φ_2 being then the VSHF mode as $\omega_2 \to 0$ when ω_1 and ω_0 remain finite and nearly equal.

Each resonant triad corresponds to a set of three triadic invariants (4.85), in which energy can be set to unity $\mathcal{E} = 1$. The plots of those invariants are shown on figure 7.2

31. Ha, Chomaz, and Ortiz, *op. cit.*
32. Bordes et al., *op. cit.*
33. Ha, Chomaz, and Ortiz, *op. cit.*

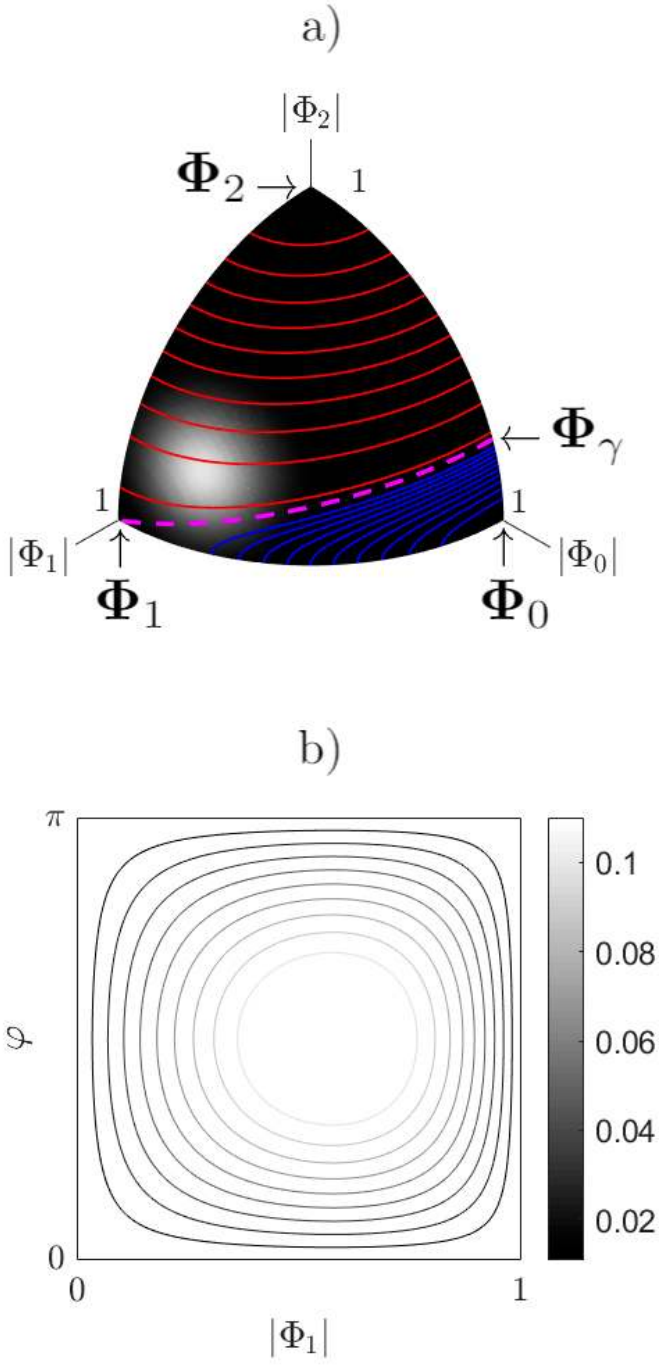

Figure 7.2: a) Plots of the trajectories solving the tradic equations (7.4) for the exemplified triad F indicated on figure 7.1 in a $(|\Phi_0|, |\Phi_1|, |\Phi_2|)$ space, obtained by intersecting the unit energy sphere $\mathcal{E} = 1$ with quadrics of pseudomomentum $\mathcal{P}_x$ varying in different ranges: trajectories corresponding to $1/c_{x0} < \mathcal{P}_x < 1/c_{x1}$ are plotted in blue, and to $1/c_{x1} < \mathcal{P}_x < 1/c_{x2}$ in red. The separatrix distinguishing the two previous regimes is defined by $\mathcal{P}_x = 1/c_{x1}$, and is plotted in dashed lines. The four points $\mathbf{\Phi_0} = (1, 0, 0)$, $\mathbf{\Phi_1} = (0, 1, 0)$, $\mathbf{\Phi_2} = (0, 0, 1)$, and $\mathbf{\Phi}_\gamma = (\sqrt{1-\gamma}, 0, \sqrt{\gamma})$, γ being defined by equation (7.9), are indicated. b) Contour plots of the phase invariant $\mathcal{K}$ in a $(|\Phi_1|, \varphi)$ plane for the separatrix represented on figure 7.2a), for different values of $\mathcal{K}$ indicated on the colorbar.

for the exemplified triad F represented on figure 7.1a). When intersecting the unit energy sphere $\mathcal{E} = 1$ with varying pseudo-momentum ellipsoids $\mathcal{P}_x$ in a $(|\Phi_0|, |\Phi_1|, |\Phi_2|)$ space, two distinct regimes appear on figure 7.2a): trajectories corresponding to $1/c_{x0} < \mathcal{P}_x < 1/c_{x1}$ and to $1/c_{x1} < \mathcal{P}_x < 1/c_{x2}$ are represented in blue and red respectively, and are separated by the separatrix of equation $\mathcal{P}_x = 1/c_{x1}$ in dashed lines. Four points:

$$\begin{gathered} \mathbf{\Phi_0} = (1,0,0), \quad \mathbf{\Phi_1} = (0,1,0), \quad \mathbf{\Phi_2} = (0,0,1), \\ \mathbf{\Phi}_\gamma = (\sqrt{1-\gamma}, 0, \sqrt{\gamma}) \end{gathered} \tag{7.10}$$

are also represented in this $(|\Phi_0|, |\Phi_1|, |\Phi_2|)$ space. With the conventions introduced in (7.7) and (7.8) and the normalization of the energy to unity, every resonant triad leads to a representation in the $(|\Phi_0|, |\Phi_1|, |\Phi_2|)$ space similar to the one represented on the present figure 7.2a), for triad F, in which $\mathbf{\Phi}_\gamma$ is closer to $\mathbf{\Phi_0}$ than to $\mathbf{\Phi_2}$ in the plane $|\Phi_1| = 0$ with respect to the energy norm, i.e. $\|\mathbf{\Phi}_\gamma - \mathbf{\Phi_0}\|_{NL}^2 < \|\mathbf{\Phi}_\gamma - \mathbf{\Phi_2}\|_{NL}^2$ with the energy norm:

$$\|\mathbf{\Phi}\|_{NL}^2 = |\Phi_0|^2 + |\Phi_1|^2 + |\Phi_2|^2 \tag{7.11}$$

for any vector $\mathbf{\Phi} = (\Phi_0, \Phi_1, \Phi_2)$. For the exemplified triad F, $\mathbf{\Phi}_\gamma$ differs greatly from $\mathbf{\Phi_0}$ with respect to the energy norm, but for the limiting classes of triads, Induced Diffusion and Elastic Scattering, $\mathbf{\Phi}_\gamma$ gets infinitely close to $\mathbf{\Phi_0}$, so, in a vicinity $O(f/N)$ of the singular points (D_1, D_2, E) along the resonant branches on figure 7.1:

$$\gamma \to 0, \quad \|\mathbf{\Phi}_\gamma - \mathbf{\Phi_0}\|_{NL}^2 \to 0, \text{ as } \frac{f}{N} \to 0 \tag{7.12}$$

In stratified weakly rotating flows, the limiting classes of triads, Induced Diffusion and Elastic Scattering, are nearly resonant, and $\mathbf{\Phi}_\gamma$ can be developed asymptotically for small values of Prandtl ratios $f/N \ll 1$ near the singular points (D_1, D_2, E):

$$\mathbf{\Phi}_\gamma = \mathbf{\Phi_0} + \frac{\mathbf{\Phi_2}}{\sqrt{\omega_0}}\sqrt{\frac{f}{N}} + o\left(\sqrt{\frac{f}{N}}\right) \tag{7.13}$$

this ultimate asymptotic expansion showing that, for Induced Diffusion and Elastic Scattering triads, an infinitely small perturbation of energy $\gamma \ll 1$ of a single traveling wave $\mathbf{\Phi_0}$ along the $\mathbf{\Phi_2}$ direction in the $(|\Phi_0|, |\Phi_1|, |\Phi_2|)$ space may experience intense nonlinear growth by a factor γ^{-1}, leading to the periodic destruction of the base state $\mathbf{\Phi_0}$ when creating the new state $\mathbf{\Phi_1}$. This small perturbation, symbolized by the vector $\mathbf{\Phi} - \mathbf{\Phi_0}$ in figure 7.2b), departs from its initial value $\mathbf{\Phi}_\gamma - \mathbf{\Phi_0}$, along the direction of the VSHF mode $\mathbf{\Phi_2}$, and reaches $\mathbf{\Phi_1} - \mathbf{\Phi_0}$. Therefore, for all the resonant triads plotted in figure 7.1a), a perturbation of the triadic system from $\mathbf{\Phi_0}$ along $\mathbf{\Phi_2}$ in the $(|\Phi_0|, |\Phi_1|, |\Phi_2|)$ space

exhibits nonlinear growth, measured by an energy gain maximized by Induced Diffusion and Elastic Scattering triads, $\mathbf{\Phi_2}$ then emerging as the VSHF mode in stratified weakly rotating flows. As $f/N \to 0$, this maximum energy gain, obtained at the singular points (D_1, D_2, E) and denoted G, goes to infinity, as $\gamma \to 0$ at those points. This infinite peak is decreased by the introduction of rotation, making it finite as the resonant branches change from figure 7.1a) to 7.1d), the value of this peak being captured by the scalings at (D_1, D_2, E):

$$\gamma \propto \frac{f}{N}, \quad G \propto \left(\frac{f}{N}\right)^{-1}, \text{ as } \frac{f}{N} \to 0 \tag{7.14}$$

those power laws being only relevant if (D_1, D_2, E) are nearly resonant, which is the case when $f/N \ll 1$.

Along the separatrix on the unit energy sphere $\mathcal{E} = 1$, for any resonant triads, the phase invariant reads $\mathcal{K} = |\Phi_1|\sqrt{(1-\gamma)\gamma(1-|\Phi_1|^2)}\sin\varphi$, whose contour plots are displayed in a $(|\Phi_1|, \varphi)$ plane for the exemplified triad F on figure 7.2b). Without loss of generality, we consider values of φ between 0 and π, and all the possible values of $\mathcal{K}$ are indicated in the colorbar from dark to light, as $\mathcal{K}$ goes from 0 to 0.15. If φ is initially nil or equal to π, $|\Phi_1|$ varies continuously between 0 and 1 as indicated by the darkest contour associated to $\mathcal{K} = 0$, and the wave amplitudes (Φ_0, Φ_1, Φ_2) remain real at all time as φ jumps from 0 to π periodically, meaning that $\Phi_0\Phi_1\Phi_2$ oscillates with equal duration spent in the positive and negative values during one period. In this case, the triadic equations (7.4) are identical to the Euler equations describing the dynamics of a rotating rigid body[34], the two integrals of motion, the energy and the pseudo-momentum of the fluid (4.85), being then replaced by the energy and the angular momentum of the solid[35], two positive definite forms (the components of the pseudo-momentum $(\mathcal{P}_x, \mathcal{P}_z)$ are not necesarily positive definite, but the two systems, stratified weakly rotating fluid and rotating solid, still exhibit the same dynamics). If φ initially differs from 0 and π, $|\Phi_1|$ and φ vary continuously between 0 and 1, and 0 and π respectively, without reaching those bounds, so the states represented by points $\mathbf{\Phi}_\gamma$ and $\mathbf{\Phi_1}$ act as repellers. In all the cases above, for a fixed initial value of φ, $|\Phi_1|$ oscillates between 0 and 1, and relaxation oscillations may occur as, for any blue or red trajectories getting close to the separatrix with respect to the energy norm, $|\Phi_1|$ oscillates with a quick passage near 0 and a long duration near 1, this duration being infinite for any given trajectory infinitely close to the separatrix. Starting from $\mathbf{\Phi_0}$, a small perturbation of energy γ along the $\mathbf{\Phi_2}$ direction experiences relaxation oscillations, characterized by an energy gain γ^{-1} that measures the nonlinear growth of the perturbation energy. This periodic evolution is universal to all resonant triads in the range of values of f/N explored here, the corresponding energy gain being maximized for Elastic Scattering and Induced

34. Euler, *op. cit.*
35. Lynch, *op. cit.*

Diffusion triads when $f/N \to 0$ as indicated by the scalings (7.14).

7.5 Transient growth of perturbation energy

The nonlinear dynamics of the triadic system (7.4), fully captured by the separatrix, shapes the response of a propagating internal wave, $\mathbf{\Phi_0}$ or $\mathbf{\Phi_1}$, called primary wave, submitted to an infinitesimal perturbation of energy along the $\mathbf{\Phi_2}$ direction. On the unit energy sphere plotted on figure 7.2a), such perturbation energy results in a linear resonant response, captured by the blue ellipsoids infinitely close to $\mathbf{\Phi_0}$ or the red hyperboloids infinitely close to $\mathbf{\Phi_1}$, derived respectively by linearizing the triadic system (7.4) when setting $d\Phi_0/dt = 0$ or $d\Phi_1/dt = 0$, so that:

$$\frac{d\mathbf{\Phi'}}{d\tau} = \mathscr{L}\mathbf{\Phi'}^* \tag{7.15}$$

with the evolution operator:

$$\mathscr{L} = \begin{pmatrix} 0 & 1 \\ \varepsilon & 0 \end{pmatrix} \tag{7.16}$$

where $\mathbf{\Phi'} = (\Phi_1, \Phi_2)$, $\tau = L_1 t$, $\varepsilon = -|\omega_2/\omega_1| = -\gamma$ when setting $\Phi_0 = 1$ without loss of generality, and $\mathbf{\Phi'} = (\Phi_0, \Phi_2)$, $\tau = L_0 t$, $\varepsilon = |\omega_2/\omega_0|$ when setting $\Phi_1 = 1$. The linearized triadic system (7.15) is either linearly stable if $\Phi_0 = 1$, resulting in bounded periodic oscillations of the perturbation $\mathbf{\Phi'}$, captured by the blue ellipsoids infinitely close to $\mathbf{\Phi_0}$ on figure 7.2a) and specific to any resonant triad along the blue or green branches on figures 7.1, or linearly unstable if $\Phi_1 = 1$, implying the exponential growth of $\mathbf{\Phi'}$ illustrated by the red hyperboloids infinitely close to $\mathbf{\Phi_1}$ and specific to any resonant triad along the red branches. The energy norm is now set to be the 2D Euclidean norm $\|\mathbf{\Phi'}\|^2$, equal to $|\Phi_1|^2 + |\Phi_2|^2$ for the blue and green resonant branches, and to $|\Phi_0|^2 + |\Phi_2|^2$ for the red resonant branches. With respect to this energy norm, $\mathscr{L}$ is normal if $\mathscr{L}\mathscr{L}^{\mathrm{H}} = \mathscr{L}^{\mathrm{H}}\mathscr{L}$, $\mathscr{L}^{\mathrm{H}}$ being the transconjugate of the evolution operator $\mathscr{L}$, which is equivalent to $\varepsilon^2 = 1$. For all the resonant triads on figure 7.1, $\varepsilon^2 \neq 1$, so $\mathscr{L}$ is always non-normal. This non-normality intensifies for resonant triads verifying $\varepsilon \ll 1$, and implies that an infinitely small perturbation of energy $\|\mathbf{\Phi'}\|^2 \ll \varepsilon$ experiences intense transient growth characterized by an energy gain equal to ε^{-1}. Those transients are maximum for Elastic Scattering and Induced Diffusion triads, ε being minimum for those two singular triads and scaling as f/N for resonant triads in a vicinity $O(f/N)$ of those two limiting classes of triads on figure 7.1. For those triadic interactions, the evolution operator $\mathscr{L}$ become singular when $f/N = 0$, so the resulting energy gain of the perturbation is infinite, even for linearly stable triads whose amplitude oscillations $\|\mathbf{\Phi'}\|^2$ now diverge.

7.6 Conclusion and discussion

Including the effect of internal waves in numerical climate models is key to accurately predict the evolution of the climate system, as the atmosphere and the ocean are substantially sensitive to the mixing resulting from internal waves activity. Internal wave-driven mixing occurs inside the atmosphere and the ocean, redistributing heat, salt, nutrients, carbon, greenhouse gases, and may result from wave interactions such as the triadic resonant instability which involves three resonating internal waves.

A single internal wave propagating in a stratified weakly rotating medium, when submitted to small perturbations, may resonate with two other internal waves through triadic resonant instability. The induced resonant triads may sustain substantial growth of perturbation energy, that is either nonlinear for small but finite perturbations, or leading to transient growth for infinitesimally small perturbation energy. In both cases, the energy gain is maximized for two types of resonant interactions, Induced Diffusion and Elastic Scattering, that correspond respectively to the diffusion of wave action to waves of nearly same wave vectors, and to the transfer of energy to waves of horizontally symmetric wave vector.

The intensification of such processes occur in the singular case when rotation effects vanishes, and is captured by the scalings of the energy gain as the inverse of the Coriolis parameter for Induced Diffusion and Elastic Scattering triads. In the purely stratified case, those limiting classes of triads involve one zero frequency wave, a time independent mode called Vertically Sheared Horizontal Flow (VSHF) which acts as a catalyst in the process of Induced Diffusion or Elastic Scattering. In stratified weakly rotating flows, the VSHF mode oscillates at the inertial frequency and its catalytic role in the two previous processes may be attenuated when the Coriolis parameter is increased.

Chapter 8

Direct numerical simulations using the MITgcm

8.1 MIT General Circulation Model (MITgcm)

The MIT General Circulation Model (MITgcm) is a numerical computer code that solves the equations of motion governing the ocean or Earth's atmosphere using the finite volume method (Marshall et al., 1997)[1]. Released back in 1997, it was one of the first non-hydrostatic models of the ocean. The MITgcm has been designed and used to model a wide range of phenomena, from convection on the scale of meters in the ocean to the global pattern of atmospheric winds as illustrated in figure 8.1.

Main characteristics of the MITgcm

- **a single hydrodynamical kernel**, implying the ability to model phenomena occurring either in the atmosphere or in the ocean,
- **the non-hydrostatic capability**, resulting in the possibility to solve multiple scales e.g. both small scale and large scale processes,
- **the finite volume techniques**, essential to capture the main features of irregular geometries.

We choose the MITgcm to run simulations and study the dynamical behavior of internal waves in the deep ocean. The MITgcm uses a finite volume method for spatial discretization and the Adams-Bashforth method[2] for explicit time-stepping in order to solve numerically the nonlinear non-hydrostatic dynamical equations in the Boussinesq approximation:

1. J. Marshall et al., "A finite-volume, incompressible Navier Stokes model for studies of the ocean on parallel computers", in: *J. Geophys. Res.: Oceans* 102.*C3* (1997), pp. 5753–5766.
2. See MITgcm user manual for further details.

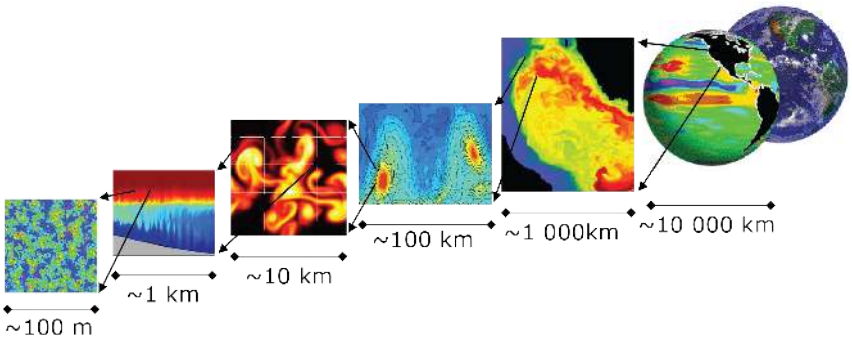

Figure 8.1: The MITgcm has non-hydrostatic capabilities, allowing the model to address a wide range of phenomena - from convection on the left, all the way through to global circulation patterns on the right. Source: MITgcm user manual.

$$\partial_x u + \partial_y v + \partial_z w = 0 \qquad \text{(incompressibility)} \tag{8.1}$$

$$D_t b + N^2 w - Pr^{-1}(\nu_h \partial_h^2 + \nu_z \partial_z^2) b = 0 \qquad \text{(continuity)} \tag{8.2}$$

$$D_t u - fv + \partial_x P - (\nu_h \partial_h^2 + \nu_z \partial_z^2) u = F_u \qquad (x\text{-momentum}) \tag{8.3}$$

$$D_t v - fu + \partial_y P - (\nu_h \partial_h^2 + \nu_z \partial_z^2) v = F_v \qquad (y\text{-momentum}) \tag{8.4}$$

$$D_t w - b + \partial_z P - (\nu_h \partial_h^2 + \nu_z \partial_z^2) w = F_w \qquad (z\text{-momentum}) \tag{8.5}$$

$$b = b(\vartheta, S, z) \qquad \text{(equation of state)} \tag{8.6}$$

$$D_t \vartheta - (\kappa_{h\vartheta} \partial_h^2 + \kappa_{z\vartheta} \partial_z^2) \vartheta = Q_\vartheta \qquad \text{(potential temperature)} \tag{8.7}$$

$$D_t S - (\kappa_{hS} \partial_h^2 + \kappa_{zS} \partial_z^2) S = Q_S \qquad \text{(salinity)} \tag{8.8}$$

with the same notations introduced in part 4.1[3], and where $\partial_h^2 = \partial_x^2 + \partial_y^2$ is the horizontal laplacian, (ν_h, ν_z) are horizontal and vertical viscosities, (F_u, F_v, F_w) are the forcing terms of the Navier-Stokes equation, and (Q_ϑ, Q_S) are the forcing terms of the heat and salinity equations in which ϑ stands for the potential temperature and S for salinity, $(\kappa_{h\vartheta}, \kappa_{z\vartheta})$ and $(\kappa_{hS}, \kappa_{zS})$ being the associated horizontal and vertical diffusivities. In all our simulations, buoyancy and stratification are due to vertical variations of potential temperature with $\kappa_{h\vartheta} = \kappa_{z\vartheta} = \kappa$ and $\nu_h = \nu_z = \nu$ so that $Pr = \nu/\kappa$. We also assume constant salinity and $\kappa_{hS} = \kappa_{zS} = 0$, and a linear equation of state (EOS) $b = b_r(1 - \alpha(\vartheta - \vartheta_r))$ where ϑ_r is the reference temperature defined by $b(\vartheta_r) = b_r$ and α the thermal expansion coefficient. Similar effects are expected if we implement salinity in a similar fashion than temperature.

3. ϑ being the potential temperature field.

8.1.1 Overcoming the hydrostatic approximation

The MITgcm overcomes the hydrostatic approximation introduced in part 4.1.2 with equation (4.52). Further details concerning this approximation are given here to understand how meaningful this approximation is for simulation purposes. Recall that the perturbed normalized pressure field and buoyancy are related through the vertical projection of the Navier-Stokes equation, which is, in the inviscid case:

$$D_t w = -P_{,z} + b \tag{8.9}$$

hence, the hydrostatic approximation consists in neglecting the vertical acceleration compared to the buoyancy:

$$D_t w \ll b \quad \Rightarrow \quad P_{,z} = b \tag{8.10}$$

w being directly deduced from the incompressibility condition.

As a measure of the velocity field amplitudes, the Froude number Fr, when being small $Fr \ll 1$, implies $D_t w \sim w_{,t} \sim \omega w$ and $\omega b \sim N^2 w$ resulting from the linearized Navier-Stokes and mass conservation equations, ω being the frequency of the considered wave. In this case, all the results developed in part 4.1.2 concerning the hydrostatic approximation in the linear theory apply. Therefore, the validity of the approximation is equivalent to $\omega \ll N$, which correspond to the case of small aspect ratios $r \ll 1$ i.e. horizontal wavenumbers dominate vertical ones. For highly nonlinear internal waves, the convective terms dominate so that the hydrostatic approximation is equivalent to $Uk_x/N \ll 1$, U and k_x being the typical amplitude of the horizontal velocity and the horizontal wavenumber respectively. When advection can't be neglected, the hydrostatic approximation is valid for flows that are either slow, or large scale, or strongly stratified.

Back in the nineties, most models were based on the hydrostatic primitive equations (HPE) in which the vertical momentum equation is reduced to a statement of hydrostatic balance. According to Marshall et al. (1997), the numerical codes needed to overcome the hydrostatic approximation when they started to numerically solve scales from 1 to 10 km, which correspond to small scale geostrophic eddies, convective phenomena or internal waves of weak wavelength radiated near rough bottom topographies.

8.1.2 Choice of parameters according to numerical stability criteria

In computational fluid dynamyics (CFD), numerical stability criteria are conditions for the stability of unstable numerical methods which ensure the convergence of the code while solving partial differential equations. Those criteria arise in the numerical analysis of explicit time integration schemes and must be fulfilled in order for the code to produce

correct results. The main purpose of those criteria is summarized by the idea that the full numerical domain of dependence must contain the physical domain of dependence, as described in the book *Computational Gasdynamics* of Culbert B. Laney[4]. To illustrate this idea, we use the following convection equation for the quantity u:

$$u_{,t} + a u_{,x} = 0 \tag{8.11}$$

with $a > 0$ the velocity magnitude. Applying a numerical discretization of this partial differential equation based on a first order explicit upwind scheme, we obtain:

$$\frac{u_i^{n+1} - u_i^n}{dt} + a\frac{u_i^n - u_{i-1}^n}{dx} = 0 \tag{8.12}$$

where dt is the timestep and dx is the length between mesh elements.

$$u_i^{n+1} = u_i^n - a\frac{dt}{dx}(u_i^n - u_{i-1}^n) = 0 \tag{8.13}$$

so replacing by the function $u(x,t)$ gives:

$$u(x, t+dt) = v(x,t) - a\frac{dt}{dx}\left(u(x,t) - u(x-dx,t)\right) \tag{8.14}$$

Now, performing a Taylor series expansion on this scheme at a fixed dt/dx:

$$\left(u_{,t} + \frac{1}{2}(dt)u_{,tt} + \cdots\right) + a\left(u_{,x} - \frac{1}{2}(dx)u_{,xx} + \cdots\right) = 0 \tag{8.15}$$

at the first order $\mathcal{O}(dt)$, so:

$$u_{,t} + a u_{,x} = \frac{1}{2}\left(a(dx)u_{,xx} - (dt)u_{,tt}\right) \tag{8.16}$$

which can be derived with respect to time:

$$u_{,tt} = -a u_{,xt} + \frac{1}{2}\left(a(dx)u_{xxt} - (dt)u_{,ttt}\right) \tag{8.17}$$

and with respect to space:

$$u_{,tx} = -a u_{xx} + \frac{1}{2}\left(a(dx)u_{,xxx} - (dt)u_{,ttx}\right) \tag{8.18}$$

Combining the last two equations at the first order $\mathcal{O}(dt)$ results in:

$$u_{,tt} = a^2 u_{,xx} + \mathcal{O}(dt) \tag{8.19}$$

4. C. B. Laney, *Computational Gasdynamics*, Cambridge University Press, June 1998.

and when replaced in (8.16):

$$u_{,t} + au_{,x} = \frac{1}{2}\left(a(dx)u_{,xx} - a^2(dt)u_{,xx}\right) + \mathcal{O}(dt^2) \tag{8.20}$$

which is simplified as the following advection-diffusion equation:

$$u_{,t} + au_{,x} = \frac{1}{2}adx(1-C)u_{,xx} \tag{8.21}$$

with the Courant number $C = adt/dx$, a being in fact the maximum speed of the considered physical phenomenon and dx/dt the maximum speed of information allowed by the spatio-temporal scheme. The diffusion coefficient on the right hand side must be positive for non-diverging solutions. Hence the numerical stability is ensured if $C \leq 1$ which is the stability limit of the upwind method. Each scheme and phenomenon leads to different definitions of the Courant number C and stability criteria $C \leq C_{\max}$ with different upper limits $C_{\max}$ as reviewed in table 8.1.2. This condition is referred to as the Advective Courant-Freidrichs-Lewy (CFL) condition[5]. In the case of the MITgcm, a list of those criteria from the MITgcm user manual is reminded in the following table when taking into account all the relevant phenomena of our simulations. CFL are only necessary conditions, but their use usually allows a first empirical choice of resolution (for example, when doubling the spatial resolution, one should divide the time-step by two).

Table 8.1: Numerical stability parameter and corresponding numerical stability criteria from the MITgcm user manual.

Paramater	Expression	Upper limit
Advective Courant-Freidrichs-Lewy (CFL)	$S_{CFL} = \frac{\lvert u\rvert dt}{dx}$	0.5
Propagating internal waves	$S_{IW} = \frac{\lVert \boldsymbol{c_g}\rVert dt}{dx}$	0.25
Horizontal Laplacian friction	$S_h = 4\frac{A_h dt}{(dx)^2}$	0.3
Vertical Laplacian friction	$S_v = 4\frac{A_v dt}{(dz)^2}$	0.3
Inertial Oscillations	$S_{IO} = (fdt)^2$	0.5

5. R. Courant, K. Friedrichs, and H. Lewy, "On the Partial Difference Equations of Mathematical Physics", in: *IBM J. Res. and Dev.* 11.*2* (Mar. 1967), pp. 215–234.

8.2 Modeling internal waves with the MITgcm

8.2.1 Physical and numerical parameters

We consider a simulation domain bounded in the vertical direction z, horizontally periodic in the x direction and consisting of a single tile in the y direction. Here is a quick overview of the different parameters used in our simulations separated into two categories[6]:

Physical parameters

- Buoyancy frequency $N = 10^{-3}\,\mathrm{s}^{-1}$
- Coriolis parameter $f = 0$
- Thermal expansion coefficient $\alpha = 2 \times 10^{-4}\,\mathrm{kg\,m^{-3}\,K^{-1}}$
- Haline contraction coefficient $\beta = 0$
- Depth $H = 3.5\,\mathrm{km}$

Numerical parameters

- Horizontal length $L = 23.6\,\mathrm{km}$ (periodic)
- Resolution $dx = dy = 29.5\,\mathrm{m}$ and $dz = 10.3\,\mathrm{m}$
- Time step $dt = 15\,\mathrm{s}$
- Viscosity $\nu = 0$
- Diffusivity $\kappa = 0$
- Horizontal grid points $n_x = 800$, $n_y = 1$ ($n_x = L/dx$)
- Vertical grid points $n_z = 350$ ($n_z = H/dz$)

where the thermal expansion and haline contractions are parametrized by $N^2 = g(\alpha\partial_z\vartheta + \beta\partial_z S)$ as a result of the linear equation of state[7]. Figure 8.2 illustrates the current simulation box, in which our goal is to initialize all the fields, horizontal velocities (u, v) and potential temperature ϑ, in the MITgcm so that the domain contains an internal wave of wave vector $\boldsymbol{k_0} = (k_{x0}, k_{z0})$, of amplitude Ψ_0, and characterized by a vertically confined profile.

6. Our choice of numerical parameters are guided by the convergence tests detailed the next section 8.3.1 and some of those parameters such as n_x may be varied depending on the run.

7. See MITgcm user manual for further details.

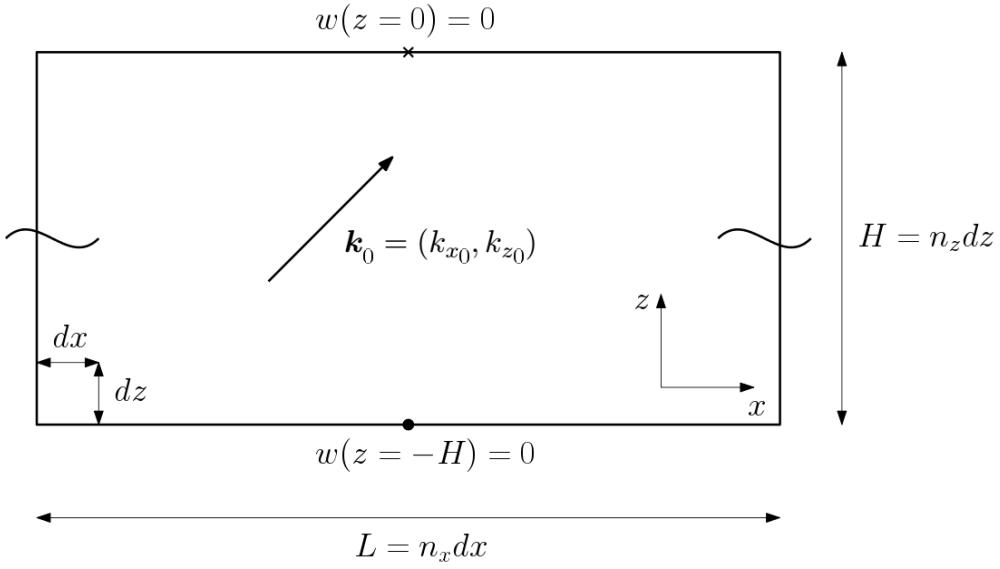

Figure 8.2: Illustration of the 2D simulation box of Cartesian coordinates (x, z) used in the MITgcm to model the properties of an internal wave of wave vector $\boldsymbol{k_0} = (k_{x0}, k_{z0})$. The boundary conditions are such that the box is periodic along the x direction, but confined in the z direction. Each tile measures dx horizontally and dz vertically so that the simulation box measures $L = n_x dx$ and $L = n_z dz$, (n_x, n_z) being the number of tiles along the (x, z) directions.

8.2.2 Theory on vertically confined internal waves

The linear wave equation given by (4.23) is recalled here:

$$\nabla^2\psi_{,tt} + N^2\psi_{,xx} + f^2\psi_{,zz} = 0 \tag{8.22}$$

with the boundary conditions at the surface and bottom of the domain $w(z = 0) = w(z = -H) = 0$ as presented in figure 8.2. As $w = -\psi_{,x}$, the boundary conditions can be written in terms of streamfunction ψ:

$$\psi_{,x}(z = 0) = \psi_{,x}(z = -H) = 0 \tag{8.23}$$

Looking for wavelike solutions in real form $\psi = F(z)\cos(k_x x - \omega t)$, then F must verify:

$$F_{,zz} + k_z^2 F = 0 \tag{8.24}$$

with the real vertical wave number k_z, knowing that $f \leq \omega \leq N$:

$$k_z = \pm k_x \sqrt{\frac{N^2 - \omega^2}{\omega^2 - f^2}} \tag{8.25}$$

solving for F, we get $F(z) = A\cos(k_z z) + B\sin(k_z z)$ where (A, B) are integration constants. The boundary conditions $F(z = 0) = F(z = -H) = 0$ give $A = 0$ and

$\sin(k_z H) = 0$ meaning that:

$$k_{zn} = \frac{n_{kzn}\pi}{H} \tag{8.26}$$

where n_{kzn} is an integer. Hence, the streamfunction is given by:

$$\psi = \sum_n \Psi_n \sin(k_{zn} z) \cos(k_{xn} x - \omega_n t) \tag{8.27}$$

where $k_{xn} = r_n k_{zn}$, r_n being the aspect ratio of the wave:

$$r_n = \pm\sqrt{\frac{\omega_n^2 - f^2}{N^2 - \omega_n^2}} \tag{8.28}$$

$$\omega_n^2 = \left(N\frac{k_{xn}}{k_n}\right)^2 + \left(f\frac{k_{zn}}{k_n}\right)^2 \tag{8.29}$$

$$k_n = \sqrt{k_{xn}^2 + k_{zn}^2} \tag{8.30}$$

In our numerical simulations, the domain is periodic in the x direction of extension L so we also get the following condition with n_{kxn} an integer:

$$k_{xn} = \frac{2n_{kxn}\pi}{L} \tag{8.31}$$

The two former conditions (8.26) and (8.31) must be implemented when initializing the MITgcm. To summarize, the domain of calculation satisfies:

$$\begin{aligned} L &= n_x dx = n_{kxn}\left(\frac{2\pi}{k_{xn}}\right) \\ H &= n_z dz = n_{kzn}\left(\frac{\pi}{k_{zn}}\right) \end{aligned} \tag{8.32}$$

where (n_x, n_z) are integers and H is fixed in our simulations to a physical value representing the typical depth of the ocean. L however can be changed, as the 2D medium can be considered infinite in the x direction.

8.3 Direct numerical simulations

8.3.1 Numerical convergence tests

In the numerical configuration of interest represented on figure 8.2, the vertical boundaries of the ocean and the periodicity along the x direction impose wavelike solutions of the form $\psi(x,z,t) = \Psi_0 \sin(k_{z0} z)\cos(k_{x0} x - \omega_0 t)$, characterized by a stationary component along z and a propagative one along x, and whose wave vector $\boldsymbol{k_0} = (k_{x0}, k_{z0})$ and fre-

quency ω_0 are taken from the simulations of Richet (2018)[8]. Such a solution is initialized in the MITgcm by setting specific initial conditions so that the horizontal velocity field (u, v) and the potential temperature ϑ initially obey to[9]:

$$u(x, z, t = 0) = k_{z0}\Psi_0 \cos(k_{z0}z)\cos(k_{x0}x) \tag{8.33}$$

$$v(x, z, t = 0) = 0 \tag{8.34}$$

$$\vartheta(x, z, t = 0) = -\frac{N^2}{\alpha g}\frac{k_{x0}}{\omega_0}\Psi_0 \sin(k_{z0}z)\cos(k_{x0}x) \tag{8.35}$$

When fixing the physical parameters of the domain to reproduce the properties of the ocean, the variations of numerical parameters may influence the convergence of the code. To guide our choice of numerical parameters which best describes the geophysical system of interest, we run six simulations consisting of a single internal gravity wave in our simulation box during a duration of 10 simulation days, by fixing the physical parameters when varying the numerical parameters to see how they affect the Advective Courant-Freidrichs-Lewy (CFL) condition, measured by the quantity S_{CFL}, and the relative error between the results of the simulation and the predictions from the theory, especially for the wave period $\Delta\tau/\tau_{\text{th}}$ and its total energy $\Delta\mathcal{E}/\mathcal{E}_{\text{th}}$. The results of those convergence tests are all collected in table 8.2 and interpreted in the present section.

The relative error in the wave period is determined when interpreting the output file of the MITgcm, and more specifically when plotting (u, v, w, ϑ) as a function of time t at a fixed location in the simulation box. In all six simulations, we observe periodic sine oscillations so that we can measure the numerical period by taking a peak to peak duration and dividing it by the number of peaks during this duration. For the relative error in energy, we plot the wave total energy, spatially averaged over the simulation box and deduced from (u, v, w, ϑ) using the formula $\mathcal{E} = \langle (u^2 + v^2 + w^2)/2 + (\alpha g\vartheta/N)^2/2\rangle_{\boldsymbol{r}}$, as a function of time t. The plots of the total energy exhibit regular oscillations (instead of being completely constant as predicted by the theory) with a mean value matching the total energy predicted by the linear theory. Thus, the error in energy consists in the relative distance between the maximum value of those oscillations and the theoretical energy. Finally, the numerical stability parameter S_{CFL} is determined by measuring the maximum velocity reached by our simulations U_m so that $S_{CFL} = U_m dt/dx$ for a set of numerical parameters dt and dx intrinsic to each simulation. Having a reasonable running time in our simulations when getting a good agreement between theory and simulation is our priority, and this calls for a good compromise between increasing the space and time

8. O. Richet, J.-M. Chomaz, and C. Muller, "Internal Tide Dissipation at Topography: Triadic Resonant Instability Equatorward and Evanescent Waves Poleward of the Critical Latitude", in: *J. Geophys. Res.* 123.*9* (2018), pp. 6136–6155.

9. Those relations are obtained using the polarization relations.

resolutions and decreasing the computational cost.

All six simulations exhibit a CFL number well below the upper limit indicated in the MITgcm user manual $S_{CFL} \ll 0.5$, meaning that the numerical stability criteria is respected, despite some small variations between each simulation that won't be commented. The dz and $\Delta\mathcal{E}/\mathcal{E}_{\text{th}}$ lines in table 8.2 reveals that increasing the vertical resolution of the domain reduces the relative error in energy: for instance, doubling n_z divides this error by 9 when looking at runs 2 and 3 in comparison with the other runs; except for run 6, which shows that quadrupling the value of n_z from runs 2-3 even leads to smaller errors. The error in energy is unaffected by the horizontal resolution as seen when comparing run 1 and 4, where only n_x and dx are changed. When comparing run 2 and 3, we deduce that the time resolutions doesn't affect the relative error in energy. On the other hand, the relative error of the wave period is attenuated when increasing the horizontal resolution and decreasing the time step. The influence of the time step on the error is shown when looking at run 2 which has a time step equal to 30 when other runs have 15. The energy error of run 2 is relatively high compared to the other runs, the other concerned parameter being the horizontal resolution. Indeed, from run 4 to run 1 up to run 5, the horizontal resolution is doubled each run, all the other parameters being fixed, leading to a decreasing relative error on the wave period which goes from 0.66 to 0.38, down to 0.27.

Results of the convergence tests

The relative errors between the simulation and the theory are affected by the variations of numerical parameters such that, in our simulation domain:

- the relative error on the internal wave period is decreased when increasing the horizontal and time resolutions (x, t),
- the relative error on the internal wave energy when increasing the vertical resolution z.

For those reasons, the set of numerical parameters used as a starting point for our upcoming simulations where three vertically confined internal waves are initialized to observe the nonlinear and transient properties of triadic resonance, is $(n_x, n_y, n_z) = (800, 1, 350)$, $dx = dy = 29.5$ m, $dz = 10.3$ m, and $dt = 15$ s. This choice of parameters, also exposed earlier in section 8.2.1, offers a good compromise between minimizing the relative errors and the duration of each run. Only n_x can be changed as the box is horizontally periodic, eventually modifying the primary wave angle θ_0, so that the three resonating waves belong to the same grid characterized by the 6 integers (n_{kxn}, n_{kzn}) from the conditions given in equations (8.32).

Table 8.2: Convergence tests of the simulation box described in 8.2 on the MITgcm. The relative error between the the simulation and the predictions from the theory are denoted $\Delta\tau/\tau_{\text{th}}$ for the wave period and $\Delta\mathcal{E}/\mathcal{E}_{\text{th}}$ for its total energy.

Physical parameters						
H [km]	3.5938					
k_{x0} [m^{-1}]	8×10^{-4}					
θ_0 [rad]	0.13					
N [s^{-1}]	1×10^{-3}					
f [$\text{rad}\,\text{s}^{-1}$]	0					
α [$\text{kg}\,\text{m}^{-3}\,\text{K}^{-1}$]	2×10^{-4}					
β [PSU^{-1}]	0					
Ψ_0 [$\text{m}^2\,\text{s}^{-1}$]	3.241					
Non-dimensional quantities						
Fr	3.11×10^{-3}					
Numerical parameters						
Run	1	2	3	4	5	6
L [km]	23.562	23.562	23.562	23.562	23.562	23.562
dx [m]	29.452	58.905	29.452	58.905	14.726	29.452
n_x	800	400	800	400	1600	800
dz [m]	10.2681	20.5362	20.5362	10.2681	10.2681	5.13405
n_z	350	175	175	350	350	700
n_{kx_0}	3	3	3	3	3	3
n_{kz_0}	7	7	7	7	7	7
dt [s]	15	30	15	15	15	15
Results						
S_{CFL}	0.01	0.01	0.01	0.005	0.02	0.01
$\Delta\tau/\tau_{\text{th}}$ [%]	0.38	0.59	0.42	0.66	0.27	0.6
$\Delta\mathcal{E}/\mathcal{E}_{\text{th}}$ [%]	0.12	0.92	0.92	0.12	0.1	0.02

8.3.2 Simulation with three resonating waves

The numerical implementation of a chosen resonant triad from the resonance locus on figure 4.5 requires the resonance condition to be achieved by the three internal waves (4.76)-(4.77) when obeying to the boundary conditions of the simulation domain resulting in equations (8.32). This leads to three resonating internal waves $(\boldsymbol{k_0}, \omega_0)$, $(\boldsymbol{k_1}, \omega_1)$, and $(\boldsymbol{k_2}, \omega_2)$, such that, for $n = 0, 1, 2$, $k_{xn} = n_{kxn}(2\pi/L)$, $k_{zn} = n_{kzn}(\pi/H)$, (n_{kxn}, n_{kzn}) being integers obeying to:

$$\begin{aligned} n_{kx0} + n_{kx1} + n_{kx2} &= 0 \\ n_{kz0} + n_{kz1} + n_{kz2} &= 0 \end{aligned} \tag{8.36}$$

so the selected triad belongs to the resonance locus and the corresponding wave vectors $(\boldsymbol{k_0}, \boldsymbol{k_1}, \boldsymbol{k_2})$ are located on the same mesh grid defined in the wave vector space (k_x, k_z), one tile being of size $(\Delta k_x, \Delta k_z) = (2\pi/L, \pi/H)$. As shown in figure 8.3, we select a triad indicated by point F along the resonance locus of internal gravity waves ($N \neq 0$ and $f = 0$), located nearby the Elastic Scattering singularity, in order to observe the transient dynamics derived theoretically in chapter 6. This leads to the following choice of integers:

$$\begin{aligned} (n_{kx0}, n_{kz0}) &= (3, 7) \\ (n_{kx1}, n_{kz1}) &= (-4, 8) \\ (n_{kx2}, n_{kz2}) &= (1, -15) \end{aligned} \tag{8.37}$$

corresponding to a wave angle $\theta_0 = 0.2$, adjusted so that the selected resonant triad belongs to the same mesh grid in the wave vector space[10].

Our goal here is to observe numerically the transient dynamics when a single wave is perturbed by a small energy. Such a process was derived theoretically with respect to a well-defined energy norm, and represented multiple times in this manuscript along the unit energy sphere in a $(|\Phi_0|, |\Phi_1|, |\Phi_2|)$ space, as seen on figures 5.4, 6.13, and 7.2. The code being dimensional, the energy won't be unity, and, knowing that $\Phi_n = k_n \Psi_n/2$, the dynamical fields on the MITgcm (u, v, ϑ) are then initialized by:

$$u(x, z, t = 0) = u_{i0}(x, z) + u_{i2}(x, z) \tag{8.38}$$

$$v(x, z, t = 0) = 0 \tag{8.39}$$

$$\vartheta(x, z, t = 0) = \vartheta_{i0}(x, z) + \vartheta_{i2}(x, z) \tag{8.40}$$

10. This is achieved by changing L through n_x as the simulation box is horizontally periodic. Although we loose precision on the time period of the simulated waves in the process of varying n_x, the convergence of the code remains fine enough to observe good agreement between nonlinear theory and simulations in terms of wave energy as a function of time as we will see later on.

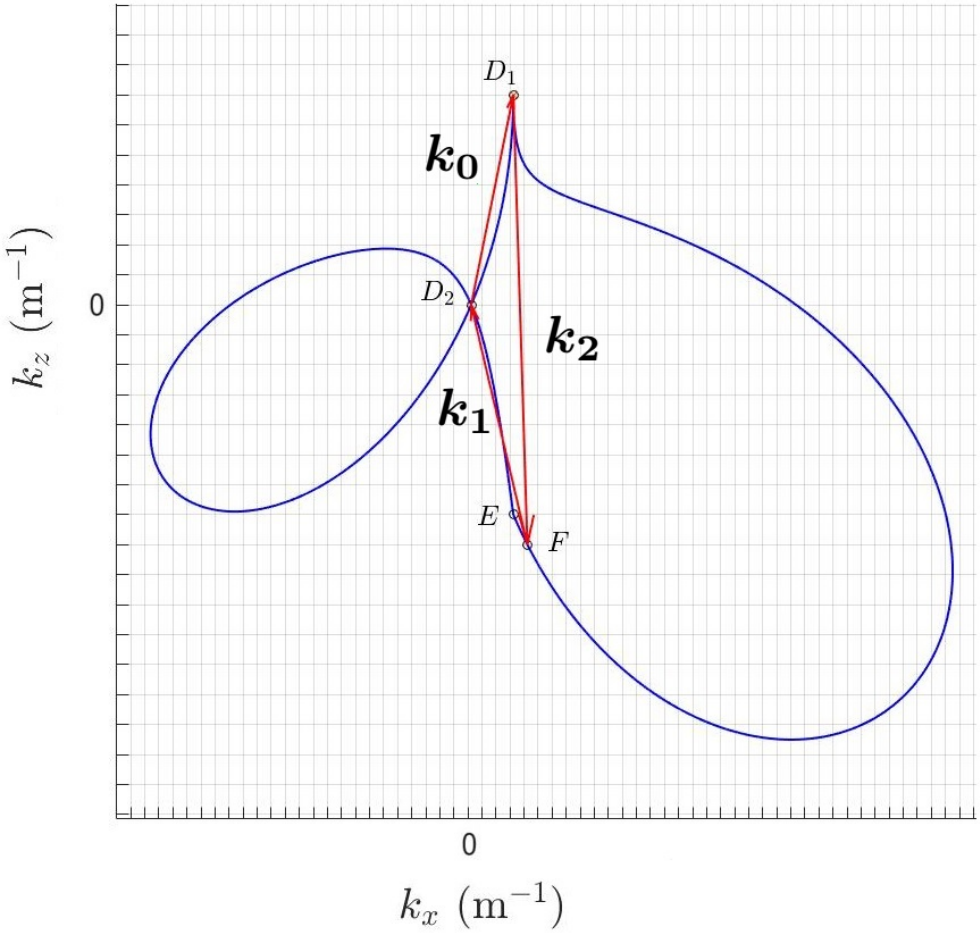

Figure 8.3: Illustration of the chosen triad F on the resonance branch corresponding to the wave frequency signs $(s_0, s_1, s_2) = (+, +, -)$. The represented mesh grid in the wave vector space (k_x, k_z) consists of tiles, each being of size $(\Delta k_x, \Delta k_z) = (2\pi/L, \pi/H)$. The wave vectors $(\boldsymbol{k_0}, \boldsymbol{k_1}, \boldsymbol{k_2})$ involved in triad F are represented in red arrows. As $k_{xn} = n_{kxn}\Delta k_x$ and $k_{zn} = n_{kzn}\Delta k_z$ to obey to the vertical boundary conditions, the selected triad F is such that $(n_{kx0}, n_{kz0}) = (3, 7)$, $(n_{kx1}, n_{kz1}) = (-4, 8)$, and $(n_{kx2}, n_{kz2}) = (1, -15)$. On the present figure, the singular triads are also indicated by letters E for Elastic Scattering, and (D_1, D_2) for Induced Diffusion.

Table 8.3: Initial conditions and corresponding pseudomomentum and Froude numbers $Fr = 2k_0\Phi_0(0)/N$ used for each simulation (A, B, C, D, E, F) on the MITgcm.

Simulation	$(\Phi_0(0), \Phi_2(0))$ $[\mathrm{m\,s^{-1}}]$	$\mathcal{P}_x$ $[\mathrm{J\,m^{-1}\,s}]$	Fr
A	(0.009999,0.000093)	0.0062	0.124820
B	(0.009957,0.000924)	0.0063	0.124292
C	(0.009810,0.001939)	0.0065	0.122456
D	(0.009585,0.002850)	0.0068	0.119648
E	(0.009292,0.003694)	0.0072	0.115994
F	(0.008627,0.005057)	0.0080	0.107689

with, for $n = 0$ or 2:

$$u_{in}(x,z) = \frac{2k_{zn}}{k_n}\Phi_n(0)\cos(k_{zn}z)\cos(k_{xn}x) \tag{8.41}$$

$$\vartheta_{in}(x,z) = -\frac{2N^2}{\alpha g}\frac{k_{xn}}{\omega_n k_n}\Phi_n(0)\sin(k_{zn}z)\cos(k_{xn}x) \tag{8.42}$$

and different values of $\Phi_0(0)$ and $\Phi_2(0)$, so that the perturbation energy is directed along $|\Phi_2|$ on the energy sphere $\mathcal{E} = |\Phi_0|^2 + |\Phi_1|^2 + |\Phi_2|^2$ in a $(|\Phi_0|, |\Phi_1|, |\Phi_2|)$ space, Φ_1 being initially nil, $\Phi_1(0) = 0$. The total energy is initialized in our simulations to $\mathcal{E} = 10^{-4}$J, and we consider six trajectories named (A, B, C, D, E, F)[11], each corresponding to a different initial pseudomomentum $\mathcal{P}_x$ as illustrated on figure 8.4. The present figure draws the energy sphere of radius $\mathcal{E} = 10^{-4}$J with the trajectories (A, B, C, D, E, F) of constant pseudomomentum obtained by solving the triadic equations for specific initial conditions $(\Phi_0(0), \Phi_1(0), \Phi_2(0))$ listed in table 8.3. Trajectories A, B, C, D and E, plotted in blue, red, green, magenta and cyan lines respectively, are located between the $|\Phi_0|$ axis and the separatrix, whereas trajectory F plotted in black is located between the separatrix and the $|\Phi_2|$ axis. Trajectory E is chosen to be close to the separatrix whereas A is chosen to be near the $|\Phi_0|$ axis.

A set of initial conditions, $(\Phi_0(0), \Phi_2(0))$, involving two waves only[12], $(\Phi_0, \boldsymbol{k_0}, \omega_0)$ and $(\Phi_2, \boldsymbol{k_2}, \omega_2)$, is defined using figure 8.4 when looking at the intersection between the energy sphere $\mathcal{E} = 10^{-4}$J and the plane $|\Phi_1| = 0$ at the start of each trajectory (A, B, C, D, E, F) on figure 8.4, to initialize each simulation on the MITgcm. Table 8.3 summarizes the chosen set of initial conditions $(\Phi_0(0), \Phi_2(0))$, and, for each trajectory, such values $(\Phi_0(0), \Phi_2(0))$ are initialized on the MITgcm using the expressions (8.38) and (8.41). Table 8.3 also indicates the pseudomomentum $\mathcal{P}_x$ and Froude number $Fr = 2k_0\Phi_0(0)/N$ associated to each simulation.

11. Every reference to a selected triad is in in italic letter e.g. (D_1, D_2, E, F), whereas the six considered trajectories are named in capital letter (A,B,C,D,E,F), so that there is no ambiguity in the notations.
12. meaning $\Phi_1(0) = 0$.

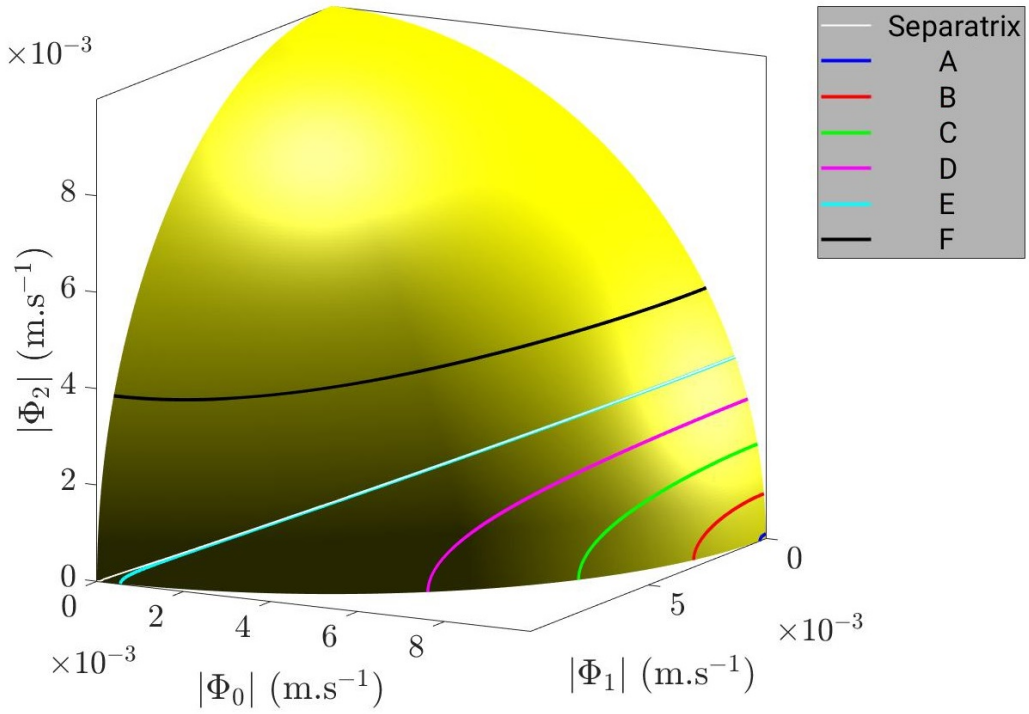

Figure 8.4: Plot of the energy sphere of radius $\mathcal{E} = 10^{-4}$J with the separatrix of equation $\mathcal{P}_x = \mathcal{E}/c_{x1}$ in white line. Six chosen trajectories designated by letters A, B, C, D, E, F, and corresponding to different values of pseudomomentum $\mathcal{P}_x$ (see table 8.3 for the pseudomomentum values) are indicated using lines of different colors on the energy sphere.

The output of each simulation on the MITgcm is interpreted with Matlab, so, using a color map, we can plot the total dynamical fields, (u, v, w) and ϑ, respectively the velocity and potential temperature fields, in the (x, z) space at different instants t until the end of each run, knowing that all simulations last 10 days. Figures 8.5, 8.6, and 8.7 show those plots (u, w, ϑ) on the left hand side at three different instants, respectively t equals to 0, 1.3 and 10 days, when initializing the MITgcm with initial conditions $(\Phi_0(0), \Phi_2(0))$ corresponding to trajectory E on the energy sphere $\mathcal{E} = 10^{-4}$J (v is not shown here as it remains equal to 0 in the domain at all time). On the right hand side of the same figures, the spatial discrete Fourier transforms of the fields $u(x, z, t)$, $w(x, z, t)$, and $\vartheta(x, z, t)$, denoted $\hat{u}(k_x, k_z, t)$, $\hat{w}(k_x, k_z, t)$, and $\hat{\vartheta}(k_x, k_z, t)$ respectively, are represented. $(\hat{u}, \hat{w}, \hat{\vartheta})$ are useful to identify the internal waves $(\Phi_0, \boldsymbol{k_0}, \omega_0)$, $(\Phi_1, \boldsymbol{k_1}, \omega_1)$, and $(\Phi_2, \boldsymbol{k_2}, \omega_2)$ involved in the triadic resonance and predicted by the theory, while identifying other harmonics eventually appearing at later instants. At each instant t, we define $(\hat{u}_n, \hat{w}_n, \hat{\vartheta}_n)$ for n equal to 0, 1 or 2, by:

$$\hat{u}_n(t) = \hat{u}(k_{xn}, k_{zn}, t) \tag{8.43}$$

$$\hat{w}_n(t) = \hat{w}(k_{xn}, k_{zn}, t) \tag{8.44}$$

$$\hat{\vartheta}_n(t) = \hat{\vartheta}(k_{xn}, k_{zn}, t) \tag{8.45}$$

Due to the vertical boundary conditions[13] and the symmetry resulting from the definition of the Fourier Transform, the presence of one wave $(\Phi_n, \boldsymbol{k_n}, \omega_n)$ with $\boldsymbol{k_n} = (k_{xn}, k_{zn})$, at a specific instant t always results in four different peaks located at (k_{xn}, k_{zn}), $(k_{xn}, -k_{zn})$, $(-k_{xn}, k_{zn})$, and $(-k_{xn}, -k_{zn})$ on the plots of $\hat{u}(k_x, k_z, t)$, $\hat{w}(k_x, k_z, t)$, and $\hat{\vartheta}(k_x, k_z, t)$, and those peaks are referred to as $\hat{u}_n$, $\hat{w}_n$, and $\hat{\vartheta}_n$ respectively on figures 8.5, 8.6, and 8.7. Looking at the Fourier transforms on the right column of figure 8.5, one wave stands out on the representation of $(\hat{u}, \hat{w}, \hat{\vartheta})$, namely $(\Phi_0, \boldsymbol{k_0}, \omega_0)$, with peak values at (k_{x0}, k_{z0}), $(k_{x0}, -k_{z0})$, $(-k_{x0}, k_{z0})$, and $(-k_{x0}, -k_{z0})$, as seen on the yellow peaks circled in red and referred to as $(\hat{u}_0, \hat{w}_0, \hat{\vartheta}_0)$ on the legends, whose intensity is of order $9 \times 10^{-3}\mathrm{m\,s^{-1}}$ along $\hat{u}$, $1.7 \times 10^{-3}\mathrm{m\,s^{-1}}$ along $\hat{w}$, and $5 \times 10^{-3}\mathrm{m\,s^{-1}}$ along $\hat{\vartheta}$. Indeed, as $\Phi_0(0) \gg \Phi_2(0)$ by almost a factor 3, we also get peaks for wave 2, $(\Phi_2, \boldsymbol{k_2}, \omega_2)$ as seen with the light blue peaks marked by triangles pointing downward and referred to as $(\hat{u}_2, \hat{w}_2, \hat{\vartheta}_2)$ on the legends of lower intensities than the previous peaks for wave 0, of order $3 \times 10^{-3}\mathrm{m\,s^{-1}}$ along $\hat{u}$, $0.3 \times 10^{-3}\mathrm{m\,s^{-1}}$ along $\hat{w}$, and $2 \times 10^{-3}\mathrm{m\,s^{-1}}$ along $\hat{\vartheta}$. The wavelike structure (standing wave along z, propagative along x) is dominated by wave 0 initially, as seen in the wave fields (u, w, ϑ) on the left column of figure 8.5, with a global periodic structure alternating

13. implying wave reflection at $z = 0$ and $z = -H$.

positive and negative velocity values at regular intervals $(\lambda_{x0}, \lambda_{z0}) = (L/n_{kx0}, 2H/n_{kx0})$ in the (x, z) domain. However, this periodic structure is slightly affected by the superimposed wave 2 as seen on the plots of (u, w, ϑ), which exhibit some irregularities compared to the typical wavelike structure of a single wave vertically confined. This corresponds to a physical reality in which the background field consists of a propagating wave 0 that is initially perturbed by a small, but finite, wave 2, identified as a nearly Vertically Sheared Horizontal Flow mode.

At $t = 1.3$ days, the right column of figure 8.6 shows that wave 1 is fully formed on the Fourier transforms $(\hat{u}, \hat{w}, \hat{\vartheta})$, with an intensity matching that of wave 2 (see green peaks marked by triangles pointing upward referred to as $(\hat{u}_1, \hat{w}_1, \hat{\vartheta}_1)$ on the legends), as predicted by the weakly nonlinear theory describing the triadic resonant interaction between three internal gravity waves. The weak nonlinearities are characterized spatially by growing irregularities when representing (u, v, w, ϑ) compared to the screenshot at $t = 0$ days on figure 8.5. A striking feature of the present numerical simulation is the birth of modes not predicted by the second order expansion in Fr of the wave equations(4.75). Such modes attributed to higher orders begin to be formed at 1 day approximately, and ultimately leads to a set of additional intense peaks that can't be neglected after 10 days of simulation, as seen on figure 8.7 when looking at the additional green and blue peaks appearing on the Fourier transforms, not indicated by any markers, and whose intensities are approximately 2 to 10 times lower than the peaks indicated by the red markers (circle and triangles). A closer inspection to those higher order modes shows that, when capturing the wave vector and frequency of such modes, they obey to the dispersion relation of internal gravity waves. This feature reveals that those modes are actually internal waves, and a further analysis (not detailed here) shows that those waves even follow a specific resonance condition different from that given in equations (4.76) and (4.77). Figures 8.5, 8.6, and 8.7 follow the evolution of the dynamical fields (u, v, w, ϑ) as well as their Fourier transforms $(\hat{u}, \hat{v}, \hat{w}, \hat{\vartheta})$ when considering initial conditions relative to the trajectory E on the energy sphere, but the growth of resonating higher order waves identified here for this specific trajectory, is also observed when initializing the simulations with initial conditions relative to the other trajectories A, B, C, D, F, this phenomenon being enhanced for the trajectories close to the separatrix as detailed later on in this section.

On the figures 8.5, 8.6, and 8.7, higher order effects appear through the birth of peaks on the Fourier transforms $(\hat{u}, \hat{w}, \hat{\vartheta})$ that are different from those characteristics of waves 0, 1 or 2, respectively located by the circle, upper and downward triangles to indicate $(\hat{u}_0, \hat{w}_0, \hat{\vartheta}_0)$, $(\hat{u}_1, \hat{w}_1, \hat{\vartheta}_1)$, and $(\hat{u}_2, \hat{w}_2, \hat{\vartheta}_2)$. We distinguish the higher order peaks from $(\hat{u}_n, \hat{w}_n, \hat{\vartheta}_n)$, by referring to them as $(\hat{u}'_p, \hat{w}'_p, \hat{\vartheta}'_p)$. From the outputs of the MITgcm (u, v, w) and ϑ, we can derive numerically the time evolution of the (second order) amplitudes $|\Phi_n|$ and compute the total energy of the waves in the simulation box $\mathcal{E}_{tot} = \mathcal{E} + \mathcal{E}'$

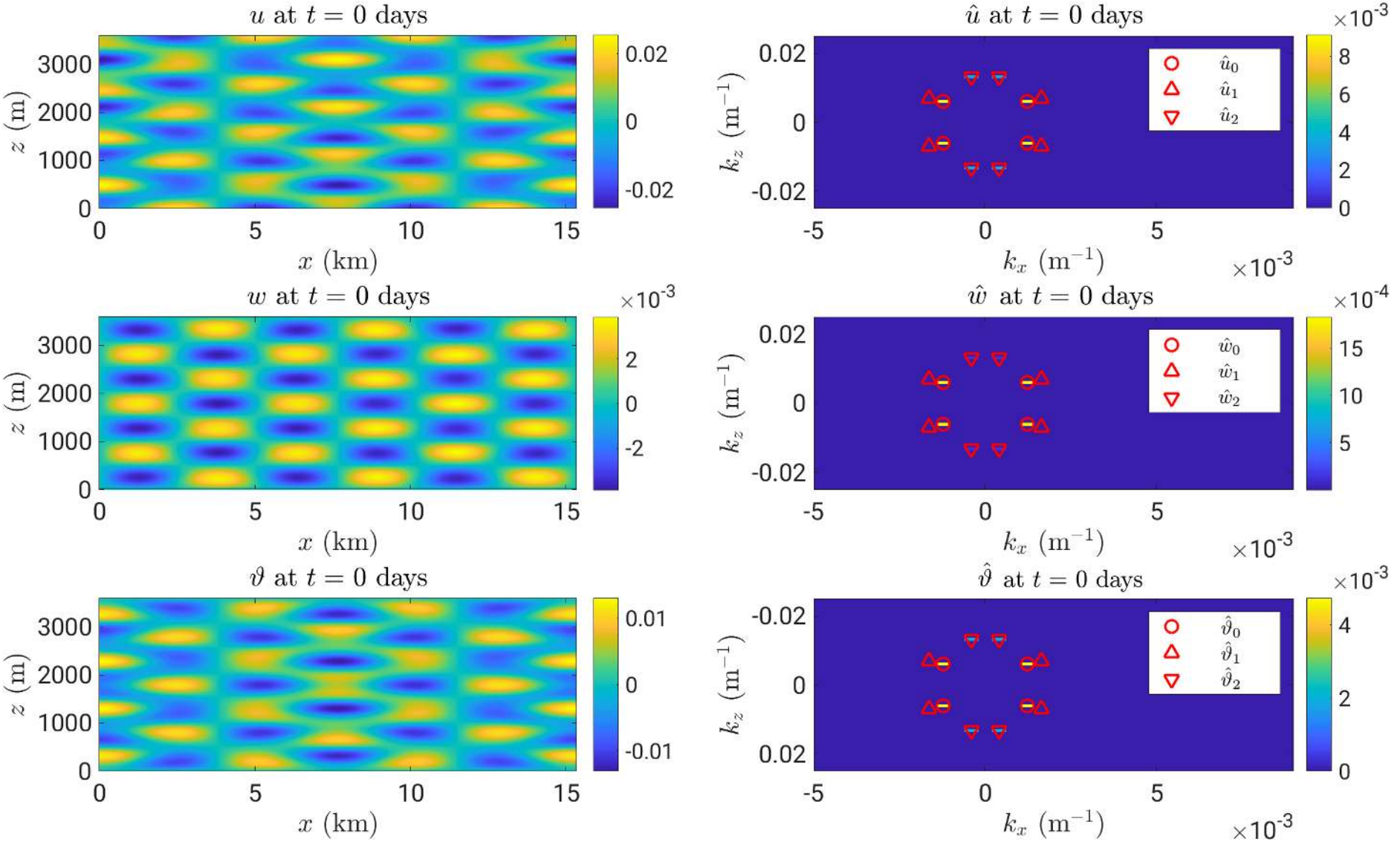

Figure 8.5: Plots at $t = 0$ days of (u, v, ϑ) on the left column, and $(\hat{u}, \hat{w}, \hat{\vartheta})$ on the right column. On the plots of $(\hat{u}, \hat{w}, \hat{\vartheta})$, the four locations corresponding to wave 0 are circled in red and denoted (k_{x0}, k_{z0}) on the legends, whereas waves 1 and 2 are indicated by red triangles pointing upward and downward respectively, when being referred to as (k_{x1}, k_{z1}) and (k_{x2}, k_{z2}) on the legends.

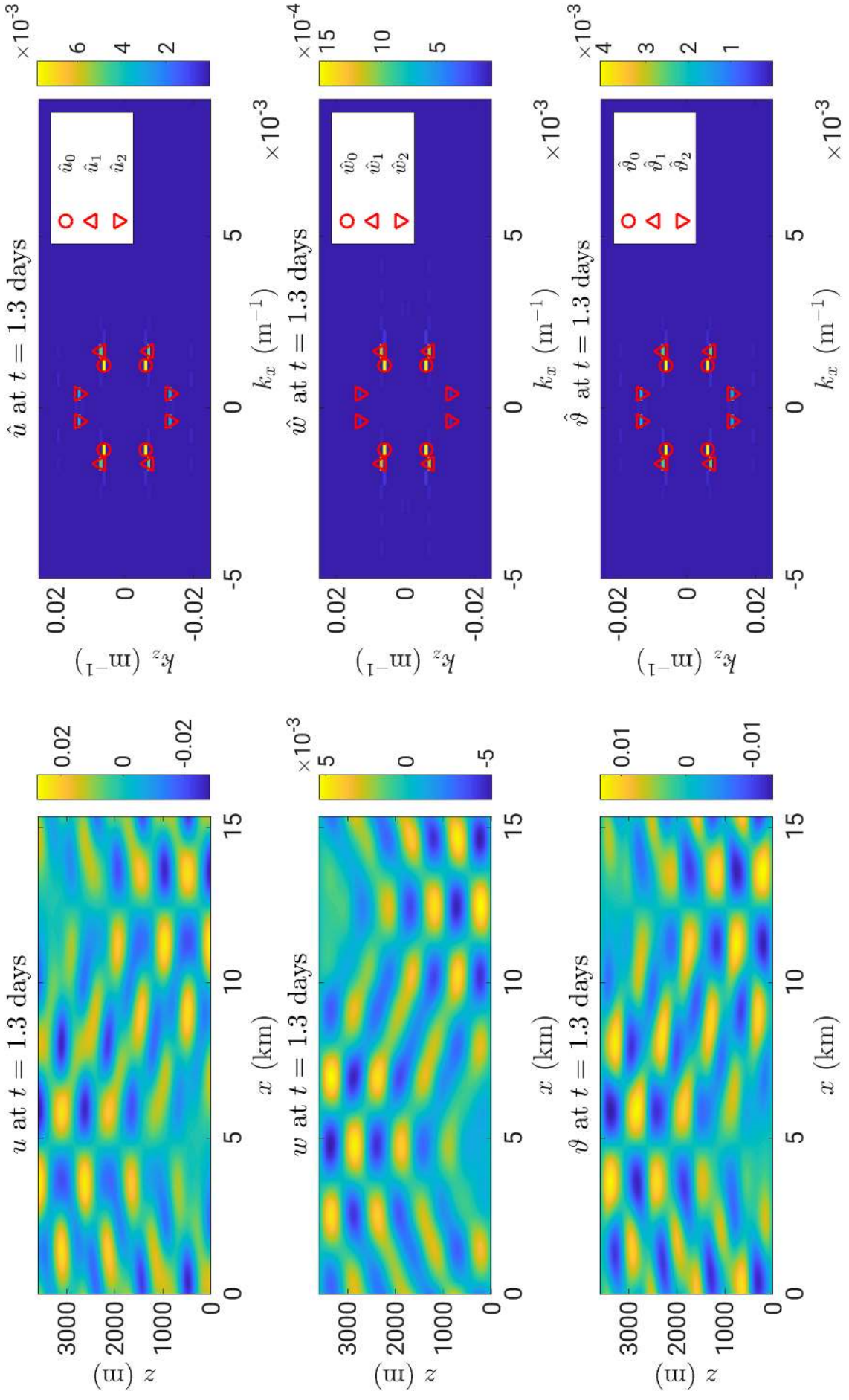

Figure 8.6: Same as 8.5, but at $t = 1.3$ days.

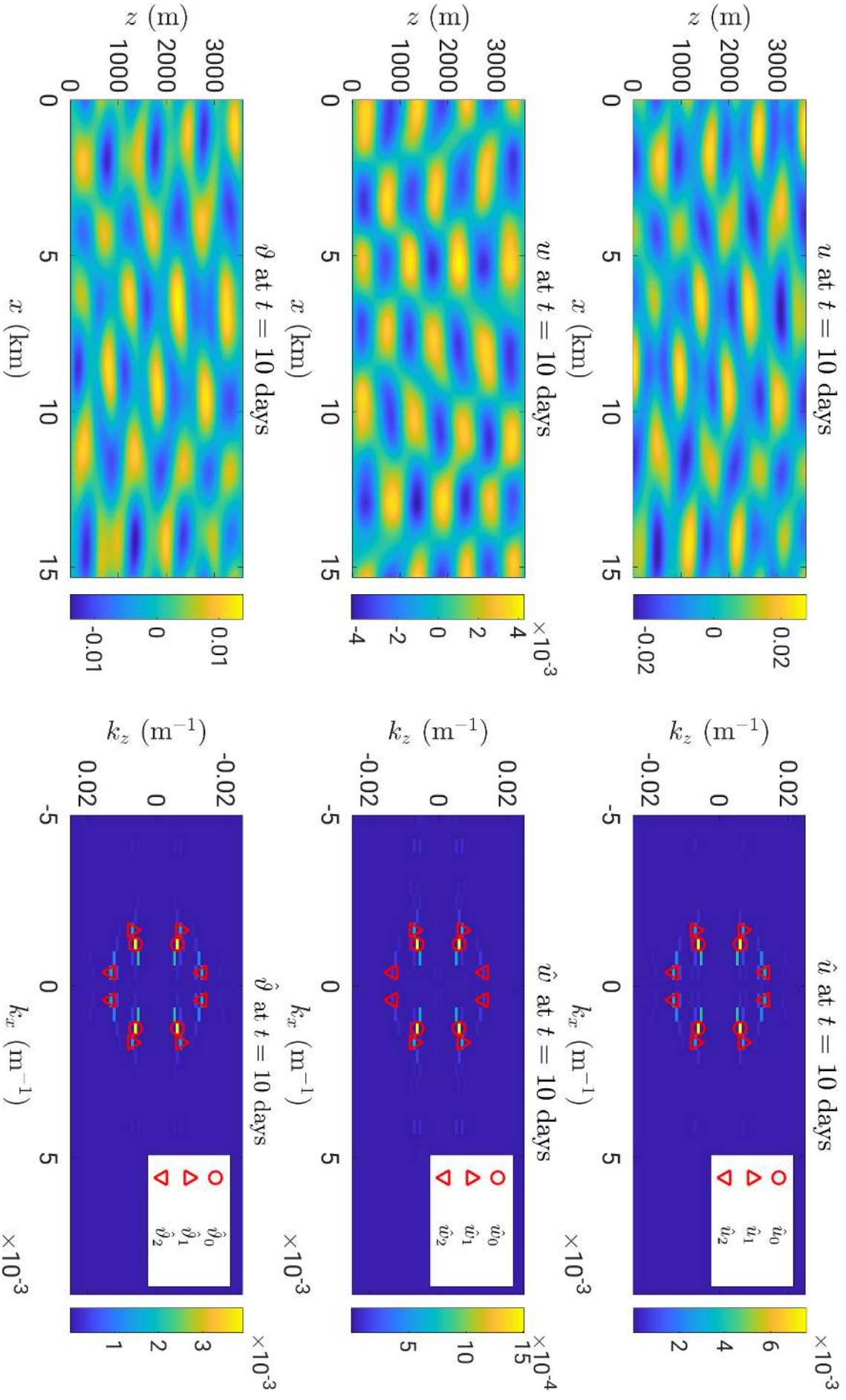

Figure 8.7: Same as 8.5, but at $t = 10$ days.

as a function of time, by decoupling the contributions from the resonating second order waves contained in $\mathcal{E}$, and the resonating higher order waves contained in $\mathcal{E}'$. Such terms are obtained using the following expressions:

$$\mathcal{E} = \frac{1}{2}\sum_{n=0}^{2} |\hat{u}_n|^2 + |\hat{w}_n|^2 + \left(\frac{\alpha g}{N}\right)^2 |\hat{\vartheta}_n|^2 \tag{8.46}$$

$$\mathcal{E}' = \frac{1}{2}\sum_{p\in\mathscr{S}} |\hat{u}'_p|^2 + |\hat{w}'_p|^2 + \left(\frac{\alpha g}{N}\right)^2 |\hat{\vartheta}'_p|^2 \tag{8.47}$$

where the set $\mathscr{S}$ gathers the (k_x, k_z) positions of the higher order peaks observed on the plots of $(\hat{u}, \hat{w}, \hat{\vartheta})$. The amplitudes $|\Phi_n|$ are obtained using the dispersion relation:

$$|\Phi_n| = \frac{k_n}{2|k_{zn}|}|\hat{u}_n| \tag{8.48}$$

as we choose to normalize the Fourier transforms such that $\max_{(k_x,k_z)} |\hat{u}| = \max_{(x,z)} |u|$, $\max_{(k_x,k_z)} |\hat{w}| = \max_{(x,z)} |w|$, and $\max_{(k_x,k_z)} |\hat{\vartheta}| = \max_{(x,z)} |\vartheta|$ at all time t. Finally, the energy of the perturbation is deduced from (8.48) as $e = |\Phi_1|^2 + |\Phi_2|^2$. The plots of the amplitudes $|\Phi_n|$ as a function of time t for the trajectories A, B, C, D, E, F are gathered in 8.8 and 8.9, and both figures compares the amplitudes derived theoretically for each trajectory by solving the triadic equations (4.87) (see left column in 8.8 and 8.9) to those derived using the MITgcm (see right column in 8.8 and 8.9). On the other hand, the time evolution of the energies $(\mathcal{E}_{tot}, \mathcal{E}, \mathcal{E}', e)$ computed numerically are displayed on figure 8.10.

Figure 8.8 shows a good agreement between the amplitudes $(|\Phi_0|, |\Phi_1|, |\Phi_2|)$ predicted by the weakly non-linear theory and those simulated by the MITgcm for the trajectories A, B, and C, close to the $|\Phi_0|$ axis. Indeed, this case corresponds to an infinitesimal perturbation affecting a primary wave $(\Phi_0, \boldsymbol{k_0}, \omega_0)$ in its course, so that the triadic system can be linearized around this base state, leading to the 2×2 equation (4.106) in which the evolution operator $\mathscr{L}$ is nonnormal and nearly singular for the chosen triad F. Such properties result in the observed periodic transients, as $(|\Phi_1|, |\Phi_2|)$ grow with periodic arches, while $|\Phi_0|$ remains nearly constant when considering trajectories A and B, or greater than the perturbation $(|\Phi_1|, |\Phi_2|)$ in C, such that the variations of $|\Phi_0|$ can be neglected compared to those of $(|\Phi_1|, |\Phi_2|)$.

On figure 8.9, the amplitudes $(|\Phi_0|, |\Phi_1|, |\Phi_2|)$ associated to trajectory D are nearly identical when comparing the theory with the simulation. However, as the initial $\Phi_2(0)$ becomes greater, the trajectory D moves towards the separatrix, and, as indicated by the curves of the amplitudes for the trajectory E close to the separatrix, the simulated waves are getting further from the theoretical prediction. The three main differences are that $|\Phi_2|$ doesn't oscillate down to 0 in the simulation contrary to the theory, the peak

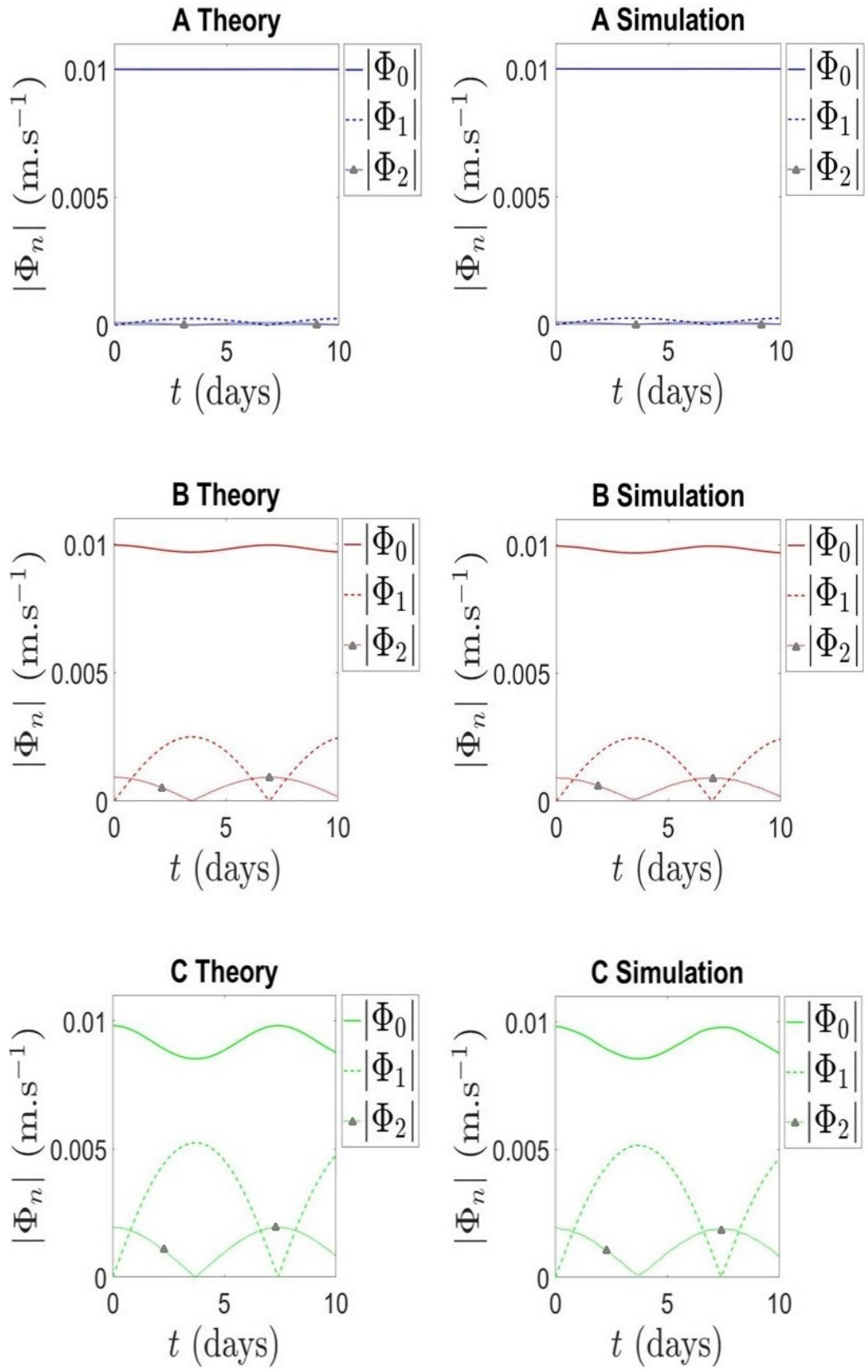

Figure 8.8: Time evolution of the amplitudes ($|\Phi_0|, |\Phi_1|, |\Phi_2|$) for the trajectories A, B, and C. The left column of the figure shows the amplitudes obtained theoretically when solving the triadic equations using Matlab, whereas the right column features the amplitudes obtained with the simulations on the MITgcm.

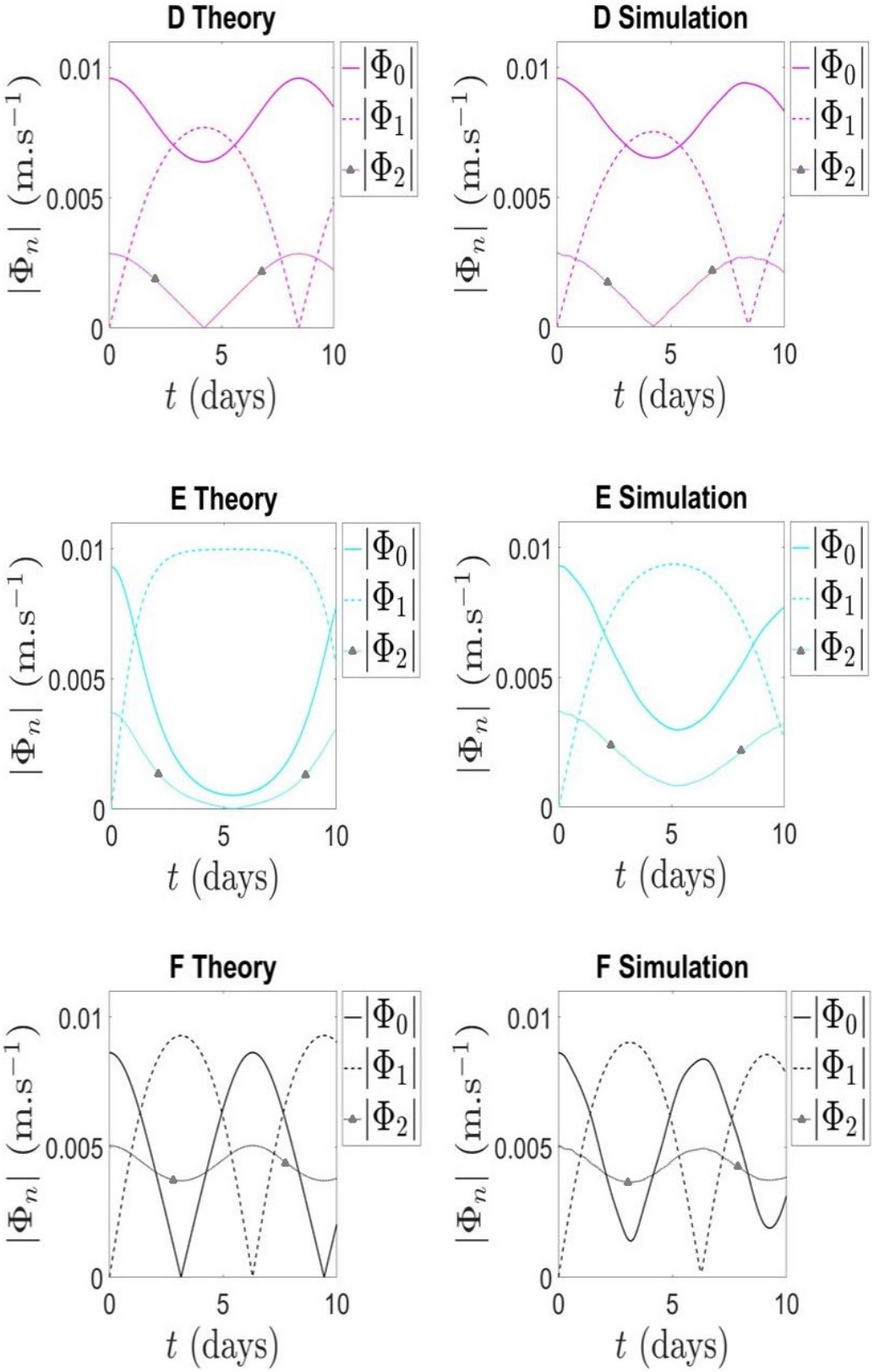

Figure 8.9: Same as figure 8.8, but for the trajectories D, E, and F.

to peak variation of $|\Phi_0|$ is less important (0.05 in the simulation compared to 0.09 in theory), and the saturation effects of $|\Phi_1|$ is more amplified in theory, with long lasting plateaux at 0.01 over approximately 5 days, while this saturation is nearly absent on the amplitudes simulated by the MITgcm. The amplification of residual modes characterized by higher order waves may play a role in the observed gap between simulation and theory for trajectories near the separatrix. Those differences seem to be attenuated when looking at the time evolution of the amplitudes corresponding to trajectory F located after the separatrix, the only main difference being that $|\Phi_2|$ still doesn't oscillate down to 0 in the simulation contrary to the theory.

The role played by the higher order waves appears when representing the time evolution of the energy $(\mathcal{E}_{tot}, \mathcal{E}, \mathcal{E}', e)$ on figure 8.10. For all six trajectories, the total energy averaged over the simulation domain $\mathcal{E}_{tot}$, is conserved. For the trajectories A, B, and C, the contribution of the higher order terms in energy $\mathcal{E}'$ is almost nil, and the curves of $\mathcal{E}_{tot}$ and $\mathcal{E}$ are nearly identical. For these three trajectories, the perturbation energy e constantly experiences transient growth at periodic intervals. For the trajectories D, E, and F, the energy of the second order triad $\mathcal{E}$ decreases, while $\mathcal{E}'$ increases starting from 0, when conserving the total energy $\mathcal{E}_{tot} = \mathcal{E} + \mathcal{E}'$. Over 10 days of simulation, $\mathcal{E} \times 10^4$ decreases from 1 to 0.9 for trajectory D, from 1 to 0.75 for E and from 1 to 0.85 for F. The higher order waves break the conservation of the triadic energy $\mathcal{E}$ predicted theoretically, and a portion of this energy feeds the growth of the resonating higher order waves. A larger portion of the energy $\mathcal{E}$ is pumped by these residual modes as nonlinear effects increase for the trajectories near the separatrix (see E). The peak to peak variations of the perturbation energy e is attenuated at each period as seen in F (also observed for D and E with simulations running for more than 10 days, but not displayed here) due to the developing higher order waves, ultimately reducing the nonlinear growth of the perturbation energy e in the long run, up until this energy becomes entirely consumed by the higher order waves.

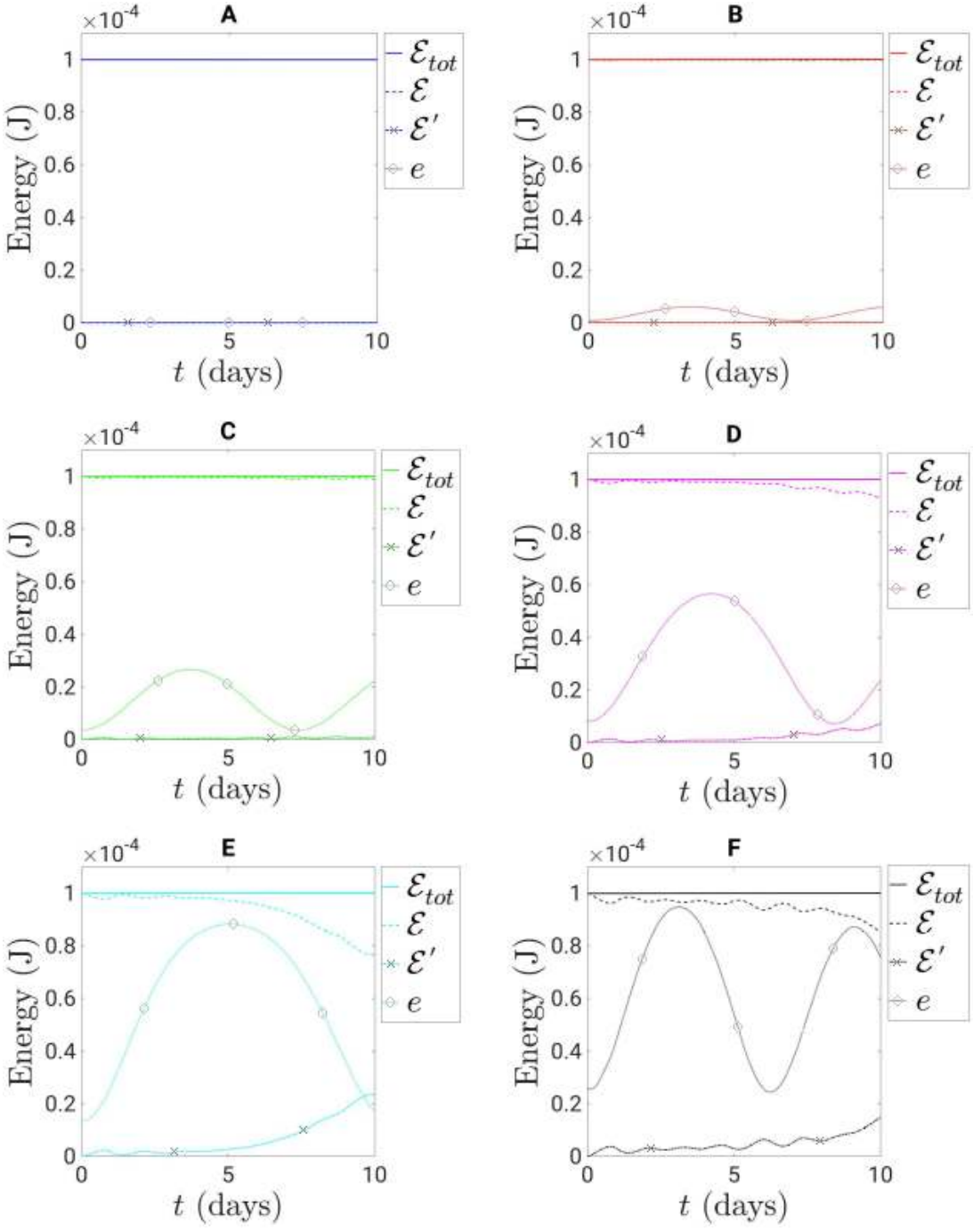

Figure 8.10: Energy as a function of time for all the six simulations A, B, C, D, E, F on the MITgcm, corresponding to each trajectory represented on figure 8.4. $\mathcal{E}_{tot}$, $\mathcal{E}$, $\mathcal{E}'$ and e designate the total energy averaged over the simulation domain, the energy associated to the triad F, the energy of higher order waves, and the perturbation energy respectively.

Part IV

Conclusions and discussions

Chapter 9

Conclusions on the project

Internal waves are an ubiquitous feature in the climate system as they strongly contribute to the turbulent mixing occurring among stratified layers in the atmosphere and the ocean. During their life cycle, those waves undergo multiple physical phenomena, from their generation at localized sites, to their propagation in a stratified medium, with the ability to become unstable and to break, ultimately generating turbulence and dissipating energy, which alters the stratification by mixing water of different densities in the ocean for instance. The production of turbulence is dominated by the dynamics of internal waves and affect the local environment in which they evolve.

In the ocean, the resulting small scale mixing from internal waves activity ranges from centimeters to meters, and contributes to sustain the global overturning circulation, while closing the ocean energy budget, but remains challenging to model due to the computational limits of climate numerical models. This project takes part in the recent progress to parametrize the internal wave driven mixing. We proposed a theory to take into account the transient evolution of a perturbation that affects a single internal wave propagating in a stratified medium. In this process we revisited the classical theories to describe the dynamics of internal waves.

This thesis offered the opportunity to deepen our knowledge of wave-wave interaction, and more specifically, on the triadic resonant instability, a nonlinear interaction between three internal waves at resonance, also one of the paths to turbulent mixing. Understanding the underlying physical processes involved in the transient dynamics of a small perturbation energy disturbing the propagation of internal waves is key to model the energy transfers between different scales triggered by the present instability. To our knowledge, the transient growth of such instability were not captured by the classical theories so far, and may play a major role in the parametrization of internal wave driven mixing in numerical climate models and of internal waves near the inertial frequency at different latitudes of the globe. This project answers the persistent need for a thorough parametrization of the physical processes the climate models are sensitive to, so as to help the understanding and modeling of the climate system despite its complexity.

9.1 Modeling the evolution of an infinitesimal perturbation from a single internal wave

Classical theories[1] of internal waves mainly predict the physical behavior of the present waves in the steady regime, and is widely used by the scientific community as a standard tool for experimental interpretation[2]and direct numerical simulations of climate[3]. Reviewing those theories as a starting point of this project highlighted how they could be completed to fully take into account the dynamics of internal waves, especially when it comes to describing their transient behavior.

When digging into former research ideas from the community investigating transient growth and stability of disturbances in hydrodynamic flows[4], we realize that the main concepts introduced in this particular field could be of good use to guide the theory describing the transient dynamics of the triadic resonant instability. More precisely, a single internal wave propagating in a stratified medium and submitted to an infinitesimal perturbation, may experience intense transient growth of perturbation energy.

Measuring how fast and strong those transients may be requires time dependent physical quantities that genuinely capture the instantaneous growth of the perturbation energy. The optimal energy and optimal growth rate were then introduced as ways to quantify those transients, making sure that they were coherent with the former classical theories. Indeed, at large time, the optimal growth rate turns out to be the classical growth rate predicted by Hasselmann theory (1967)[5], and the properties of linear stability of resonant triads remain valid.

While the growth rate predicted by the classical theory for linearly stable triads remains nil, a more important growth rate was observed at short times for linearly stable triads than unstable ones when plotting the optimal growth rate along the resonant curves at different instants. This property is barely affected by the introduction of viscous effects, but this difference of growth rate is largely enhanced for primary waves with nearly vertical wave vector. The frontier between linear stability and instability may be clearly defined at large time, however, during the transient regime, this frontier needs to be redefined in some ways that take into account the transient dynamics dominated by linearly stable triads. One major consequence is that the Parametric Subharmonic Instability, although being classically investigated to model energy transfers to small scales in the ocean, is not the only candidate among wave-wave interactions responsible for developing instabilities and transferring energy between scales, the Parametric Subharmonic Instability being even quickly overwhelmed by linearly some stable triads, which initially grow at a faster

1. Davis and Acrivos, *op. cit.*; Hasselmann, *op. cit.*
2. Bordes et al., *op. cit.*
3. Richet, Chomaz, and Muller, *op. cit.*
4. Reddy and Henningson, *op. cit.*
5. Hasselmann, *op. cit.*

and stronger pace.

Investigating the optimal energy growth of the perturbation for internal gravity waves, some specific classes of resonant triads cause more important transients to develop. Those triads involve one wave of nearly vertical wave vector standing out from the others, and were given names in the field of stratified turbulence, Elastic Scattering and Induced Diffusion[6], relative to the turbulence they induce. Such generated singular wave has zero frequency for a nil Coriolis parameter, inertial frequency otherwise, and induces shear, hence being known as the Vertically Sheared Horizontal Flow mode. Transient growth of perturbation energy occur for triads near this singularity and are intrinsically link to the nonnormality of the 2×2 evolution operator (relative to the fixed energy norm, the Euclidean norm of the waves normalized amplitudes being the energy of the perturbation) describing the behavior of the linearized triadic system around its base state. This transient dynamics is enhanced as the evolution operator becomes nonnormal and singular. To our knowledge, the introduction to the concept of nonnormality in the field of wave-wave interaction to describe the short time behavior of the linearized triadic system seems to be novel, raises many questions concerning the sensitivity of climate models to such phenomenon, and opens new areas of research that need to be explored, from numerical simulation to experimental evidence confirming the importance of such transient dynamics in the process of generating small scale turbulence.

9.2 Quantifying the growth of a finite perturbation from the instability generated by waves

A small but finite disturbance may result in nonlinear effects that condition the growth of the perturbation energy. This question was raised by a member of the audience during the November 2019 meeting of the American Physics Society, in which the previously highlighted results for infinitely small perturbation were presented in conference. This is how our former studies were extended from the linearized system considering an infinitesimal perturbation to the fully nonlinear problem involving a finite perturbation.

The similarities between the nonlinear triadic equations for wave-wave resonant interaction and Euler equations for the rotation of a rigid body around its three principal axes was the starting point to analyze and discuss the analogy between rotating solid and fluid. Both systems conserve two quadratic quantities, total energy and momentum for the rigid body and total energy and helicity (equivalent to the vertical component of the pseudomomentum) for the triadic system. While the three components of the angular momentum in each direction are real in the nonlinear equations describing the rotation of the rigid body, the three amplitudes of the resonant inertial waves are complex in the

6. McComas and Bretherton, *op. cit.*

triadic equations, thus adding an extra constraint, modeled by a phase invariant, known as the Hamiltonian, as a third integral of motion.

When linearizing both systems, we were able to retrieve the identical transient growth of an infinitely small perturbation energy measured by the optimal energy gain. In such linearized problems, the perturbation is infinitely small, and the smaller it is, the greater the transients are, since the evolution of the energy gain features high periodic arches whose peaks scale as the inverse of the perturbation to the base state. In the case of a rotating solid, the base state is a rigid body with two equal moments of inertia, let's say the greatest and the intermediate ones, the last one being different from the two firsts, and the perturbation consists of an infinitely small defect along the intermediate moment of inertia, hence becoming different from the greatest one. For the inertial wave system, the base state is a single inertial wave, called primary wave, perturbed when propagating by an infinitesimal energy, which results in the growth of two inertial waves forming the perturbation, one wave being nearly time independent with a horizontal wave vector, when the two others are either nearly identical or have symmetrical wave vector with respect to the vertical axis. Looking at the transients of the optimal energy gain, the primary wave periodically transfers energy to the perturbation.

The work done for inertial waves was then generalized to any wave system undergoing triadic resonant instability utilizing Craik's work (1978)[7]. The present extension was useful to the description of finite nonlinearities for internal waves generating instability in stratified rotating flows. The periodic evolution described previously remains relevant to any triadic wave system when taking into account nonlinear effects. By fixing the energy norm to be the Euclidean norm of the wave amplitudes, nonlinearities are well represented in a three-wave-amplitude space by the intersection between the unit energy sphere and the pseudomomentum ellipsoids, forming all the possible trajectories obtained when solving the triadic equations. Two stable regimes represented by two different axes of the three-wave-amplitude space surrounded by pseudomomentum ellipsoids appear. The separatrix distinguishes those two stable regimes, and gives rise to a third regime of instability when crossing the last axis. While the weak nonlinearities appear when considering trajectories in a plane crossing the energy sphere near one of the axes of the three-wave-amplitude space, the nonlinearities are captured by the dynamics of the edge states along the separatrix. For resonant triads characterized by two nearly identical phase velocities, the separatrix gets infinitely close to one axis, causing a small perturbation to exhibit large growth. When getting infinitely close to the separatrix, the trajectories turn out to oscillate periodically with an infinite duration spent near one axis, the attractor, and eventually a very short time spent near another axis, the repeller, the base state being either the attractor or the repeller depending on the linear stability of the considered resonant

7. A. D. D. Craik, J. A. Adam, and K. Stewartson, "Evolution in space and time of resonant wave triads - I. The 'pump-wave approximation'", in: *Proc. Roy. Soc. Lond.* 363.*1713* (Nov. 1978), pp. 243–255.

triad. Those relaxation oscillations correspond to a nutating perturbation energy in the three-wave-amplitude space, and result in the periodic destruction of the primary wave, whose energy is transferred back and forth between the base state and the perturbation.

The direct numerical simulations conducted on the MITgcm to model the triadic resonant interaction between three internal gravity waves reveal the limits of the weakly nonlinear theory when it comes to modeling small but finite perturbations to a single propagating wave as the base state. The conservation of the triadic energy remains true for infinitesimal perturbations (see trajectories A, B, and C on figure 8.10), but this conservation drops for more intense perturbations, implying the growth of resonating higher order waves that pump energy from the triadic reservoir (see trajectories D, E, F on figure 8.10). This phenomenon is enhanced for the trajectories near the separatrix (see E on figure 8.10), so the energy of higher order waves grows significantly more as nonlinear effects increase, ultimately attenuating the nonlinear growth of the second order perturbation.

Chapter 10

Discussion, future work and perspectives

10.1 Discussion

Both the atmosphere and the ocean are sensitive to the distribution and magnitude of the localized internal wave driven mixing, whose parametrization remains challenging and impact the reliability of General Circulation Models predicting the evolution of the climate system. The diffusivity induced by the internal wave field occurs at scales smaller than those captured by the GCM, and only a few heuristic parametrization for this diffusivity exist to measure the sensitivity of numerical climate models to varying mixing schemes. Speaking of sensitivity, recent studies show that small changes in this parametrization or in the distribution of the diffusivity have a great impact on global models by modifying radically the predicted temperature, circulation and fluxes in the atmosphre and the ocean. Such observation calls for a shift from an heuristic representation to a physical parametrization of the mixing dynamics which needs to be supported by theoretical studies to understand the underlying physics. How the transient dynamics and the nonlinear growth of a small perturbation highlighted in the present project could affect the current parametrizations is key when seeking to improve them. Developing physical parametrizations is the first step to adapt numerical models to predict situations not yet observed up until now and induced by global warming.

10.2 Future work

In the light of recent studies dedicated to improving the representations of ocean and atmosphere in climate models, the results of the present project raises some possible thoughts on the future of numerical parametrization and on the understanding of the physical processes involved. The physics of mixing due to breaking internal waves still remains incompletely understood and represents a challenge in the numerical representation of the ocean and atmosphere. Further investigations are needed to understand how the transient dynamics found here may form energy pathways that drive the turbulent mixing and the breaking of waves. The transfer of physical quantities intrinsic to internal

waves, such as energy and pseudomomentum, to different scales may be guided at first by the transient and nonlinear growth emanating from triadic resonance. However, the physics behind the origins of such growth needs to analyzed, also experimentally, to point out what causes an internal wave to be disturbed at a certain stage of its life cycle, leading to any form of transient instability.

During the pandemic, a laboratory set up similar to the one used by Aguilar et al. (2006)[1] was built in our laboratory (LadHyX) to observe the finite time evolution of internal wave instabilities generated by a 3D printed sinusoidal topography towed at constant speed in a tank filled with linearly salt stratified water as shown in figure 10.1. The tank is $L = 6$ m long, $W = 50$ cm wide, filled by salty water of maximum height $H = 50$ cm, such that the BruntVäisälä frequency equals $N = 1.1$ rad s^{-1}, and the topography can be towed with speed U up to 1.1 m s^{-1}. In comparison, the set up of Aguilar et al. has characteristics $L = 197$ cm, $W = 17.5$ cm, $H = 27$ cm, $N = 1.1$ rad s^{-1}, and U in the range $0.9 - 4.9$ cm s^{-1}. The linear stratification $N = 1.1$ rad s^{-1} is reached by having clear water of density $\rho_c = 1000$ kg m^{-3} at the surface and a brine solution of density ρ_b such that $\Delta\rho = \rho_b - \rho_c = N^2 H/g = 0.06$ kg m^{-3} at the bottom. The identical experiment may be reproduced at first to successfully observe the generation of vertically-propagating internal waves and boundary-trapped lee waves, by adapting the speed U to the ranges of Aguilar et al. when reproducing their dimensions for the 3D printed topography. This is exactly what guided our choice of dimensions when printing the topography pictured in figure 10.2 of wavelength $\lambda = 13.7$ cm, and height $h = 2.6$ cm, corresponding to an aspect ratio of $h/\lambda = 0.2$. The corresponding vertical and horizontal Froude numbers defined in Aguilar et al. (2006)[2] are $Fr_v = U/(Nh)$ and $Fr_h = U/(N\lambda)$ respectively, and linear theory predicts propagating waves if $Fr_h < 1$, and the flow is hydrostatic if $Fr_h \ll 1$. In their paper, Aguilar et al. focus on the weakly ($Fr_v^{-1} \leq 1$) and nonlinear ($Fr_v^{-1} > 1$) regimes measured by the vertical Froude number.

Their laboratory experiment may be adapted to challenge the theoretical results of our investigations found in the weakly nonlinear regime ($Fr_v = 1$) from an experimental perspective. Indeed, the topography may be towed over larger distances, for longer durations, and eventually with a grid placed at the front end of the topography so that the grid produces noise (hence disturbing the passive generation of waves over the topography), to observe the growth of an instability and its evolution at finite time. We can choose at first $U = 0.55$ cm s^{-1} so that the generated waves have a frequency $\omega = U(2\pi/\lambda) = 0.25$ rad s^{-1} ($\omega < N$) corresponding to the wave angle $\theta = 0.25$ chosen in part 6. For the interpretation of the experimental results, their vertical Froude number $Fr_v = U/(Nh)$, related to the characteristics of the topography, must be linked at first with the theoretical

1. D. A. Aguilar, B. R. Sutherland, and D. J. Muraki, "Laboratory generation of internal waves from sinusoidal topography", in: *Deep Sea Research Part II: Topical Studies in Oceanography*, Ocean Mixing 53.*1* (Jan. 2006), pp. 96–115.

2. *Ibid.*

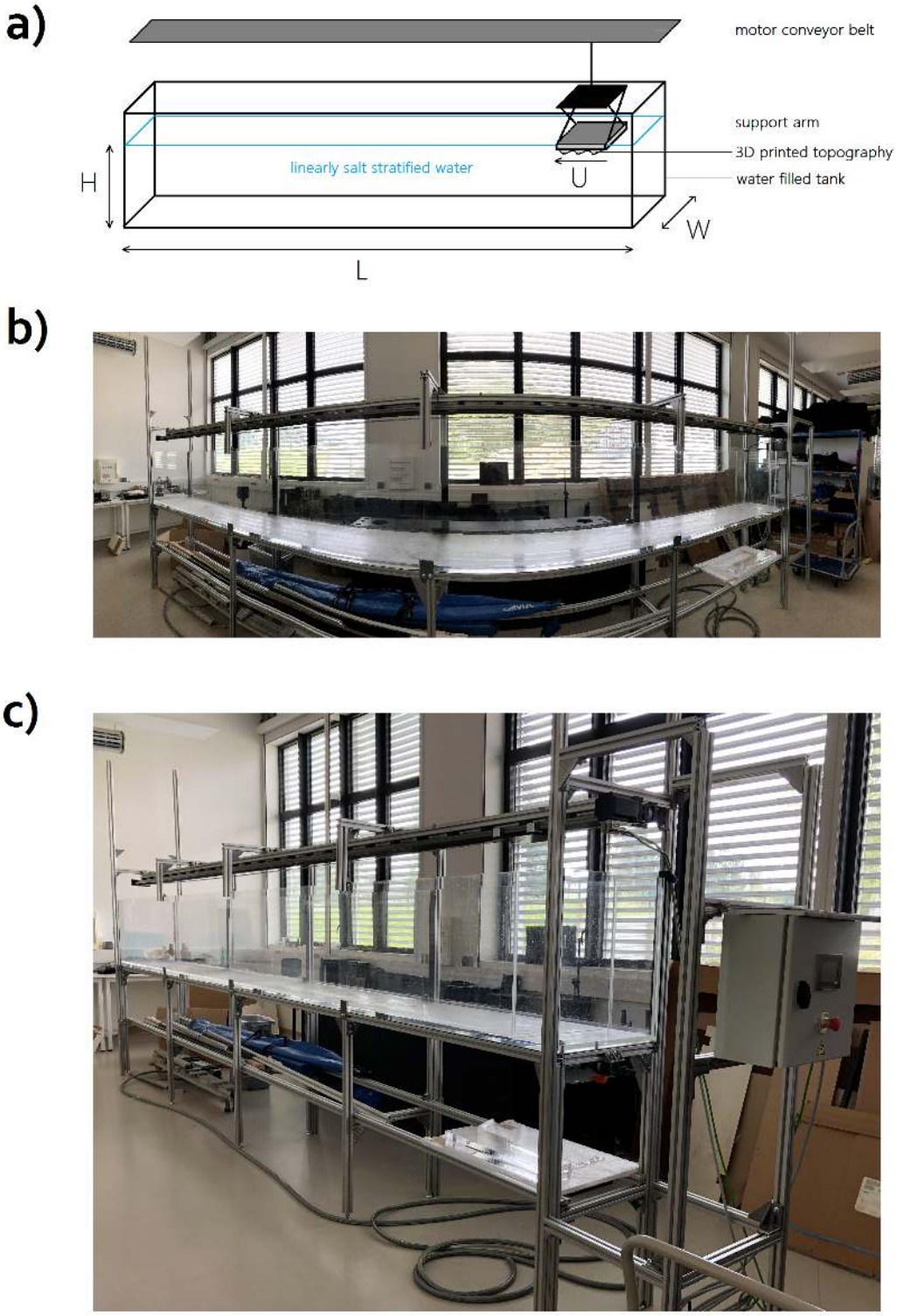

Figure 10.1: a) Schematics of the laboratory set up at LadHyX, similar to the one used by Aguilar et al. (2006), but with a larger tank, measuring $L = 6$ m long, $W = 50$ cm wide, filled by salty water of maximum height $H = 50$ cm, such that the buoyancy frequency equals $N = 1.1\ \mathrm{rad\,s^{-1}}$. The topography mounted on an adjustable support arm can reach speed U up to $1\ \mathrm{m\,s^{-1}}$. b) Panoramic photo of the (empty) tank at LadHyX (sideview). c) Photo of the experimental setup from another perspective, showing the console piloting the motor conveyor belt placed at the top right end of the tank. The console controls the speed of the towed topography, and durations of the acceleration and deceleration phases.

Figure 10.2: a) Schematics of the sinusoidal shaped topography, which is 3D printed in three separated parts and then assembled before being mounted over the support arm and towed in the tank. b) Photos of the middle piece of the 3D printed topography.

definition used in the present manuscript $Fr = \Psi_0(0)/(NL_0^2)$, intrinsic to the generated internal waves, leading to $Fr = U/(Nh)Fr_v = 0.2$, as $Fr_v = 1$ in the weakly nonlinear regime. Then, the grid located in front of the topography perturbs the flow over the hills, and such an instability may be observed using shadowgraph technique.

In the proposed experiment, the placement of the grid relative to the position of the topography on the support arm is dictated by the grid induced turbulence so that its intensity is maximized to perturb the flow over the hills, and, ultimately, the internal wave radiation. Indeed, the work conducted by Irps (2016)[3] when observing the turbulence generated by a grid placed in a wind tunnel illustrated in figure 10.3a) recalls that the presence of the grid modifies the flow and the boundary layer development directly downstream of the grid. When defining five locations along his tunnel as shown in figure 10.3b), Irps was able to observe a clear modification of the boundary layer near the grid downstream, as pictured in 10.3c) where the horizontal velocity profile of location 2 (profile B, captured at 21.5 mm downstream of the grid) is characterized by a alternate wake and jet pattern in presence of the grid (solid lines), compared to the case without grid (dashed lines). At location 1 upstream (profile A, at 16.5 mm upstream), the u profile is almost unaffected by the presence of the grid, whereas, at locations 3 and 4 (profiles C and D at 151.5 mm and 281.5 mm downstream respectively), u experiences overshoot near the surface lower wall, this overshoot being attenuated when getting further downstream. In fact, Irps used five different grids in his experiments are manufactured from 2 mm thick aluminium sheets and made following the design criteria described by Roach

3. T. Irps and V. Kanjirakkad, "On the interaction between turbulence grids and boundary layers", in: *EPJ Web of Conferences* 114 (2016), p. 02048.

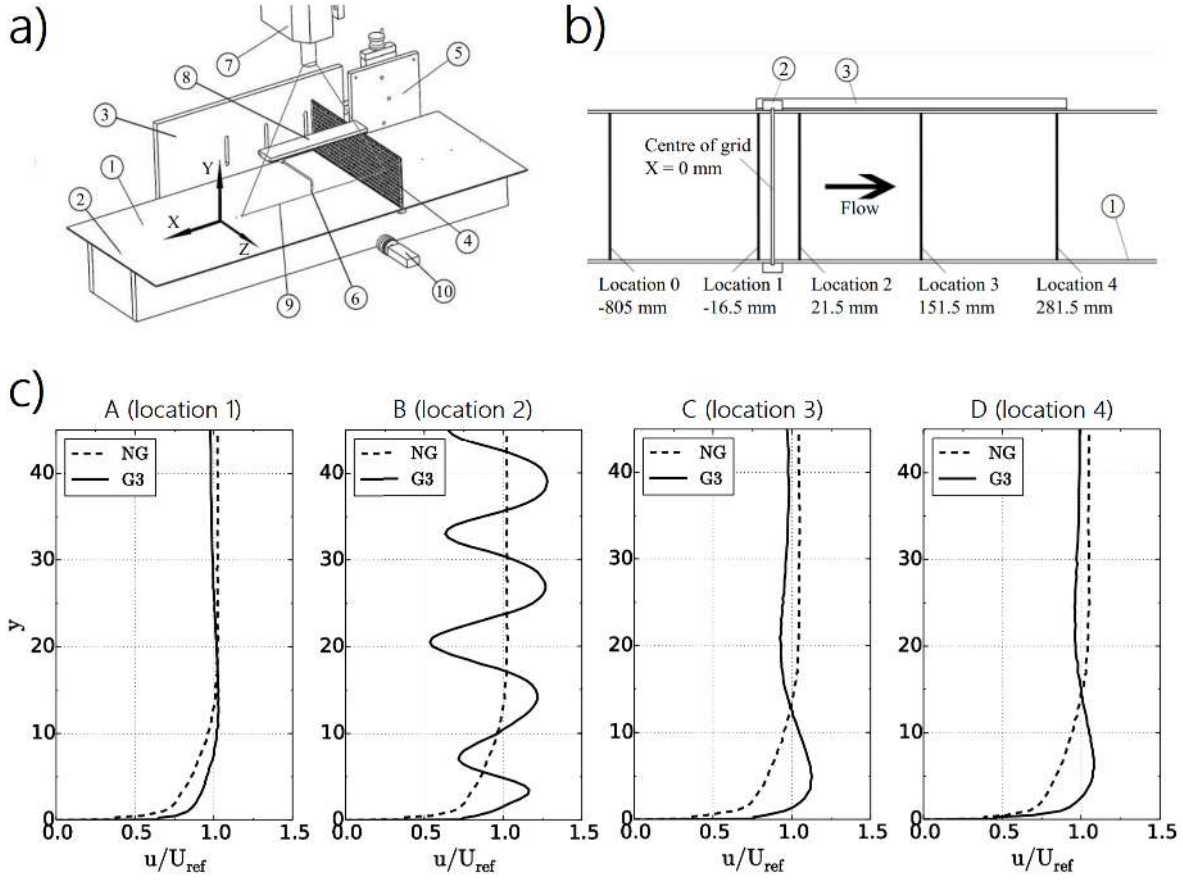

Figure 10.3: a) Experimental setup of Irps (2016) with a fixed surface lower wall in (1) where boundary layer flow is tracked. In (2), pressure tappings along the center line of the lower wall are used to measure pressure drops along the duct. (3) points out a background window with slots containing hot-wires, (4) is the grid around which pneumatic probe traverses in the wall normal direction (Y axis) at five selected locations defined on figure b). A linear actuator mechanism for traversing the probe is fixed on the outside of the wind-tunnel (5). Non-intrusive PIV setup is used for visualising the horizontal velocity field u in the intended measuring area (9) and is composed of a non-reflective glass (8), a laser head (7), a the camera (10). b) View of the tunnel from above defining five locations. c) Horizontal velocity profile for a grid G3 of 9 mm holes, 3 mm strut, with a porosity 0.563 and a pressure drop factor 2.27, at the four locations 1, 2, 3 and 4, corresponding to the plots A, B, C and D respectively, U_{ref} being a referenced velocity. Dashed curves correspond to the absence of grid, and the continuous curves to the presence of grid G3. From Irps (2016).

(1987)[4] with square-mesh arrays of square bars (SMS). The induced turbulence depends on the parameters of the chosen grid in terms of sizes of the holes, strut widths, porosities, and pressure drop coefficient, as stated by Roach (1987)[5] who also showed the attenuation of the turbulence far from the grid with an empirical scaling $Tu = C(X/d)^{-5/7}$, Tu being the turbulence intensity, $X > 0$ the distance downstream from the grid, d the strut width, and C a coefficient equal to 1.13 for grids of the SMS type. Tu is determined experimentally by calculating the rms of the horizontal velocity field above the lower wall in presence of the grid, and dividing it by the rms value of same field when the grid is absent. The scaling law of Tu, inversely proportional to X, suggests that the grid must be placed directly at the front edge of the 3D printed topography in order to maximize the induced turbulence affecting the flow over the topography. For our setup, we can first choose one of the SMS grid listed in Irps work (2016)[6], whose induced turbulence on a basic flow is well-known, but eventually measured again in our configuration when towing the support only, without the 3D printed topography on it. A possible grid could have 9 mm holes, 3 mm strut, for a porosity 0.563 and a pressure drop factor 2.27, corresponding to grid G3 in Irps work and whose turbulence is illustrated on figure 10.3.

The presence of the grid perturbs the downstream flow such that this perturbation may grow at finite time, characterized by a measured experimental growth rate $\sigma_{\text{exp}}(t)$ corresponding to one of the points in the curves computed theoretically on figure 6.8, i.e. $\sigma(T, k_1)$ for a fixed k_1 at a certain stage $t = T/(NFr) \sim 5T$ s of the experiment, corresponding to a localization $x = Ut \sim 2.8T$ cm in the frame of the topography as we capture pictures using a camera that follows the translation of the hills. The noise of the grid being random, $\sigma_{\text{exp}}(t)$ may be equal to $\sigma(T, k_1)$ for a certain triad of the resonant spectrum identified by its wave vector norm k_1, hence giving information on the nature of the generated triadic instability (linearly stable or unstable). The transient amplification of linearly stable triads highlighted on figure 6.8 for short times, $T = 0.1$ up to $T = 3$ for a wave angle $\theta_0 = 0.25$ corresponding to the positions $x = 0.28$ cm up to $x = 8.4$ cm downstream of the grid, are expected to be observed. The reconstitution of the curves $\sigma(T, k_1)$ on figure 6.8 requires a set of experiments and measures involving different grid properties (hole size, strut width, porosity, and pressure drop factor of SMS grids) for one 3D printed topography, and the nonlinear effects may also be explored by increasing the towing speed U up to the permitted experimental range, or by building steeper topographies.

The analysis may be pushed further by taking into account detuning effects on the transient dynamics identified here. The transient growth of a small perturbation in the course of a propagating internal wave is already sensitive to different parameters of the system

4. P. E. Roach, "The generation of nearly isotropic turbulence by means of grids", in: *International J. Heat and Fluid Flow* 8.*2* (June 1987), pp. 82–92.

5. *Ibid.*

6. Irps and Kanjirakkad, *op. cit.*

such as those studied in the present project: primary wave angle, viscosity/diffusivity, and Earth rotation. When increasing nonlinearities, some universal scaling laws were found to quantify the sensitivity of the transient dynamics to the modification of Earth rotation in a range that corresponds to a geophysical reality. How would the detuning of resonant wave triads affect the relaxations oscillations of a nutating perturbation in a three-wave-amplitude space theoretically demonstrated here? It would be interesting to reprise the theoretical and experimental investigations conducted by McEwan & Plumb (1977), to answer this open question. Indeed, their setup mentioned in section 2.1 and whose results are presented on figure 2.3 uses one fine-scale wave generator consisting of an oscillating cylinder and one large scale wave maker to produce two slightly detuned waves in a 5.5 m long channel filled with a salt solution. As stated by McEwan & Plumb (1977):

> *The beams, being of fine scale, weakened rapidly with distance from the generating cylinder and likewise decayed rapidly when the cylinder was withdrawn from the water. They were the realization of a discrete, spatially non uniform fine-scale internal wave packet.*

In our intended setup, a 3D topography being towed in a 6 m tank, we may add the wave maker in the course of the topography to generate a second wave, in addition to those generated passively at the hills, adjusting the period of the oscillating cylinder so that the second wave is slightly detuned from the waves of frequency $\omega = U(2\pi/\lambda)$, to observe the effects of detuning on the emerging transient and nonlinear dynamics in the interacting region, sufficiently close to the wave maker to avoid the rapid decay of the fine-scale wave. When there is no detuning, we may recover the results of our theoretical study in which two resonant waves, $(\Phi_0, \boldsymbol{k_0}, \omega_0)$ and $(\Phi_2, \boldsymbol{k_2}, \omega_2)$, are initially considered, describing a trajectory of constant pseudomomentum on a sphere of fixed energy in the amplitudes space $(|\Phi_0|, |\Phi_1|, |\Phi_2|)$, then forming the third resonant wave $(\Phi_1, \boldsymbol{k_1}, \omega_1)$. The triadic system corresponds to a trajectory exhibiting high transient and nonlinear growth for triads close to Elastic Scattering and Induced Diffusion, along with the generation of Vertically Sheared Horizontal Flow modes (VSHF), so this criterion will guide our choice on the forcing frequencies of the two inital waves (radiated from the hills and generated by the cylinder) in order to get nearly singular triads. It would be interesting to set multiple cylinders vertically aligned at a fixed horizontal position and oscillating at the same detuned frequency to eventually enlarge the interacting zone of the three resonating waves.

10.3 Perspectives

Fundamental knowledge gaps still exist when it comes to understanding the physical processes that transfer energy within the internal wave field, ultimately leading to dissi-

pation and turbulent mixing. The transfer of physical quantities, such as energy and pseudomomentum, across different length scales and frequencies remains poorly understood. This transfer is ensured by numerous physical processes, such as wave-wave interaction, topographic scattering and reflection, and interaction of the waves with the mean current, that may be all concomitant. This study focused on one of the above mechanisms and must be completed by further analysis to include the combination of the mentioned physical processes.

To understand the observed features of internal wave spectrum, we suggested an alternative to the classical Parametric Subharmonic Instability when modeling the energy transfer between scales by focusing on two singular triads, Elastic Scattering and Induced Diffusion. Those two triadic resonant interactions were thoroughly investigated in the present project from a novel perspective, as they induce the strong transient (and nonlinear) growth of a small perturbation energy, along with sustaining Vertically Sheared Horizontal Flow modes (VSHF). The resulting shear could imply a radically different horizontal and vertical distribution of the turbulent mixing induced by internal waves, and may explain how the radiation of internal waves by modes of instability modifies the mixing induced by shear, such that it occurs at a different height/depth, possibly modifying the spatial, temporal, and directional properties of shear[7]. Such dynamics may affect the ocean, transferring the mixing from the thermocline to the deep ocean, as well as the atmospheric boundary layer in stable configuration, blocking its mixing and transferring wave breaking to higher layers.

7. M. H. Alford et al., "SpaceTime Scales of Shear in the North Pacific", in: *J. Phys. Oceanogr.* 47.*10* (Oct. 2017), pp. 2455–2478.

Appendices

Appendix A: Relation between the pseudomomentum and the helicity for inertial waves

We use the formalism introduced by Moffatt (2014) to make the link between the z component of the pseudomomentum $\mathcal{P}_z = \boldsymbol{\mathcal{P}} \cdot \boldsymbol{e_z}$ and the helicity, denoted $\mathcal{H}$, which is in our case, an invariant of the Euler equations[8] of fluid flow. The mean helicity of the wave is defined by $\mathcal{H} = \langle \boldsymbol{u} \cdot \boldsymbol{\omega} \rangle$, where $\boldsymbol{\omega} = \nabla \times \boldsymbol{u}$ is the vorticity of the fluid parcel which turns out to be:

$$\boldsymbol{\omega} = \begin{pmatrix} -v_{,z} \\ \nabla^2 \psi \\ v_{,x} \end{pmatrix} \tag{1}$$

so the helicity can be written as:

$$\begin{aligned} \mathcal{H} &= \langle \nabla^2 \psi v \rangle - \langle \psi_{,x} v_{,x} \rangle - \langle \psi_{,z} v_{,z} \rangle \\ &= \langle \nabla^2 \psi v \rangle + \langle \psi_{,xx} v \rangle + \langle \psi_{,zz} v \rangle \\ &= 2 \langle \nabla^2 \psi v \rangle \\ &= 2 \langle \omega_y v \rangle \end{aligned} \tag{2}$$

Now let, $\boldsymbol{F} = (F_0, F_1, F_2)$, $\boldsymbol{G} = (G_0, G_1, G_2)$ and $\boldsymbol{H} = (H_0, H_1, H_2)$ and:

$$\psi = \sum_n F_n(t) \mathrm{e}^{i \boldsymbol{k_n} \cdot \boldsymbol{r}} + c.c \tag{3}$$

$$v = \sum_n G_n(t) \mathrm{e}^{i \boldsymbol{k_n} \cdot \boldsymbol{r}} + c.c \tag{4}$$

$$\omega_y = \sum_n H_n(t) \mathrm{e}^{i \boldsymbol{k_n} \cdot \boldsymbol{r}} + c.c \tag{5}$$

so $H_n = -k_n^2 F_n$. Combining the polarization relation (4.74) with the dispersion relation of inertial waves, $\omega_n k_n = \sigma_{zn} f k_{zn}$ with $\sigma_{zn} = \mathrm{sign}(\omega_n k_{zn})$, we get $G_n = -\sigma_{zn} k_n F_n$, so:

8. Navier-Stokes equations in the inviscid case $\nu = \kappa = 0$.

$$\begin{aligned}\mathcal{H} &= 2\langle \omega_y v \rangle \\ &= 2\sum_n \frac{1}{4}\Re(\boldsymbol{G_n}\cdot\boldsymbol{H_n}^*) \\ &= \frac{1}{2}\sum_n \sigma_{zn} k_n^3 |F_n|^2 \\ &= 2\sum_n \sigma_{zn} k_n |\phi_n|^2\end{aligned} \tag{6}$$

keeping in mind that $\phi_n = k_n F_n/2$, and:

$$\begin{aligned}\mathcal{P}_z &= \boldsymbol{\mathcal{P}}\cdot\boldsymbol{e_z} \\ &= \sum_n \mathcal{A}_n k_{zn} \\ &= \sum_n \frac{\sigma_{zn} k_n |\phi_n|^2}{f}\end{aligned} \tag{7}$$

or in other terms $\mathcal{H} = 2\langle \omega_y v \rangle = 2f\mathcal{P}_z$ hence, in the purely rotating case[9], the z components of the pseudomomentum $\mathcal{P}_z$ and of the momentum $\mathcal{P}_z$ are equal to the helicity of the inertial wave, up to a factor $2f$.

9. in the purely stratified case, the same derivation gives $\mathcal{P}_x = \langle \omega_y b \rangle = \sum_n \sigma_{xn} k_n |\phi_n|^2$

Appendix B: Global invariants

Here we demonstrate that the total mean energy and helicity are global invariants of the full dynamical system of nonlinear equations, meaning that the result in part 4.2 is valid at all order of disturbances and does not depend on the internal waves definition. For full generality, we consider the stratified rotating case by keeping the same notations introduced in part 4.1[10] and only making one single assumption, the Boussinesq approximation[11] in the Reynolds decomposition given by (4.4) to show the general[12] conservation of energy and helicity:

$$\begin{aligned} \boldsymbol{\nabla}\cdot\boldsymbol{u} &= 0 && (8)\\ D_t b &= -N^2 w + \mathcal{D}_b(b) && (9)\\ D_t\boldsymbol{u} &= -\boldsymbol{\nabla}P + b\boldsymbol{e_z} - f\left(\boldsymbol{e_z}\times\boldsymbol{u}\right) + \mathcal{D}_m(\boldsymbol{u}) && (10) \end{aligned}$$

where $\mathcal{D}_b$ and $\mathcal{D}_m$ are dissipation terms. Taking the curl of the last equation, the vorticity vector $\boldsymbol{\omega} = \boldsymbol{\nabla}\times\boldsymbol{u}$ obeys:

$$D_t\boldsymbol{\omega} + J(\boldsymbol{u}, v) = -f\boldsymbol{u}_{,z} - b_{,x}\boldsymbol{e_y} + \boldsymbol{\nabla}\times\mathcal{D}_m(\boldsymbol{u}) \qquad (11)$$

Conservation of the mean total energy in inviscid stratified rotating flows

By definition, the mean total energy $\mathcal{E}$ is:

$$\mathcal{E} = \langle e_{tot}\rangle_{\boldsymbol{r}} \qquad (12)$$

with e_{tot} the total energy, sum of the kinetic and potential energies (e_k, e_p) defined by:

$$\begin{aligned} e_{tot} &= e_k + e_p && (13)\\ e_k &= \frac{1}{2}\boldsymbol{u}^2 && (14)\\ e_p &= \frac{1}{2}\left(\frac{b}{N}\right)^2 && (15) \end{aligned}$$

multiplying (9) by b and (10) by $\boldsymbol{u}$, and using (8)[13], we get[14]:

10. in which all equations were dimensional.
11. which assumes small density fluctuations $\rho' \ll \rho_r$.
12. at all order of disturbances, instead of assuming small Fr numbers.
13. $\boldsymbol{\nabla}\cdot(Pu) = \boldsymbol{\nabla}P\cdot\boldsymbol{u} + P\boldsymbol{\nabla}\cdot\boldsymbol{u}$ and $\boldsymbol{\nabla}\cdot\boldsymbol{u} = 0$.
14. keeping also in mind that $D_t(fh) = hD_tf + fD_th$.

$$D_t e_p = -wb + b\mathcal{D}_b(b)/N^2 \quad (16)$$

$$D_t e_k = -\boldsymbol{\nabla}\cdot\boldsymbol{S} + wb + \boldsymbol{u}\cdot\mathcal{D}_m(\boldsymbol{u}) \quad (17)$$

with the energy flux $\boldsymbol{S} = P\boldsymbol{u}$, so that:

$$D_t e_{tot} = -\boldsymbol{\nabla}\cdot\boldsymbol{S} + \boldsymbol{u}\cdot\mathcal{D}_m(\boldsymbol{u}) + b\mathcal{D}_b(b) \quad (18)$$

Calculations of the convective term concerning the total energy e_{tot} result in[15], we get:

$$\begin{aligned}\langle(\boldsymbol{u}\cdot\boldsymbol{\nabla})e_{tot}\rangle_{\boldsymbol{r}} &= \langle u e_{tot,x}\rangle_{\boldsymbol{r}} + \langle w e_{tot,z}\rangle_{\boldsymbol{r}} \\ &= -\langle u_{,x} e_{tot}\rangle_{\boldsymbol{r}} - \langle w_{,z} e_{tot}\rangle_{\boldsymbol{r}} \\ &= -\langle(\boldsymbol{\nabla}\cdot\boldsymbol{u})e_{tot}\rangle_{\boldsymbol{r}} \\ &= 0\end{aligned} \quad (19)$$

so $\langle D_t e_{tot}\rangle_{\boldsymbol{r}} = \mathcal{E}_{,t}$ and taking the spatial mean of (18) finally ends up to:

$$\mathcal{E}_{,t} = \langle \boldsymbol{u}\cdot\mathcal{D}_m(\boldsymbol{u}) + b\mathcal{D}_b(b)\rangle_{\boldsymbol{r}} \quad (20)$$

the right hand side being 0 in the inviscid case which implies the time conservation of the mean total energy.

Conservation of the mean helicity in inviscid rotating flows

Recall that the mean helicity $\mathcal{H}$ can be written as $\mathcal{H} = \langle\boldsymbol{u}\cdot\boldsymbol{\omega}\rangle_{\boldsymbol{r}}$, with $\boldsymbol{\omega} = \boldsymbol{\nabla}\times\boldsymbol{u}$ being the vorticity vector. Now:

$$D_t(\boldsymbol{u}\cdot\boldsymbol{\omega}) = \boldsymbol{\omega}\cdot D_t\boldsymbol{u} + \boldsymbol{u}\cdot D_t\boldsymbol{\omega} \quad (21)$$

so using (10) combined with (11), and noticing[16] that $\langle\boldsymbol{u}\cdot J(\boldsymbol{u},v)\rangle_{\boldsymbol{r}} = 0$, $\langle D_t(\boldsymbol{u}\cdot\boldsymbol{\omega})\rangle_{\boldsymbol{r}} = \mathcal{H}_{,t}$ and $\langle\boldsymbol{\omega}\cdot(b_{,x}\boldsymbol{e_y})\rangle_{\boldsymbol{r}} = 0$, we get:

$$\mathcal{H}_{,t} = 2\langle b v_{,x}\rangle_{\boldsymbol{r}} + \langle\boldsymbol{\omega}\cdot\mathcal{D}_m(\boldsymbol{u}) + \boldsymbol{u}\cdot\nabla\times\mathcal{D}_m(\boldsymbol{u})\rangle_{\boldsymbol{r}} \quad (22)$$

In the purely rotating[17] inviscid case, (9) becomes $D_t b = 0$ so b is constant and $\langle b v_{,x}\rangle_{\boldsymbol{r}} = b\langle v_{,x}\rangle_{\boldsymbol{r}} = 0$, hence the right hand side of (22) is 0 which implies the time conservation of the mean total helicity for a purely rotating inviscid fluid.

15. keeping in mind that $\langle f h_{,x_i}\rangle_{\boldsymbol{r}} = -\langle f_{,x_i} h\rangle_{\boldsymbol{r}}$ and $\langle f_{,x_i}\rangle_{\boldsymbol{r}} = 0$ with x_i being x, y, z or $\boldsymbol{r} = (x,y,z)$
16. same calculations as (19)
17. non-stratified case $N = 0$, $f \neq 0$

Bibliography

Aguilar, D. A., B. R. Sutherland, and D. J. Muraki, "Laboratory generation of internal waves from sinusoidal topography", in: *Deep Sea Research Part II: Topical Studies in Oceanography*, Ocean Mixing 53.*1* (Jan. 2006), pp. 96–115.

Alford, M. H. et al., "SpaceTime Scales of Shear in the North Pacific", in: *J. Phys. Oceanogr.* 47.*10* (Oct. 2017), pp. 2455–2478.

Anderson, L. and J. Sarmiento, "Redfield Ratios Of Remineralization Determined By Nutrient Data-Analysis", in: *Glob. Biogeochem. Cycles* 8 (Mar. 1994), pp. 65–80.

Andrews, D. G. and M. E. Mcintyre, "On wave-action and its relatives", in: *J. Fluid Mech.* 89.*4* (Dec. 1978), pp. 647–664.

Armstrong, J. A. et al., "Interactions between Light Waves in a Nonlinear Dielectric", in: *Phys. Rev.* 127.*6* (Sept. 1962), pp. 1918–1939.

Ball, F. K., "Energy transfer between external and internal gravity waves", in: *J. Fluid Mech.* 19.*3* (July 1964), pp. 465–478.

Bender, C. M. and S. A. Orszag, "Advanced Mathematical Methods for Scientists and Engineers I: Asymptotic Methods and Perturbation Theory", in: *Advanced Mathematical Methods for Scientists and Engineers I: Asymptotic Methods and Perturbation Theory*, New York, NY: Springer, 1999, pp. 484–543.

Biskamp, D., E. Schwarz, and J. F. Drake, "Two-Dimensional Electron Magnetohydrodynamic Turbulence", in: *Phys. Rev. Lett.* 76.*8* (Feb. 1996), pp. 1264–1267.

Bordes, G. et al., "Experimental evidence of a triadic resonance of plane inertial waves in a rotating fluid", in: *Phys. Fluids* 24.*1* (Jan. 2012), p. 014105.

Bretherton, F. P., "Resonant interactions between waves. The case of discrete oscillations", in: *J. Fluid Mech.* 20.*3* (1964), pp. 457–479.

Cairns, R. A., "The role of negative energy waves in some instabilities of parallel flows", in: *J. Fluid Mech.* 92.*1* (May 1979), pp. 1–14.

Coppi, B, M. N. Rosenbluth, and R. N. Sudan, "Nonlinear interactions of positive and negative energy modes in rarefied plasmas (I)", in: *Annals of Physics* 55.*2* (Nov. 1969), pp. 207–247.

Courant, R., K. Friedrichs, and H. Lewy, "On the Partial Difference Equations of Mathematical Physics", in: *IBM J. Res. and Dev.* 11.*2* (Mar. 1967), pp. 215–234.

Craik, A. D. D., *Wave interactions and fluid flows*, Cambridge monographs on mechanics and applied mathematics, Cambridge [Cambridgeshire] ; New York: Cambridge University Press, 1985.

Craik, A. D. D. and J. A. Adam, "Explosive resonant wave interactions in a three-layer fluid flow", in: *J. Fluid Mech.* 92.*1* (May 1979), pp. 15–33.

Craik, A. D. D., J. A. Adam, and K. Stewartson, "Evolution in space and time of resonant wave triads - I. The 'pump-wave approximation'", in: *Proc. Roy. Soc. Lond.* 363.*1713* (Nov. 1978), pp. 243–255.

Dauxois, T. et al., "Instabilities of Internal Gravity Wave Beams", in: *Annu. Rev. Fluid Mech.* 50.*1* (2018), pp. 131–156.

Davis, R. E. and A. Acrivos, "The stability of oscillatory internal waves", in: *J. Fluid Mech.* 30.*4* (Dec. 1967), pp. 723–736.

De Bruyn Kops, S.M. and J. J. Riley, "Dynamics of Turbulence Strongly Influenced by Buoyancy", in: (Nov. 2002), p. 7.

Delorme, B. and Y. Eddebbar, "Ocean Circulation and Climate: an Overview", in: (2016), p. 8.

Eckhaus, W., *Studies in Non-Linear Stability Theory*, Springer Tracts in Natural Philosophy, Berlin Heidelberg: Springer-Verlag, 1965.

Eloy, C., P. Le Gal, and S. Le Dizès, "Experimental Study of the Multipolar Vortex Instability", in: *Phys. Rev. Lett.* 85.*16* (Oct. 2000), pp. 3400–3403.

Euler, L., "Du mouvement de rotation des corps solides autour d'un axe variable", in: *Memoires de l'academie des sciences de Berlin* 8.*14* (1758), pp. 154–193.

Farrell, B. F. and P. J. Ioannou, "Variance maintained by stochastic forcing of non-normal dynamical systems associated with linearly stable shear flows", in: *Phys. Rev. Lett.* 72.*8* (Feb. 1994), pp. 1188–1191.

Ferrari, R. and C. Wunsch, "Ocean Circulation Kinetic Energy: Reservoirs, Sources, and Sinks", in: *Annu. Rev. Fluid Mech.* 41.*1* (2009), pp. 253–282.

Garrett, C. and E. Kunze, "Internal Tide Generation in the Deep Ocean", in: *Annu. Rev. Fluid Mech.* 39.*1* (2007), pp. 57–87.

Garrett, C. and W. Munk, "Internal Waves in the Ocean", in: *Annu. Rev. Fluid Mech.* 11.*1* (1979), pp. 339–369.

— "Space-time scales of internal waves: A progress report", in: *J. Geophys. Res.* 80.*3* (1975), pp. 291–297.

Gill, A. E., *Atmosphere-ocean dynamics*, International geophysics series, New York: Academic Press, 1982.

Godreche, C. and P. Manneville, "Hydrodynamics and nonlinear instabilities", in: *Cambridge University Press* 9.*45* (1998), p. 1723.

Ha, K., J-M. Chomaz, and S. Ortiz, "Transient growth, edge states, and repeller in rotating solid and fluid", in: *Phys. Rev. E* 103.*3* (Mar. 2021), p. 033102.

Hasselmann, K., "A criterion for nonlinear wave stability", in: *J. Fluid Mech.* 30.*4* (Dec. 1967), pp. 737–739.

Hieronymus, M. et al., “Oceanic Overturning and Heat Transport: The Role of Background Diffusivity”, in: *J. Climate* 32.*3* (Feb. 2019), pp. 701–716.

Holm, D. D. and P. Lynch, “Stepwise Precession of the Resonant Swinging Spring”, in: *SIAM J. Appl. Dyn. Syst.* 1.*1* (Jan. 2002), pp. 44–64.

Holton, J. et al., “Stratosphere-Troposphere Exchange”, in: *Rev. Geophys.* 33 (Nov. 1995), pp. 403–439.

Huang, R. X., *Ocean Circulation: Wind-Driven and Thermohaline Processes*, Cambridge University Press, 2010.

Irps, T. and V. Kanjirakkad, “On the interaction between turbulence grids and boundary layers”, in: *EPJ Web of Conferences* 114 (2016), p. 02048.

Itoh, N., “Nonlinear stability of parallel flows with subcritical Reynolds numbers. Part 2. Stability of pipe Poiseuille flow to finite axisymmetric disturbances”, in: *J. Fluid Mech.* 82.*3* (Sept. 1977), pp. 469–479.

Jochum, M. et al., “The Impact of Oceanic Near-Inertial Waves on Climate”, in: *J. Climate* 26.*9* (May 2013), pp. 2833–2844.

Joyce, T. M., “Nonlinear interactions among standing surface and internal gravity waves”, in: *J. Fluid Mech.* 63.*4* (May 1974), pp. 801–825.

Jurkus, A. and P. N. Robson, “Saturation effects in a travelling-wave parametric amplifier”, in: *Proc. IEE. B, Electron. Commun. Eng.* 107.*32* (Mar. 1960), pp. 119–122.

Klymak, J. M., S. Legg, and R. Pinkel, “A Simple Parameterization of Turbulent Tidal Mixing near Supercritical Topography”, in: *J. Phys. Oceanogr.* 40.*9* (May 2010), pp. 2059–2074.

Koudella, C. R. and C. Staquet, “Instability mechanisms of a two-dimensional progressive internal gravity wave”, in: *J. Fluid Mech.* 548 (Feb. 2006), pp. 165–196.

Kunze, E., “The Internal-Wave-Driven Meridional Overturning Circulation”, in: *J. Phys. Oceanogr.* 47.*11* (Nov. 2017), pp. 2673–2689.

Laney, C. B., *Computational Gasdynamics*, Cambridge University Press, June 1998.

Le Bars, M., D. Cebron, and P. Le Gal, “Flows Driven by Libration, Precession, and Tides”, in: *Annu. Rev. of Fluid Mech.* 47.*1* (2015), pp. 163–193.

Lefauve, A., C. Muller, and A. Melet, “A three-dimensional map of tidal dissipation over abyssal hills”, in: *J. Geophys. Res.: Oceans* 120.*7* (2015), pp. 4760–4777.

Legg, S., “Scattering of Low-Mode Internal Waves at Finite Isolated Topography”, in: *J. Phys. Oceanogr.* 44.*1* (Jan. 2014), pp. 359–383.

Legg, S. and A. Adcroft, “Internal Wave Breaking at Concave and Convex Continental Slopes*”, in: *J. Phys. Oceanogr.* 33 (Jan. 2002).

Lynch, P., “Resonant Rossby Wave Triads and the Swinging Spring”, in: *Bull. Amer. Meteor. Soc.* 84.*5* (May 2003), pp. 605–616.

MacKinnon, J. A. et al., “Climate Process Team on Internal Wave-Driven Ocean Mixing”, in: *Bull. Am. Meteorol. Soc.* 98.*11* (Nov. 2017), pp. 2429–2454.

MacKinnon, J. A. et al., "Parametric Subharmonic Instability of the Internal Tide at 29řN", in: *J. Phys. Oceanogr.* 43.*1* (Jan. 2013), pp. 17–28.

Manley, J. M. and H. E. Rowe, "Some General Properties of Nonlinear Elements-Part I. General Energy Relations", in: *Proc. IRE* 44.*7* (July 1956), pp. 904–913.

Marshall, J. et al., "A finite-volume, incompressible Navier Stokes model for studies of the ocean on parallel computers", in: *J. Geophys. Res.: Oceans* 102.*C3* (1997), pp. 5753–5766.

Martini, K. et al., "Internal bores and breaking internal tides on the Oregon continental slope", in: (2013).

McComas, C. H. and F. P. Bretherton, "Resonant interaction of oceanic internal waves", in: *J. Geophys. Res.* 82.*9* (Mar. 1977), pp. 1397–1412.

McEwan, A. D., "Degeneration of resonantly-excited standing internal gravity waves", in: *J. Fluid Mech.* 50.*3* (Dec. 1971), pp. 431–448.

McEwan, A. D. and R. A. Plumb, "Off-resonant amplification of finite internal wave packets", in: *Dynam. Atmos. Oceans* 2.*1* (Dec. 1977), pp. 83–105.

McGoldrick, L. F., "Resonant interactions among capillary-gravity waves", in: *J. Fluid Mech.* 21.*2* (Feb. 1965), pp. 305–331.

Melet, A., S. Legg, and R. Hallberg, "Climatic Impacts of Parameterized Local and Remote Tidal Mixing", in: *J. Climate* 29.*10* (Dec. 2015), pp. 3473–3500.

Melet, A. et al., "Sensitivity of the Ocean State to Lee Wave-Driven Mixing", in: *J. Phys. Oceanogr.* 44.*3* (Mar. 2014), pp. 900–921.

Melet, A. et al., "Sensitivity of the Ocean State to the Vertical Distribution of Internal-Tide-Driven Mixing", in: *J. Phys. Oceanogr.* 43.*3* (Dec. 2012), pp. 602–615.

Mied, R. P., "The occurrence of parametric instabilities in finite-amplitude internal gravity waves", in: *J. Fluid Mech.* 78.*4* (Dec. 1976), pp. 763–784.

Moffatt, H. K., "Note on the triad interactions of homogeneous turbulence", in: *J. Fluid Mech.* 741 (Feb. 2014), R3.

Mowbray, D. E. and B. S. H. Rarity, "A theoretical and experimental investigation of the phase configuration of internal waves of small amplitude in a density stratified liquid", in: *J. Fluid Mech.* 28.*1* (Apr. 1967), pp. 1–16.

— "The internal wave pattern produced by a sphere moving vertically in a density stratified liquid", in: *J. Fluid Mech.* 30.*3* (Nov. 1967), pp. 489–495.

Müller, P. and D. J. Olbers, "On the dynamics of internal waves in the deep ocean", in: *J. Geophys. Res.* 80.*27* (1975), pp. 3848–3860.

Munk, W. and C. Wunsch, "Abyssal recipes II: energetics of tidal and wind mixing", in: *Deep Sea Res. I* 45.*12* (Dec. 1998), pp. 1977–2010.

Mysak, L. A. and M. S. Howe, "A kinetic theory for internal waves in a randomly stratified fluid", in: *Dynam. Atmos. Oceans* 1.*1* (July 1976), pp. 3–31.

Oks, D. et al., “Inverse cascades and resonant triads in rotating and stratified turbulence”, in: *Phys. Fluids* 29.*11* (Nov. 2017), p. 111109.

Phillips, O. M., “Energy Transfer in Rotating Fluids by Reflection of Inertial Waves”, in: *Phys. Fluids* 6.*4* (Apr. 1963), pp. 513–520.

— “On the dynamics of unsteady gravity waves of finite amplitude Part 1. The elementary interactions”, in: *J. Fluid Mech.* 9.*2* (Oct. 1960), pp. 193–217.

— *The dynamics of the upper ocean*, 2d ed, Cambridge monographs on mechanics and applied mathematics, Cambridge ; New York: Cambridge University Press, 1966.

— “The interaction trapping of internal gravity waves”, in: *J. Fluid Mech.* 34.*2* (1968), pp. 407–416.

Pippard, A. B., “Momentum and pseudo-momentum: I. classical pseudo-momentum and wave pressure”, in: *Eur. J. Phys.* 13.*2* (Mar. 1992), pp. 82–87.

Reddy, S. C. and D. S. Henningson, “Energy growth in viscous channel flows”, in: *J. Fluid Mech.* 252 (July 1993), pp. 209–238.

Richet, O., J.-M. Chomaz, and C. Muller, “Internal Tide Dissipation at Topography: Triadic Resonant Instability Equatorward and Evanescent Waves Poleward of the Critical Latitude”, in: *J. Geophys. Res.* 123.*9* (2018), pp. 6136–6155.

Ripa, P., “On the theory of nonlinear wave-wave interactions among geophysical waves”, in: *J. Fluid Mech.* 103 (Feb. 1981), pp. 87–115.

Roach, P. E., “The generation of nearly isotropic turbulence by means of grids”, in: *International J. Heat and Fluid Flow* 8.*2* (June 1987), pp. 82–92.

Schmid, P. J. and D. S. Henningson, “Optimal energy density growth in Hagen-Poiseuille flow”, in: *J. Fluid Mech.* 277 (Oct. 1994), pp. 197–225.

Schneider, T. M. and B. Eckhardt, “Edge states intermediate between laminar and turbulent dynamics in pipe flow”, in: *Philos. Trans. R. Soc. A* 367.*1888* (Feb. 2009), pp. 577–587.

Siedler, G., J. Church, and J. Gould, *Ocean circulation and climate: observing and modelling the global ocean*, San Diego: Academic Press, 2001.

Simmons, W. F. and M. J. Lighthill, “A variational method for weak resonant wave interactions”, in: *Proc. Roy. Soc. Lond.* 309.*1499* (Apr. 1969), pp. 551–577.

Smith, L. M. and F. Waleffe, “Generation of slow large scales in forced rotating stratified turbulence”, in: *J. Fluid Mech.* 451 (Jan. 2002), pp. 145–168.

— “Transfer of energy to two-dimensional large scales in forced, rotating three-dimensional turbulence”, in: *Phys. Fluids* 11.*6* (June 1999), pp. 1608–1622.

Sutherland, B. R., “Large-amplitude internal wave generation in the lee of step-shaped topography”, in: *Geophys. Res. Lett.* 29.*16* (2002), pp. 16–1–16–4.

Talley, L., “Closure of the Global Overturning Circulation Through the Indian, Pacific, and Southern Oceans: Schematics and Transports”, in: *Oceanogr.* 26 (Mar. 2013), pp. 80–97.

Thomson, W., “On An Experimental Illustration of Minimum Energy”, in: *Nature* 23.*577* (Nov. 1880), pp. 69–70.

Trefethen, L. N. et al., “Hydrodynamic Stability Without Eigenvalues”, in: *Science* 261.*5121* (July 1993), pp. 578–584.

Tuerena, R. E. et al., “Internal Tides Drive Nutrient Fluxes Into the Deep Chlorophyll Maximum Over Mid-ocean Ridges”, in: *Glob. Biogeochem. Cycles* 33.*8* (2019), pp. 995–1009.

Van Damme, L., P. Mardesic, and D. Sugny, “The tennis racket effect in a three-dimensional rigid body”, in: *Physica D* 338 (Jan. 2017), pp. 17–25.

Waleffe, F., “The nature of triad interactions in homogeneous turbulence”, in: *Phys. Fluids* 4.*2* (Feb. 1992), pp. 350–363.

Weiland, J. and H. Wilhelmsson, “Coherent non-linear interaction of waves in plasmas”, in: *Oxford : Pergamon* 88 (1977).

Whalen, C., J. MacKinnon, and L. Talley, “Large-scale impacts of the mesoscale environment on mixing from wind-driven internal waves”, in: *Nat. Geosci.* 11 (Nov. 2018).

Whalen, C. et al., “Internal wave-driven mixing: governing processes and consequences for climate”, in: *Nature Reviews Earth & Environment* (Oct. 2020), pp. 1–16.

Whitham, G. B., “A general approach to linear and non-linear dispersive waves using a Lagrangian”, in: *J. Fluid Mech.* 22.*2* (June 1965), pp. 273–283.

Wunsch, C. and R. Ferrari, “Vertical Mixing, Energy, and the General Circulation of the Oceans”, in: *Annu. Rev. Fluid Mech.* 36.*1* (2004), pp. 281–314.

ECOLE DOCTORALE

Titre : Dynamique transitoire et nonlinéaire de la résonance triadique des ondes internes

Mots clés : croissance transitoire, ondes internes, instabilité triadique résonante

Résumé : La régulation du réchauffement climatique par l'océan dépend du mélange vertical de masses d'eau profondes résultant du déferlement d'ondes internes générées par l'interaction entre la marée barotrope et la topographie du fond marin. Le mélange induit par ces ondes internes entre les couches stratifiées de l'océan profond joue un rôle essentiel dans la remontée des eaux abyssales froides, contribuant au transport de chaleur et de sel, ainsi que de nutriments et de carbone, à travers l'océan entier sur des cycles de l'ordre de 1000 ans.
Les interactions onde-onde sont l'un des mécanismes responsables de la dissipation, du mélange et du déferlement des ondes internes en transférant de l'énergie à différentes échelles. Trois ondes internes sont susceptibles d'interagir à travers l'interaction triadique résonante, une interaction faiblement non linéaire qui se produit lorsqu'une onde propagative est perturbée par deux autres ondes, les trois ondes devant obéir à des conditions de résonances spatio-temporelles. Les théories classiques ont montré que ce système triadique devient instable si le critère d'Hasselmann est respecté. Cependant, aucune théorie existante n'explique le comportement court terme de l'instabilité triadique résonante.
Ce projet propose d'analyser la dynamique initiale des triades résonantes en montrant qu'une perturbation de petite énergie affectant l'état de base, une onde interne se propageant dans un milieu stratifié tournant, pourrait être affectée par des croissances transitoires intenses par rapport à une norme énergie bien définie, cette amplification étant plus fortes initialement pour des triades linéairement stables plutôt qu'instables. Les plus fortes transitoires sont caractéristiques de triades à l'origine d'un mode quasi-inertiel générant du cisaillement : le mode horizontal cisaillé verticalement. La sensibilité de tels transitoires à différents paramètres physiques comme la rotation terrestre, la viscosité et les effets non linéaires est testée à l'aide de simulations théoriques, et dans des configurations géophysiques reproduites par un code numérique du climat, le MITgcm.

Title : Transient and nonlinear dynamics of triadic resonance for internal waves

Keywords : transient growth, internal waves, triadic resonant instability

Abstract : Global warming regulation by the ocean depends on the vertical mixing of deep water masses resulting from the breaking of internal waves generated by the interaction between barotropic tides with the ocean floor topography. Internal wave driven mixing of stratified layers in the deep ocean plays an important role in the rise of abyssal cold water, ultimately contributing to the transport of heat and salt, as well as nutrients and carbon, throughout the entire ocean over 1000-year cycles.
Wave-wave interactions are one of the physical mechanisms responsible for the dissipation, mixing and breaking of internal waves by transferring energy to different scales. Three internal waves may interact through triadic resonance, a weakly nonlinear interaction that occurs when a single propagating wave is perturbed by two other waves, all three waves obeying to the spatial and temporal resonance conditions. Classical theories have shown that the present triadic system becomes unstable if Hasselmann's criterion is respected. However, none of the existing theories explains the short term behavior of the triadic resonant instability.
The present project investigates the early stage dynamics of resonant triads by showing that a small energy perturbation to the base state, a single internal wave propagating in a stratified rotating medium, may experience tremendous transient growth with respect to a well-defined energy norm, this amplification being higher at initial instants for linearly stable triads than unstable ones. The maximum transients are found for triads involving one nearly inertial mode that generates shear : the vertically sheared horizontal flow mode. The sensitivity of these transients to different physical parameters such as Earth rotation, viscosity and nonlinear effects is tested with theoretical simulations, and in geophysical configurations using a numerical code for climate modeling, the MITgcm.

Institut Polytechnique de Paris
91120 Palaiseau, France